

# Solar-Thermal Conversion to Electricity Utilizing a Central Receiver, Open-Cycle Gas Turbine Design

JD

**EPRI**

EPRI ER-652  
Project 475-1  
Final Report  
March 1978

Keywords:

Solar-Thermal Conversion  
Solar-Energy  
Central Receiver Electric Power  
Open-Cycle Gas Turbine

475-1

Prepared by  
Black & Veatch Consulting Engineers  
Kansas City, Missouri

**ELECTRIC POWER RESEARCH INSTITUTE**

Solar-Thermal Conversion to Electricity  
Utilizing a Central Receiver, Open-Cycle,  
Gas Turbine Design

---

ER-652  
Research Project 475-1

Final Report, March 1978

Prepared by

BLACK & VEATCH CONSULTING ENGINEERS  
P.O. Box 8405  
Kansas City, Missouri 64114

Principal Investigator  
J. C. Grosskreutz

Prepared for

Electric Power Research Institute  
3412 Hillview Avenue  
Palo Alto, California 94304

EPRI Project Manager  
John E. Cummings  
Fossil Fuel and Advanced Systems Division

LEGAL NOTICE

This report was prepared by Black & Veatch Consulting Engineers (B&V), as an account of work sponsored by the Electric Power Research Institute, Inc. (EPRI). Neither EPRI, members of EPRI, B&V, or any person acting on behalf of either: (a) makes any warranty or representation, express or implied, with respect to the accuracy, completeness, or usefulness of the information contained in this report, or that the use of any information, apparatus, method, or process disclosed in this report may not infringe privately owned rights; or (b) assumes any liabilities with respect to the use of, or the damages resulting from the use of, any information, apparatus, method, or process disclosed in this report.

## ABSTRACT

This project was the initial activity in a program to develop a solar/electric power plant which utilizes an open cycle gas turbine as the prime mover. Black & Veatch was the prime contractor; Honeywell, Inc. and the Engineering Experiment Station at the Georgia Institute of Technology were subcontractors to Black & Veatch.

A conceptual design for a commercial-scale plant, with a nominal rating of 60 MWe, was prepared. The characteristics of that baseline design, which employs an elevated central receiver surrounded by a field of heliostats, are presented. The turbine is a General Electric MS 7001R, and is located near the top of a 213 M (700 ft) tower. There are four receiver cavities, located at the top of that tower, each facing one quadrant of the heliostat field. That heliostat field contains about seven thousand heliostats, each with a reflecting surface area of  $37.2 \text{ M}^2$  ( $400 \text{ ft}^2$ ). Energy storage, both buffer and long-term, is provided by fossil fuels. The fuel, either oil or gas, is burned in combustors which are in a parallel arrangement with the solar receivers.

The turbine inlet gas temperature is  $982\text{-}1066^\circ\text{C}$  ( $1800\text{-}1950^\circ\text{F}$ ). Because these temperatures preclude the use of any available metal for the heat transfer surface, ceramics are employed. Each of the four receiver cavities contains about seventy U-tubes. Each leg of each U-tube is about 12 M (40 ft) in length; the tubes are 10 CM (4 inches) in diameter; the tube material is silicon carbide. Although many of the properties of silicon carbide are well documented, this material has never been utilized in an application of this type. Therefore, a series of experiments were carried out at Georgia Tech. These experiments verified the suitability of silicon carbide for an application of this type and also verified the analytic methodology which had been used in the receiver design activities.

Certain components of the system are not currently commercially available. These components have been identified.

The next activity in this program is the design, fabrication, and testing of a bench model solar receiver, employing silicon carbide tubes. Preliminary estimates of the physical and operating characteristics of such a bench model were developed.

## ACKNOWLEDGEMENTS

The prime contractor for the work described in this report has been Black & Veatch Consulting Engineers, Kansas City, Missouri. Black & Veatch responsibilities were project management, heat exchanger configuration and heat transfer analysis, receiver/turbine interface design, and overall system baseline design. Black & Veatch was assisted by two subcontractors, Honeywell Systems and Research Center, Minneapolis, Minnesota, and the Engineering Experiment Station, Georgia Institute of Technology, Atlanta, Georgia. The primary responsibilities of these two subcontractors were: Honeywell, heliostat field/receiver geometry and solar flux maps in the receiver cavity; Georgia Tech, candidate receiver materials testing and heat exchanger configuration testing (thermal cycling).

Personnel participating in the project from the three institutions were as follows:

Black & Veatch:

D.C. Gray  
J.C. Grosskreutz  
J.K. Kintigh  
S.L. Levy  
E.J. McBride  
H.W. Strohm

Honeywell:

E. Fourakis  
Paul Mitchell

Georgia Tech:

J. N. Harris  
Art Sayles  
Jim Tarter  
J.D. Walton

Project Manager for the project was J.C. Grosskreutz of Black & Veatch.

The interest, constructive advice and support of EPRI personnel and utility representatives is gratefully acknowledged. Dr. John Cummings was Project Manager for EPRI and the project was part of the general EPRI solar program under the direction of Mr. Piet Bos.

## CONTENTS

<u>Section</u>		<u>Page</u>
1	INTRODUCTION	1-1
	PROJECT APPROACH	1-1
	FINAL REPORT STRUCTURE	1-2
2	SUMMARY	2-1
	THE OPEN BRAYTON CYCLE	2-1
	THE OPEN-CYCLE, SOLAR-THERMAL, CENTRAL-RECEIVER SYSTEM	2-2
	MAJOR SUBSYSTEMS	2-3
	Heliostat Field/Receiver Configuration	2-3
	Electric Power Generation Equipment	2-4
	Receiver Cavity/Heat Exchanger	2-4
	Storage Devices	2-5
	BASELINE CONCEPTUAL DESIGN	2-6
	System Layout and Specification Summary	2-6
	System Performance	2-7
	Categorization of Loss Mechanisms	2-7
	System Cost Summary	2-9
	Origin of Cost Estimates	2-9
3	HELIOSTAT FIELD/RECEIVER CONFIGURATION DESIGN	3-1
	CONFIGURATION OPTIONS AND CHOICES	3-2
	Heliostat Field	3-3
	Receiver	3-6
	HELIOSTAT FIELD LAYOUT	3-15
	Ground Cover Design Option	3-16
	Nonuniform Field Design	3-24
	Baseline Field Analysis	3-29
4	RECEIVER CAVITY AND HEAT EXCHANGER DESIGN	4-1
	FUNDAMENTALS OF HIGH-TEMPERATURE, CAVITY-TYPE HEAT EXCHANGERS	4-1
	Important Parameters	4-1
	Cavity Efficiency	4-2

CONTENTS (Cont.)

<u>Section</u>	<u>Page</u>
HEAT TRANSFER SURFACE CANDIDATE MATERIALS	4-3
Metals	4-3
Ceramics	4-5
HEAT TRANSFER SURFACE GEOMETRIES	4-6
Tube-Type Geometry	4-6
Extended Surface Geometry	4-7
HEAT TRANSFER SURFACE DESIGN ANALYSIS	4-9
Analytic Methodology	4-9
Results of Analyses	4-10
SELECTION OF HEAT TRANSFER SURFACE GEOMETRY	4-14
MATERIALS SELECTION	4-15
CAVITY HEAT EXCHANGER DESIGN	4-16
U-Tube Design	4-16
Cavity Sizing	4-17
Receiver Housing	4-19
CAVITY PERFORMANCE	4-20
Detailed Cavity Performance	4-20
Cavity Efficiency	4-23
Transient Effects	4-25
5 HEAT EXCHANGER TUBE TESTS AND EVALUATIONS	5-1
TEST PHILOSOPHY AND OBJECTIVES	5-1
SUMMARY OF CONCLUSIONS	5-1
THERMOOPTICAL PROPERTY DETERMINATION	5-2
VERIFICATION OF ANALYTICAL METHODOLOGY	5-2
Experiment Setup	5-4
Test Procedure	5-5
Data Acquisition	5-5
Test Results	5-5
Conclusions	5-7
HEAT EXCHANGER CONFIGURATION TESTING	5-7
Thermal-Cycling Resistance	5-7
Experiment Design	5-7
Experiment Setup	5-8
Test Procedure	5-8
Data Acquisition	5-8

CONTENTS (Cont.)

<u>Section</u>		<u>Page</u>
	Test Specimen	5-10
	Thermal-Cycling Test Results	5-10
	Conclusions	5-11
6	GAS TURBINE SELECTION, INTERFACES, AND HYBRID OPERATION	6-1
	OBJECTIVES	6-1
	GAS TURBINE SELECTION	6-2
	Simple vs. Regenerative Cycle	6-2
	Calculation of Cycle Efficiency	6-3
	Selection of Commercial Baseline Turbine	6-7
	Potential Choice of Small, 2- to 3-MWe Pilot Plant Turbine	6-10
	HYBRID OPERATION	6-11
	Objectives	6-12
	Arrangement Options and Choice	6-12
	Adaptability of Baseline Turbine to Hybrid Operation	6-16
	Conceptual Design/Performance	6-17
	INTERFACE DUCTING	6-21
	Objectives	6-21
	Requirements	6-21
	High-Temperature Ducting Design/Test	6-23
	High-Temperature Isolation Valve Design	6-25
	Turbine Interface Layout	6-26
7	RECEIVER TOWER DESIGN	7-1
	REQUIREMENTS AND DESIGN CHOICES	7-1
8	SYSTEM COSTS	8-1
	COLLECTOR/CONCENTRATION SUBSYSTEM	8-1
	HEAT TRANSFER SUBSYSTEM	8-2
	ELECTRIC POWER GENERATION SUBSYSTEM	8-3
	RECEIVER TOWER SUBSYSTEM	8-4
	BALANCE OF PLANT SUBSYSTEM	8-6
	SYSTEM CAPITAL COST SUMMARY	8-7
	COMPARISON WITH EPRI STRAWMAN CAPITAL COST	8-8
	COMPARISON WITH EPRI STRAWMAN PERFORMANCE	8-10
9	BENCH-MODEL RECEIVER	9-1
	BENCH-MODEL RECEIVER DESIGN	9-1

CONTENTS (Cont.)

<u>Section</u>		<u>Page</u>
10	PROJECT CONCLUSIONS AND DEFINITION OF FUTURE DEVELOPMENT NEEDS	10-1
	FUTURE DEVELOPMENT REQUIREMENTS AND RECOMMENDATIONS	10-2
Appendix A	POTENTIAL CERAMIC MATERIALS FOR HEAT EXCHANGER APPLICATIONS	A-1
Appendix B	MEASUREMENT OF THE RADIATIVE PROPERTIES OF TWO MATERIALS: SILICON CARBIDE AND CORDIERITE	B-1
	INTRODUCTION	B-2
	METHOD OF MEASUREMENT	B-2
	RESULTS	B-3
	REFERENCES	B-3
Appendix C	EXPERIMENTAL VALIDATION OF THE ANALYTICAL HEAT TRANSFER MODEL	C-1
	INTRODUCTION	C-2
	EXPERIMENT SETUP	C-2
	TEST PROCEDURE	C-3
	DATA ACQUISITION	C-6
	TEST RESULTS	C-7
	Flux Level Measurements	C-7
	Silicon-Carbide Tube Tests	C-10
	Cordierite Tube Tests	C-10
	Fused-Silica Tube Tests	C-10
	ANALYTICAL MODEL VALIDATION	C-13
	CONCLUSIONS	C-14
Appendix D	THERMAL-CYCLE TESTING OF THE HEAT EXCHANGER U-TUBE CONFIGURATION	D-1
	INTRODUCTION	D-2
	TESTING METHODOLOGY	D-2
	EXPERIMENT DESIGN	D-2
	EXPERIMENT SETUP	D-3
	TEST PROCEDURE	D-8
	DATA ACQUISITION	D-8
	TEST SPECIMEN	D-9
	TEST RESULTS	D-11
	CONCLUSIONS	D-13

CONTENTS (Cont.)

<u>Section</u>		<u>Page</u>
Appendix E	SUITABILITY OF SiC FOR HIGH-TEMPERATURE SOLAR COLLECTOR/ HEAT EXCHANGERS	E-1
	INTRODUCTION	E-2
	SiC GRAIN PRODUCTION	E-2
	FORMATION OF DENSIFIED SiC	E-5
	PROPERTIES OF SiC	E-7
	Strength	E-8
	Creep/Fatigue Resistance	E-9
	Physical Properties	E-10
	JOINING TECHNIQUES	E-10
	Ceramic-Ceramic Joints	E-10
	Ceramic-Metal Joints	E-12
	CERAMIC DESIGN METHODOLOGY	E-12
	FABRICATION OF LARGE SiC STRUCTURES	E-14
	SUMMARY	E-14
	REFERENCES	E-15
Appendix F	RECEIVER TOWER DESIGN	F-1
	OBJECTIVE	F-2
	DESIGN CRITERIA	F-2
	Plant Site Criteria Affecting the Structural Design	F-2
	Tower-Height Considerations	F-2
	Geometry	F-2
	Loads	F-2
	Structural Materials	F-3
	Design Codes and References	F-3
	Construction and Erection Considerations	F-3
	STRUCTURAL DESIGN OF SUPPORT TOWER	F-4
	Design Criteria	F-4
	Economic Criteria	F-4
	Analysis and Design Procedure	F-4
	Results of the Study of Four Possible Configurations	F-5
	Conclusions	F-8
	STRUCTURAL DESIGN OF TOWER FOUNDATION	F-8
	Design Criteria	F-8
	Analysis and Design Procedure	F-8

CONTENTS (Cont.)

<u>Section</u>	<u>Page</u>
Results of the Study of Four Possible Configurations	F-9
ECONOMIC COMPARISON OF THE FOUR POSSIBLE CONFIGURATIONS	F-9
Comparison Criteria	F-9
Results of the Comparative Study	F-9
Conclusions	F-9
WIND DEFLECTIONS OF TOWER	F-9
STRUCTURAL DESIGN OF TURBINE GENERATOR SUPPORT STRUCTURE	F-10
Design Criteria	F-10
Conceptual Design of the Support Structure	F-11
STRUCTURAL DESIGN OF CAVITY RECEIVERS AND SUPPORT STRUCTURE	F-13
Design Criteria	F-13
Conceptual Design of the Receiver Support Structure	F-13
STRUCTURAL DESIGN OF BRACING SYSTEM	F-13
Design Criteria	F-13
Conceptual Design of the Bracing System	F-13
CONSTRUCTION AND INSTALLATION PROCEDURES	F-13
Foundation Mat Construction	F-13
Chimney Construction	F-15
Erection of Structural Steel for the Turbine Generator Support Structure	F-15
Erection of Structural Steel for the Cavity Receiver Support Structure	F-15
Installation of the Equipment	F-15
ELEVATORS, STAIRS, AND LADDERS	F-17

## ILLUSTRATIONS

<u>Figure</u>		<u>Page</u>
2-1	Open-Cycle Regenerative Gas Turbine Flow Diagram	2-2
2-2	Cutaway of Tube-Type Cavity Receiver/Heat Exchanger	2-5
2-3	Baseline Design System Flow Diagram	2-6
2-4	Perspective View of the Open-Cycle, Solar-Thermal, Central-Receiver System	2-7
2-5	Solar-Thermal, Hybrid Open-Cycle Gas Turbine System Performance (Single Timepoint)	2-9
3-1	North-Field Concept	3-4
3-2	Cosine Effect on Available Area of Mirror	3-4
3-3	360°-Field Concept	3-5
3-4	Cosine Effects on Field Efficiency	3-6
3-5	Alternative Field Configuration Costs	3-7
3-6	Baseline Multiple-Bullseye Cavity Receiver	3-7
3-7	Typical Plot for Optimizing Aperture Size	3-10
3-8	Illustration of Multiple-Bullseye Receiver Optical Path	3-11
3-9	Annulus Cavity Configuration	3-12
3-10	Two Duct Chimney Cavity Sizes	3-13
3-11	Illustration of Annulus Receiver Optical Paths	3-14
3-12	Annulus Dimensions	3-15
3-13	North-South Heliostat Spacing Ratio Geometry	3-19
3-14	Nonuniform Field North-South Mirror Spacing Ratio	3-20
3-15	North-South Spacing Ratio for Field Number 3	3-21
3-16	Percent of Area Blocking, North-South, Field Number 3	3-21
3-17	East-West Heliostat Spacing Ratio Geometry	3-22
3-18	Nonuniform Field West-East Mirror Spacing Ratio for No Shadowing or Blocking Between 9:00 a.m. and 3:00 p.m. on June 21	3-23
3-19	East-West Spacing Ratio Criteria for Field Number 3	3-23
3-20	Percent of Area Overlap, East-West, Field Number 3	3-24
3-21	Heliostat Field Number 1	3-26
3-22	Heliostat Field Number 2	3-27

ILLUSTRATIONS (Cont.)

<u>Figure</u>		<u>Page</u>
3-23	Heliostat Field Number 3	3-28
3-24	Plan View of Baseline Design Heliostat Field	3-28
4-1	Estimated Cavity Efficiency	4-4
4-2	Tube-Type Heat Transfer Surface Geometry	4-7
4-3	Extended Surface Heat Transfer Geometry	4-8
4-4	Tube-Type Receiver Layout	4-12
4-5	Tube Stresses as a Function of Design Parameters	4-12
4-6	Cutaway of Tube-Type Cavity Receiver/Heat Exchanger	4-17
4-7	North Cavity Wall Flux Map	4-21
4-8	North Cavity Ceiling Flux Map	4-21
4-9	North Cavity Wall Flux Map	4-22
4-10	North Cavity Wall Flux Map	4-23
4-11	North Cavity Maximum Tube Temperature	4-24
5-1	Directional Spectral Reflectance	5-3
5-2	Photograph of Single-Tube Test Apparatus	5-4
5-3	Comparison of Experimental and Calculated Temperature Distributions on Single Tube	5-6
5-4	Photograph of the Heat Exchanger U-Tube Test Apparatus	5-9
6-1	Simple and Regenerative, Ideal Brayton Cycles	6-3
6-2	Comparison of an Ideal Brayton Cycle to the Real Gas Turbine Cycle	6-5
6-3	Regenerative Gas Turbine Performance	6-6
6-4	Orientation Photograph of MS 7001R	6-8
6-5	Cutaway of MS 7001R	6-9
6-6	Orientation Picture of Solar Centaur	6-11
6-7	Possible Heat Source Arrangements	6-13
6-8	Flow Diagram of the Solar-Powered Open-Cycle Gas Turbine with Hybrid Operation Capability	6-18
6-9	External Combustor Subsystem (Conceptual)	6-20
6-10	Hot Air Duct Insulation	6-25
6-11	Perspective View of Receivers and Turbine Enclosure Atop the Tower	6-27
6-12	Elevation View of the Receiver/Turbine/Combustor System Arrangement	6-27
6-13	Turbine Operating Floor--Plan View	6-28
6-14	External Combustor Operating Floor--Plan View	6-28

ILLUSTRATIONS (Cont.)

<u>Figure</u>		<u>Page</u>
6-15	Cutaway of Tube-Type Cavity Receiver/Heat Exchanger	6-29
6-16	Plan View of the Cavity Receiver's Interfacing Piping Beneath the Cavity Support Structure	6-30
6-17	Plan View of the Cavity Receiver Arrangement Atop the Tower	6-31
6-18	Perspective of the Turbine/Central Receiver Interface Piping	6-33
7-1	Open-Cycle Gas Turbine Support Tower	7-3
8-1	Solar-Thermal, Hybrid Open-Cycle Gas Turbine System Performance	8-12
8-2	Baseline System Performance	8-12
B-1	Directional Spectral Reflectance	B-5
B-2	Directional Spectral Reflectance	B-6
B-3	Directional Spectral Reflectance	B-7
B-4	Directional Spectral Reflectance	B-8
B-5	Directional Spectral Reflectance	B-9
B-6	Directional Spectral Reflectance	B-10
B-7	Directional Spectral Reflectance	B-11
B-8	Directional Spectral Reflectance	B-12
B-9	Directional Spectral Reflectance	B-13
C-1	Photograph of Single-Tube Test Apparatus Without Reflector in Place	C-3
C-2	Flow Diagram for Single-Tube Test Apparatus	C-4
C-3	Electric Preheater-Ceramic Interface	C-5
C-4	Output Interface	C-6
C-5	Diagram of Tube Surface Thermocouple (T/C) Locations	C-7
C-6	Diagram of Heat Flux Sensor Locations	C-8
C-7	Comparison of Experimental and Calculated Temperature Distributions on Single Tube	C-15
C-8	Comparison of Experimental and Calculated Temperature Distributions on Single Tube	C-15
C-9	Comparison of Experimental and Calculated Temperature Distributions on Single Tube	C-16
C-10	Comparison of Experimental and Calculated Temperature Distributions on Single Tube	C-16
D-1	U-Tube Configuration, Thermal-Cycle Test Apparatus	D-4
D-2	Front View of Lamp Module	D-5
D-3	Reflecting Cavity of Thermal-Cycle Test Facility with Tube in Place	D-6

ILLUSTRATIONS (Cont.)

<u>Figure</u>		<u>Page</u>
D-4	U-Tube Thermal-Cycling Experiment Configuration	D-7
D-5	Hot-Side Header for Thermal-Cycle Test Apparatus	D-8
D-6	Cross Section of Cordierite Sleeve with Interior Shoulder	D-10
E-1	The Acheson Furnace for SiC Grain Production	E-3
E-2	Super KT-SiC Components Fabricated for EPRI Coal-Fired Heat Exchanger Program	E-6
E-3	Sintered $\alpha$ -SiC Components	E-7
E-4	Strength (3 pT Bend) of High-Performance Materials	E-9
F-1	EPRI Gas Turbine Support Tower	F-3
F-2	Loads	F-5
F-3	Plan View of Framing for Floor of Turbine Room	F-12
F-4	Plan View of Framing for Roof of Turbine Room	F-12
F-5	Structural Framing for Cavity Receiver/Heat Exchanger	F-14
F-6	Plan View of Framing for Cavity Support Floor	F-14
F-7	Equipment Installation Hoist	F-16

TABLES

<u>Table</u>		<u>Page</u>
2-1	Baseline Conceptual Design Summary	2-8
2-2	60-MWe Open-Cycle, Gas Turbine, Solar-Electric System-- Estimated Cost Summary (1976 Dollars)	2-10
3-1	Heliostat Characteristics	3-2
3-2	Heliostat Field Number 1--Field Characteristics	3-25
3-3	Heliostat Field Number 1--Receiver Characteristics	3-25
3-4	Heliostat Field Number 2--Characteristics	3-27
4-1	Cavity Size Analysis, Based on Four Sections of Heliostat Field at Noon, March 21	4-18
4-2	Cavity Diameters and Number of U-Tubes per Cavity	4-19
4-3	Cavity Aperture Diameters, Based on Analysis at Noon, March 21	4-19
4-4	Receiver Housing Materials and Thicknesses	4-20
4-5	Cavity Efficiencies	4-25
5-1	Emittance of Cordierite and Silicon Carbide	5-3
5-2	Convective Heat Transfer Coefficient	5-6
8-1	Estimated Collector/Concentrator Subsystem Costs (1976 Dollars)	8-2
8-2	Estimated Heat Transfer Subsystem Costs (1976 Dollars)	8-3
8-3	Estimated Electric Power Generation Subsystem Costs (1976 Dollars)	8-5
8-4	Estimated Receiver Support Subsystem Costs (1976 Dollars)	8-6
8-5	Estimated Balance of Plant Costs (1976 Dollars)	8-7
8-6	60-MWe Open-Cycle Gas Turbine Solar-Electric System Estimated Cost Summary (1976 Dollars)	8-8
8-7	Power Plant Cost Estimates Central Receiver Concept	8-9
9-1	Results of Bench-Model Design Preliminary Analysis	9-2
A-1	Thermophysical Properties of Selected Refractory Materials	A-2
B-1	Emittance of Cordierite and Silicon-Carbide Specimens	B-4
C-1	Measured Flux Levels	C-9
C-2	Heat Transfer Data for Silicon-Carbide Tube	C-11
C-3	Heat Transfer Data for Cordierite Tube	C-12

TABLES (Cont.)

<u>Table</u>		<u>Page</u>
C-4	Heat Transfer Data for Fused-Silica Tube	C-13
C-5	Convective Heat Transfer Coefficient	C-14
D-1	Thermal-Cycle Test Data on First Cordierite U-Tube	D-12
D-2	Thermal-Cycle Test Data on Second Cordierite U-Tube	D-14
E-1	Physical Properties of Ceramic Materials	E-10
F-1	Cost Comparison	F-6
F-2	Deflections at Turbine Floor Due to Wind	F-10

## Section 1

### INTRODUCTION

This project was initiated to develop a conceptual design of a central-receiver, solar-electric system which utilizes an open-cycle gas turbine as a prime mover. The two primary objectives of the project were to:

- Prepare a conceptual design for a high-temperature cavity receiver/heat exchanger suitable for commercial applications (100 to 200 Mwt) and capable of delivering compressed air at approximately 0.97 MPa (140 psia) and 982 to 1093°C (1800 to 2000°F)
- Identify practicable means and interfaces necessary for hybrid operation from either the solar receiver or a fossil fuel combustor, using existing turbomachinery to the maximum extent possible

Other important objectives were: to verify the performance of promising heat exchanger materials and design concepts by means of small-scale laboratory tests; to design the heliostat field and receiver cavity geometry for the most efficient operation of the open Brayton cycle; and to develop costs for the overall system design.

### PROJECT APPROACH

The approach to the conceptual design of the open-Brayton-cycle, solar-electric conversion system was as follows: First, the conceptual design of a commercial-size utility system (50 to 100 MWe) was addressed under the assumption that if this design were not feasible, then further development of small-scale pilot systems would not be justified. Second, because the conceptual design of the high-temperature solar receiver/heat exchanger required extension beyond the current state-of-the-art in the use of high-temperature materials, it was deemed necessary to subject both receiver materials and design concepts to qualification testing before selecting the final design. Third, after developing a feasible, commercial-scale system design, the requirements for design and test of a scaled-down, bench-model receiver were addressed. Although this design is preliminary in nature, it served to outline the scope and estimate the costs of a bench-model fabrication and testing program.

## FINAL REPORT STRUCTURE

This final report is a detailed account of the results obtained in achieving the objectives outlined above. The report begins with a summary of the final commercial baseline system design, including a brief description of the major subsystems. Following this summary, the next five sections describe the analysis and conceptual design of each subsystem: heliostat field/receiver configuration; receiver cavity/heat exchanger, including small-scale tests and evaluation; gas turbine selection; interfaces and hybrid operation; and receiver tower. System costs are then developed and the proposed 1-MWt bench-model receiver design is described. The appendices are devoted to the description of material properties, test results, tower design, and the suitability of silicon-carbide tubes for high-temperature solar heat exchangers.

## Section 2

### SUMMARY

Using the open Brayton cycle to convert solar energy to electricity requires that a system be designed that is substantially different from those which use the more familiar water/steam, Rankine cycle. The heliostat field/tower configuration and the receiver design must accommodate the much higher temperatures of the Brayton cycle (982 to 1093°C [1800 to 2000°F] air compared to 538°C [1000°F] steam) and keep radiation losses from the receiver to a minimum. Further, the gas turbine generator must be near the top of the receiver tower in order to minimize pressure losses. Finally, buffer and long-term storage must be provided by hybrid operation of the open-cycle gas turbine with fossil fuel during periods of solar outage.

This section presents an introductory system overview. The open Brayton cycle, the major subsystems, and the system baseline design are briefly described. A system efficiency and cost summary are also included.

### THE OPEN BRAYTON CYCLE

A schematic flow diagram for the open Brayton cycle is shown in Figure 2-1. The cycle operates as follows: Ambient air is compressed to about 0.931 MPa (135 psia) by means of a compressor, usually on a common shaft with the gas turbine that drives it. In hot climates an evaporative cooler may be used to cool the intake air, thus reducing the work of compression. Compression to 0.931 MPa (135 psia) normally raises the air temperature to ~288°C (~550°F). In the regenerative Brayton cycle further preheating is achieved by passing the compressed air through a regenerative heat exchanger where heat from turbine exhaust gases raises the air temperature to ~482°C (~900°F).

From this point, the preheated air may enter either a fossil fuel combustor or a solar receiver heat source where it is heated to a turbine inlet temperature of 982 to 1093°C (1800 to 2000°F). Finally, the heated air expands through the turbine and is exhausted through the regenerator. More than half of the work done by the turbine is used to drive the compressor. The remaining work is available for electric power generation.

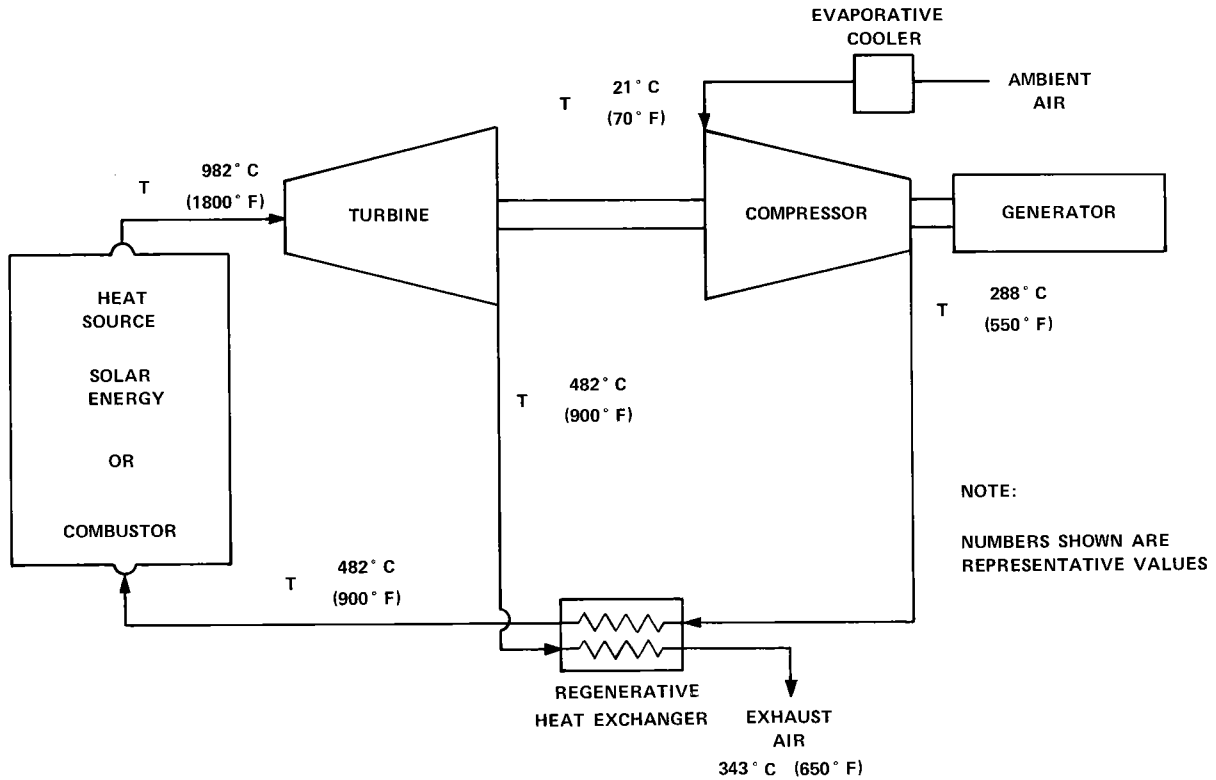


Figure 2-1. Open-Cycle Regenerative Gas Turbine Flow Diagram

THE OPEN-CYCLE, SOLAR-THERMAL, CENTRAL-RECEIVER SYSTEM

This system uses an array of tracking heliostats to concentrate solar radiation into a central receiver placed on top of a tower. Within the receiver the concentrated solar radiation heats compressed air which in turn drives a gas turbine as previously described.

This system has several outstanding advantages:

- Thermal-cycle efficiencies of 40- to 45-percent are possible (based on regenerative-cycle gas turbines with 982 to 1093°C [1800 to 2000°F] turbine inlet air).
- The open-cycle gas turbine does not require a cooling tower.
- Only a small amount of water is required, e.g., personnel and maintenance requirements.
- Gas turbines may be designed for mounting near the top of the receiver tower.
- Auxiliary fuel can provide energy during periods of solar outage.
- Gas turbines are designed for cycling and quick starts.
- Capital costs per installed kilowatt are substantially less than for water/steam Rankine-cycle designs.

In order to reap these advantages, the system designed must (1) be capable of heating air to the desired temperatures with solar radiation and (2) use existing gas turbines with a minimum of modification.

#### MAJOR SUBSYSTEMS

The open-cycle, solar-thermal, central-receiver system has four major subsystems: the heliostat field/receiver configuration, electric power generation equipment, the receiver cavity/heat exchanger, and the storage devices. These subsystems are interdependent, and each subsystem was designed by considering the constraints and requirements imposed by the other subsystems.

#### Heliostat Field/Receiver Configuration

In the central receiver system, the heliostat field/receiver configuration collects the solar radiation falling on a large area of ground and concentrates it at a central point. This configuration can be thought of as a degenerate parabolic dish spread flat upon the ground and made up of individual facets (heliostats) which track the sun. The focal point of this dish is the receiver located on top of a tower in the heliostat field. The field/receiver configuration is therefore an interdependent design problem.

The position of the receiver tower in the field is determined by the latitude of the field. At the equator the tower would be in the center of the field. In the northern hemisphere the tower is located south of center, the exact position depending on latitude and the specific design characteristics of the heliostat field and the receiver. If the tower is completely surrounded by heliostats, the configuration is called a 360° field; if the tower is located at the extreme southern edge of the field, it is called a north-field (N-field) configuration. Both 360° fields and N-fields were considered in the subsystem design. A 360° heliostat field was chosen because it achieves lower total heliostat-tower costs, lower tower height, and higher receiver efficiency. The tower is located about one-third the distance from the center to the south edge of the field.

With a 360°-field configuration, the receiver may be either a single cavity with multiple apertures to admit the concentrated solar radiation, or multiple cavities, each with a single aperture. Four independent cavities, each facing a 90° sector of the heliostat field, were chosen for the central receiver configuration because overall system efficiency and operational flexibility were enhanced and because turbine/receiver interface ducting was simplified.

The height of the receiver tower was established to minimize the trade-off between shadowing and blocking of neighboring heliostats and tower cost.

#### Electric Power Generation Equipment

The gas turbine for the electric power generation subsystem has several design requirements. The heat rate (or cycle efficiency) of the turbine establishes the amount of solar-thermal energy required from the receiver and, hence, the size of the heliostat field/receiver subsystem. The firing temperature of the turbine specifies the required heat exchanger outlet air temperature, and the compression ratio establishes the compressor outlet air pressure. The General Electric MS 7001R gas turbine, nominally rated at 60 MWe, was selected for the conceptual baseline design because it is the largest regenerative gas turbine expected to be commercially available in the mid-1980s.

#### Receiver Cavity/Heat Exchanger

Design of the receiver cavity/heat exchanger is the most important problem addressed in this project. The receiver must be capable of:

- Producing outlet air temperature in the range of 982 to 1093°C (1800 to 2000°F)
- Minimizing pressure drop between compressor and turbine
- Withstanding internal gas pressure of ~0.931 MPa (~135 psia) and total tensile stresses of 34 to 68 MPa (5000 to 10,000 psi) at working temperatures of ~1200°C (2200°F)
- Minimizing losses by reradiation, reflection, and convection

Because of the importance of this subsystem to the success of the overall open-cycle conversion system, laboratory tests of candidate materials and model heat exchanger designs were carried out to support the final conceptual design.

The receiver design consists of a right, octagonal cylindrical cavity with a vertical aperture facing a 90° heliostat field sector. The cavity heat transfer surface is a series of parallel, vertical U-tubes spaced circumferentially around the inside perimeter of the cavity. The U-tube cavity is shown in Figure 2-2. Both the inlet and outlet headers are beneath the cavity floor.

The U-tubes, constructed of 10-centimeter (4-inch) diameter, thin-walled, silicon-carbide tubes, are all 12.2-meters (40-feet) tall in the commercial-size receiver, but the four cavities vary in width according to which sector of the heliostat

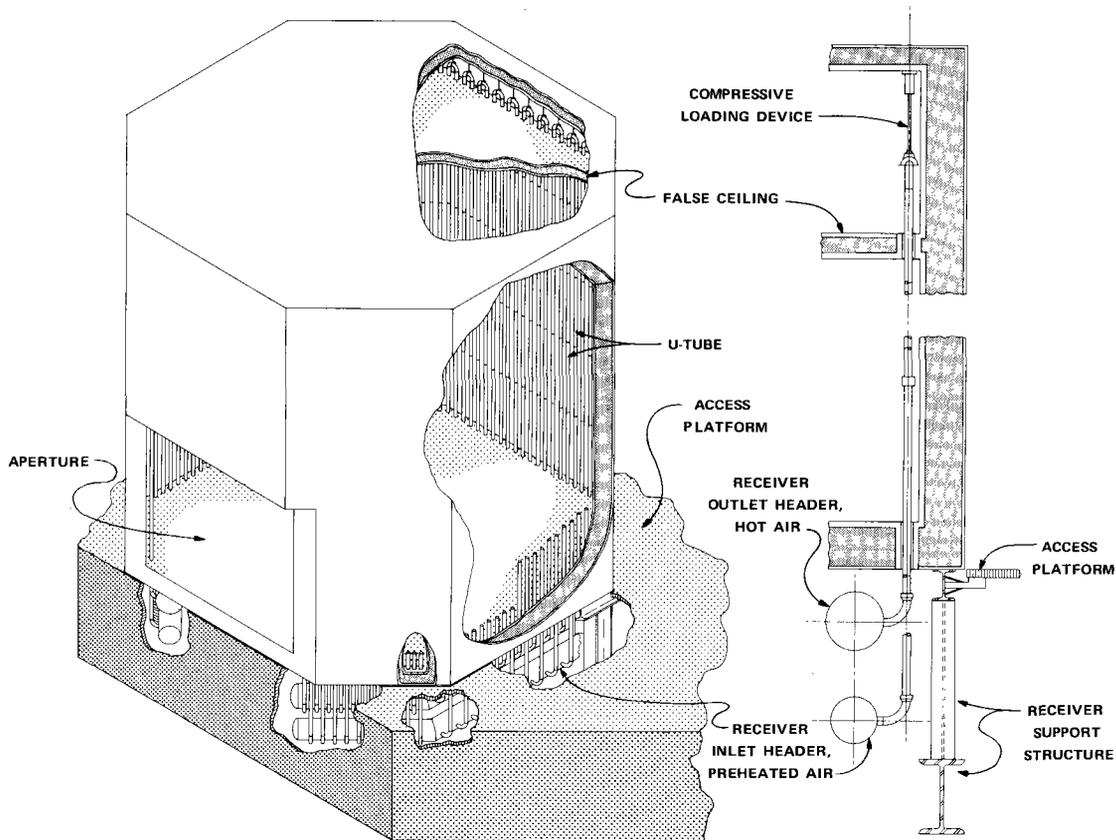


Figure 2-2. Cutaway of Tube-Type Cavity Receiver/Heat Exchanger

field they face and hence, the amount of solar energy they receive. A nominal cavity dimension is 14.6 meters (48 feet) between opposite octagonal faces. Each cavity houses approximately 70 U-tubes.

#### Storage Devices

Storage in the system is provided by operating the turbine from conventional fossil fuels (fuel oil or gas) during periods of solar outage. Hybrid operation of the turbine represents one of the principal advantages of the open-cycle system. Both buffer (rapid response) and long-term storage can be provided in this way. The design requirement is to interface the turbine with both solar and fossil heat sources so that rapid transition between heat sources or simultaneous operation with solar and fossil energy can occur.

The conceptual design uses a parallel arrangement of fossil fuel combustors and the solar heat exchanger cavities as shown in Figure 2-3. An external combustor

**LEGEND:**  
 C - COMPRESSOR  
 R - REGENERATOR  
 S - SOLAR HEAT EXCHANGER  
 F - FOSSIL FUEL COMBUSTOR  
 T - TURBINE  
 G - GENERATOR

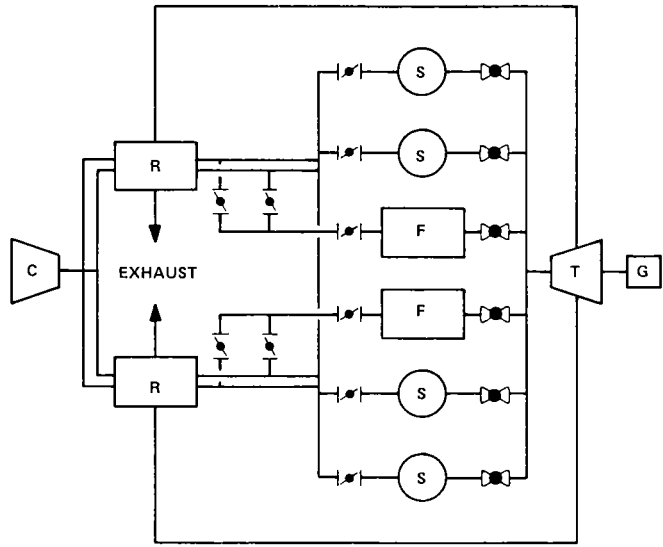


Figure 2-3. Baseline Design System Flow Diagram

location is required to implement this parallel heat source arrangement. The external combustors would replace the existing internal combustors in the combustion wrapper of the GE MS 7001R. Preliminary discussions with General Electric indicate that such a modification is feasible.

BASELINE CONCEPTUAL DESIGN

The 60-MWe system conceptual design is summarized in the following paragraphs.

System Layout and Specification Summary

A perspective view of the open-cycle, solar-thermal, central-receiver system is shown in Figure 2-4. To minimize the airflow paths from the compressors to the heat source to the turbine, the turbine generator is mounted immediately below the central receiver cavities (one for each field quadrant) as shown in the inset. The heliostat field design is based on a nonuniform density of heliostats (ground cover ratio) in each of the four field quadrants. The most closely-packed helio-

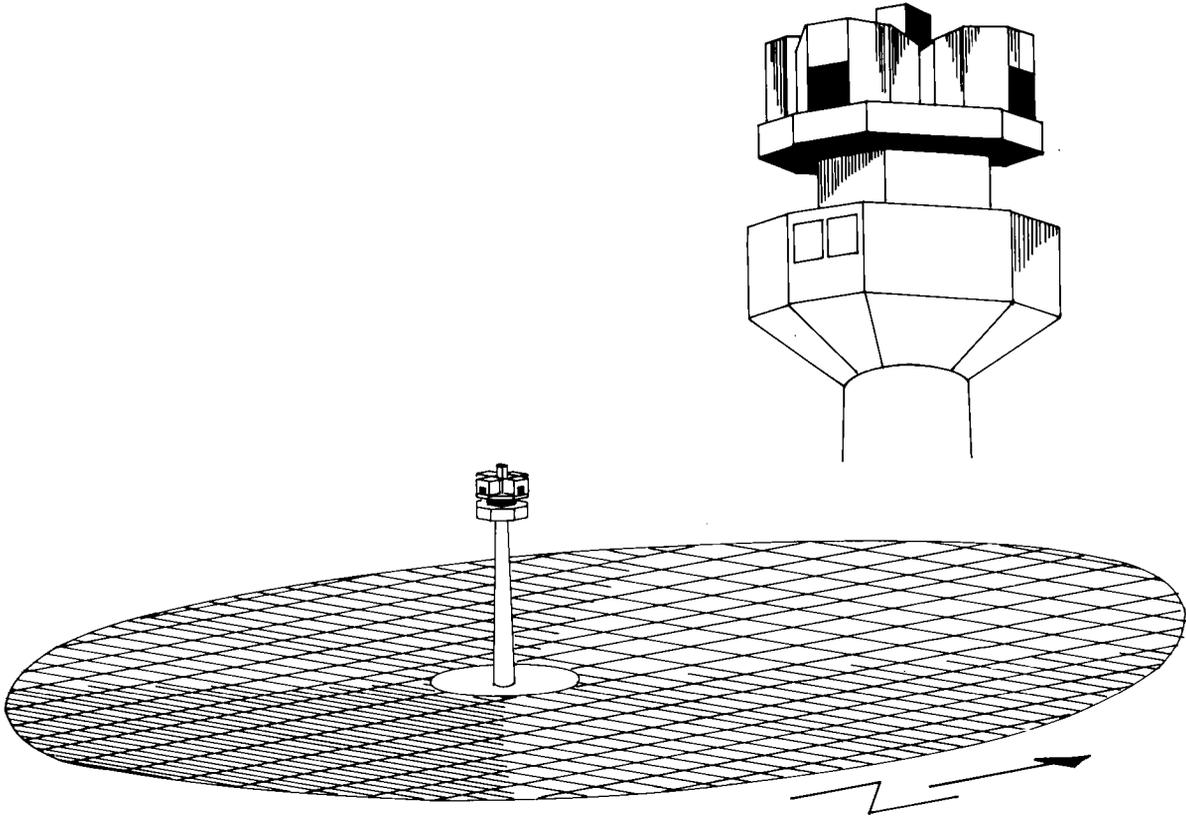


Figure 2-4. Perspective View of the Open-Cycle, Solar-Thermal, Central-Receiver System

stats are near the base of the tower in each quadrant; the south quadrant has the highest average ground cover. The north quadrant is larger because of the larger effective mirror efficiency for this part of the field in the northern hemisphere. A summary of the baseline conceptual design is given in Table 2-1.

#### System Performance

Commercially available turbomachinery can achieve an estimated 21.7 percent design timepoint (17.6 percent annual average, see Figure 8-2) overall efficiency for the complete energy conversion process. This value is approximately 20 percent higher than comparable water/steam, Rankine-cycle, central-receiver system efficiencies.

#### Categorization of Loss Mechanisms

The estimated efficiency of this hybrid system, subdivided into pertinent loss mechanisms for the major systems, is shown in Figure 2-5. Heliostat field per-

Table 2-1

## BASELINE CONCEPTUAL DESIGN SUMMARY

Nominal Plant Capacity	60 MWe
Nominal Turbine Heat Rate	9812 kJ/kW (9300 Btu/kWh)
Heliostat Field/Receiver Configuration	
Total land area	643,000 m <sup>2</sup>
Field shape	Oval
Number of heliostats	6990
Average ground cover	0.42
Total heliostat (mirror) area	260,000 m <sup>2</sup>
Heliostat area	37.17 m <sup>2</sup> (circular)
Receiver configuration	4 octagonal, cylindrical cavities
Receiver tower height	213 m (700 ft)
Receiver Cavity/Heat Exchanger	
Type	Multiple U-tube
U-tube length/diameter	12.2 m/10 cm (40 ft/4 in)
Number of U-tubes (4 cavities)	280
U-tube material	Silicon carbide
Air inlet conditions, nominal	0.93 MPa, 482°C (135 psia, 900°F)
Air outlet conditions, nominal	0.90 MPa, 1038°C (130 psia, 1900°F)
Energy Storage	
System type	Hybrid—solar and combustion
Storage medium	Fossil fuel
Receiver Tower	
Tower structure	Steel-reinforced concrete
Turbine/Receiver platform	Structural steel space frame

formance is impaired by three factors: mirror foreshortening, heliostat shadowing and blocking, and mirror reflectivity. Aperture efficiency and cavity efficiency, collectively, describe the central receiver's ability to capture redirected solar energy and to subsequently transfer this energy to the working fluid of the gas turbine. There are minor system performance losses due to thermal and pressure losses in the network that links the central receiver to the turbine. No losses are encountered in the energy storage subsystem because of the hybrid nature of the solar-thermal, open-cycle concept.

The solar-related subsystems convert 58.8 percent of the maximum possible solar energy into usable thermal energy. The General Electric MS 7001R regenerative gas turbine, with a quoted thermal efficiency of 37 percent, is coupled with the solar subsystems to give an overall system efficiency of 21.7 percent for the design timepoint of solar noon, March 21.

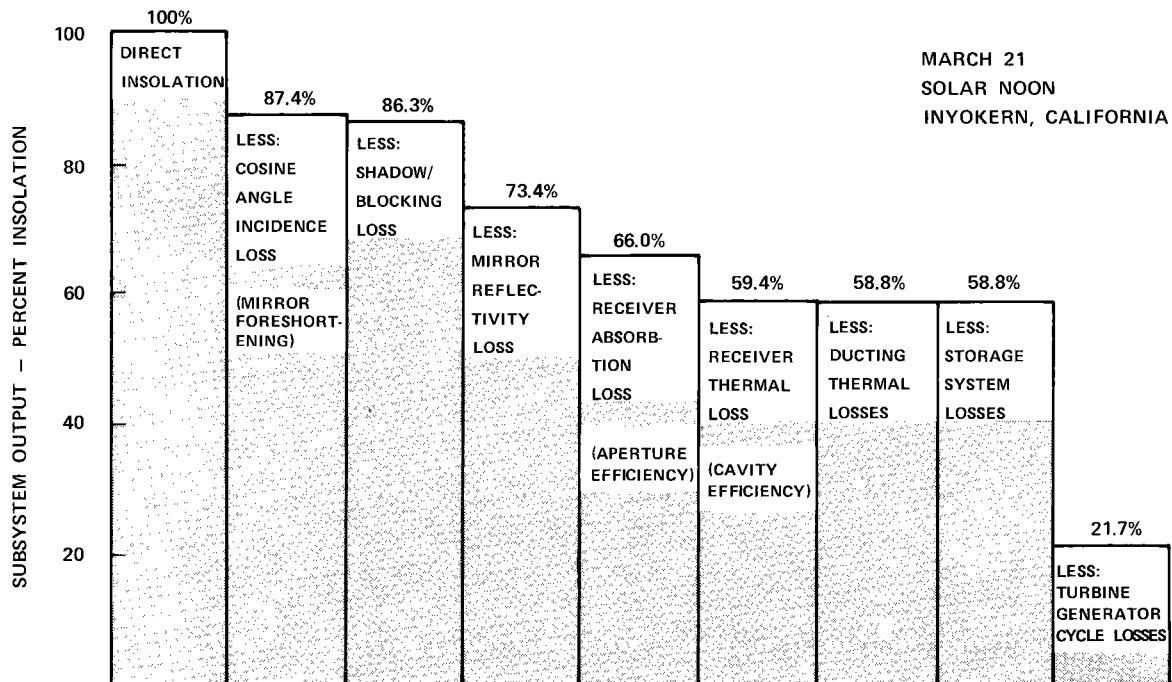


Figure 2-5. Solar-Thermal, Hybrid Open-Cycle Gas Turbine System Performance (Single Timepoint)

System Cost Summary

The projected cost of the open-cycle, solar-electric system ranges from \$1200/kW to \$1600/kW, depending upon the cost of the heliostat field system. The total estimated cost at commercial operation of a nominally 60-MWe plant is \$82,639,000, assuming a median heliostat subsystem cost of \$100/m<sup>2</sup>.

Origin of Cost Estimates

The costs displayed in Table 2-2 were generated by breaking the various subsystems into their principal components. Costs were subsequently gathered from the appropriate manufacturers and integrated using the power plant cost-estimating experience of Black & Veatch. The total projected cost includes allowances for estimated interest during construction and for construction contingencies.

Allowances for the development efforts are not included. Additional information supporting this cost summary is in Section 8 of this report.

While the costs of many system elements can be identified rather clearly, the immaturity of some technologies precludes the projection of related costs with certainty. A notable area of concern is the heliostat field. To allow for the significant heliostat cost uncertainty, a \$60/m<sup>2</sup> to \$125/m<sup>2</sup> range of heliostat subsystem costs was used to calculate the costs per kilowatt quoted above. This range of heliostat costs is anticipated to bracket the commercial application price of heliostat systems, based on the present expectations of various DOE development programs.

Table 2-2

60-MWe OPEN-CYCLE, GAS TURBINE, SOLAR-ELECTRIC SYSTEM—ESTIMATED  
COST SUMMARY (1976 DOLLARS)

Collector/Concentrator Subsystem		
	(\$)	
Land and fencing	210,000	
Heliostats at \$100/m <sup>2</sup>	25,989,000	
		\$26,199,000
Heat Transfer Subsystem		
Heat exchangers	5,626,000	
Receiver cavities	2,865,000	
Balance	1,380,000	
		9,871,000
Electric Power Generation Subsystem		
Turbine Generator	10,200,000	
Electrical equipment	1,600,000	
Fuel storage equipment	240,000	
Balance	2,500,000	
		14,540,000
Receiver Support Tower		
Tower and foundation	5,900,000	
Cavity and turbine pedestals	2,100,000	
Balance	1,275,000	
		9,275,000
Balance of Plant		<u>2,600,000</u>
Total Direct Cost		\$62,485,000
Contingency and Spare Parts (5%)		3,125,000
Indirect Cost (10%)		<u>6,250,000</u>
Total Capital Investment (1976)		\$71,860,000
Interest During Construction (15%)		<u>10,779,000</u>
Total Cost at Commercial Operation		\$82,639,000
Cost per Peak Kilowatt		\$ 1,503

### Section 3

#### HELIOSTAT FIELD/RECEIVER CONFIGURATION DESIGN

The conceptual design of a heliostat field/receiver configuration consistent with the constraints of the open-cycle gas turbine concept was assisted by the use of computer software developed under previous contracts. This software was further developed under this contract and other currently ongoing work funded by ERDA. This reliance on past accomplishments, and inclusion of information from the current analysis and development of a steam generator/central receiver, has greatly facilitated the conceptual design of the open-cycle gas turbine concept.

The computer model used in these design tasks simulates the relationships among the components of the sun-heliostat-receiver system. The model uses Monte Carlo (random variable) techniques to mechanize optical ray-trace logic based on vector algebra. The Monte Carlo approach allows a wide range of variables to be used in simulating the sun-heliostat-receiver system. The sun is described not only in terms of position, but as a finite disk with intensity variations over its surface, and with a spectrum of energy frequencies. The intervening atmosphere is modeled as a clear air atmosphere which causes absorption and refraction. Heliostats can be modeled in terms of mirror size, shape, reflectivity, method of focus, type of tracking, and position in the field. The receivers can be characterized by position, the size, shape, and orientation of the aperture, and the size and shape of the cavity. The Monte Carlo variables include mirror surface slope errors (two dimensions), tracking errors (two dimensions), solar intensity variations, and solar position variations. Output parameters include power on the field, power through the aperture, efficiencies, ray counts (hits, misses, obscurations), yearly integrated energy, an aperture flux map, a field power map, and flux maps inside the cavity (wall, ceiling).

The following subsections describe heliostat field design, receiver evaluation, and flux map generation using this computer model.

## CONFIGURATION OPTIONS AND CHOICES

The following configuration options and choices were evaluated in this program.

- Heliostat Field
  - North
  - 360°
- Receiver
  - Annulus
  - Multiple bullseye

The details of these analyses are presented in the subsections below.

The heliostat design was held constant. The characteristics of the heliostats are shown in Table 3-1. Progress in developing alternate heliostat designs (in other programs) was monitored but not incorporated in this conceptual design of an open-cycle gas turbine system. Potential improvements in performance by using alternate heliostat designs (e.g., smaller mirrors, multifacets, different tracking) would be an appropriate task in a detailed design study.

Table 3-1  
HELIOSTAT CHARACTERISTICS

Mirror Characteristics	
Shape	Round
Size	6.876 m (22.56 ft) diameter (37.2 m <sup>2</sup> [400 sq ft] area)
Focus	Fixed (equal to slant range to receiver)
Optical Surface	Spherical (rms slope error of 1 milliradian)
Tracking Characteristics	
Gimbal Type	Azimuth-elevation
Gimbal Accuracy	rms 1 milliradian

A rectilinear heliostat field was used throughout this study. The rectilinear field consists of rows of heliostats running north-south and rows running east-west forming a rectilinear grid of heliostat positions.

The following subsections address the four options and choices.

### Heliostat Field

Heliostat field design involves a wide variety of variables. Since the computer simulation uses the field as an input and calculates the power level, an iterative process was followed to define a field that meets a given power requirement. The variables involved in the field optimization are as follows.

- Parameters Held Constant
  - Heliostat Type--single facet, azimuth-elevation
  - Heliostat Size (area of mirror)
  - Mirror Type--circular, focusing
  - Heliostat Spacing--rectilinear
- Parameters Varied
  - Field Shape--360° or segment (north)
  - Field Size--inner and outer radii
  - Heliostat Spacing--uniform (ground cover ratio) or non-uniform (spacing criteria)
  - Tower Height
  - Receiver Aperture Shape--circular or square
  - Receiver Aperture Size (area)
  - Receiver Aperture Position (slope or tip)
  - Power--through aperture, on edges of aperture
  - Energy

North Field Only. Figure 3-1 is an illustration of the north-field concept. A pie-segment field of mirrors to the north of the tower redirects sunlight into a cavity receiver at the top of the tower. A cutout exists in the field near the tower. In comparison with a 360° field, this configuration has the following advantages and disadvantages.

- It affects the receiver configuration. Since all of the energy is coming from the same general direction, the receiver opening must be designed accordingly.
- It improves field efficiency through the cosine effect (projected mirror area). As shown in Figure 3-2, the sun and the receiver only "see" a fraction of the total mirror area, and that fraction is a function of the sun-heliostat-receiver geometry (and hence the position of the heliostat in the field). This cosine effect is minimized in the north field.
- It places a larger percentage of the heliostats far from the tower. For any given power requirement, and the associated amount of mirror area, confining the heliostat placement to the north field

results in the outer mirrors being considerably farther from the tower than if they were placed all around the tower (360° field). The implication is that the tower height/shadowing and blocking/image-size/image-position relationship leads to poorer performance. For a 60-MWe system, the tower height/shadowing and blocking/image-size/image-position relationship results in an approximately 792-m (2600-foot) field radius and a 396-m (1300-foot) tower height. This represents an extremely tall tower and a relatively large field.

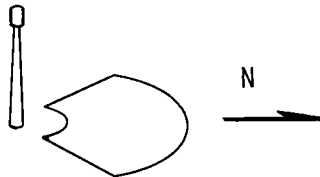


Figure 3-1. North-Field Concept

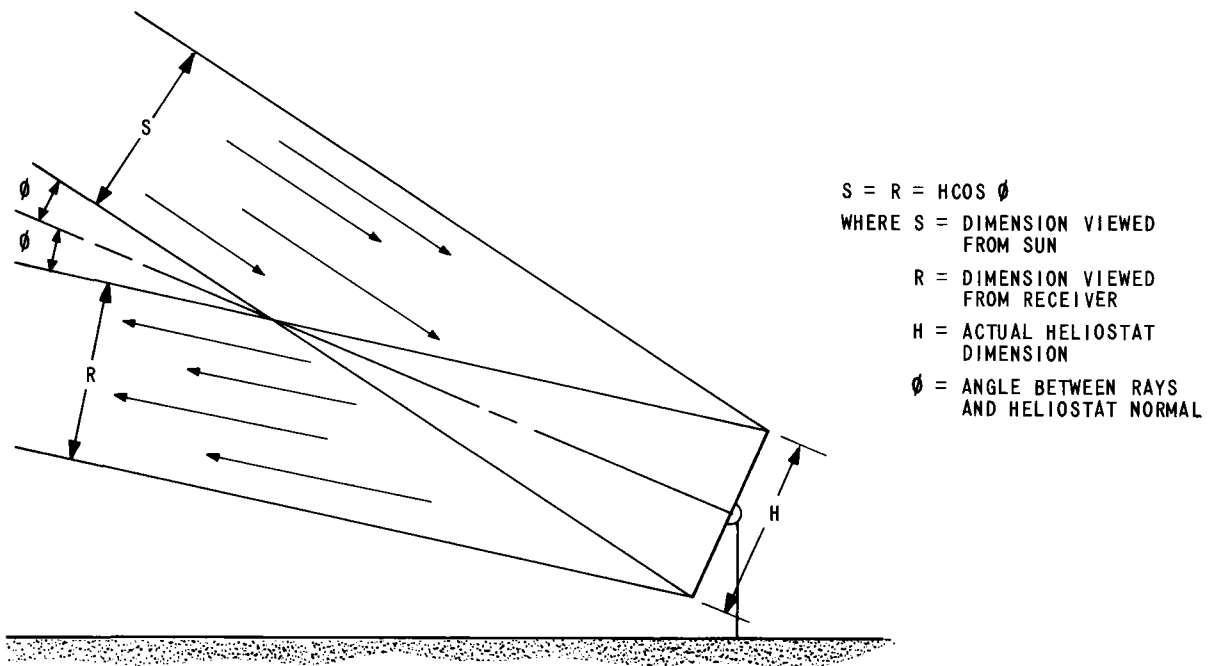


Figure 3-2. Cosine Effect on Available Area of Mirror

360° Field. Figure 3-3 is an illustration of the 360°-field concept. The field has a cutout near the tower and the mirrors completely encircle the tower/receiver. In comparison with a north-only field, this configuration has the following advantages and disadvantages.

- It affects the receiver configuration. The receiver associated with this field must be designed to accept energy from the complete 360°. As shown below, this can be an annulus cavity or a number of bullseye cavities.
- The factor of field efficiency called projected mirror area is reduced in comparison with the north-only field (the cosine effect is increased). Figure 3-4 is a graph of cosine effects showing the comparison. South of the tower, projected area is significantly less than north. For other timepoints (6/21 noon shown) the effect is even more pronounced. In addition, the east field is like the south in the morning (west is like north) so that the farther from north the heliostats are placed, the lower the projected area of the mirror.
- However, for a given number of heliostats, the 360° field places the mirrors significantly closer to the tower. This allows the image-size, pointing-error portion of the tower height/shadowing and blocking/image-size/pointing-error relationship to overcome the disadvantage of the reduced amount of projected mirror area. In fact, the computer simulations showed that for a 60-MWe system, the number of heliostats required was very similar for the two field types (7000 to 8000).
- Using a 360° field, the tower height requirement was 213 m (700 feet). Although performance does not peak at this value, the improvements in performance were small at heights above 213 m (700 ft). Further refinement of this parameter, with respect to performance value versus increased cost, would be appropriate in a detailed design study.

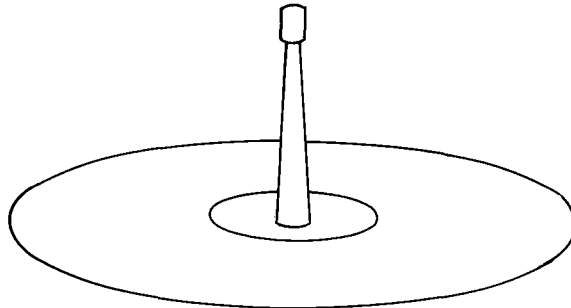


Figure 3-3. 360°-Field Concept

ISOPLETHS OF THE COSINE EFFECT

TIMEPOINT: JUNE 21 NOON

DIMENSIONS ON AXIS ARE IN TOWER HEIGHTS

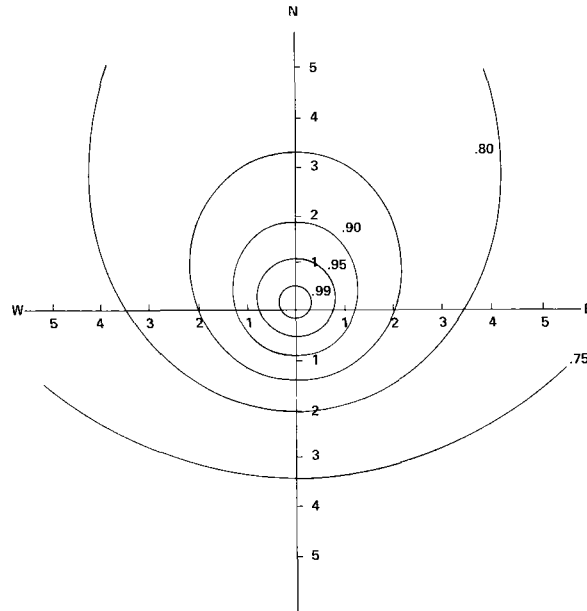


Figure 3-4. Cosine Effects on Field Efficiency

Configuration Choice. Central receiver designs have shown that the heliostats are the most significant subsystem in the system cost. Therefore, reducing the number of heliostats has been the paramount consideration in defining a heliostat field configuration. Our comparison between the north field and a 360° field has shown that for the constraints of the open-cycle gas turbine conceptual design, the north field requires approximately 8 percent fewer heliostats. However, since the north-field configuration requires a taller tower, tower cost was combined with the heliostat cost (parametrically) to define the most cost-effective configuration. Figure 3-5 shows that over the range of heliostat costs of interest, the 360° field is more cost effective in terms of MWth per dollar cost (heliostat plus tower).

Receiver

Given the superiority of the 360° field, the receiver options investigated were the annulus aperture cavity and the multiple-bullseye aperture cavity.

Multiple-Bullseye Aperture. A multiple-bullseye cavity configuration is shown in Figure 3-6. The turbine generator platform is below the cavity platform and the chimney is among the cavities. This chimney exhausts the spent working fluid

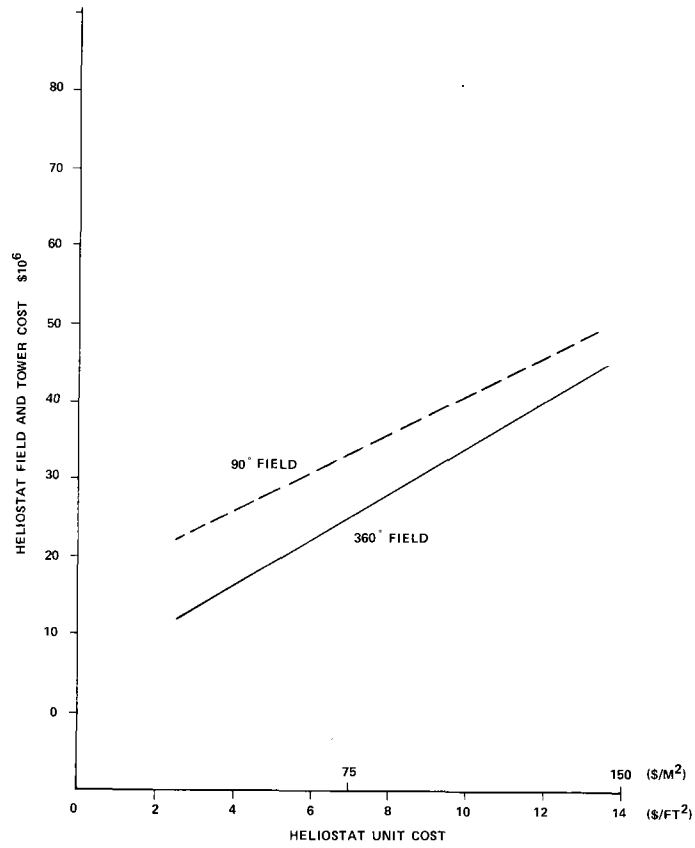


Figure 3-5. Alternative Field Configuration Costs

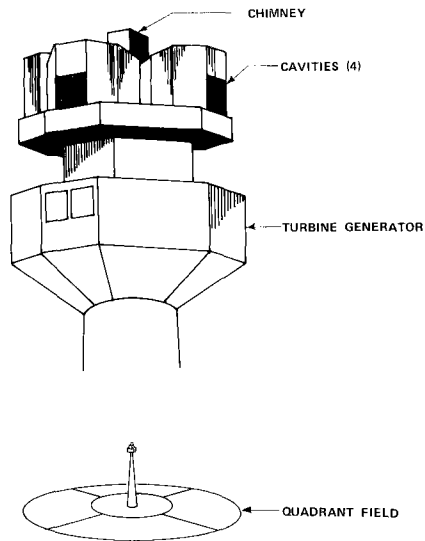


Figure 3-6. Baseline Multiple-Bullseye Cavity Receiver

(air) to the atmosphere. The multiple-bullseye cavity system investigated (and shown in Figure 3-6) consists of four cavities, each receiving energy from a 90° sector of the heliostat field.

Advantages and Disadvantages. This multiple-cavity configuration has several advantages and disadvantages, as follows.

- The gas turbine ducting design is relatively straightforward (as compared to the annulus). Outside air enters the gas turbine system at the lower platform level, is compressed, heated in a regenerator, and then sent up to the four cavities. The heated air is ducted down from the cavities to the turbine, out to the regenerator, and then to the exhaust stack which goes up among the cavities. There is no conflict between these ducting paths and the optical path from the heliostats to the receiver.
- The receiver is modular, allowing staged construction in either a test or demonstration situation. Furthermore, the modularity provides flexibility in operating strategies in terms of:
  - Full operation of two or three cavities (morning or evening) while the other one or two are not at operating temperature.
  - Full operation of three cavities while one is down during maintenance or repair.\*
- The flux incident on the cavity walls and ceiling from the heliostats (incoming energy, not reflected or reradiated) is localized; that is, it all falls on the back and top of the cavity and none falls on the front or floor.

For the purposes of the field layout definition, the bullseye cavity is considered to be a circle (hoop) in the sky at which the heliostat aims the image of the sun (hence the name bullseye). The cavity characteristics (size, shape) are not utilized, only the energy through (and missing) the bullseye is of importance. The parameters involved are bullseye radius and angle of the bullseye to the vertical (and of course azimuth, consistent with the field being evaluated).

Because of the simplified constructability of a square or rectangular aperture, some evaluation of this configuration was conducted. In general, because of the symmetry in the pointing-error distribution, the circular aperture collects more energy than the square aperture (of equal area). The trade-off between construction costs and power loss was not undertaken in this conceptual design but would be appropriate in a detailed system design.

---

\* Personnel would not do maintenance or repair on a cavity during daylight operating hours. This would be done at night. However, the system could operate (degraded) with one cavity shut down for maintenance or repair.

In this investigation, bullseye apertures of up to 15 m (50 feet) in diameter were investigated. For the range of fields and powers consistent with a 60-MWe system, the apertures are 6 to 9 m (20 to 30 feet) in diameter.

The optimum angle of the bullseye from the vertical is 30° (the bullseye looks 30° down from the horizontal, 60° up from the base of the tower). However, the system performance is not highly sensitive to this angle. Therefore, to simplify cavity construction costs, in the baseline concept configuration, the aperture is vertical--the plane of the aperture is vertical and the bullseye "looks" out to the horizon. A trade-off between this performance penalty and the construction cost penalty would be an appropriate topic in the detailed design of this receiver.

The aperture efficiency is defined as the ratio of the power through the aperture to the power cleanly redirected from the field. Thus it is a measure of how much power misses the cavity due to pointing errors (tracking errors and mirror slope misalignment errors). As discussed above, for a given set of heliostat characteristics, the farther a heliostat is from the tower, the larger its image of the sun, and the larger its pointing errors (in distance). Thus for large fields, the receiver needs a bigger aperture to collect the power. The power loss due to reflection and reradiation out of the aperture limits the size of the aperture. The aperture efficiencies realized with the baseline designs ranged from 0.94 to 0.97 with a circular aperture (0.91 to 0.96 with a square aperture). These efficiencies were calculated for apertures configured for a high cavity efficiency. At gas turbine operating temperatures, losses are very sensitive to the aperture size and therefore the energy collection--energy loss trade-off is a critical one. As previously discussed in this section, this problem is minimized by using a 360° field and keeping the heliostats as close as possible to the receiver.

The optimum aperture size was defined as the aperture collecting the highest net power, where net power refers to gross power minus reradiation losses and gross power is the amount of energy entering the hole. Figure 3-7 shows a typical plot of gross power, losses, and net power for a north-facing cavity. This type of plot was utilized for optimizing the aperture size. The flux density across the aperture (and onto the outside of the cavity) was also calculated and showed intensities of up to 500 kW/m<sup>2</sup> spillage, usually at noon (west field power is highest near 10:00 a.m., east field power is highest near 2:00 p.m.).

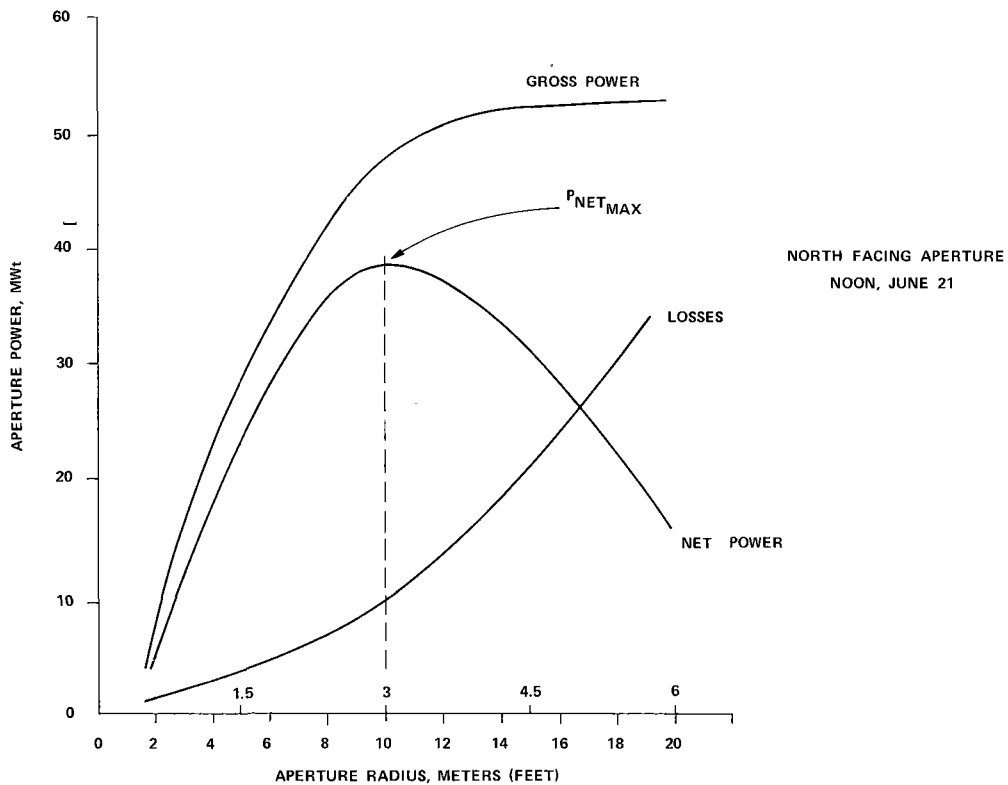


Figure 3-7. Typical Plot for Optimizing Aperture Size

Other Considerations. Several other considerations are involved in the evaluation of the multiple-bullseye aperture configuration. These involve the cavity/generator-platform position, the aim strategy, and the similarity between the two concepts (multiple bullseye and annulus), as far as the field is concerned.

As discussed in the conceptual design, the turbine generator is located atop the tower and beneath the receiver. The large size of the turbine generator results in a potential shadowing of the receiver by the turbine generator platform unless measures are taken to avoid it. The multiple-bullseye concept (unlike the annulus) is flexible in outside diameter and enables the cavities to be placed physically close to the turbine generator and still not be shadowed by the platform (Figure 3-8).

The aim strategy for the bullseye receiver is simply to aim for the center of the bullseye. This results in a circular distribution of flux at the aperture. In general, aiming in any other manner will strongly impact the spillage and the power through the aperture.

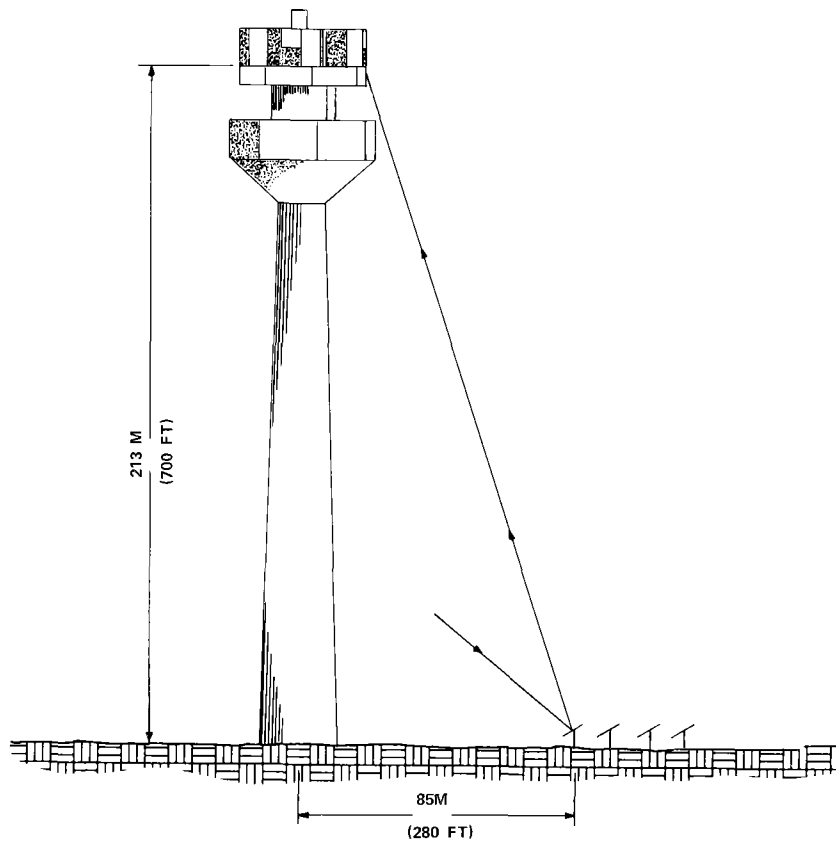


Figure 3-8. Illustration of Multiple-Bullseye Receiver Optical Path

It should be noted that the multiple-bullseye receiver concept, as viewed from the outside of the cavity, is very similar to an annulus receiver with four supports. As the annulus supports increase in size, and the openings decrease, the annulus-receiver type degenerates into a multiple-bullseye receiver.

Annulus Aperture. An annulus cavity configuration is shown in Figure 3-9. This illustration shows three receiver supports (corbels) and the turbine generator platform is not shown.

Advantages and Disadvantages. This cavity configuration has several advantages and disadvantages, as follows.

- The shape of the annulus opening (as seen from a heliostat position) allows for some variation in aim strategy to modify the flux distribution on the cavity walls. Furthermore, the annulus size and shape consistent with the outer heliostat image size allows the inner heliostats some variation in their aim strategy in the vertical plane.
- The "open" characteristic of the configuration, which enhances the optical desirability of this type of cavity, is

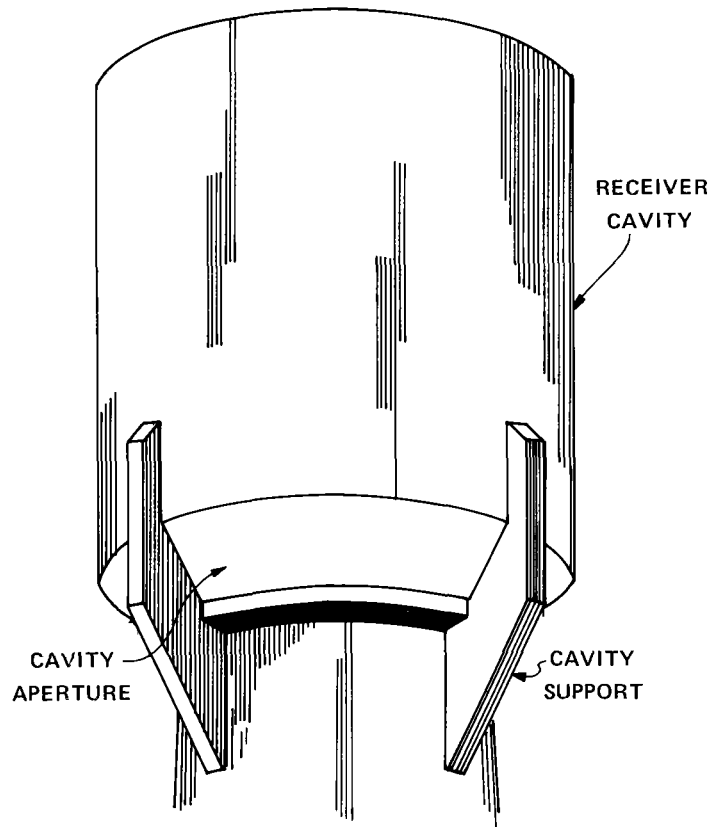


Figure 3-9. Annulus Cavity Configuration

compromised by the requirement to duct the air up to and down from the cavity. Duct sizes consistent with this conceptual design are considerably larger than the supports and dominate the support-size design. Furthermore, spent air from the regenerator must be exhausted, either below the cavity and into the optical path, or up a chimney through the center of the annulus cavity. Several duct, chimney, and cavity sizes were evaluated to determine the effects of these constraints. Figure 3-10 illustrates the relative size of these components for low (30 m/sec [100 ft/sec]) and high (60 m/sec [200 ft/sec]) velocity systems. These results showed that (a) the flux density on the chimney was too high to accommodate this exhaust scheme and the exhaust would have to exit below the cavity, and (b) the ducts and supports constricted the annulus opening to a point where most of the flexibility in aim strategy was lost, and the resulting annulus looked like three bullseye apertures with a common cavity.

- As will be discussed later in this section, the turbine generator platform is sufficiently large to cause shadowing of the annulus aperture. Figure 3-11 shows a schematic drawing of this configuration and indicates that the annulus configuration would have to be farther above the platform than the multiple-bullseye cavities.
- The annulus cavity configuration does not lend itself to a modular approach to testing or operating. It requires the full 360° field for representative operation and scaling the size down would require appropriate scaling of the optical image--a difficult task at the present heliostat state-of-the-art.

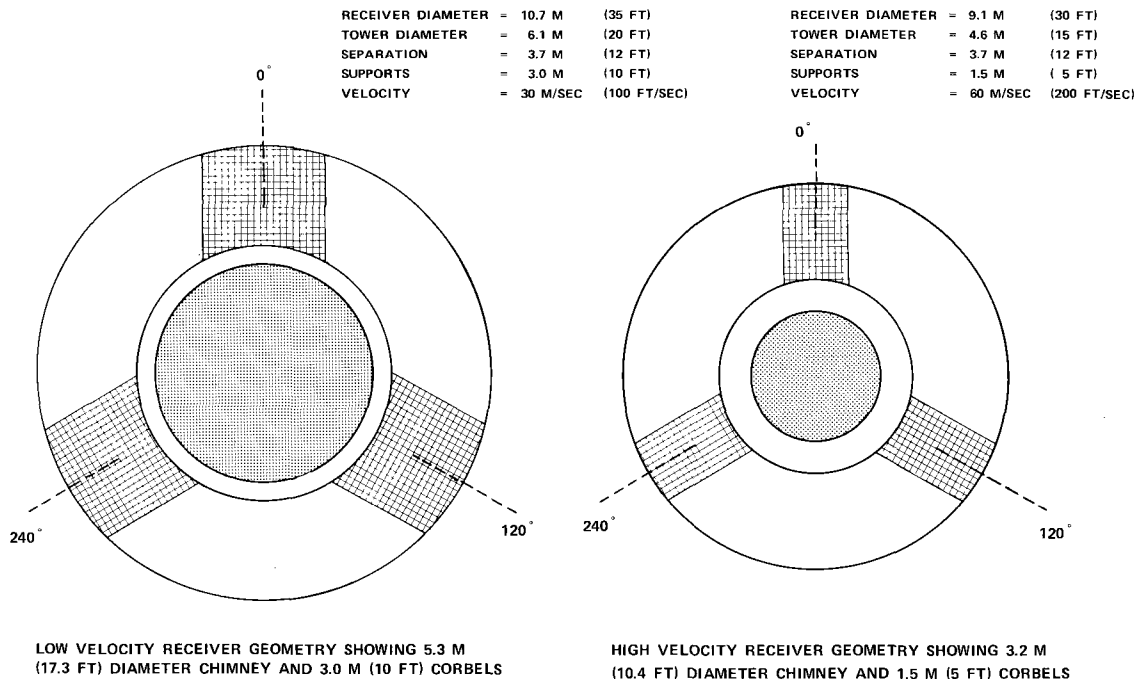


Figure 3-10. Two Duct Chimney Cavity Sizes

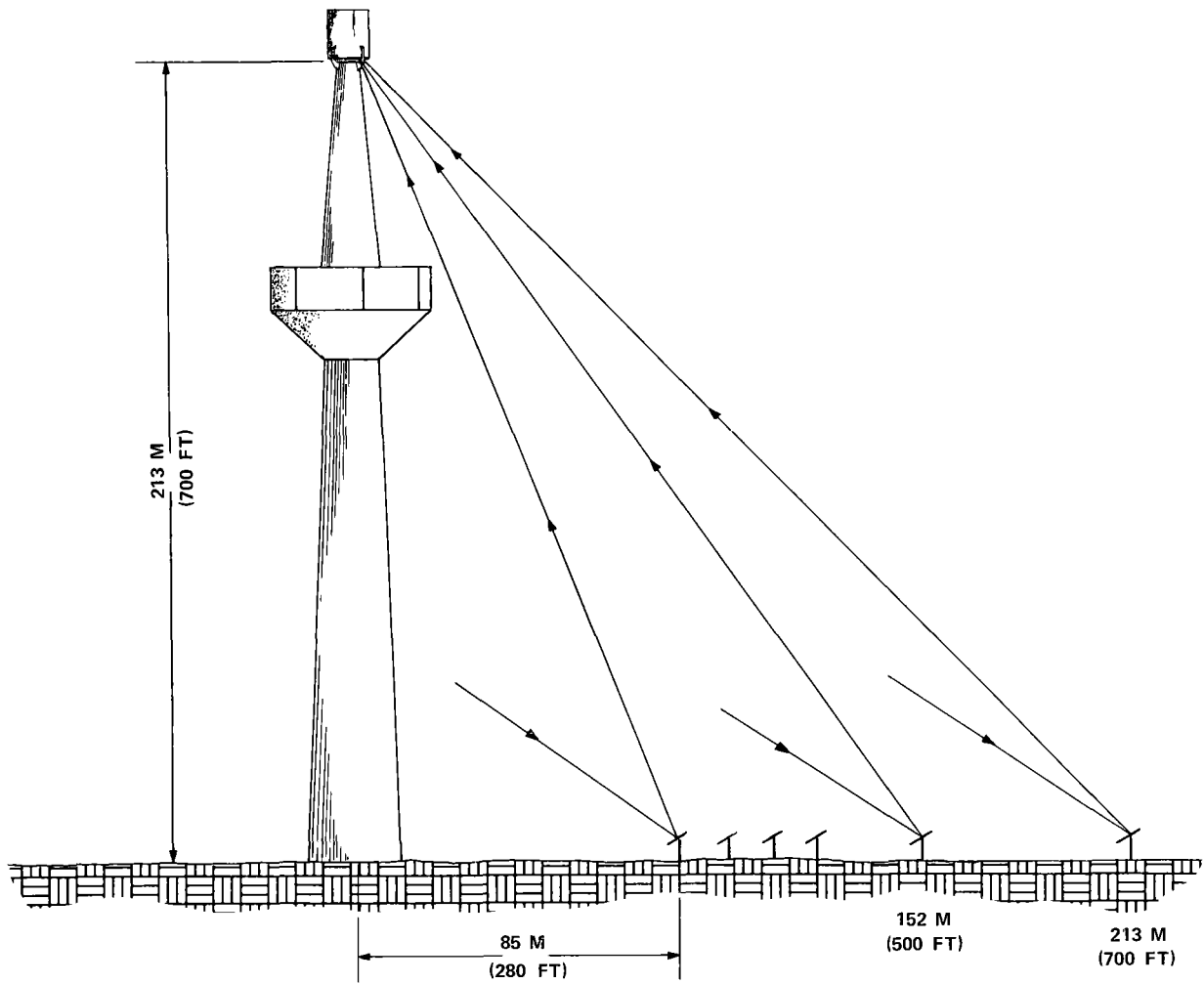


Figure 3-11. Illustration of Annulus Receiver Optical Paths

The baseline annulus cavity design, shown in Figure 3-12, is 12.2 m (40 feet) high and has aperture diameters of 4.6 m (15 feet) bottom and 8.5 m (28 feet) top. The annulus height (distance from top of tower to cavity bottom) is 3.7 m (12 feet). The resulting slope of the annulus is 32 degrees and the projected opening size is 75 m<sup>2</sup> (810 square feet [annulus area]). The aperture efficiency of this configuration is approximately 0.96.\* This cavity, with a bottom opening of 57 m<sup>2</sup> (616 square feet), can be expected to have a much higher cavity efficiency than the multiple bullseye which has a combined area (all four apertures) of 156.2 m<sup>2</sup> (1680 square feet).

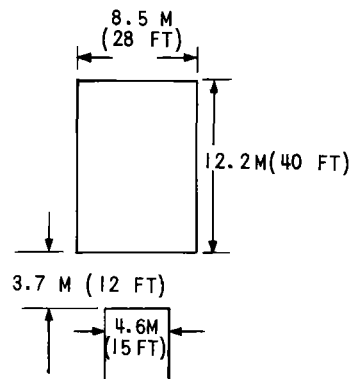


Figure 3-12. Annulus Dimensions

Configuration Choice. Both the multiple-bullseye aperture configuration and the annulus aperture configuration were optimized using a 360° heliostat field. To meet the design power specification of 60 MWe, at noon, March 21, a nearly equal number of heliostats is required (7500). Therefore, other criteria were used to decide between the two receiver configurations.

Given the similarity in heliostat field cost, the primary reason for choosing the multiple-bullseye configuration is the ducting problems in the annulus. Significant, but of secondary importance in the decision, is the flexibility of the modularity of the multiple-bullseye configuration.

#### HELIOSTAT FIELD LAYOUT

In designing the 360° heliostat field, both uniform and nonuniform ground cover fields were investigated. The initial field designs incorporated uniform ground

\* No corbels.

cover, i.e., the spacing between heliostats was equal throughout the field in both directions. Several fields were designed using about 8000 heliostats and ground cover ratios of 0.29 to 0.45. These two fields appeared to be the limit of efficiency in that (1) lower ground cover will result in the outer heliostats having too long a slant range (for accurate pointing), and (2) higher ground cover will result in the outer heliostats producing too many obscurations. The following subsections discuss the advantages of utilizing a nonuniform ground cover, the criteria for our nonuniform field design, and the characteristics of our baseline heliostat field design.

#### Ground Cover Design Option

Collector field efficiency in a central receiver system is related to the geometry of the sun-heliostat-receiver optical path which includes energy loss effects due to:

- Cosine effects on the projected mirror area
- Shadowing and blocking between heliostats
- Misdirected energy due to pointing errors (tracking errors, mirror surface slope errors)

In designing a collector field, the ground cover ratio (ratio of total mirror area to field area) of a field with uniform heliostat spacing is a compromise between the near heliostats, which can be spaced relatively close together and the distant heliostats, which need to be spaced farther apart to avoid obscurations.\* The blocking and shadowing effect of heliostats on their neighbors can be reduced by adjusting the spacing of the heliostats as a function of the tower-heliostat position geometry. This results in a nonuniform collector field.

A progression of baseline open-cycle gas turbine heliostat field designs was developed consistent with the thermal power requirement of a 60-MWe gas turbine powered generating plant. The initial designs utilized a uniform heliostat spacing in the field and later designs utilized a nonuniform spacing in the field. Several spacing criteria were used and sector radius was varied parametrically to identify the most efficient sector sizes.

Spacing Criteria. The nonuniform rectilinear heliostat field is defined in terms of the north-south and the east-west heliostat spacing. That is, knowing the

---

\* Obscurations are shadowing, when part of a heliostat is shadowed from the sun by another heliostat, and blocking, when power reflected from a heliostat is blocked by another heliostat.

spacing between heliostats in the north-south direction and in the east-west direction, allows the establishment of a rectangular grid that defines the location of all the heliostats. Three nonuniform fields were examined in this study. The criteria for the spacing in each of these nonuniform fields are listed below.

Field Number 1. This initial nonuniform field was designed to place the heliostats as close together as possible with no blocking or shadowing. Thus it is a baseline from which smaller fields can be designed and compared. It represents the largest (in size) field necessary and the lowest possible level of obscurations. The specific criteria are as follows.

- North-south--there shall be no blocking or shadowing between the heliostats on the north-south field diameter at noon on any day of the year. (Further consideration of this requirement shows that if it is met, there is only very minimal north-south blocking and shadowing for all north-south rows at all times of the day.)
- East-West--there shall be no blocking or shadowing between the heliostats on the east-west field diameter from 9:00 a.m. to 3:00 p.m. on June 21. (Further consideration of this requirement shows that when it is met, there is only very minimal blocking and shadowing for all east-west rows from 8:00 a.m. to 4:00 p.m. from March through September, and from 9:00 a.m. to 3:00 p.m. the other six months.)

Field Number 2. This field was designed to reduce the land area requirements of the heliostat field. It is based on maintaining the noon, March 21 peak power and accepting some reduction in off-peak power due to obscurations. The criteria are as follows.

- North-South--There shall be no blocking or shadowing between the heliostats on the north-south field diameter at noon on March 21.
- East-West--criteria identical to Field Number 1.

Field Number 3. This field was designed to further reduce the land area requirements of the heliostat field. The heliostats in the shadowing portion of the field remain in the positions defined in Field Number 2. The heliostats in the blocking portion of the field are moved closer together to reduce the distance to the tower at the expense of obscurations. This modification of the heliostat positions was designed to achieve 10 to 15 percent blocking at the edge of the field. The actual blocking that resulted from this field will be shown below.

Geometric Relationships. Using these criteria, geometric relationships were developed in terms of the heliostat spacing ratio,  $R_s$ , and the heliostat position

ratio,  $R_p$ , to define a dimensionless relationship which applies to any size heliostat, any tower height, and any field dimension.

The heliostat spacing ratio,  $R_s$ , is defined as the ratio of the heliostat diameter to the center-to-center heliostat spacing.

$$R_s = D/S_h \quad (3-1)$$

where

D = heliostat diameter

$S_h$  = heliostat spacing (center-to-center)

The heliostat position ratio,  $R_p$ , is defined as the ratio of the heliostat position in the field (distance from tower along the north-south or east-west axis) to the tower height.

$$R_p = TH/Q \quad (3-2)$$

where

TH = tower height

Q = distance from tower

= Y in north-south direction

= X in east-west direction

North-South Relationships. As shown in Figure 3-13, the spacing in the north-south direction is calculated from three different relationships associated with three zones.

These zones are defined by,

$$Y = \pm TH \cdot \tan Z \quad (3-3)$$

where

Z = solar noon zenith angle (given day of year)

In the north zone, the incident ray always strikes the mirror from above the mirror normal and is redirected below the mirror normal. Thus blocking is the predominant mechanism in this zone. When blocking is eliminated, no shadowing or blocking exists. To eliminate blocking, heliostats should be placed according to the following relationship.

$$R_s = \frac{\cos(\arctan R_p)}{\cos\left(\frac{Z - \arctan R_p}{2}\right)} \quad (3-4)$$

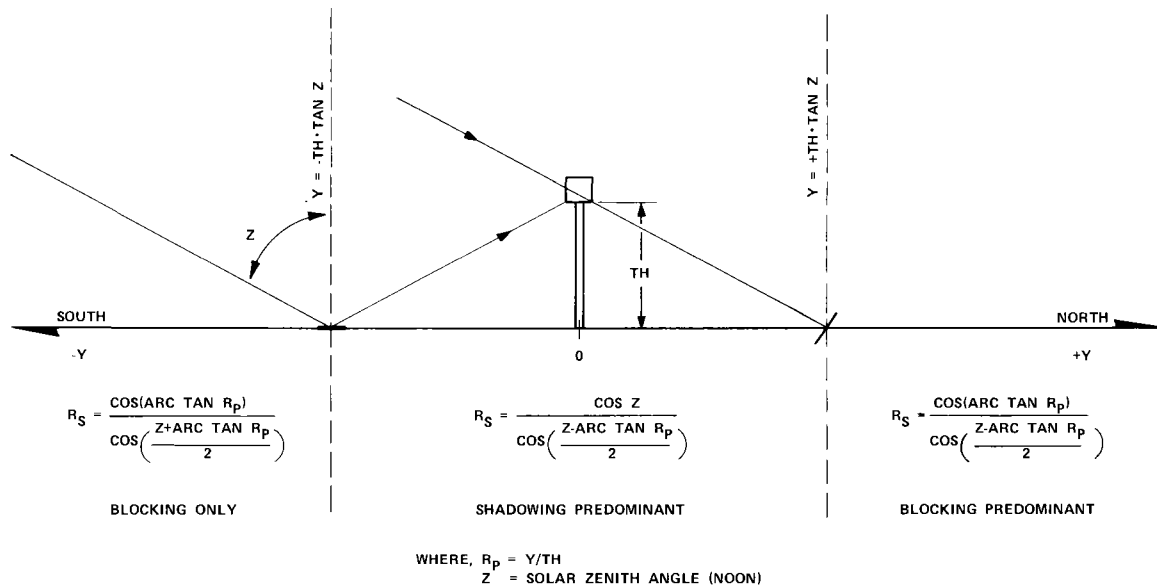


Figure 3-13. North-South Heliostat Spacing Ratio Geometry

In the middle zone, the incident ray always strikes the mirror from below the mirror normal and is redirected above the normal. Thus shadowing is the predominant mechanism. Therefore, when shadowing is eliminated in the middle zone, no shadowing or blocking exists. To eliminate shadowing, heliostats should be spaced according to the following relationship.

$$R_s = \frac{\cos Z}{\cos\left(\frac{Z - \arctan R_p}{2}\right)} \quad (3-5)$$

In the south zone, the mirror position is such that blocking is the only obscuration for heliostats on a common level. To eliminate this blocking, heliostats should be spaced according to the following relationship.

$$R_s = \frac{\cos(\arctan R_p)}{\cos\left(\frac{Z + \arctan R_p}{2}\right)} \quad (3-6)$$

These blocking and shadowing relationships were evaluated for three timepoints.

Noon, March 21.  
 Noon, June 21.  
 Noon, December 21.

The results, plotted in terms of spacing ratio versus position ratio, are shown as the three curves in Figure 3-14. The heavy curve is the relationship used to define the north-south spacing in Field Number 1. It represents the extreme spacing for the three timepoints shown and, in fact, for the complete year. Thus, using this criteria, north-south blocking and shadowing are not only eliminated for a single timepoint but for the complete year at the noon solar zenith.

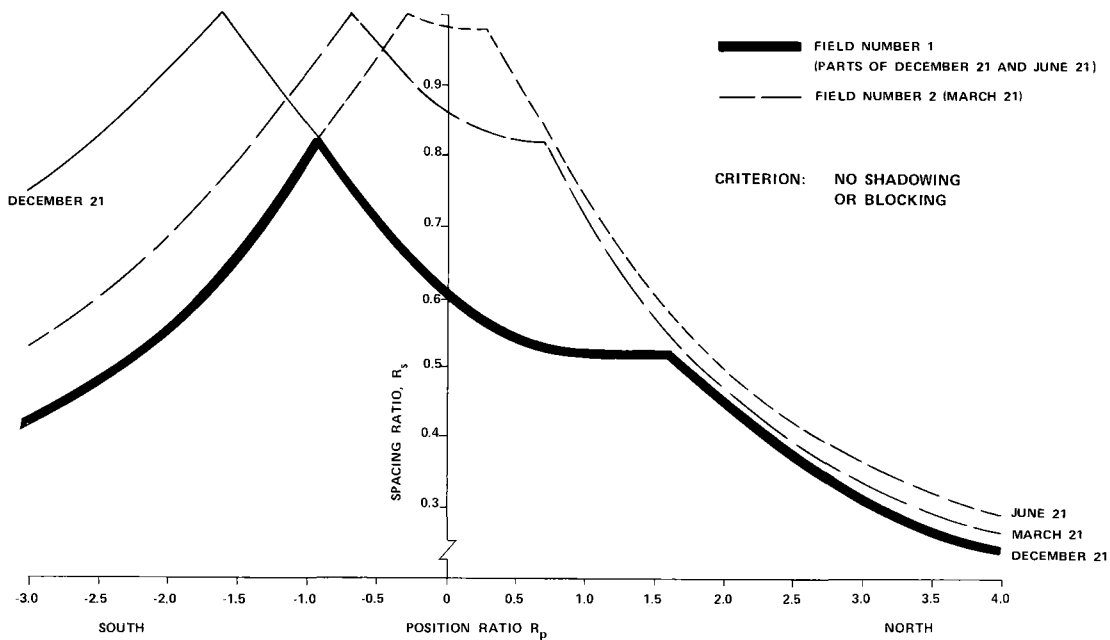


Figure 3-14. Nonuniform Field North-South Mirror Spacing Ratio

The curve used to define the north-south spacing for Field Number 2 is also shown in Figure 3-14. It is the dashed line marked March 21. Although no obscurations occur at noon, March 21, blocking and shadowing will occur at other times of the year as shown by the December 21 curve and the June 21 curve.

The curve used to define the north-south spacing for Field Number 3 is shown in Figure 3-15. Also shown in this figure is the March 21 curve from which it was derived. Heliostat spacing has been decreased for the outer heliostats to achieve a shrinking of the field at some cost in obscurations. Figure 3-16 shows the percent of area blocking that exists at noon, March 21 with this heliostat spacing.

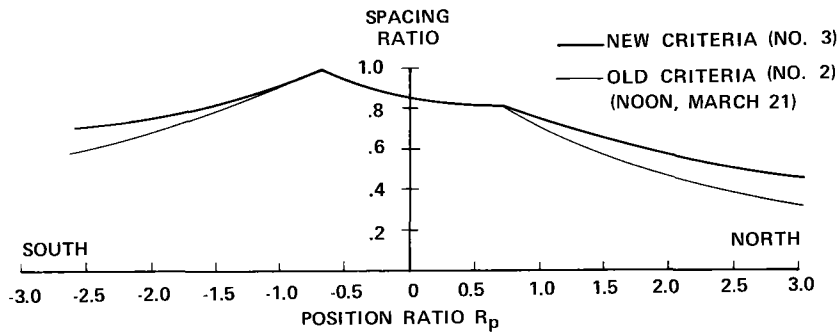


Figure 3-15. North-South Spacing Ratio for Field Number 3

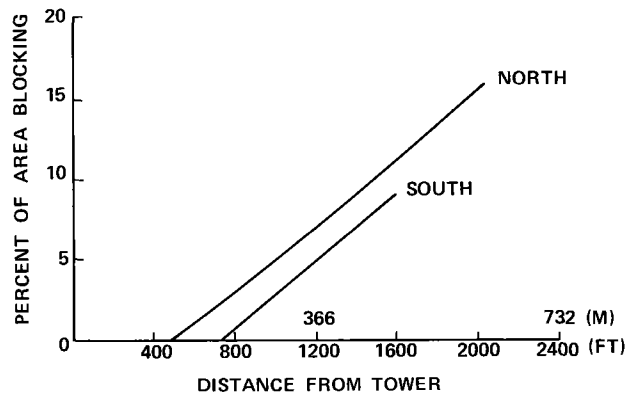


Figure 3-16. Percent of Area Blocking, North-South, Field Number 3

East-West Relationships. Figure 3-17, which defines the east-west geometric relationships, is merely Figure 3-13 redrawn with the axis relabeled east and west. In this east-west figure, the sun's rays represent a solar elevation (some time-of-day) other than the solar noon zenith angle. The north-south relationship has shown that the field nearest the sun (south in Figure 3-13, east in Figure 3-17) has the closest spacing. Therefore, it is the west field in the morning (and the east field in the afternoon) that dictates the spacing of the east-west field. The relationships used to define the west-field heliostat spacing ratio are the same as in the north-south case with a new solar zenith angle,  $Z$ , corresponding to the specified time of day.

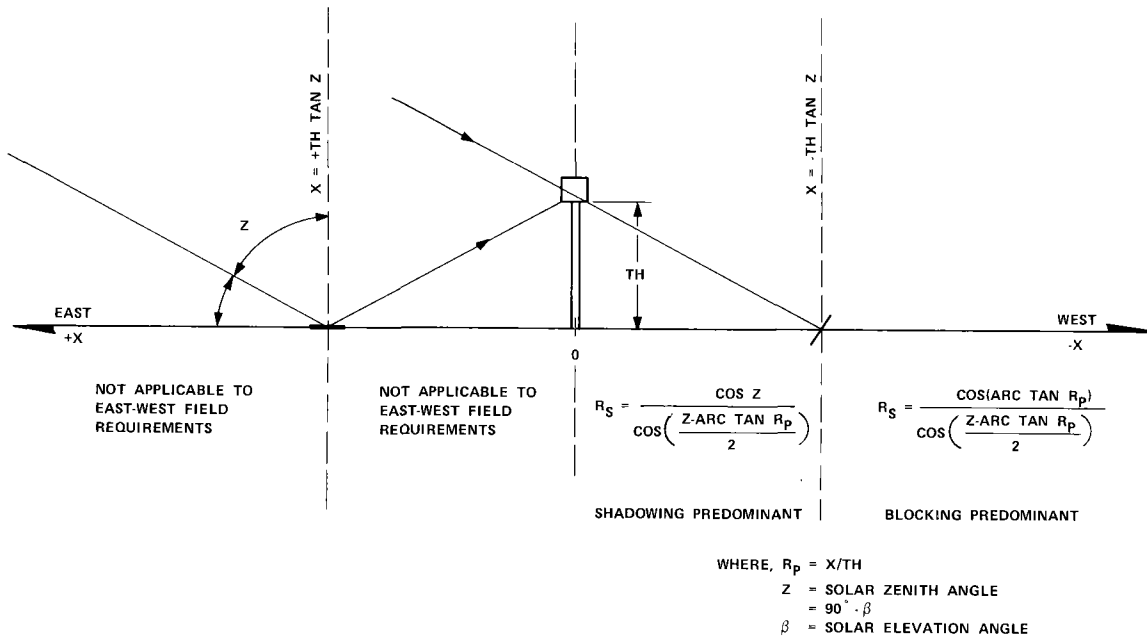


Figure 3-17. East-West Heliostat Spacing Ratio Geometry

To define Field Number 1 and Field Number 2, the west field was designed for no blocking or shadowing at 9:00 a.m. on June 21 and the east field was constructed symmetric to the west. The result, plotted in terms of spacing ratio versus position ratio, is shown in Figure 3-18. This field provides no east-west blocking or shadowing from 9:00 a.m. to 3:00 p.m. in June.

The curve used to define the east-west spacing for Field Number 3 is shown in Figure 3-19. Also shown in this figure is the curve from which it was derived (the Figure 3-18 curve). Heliostat

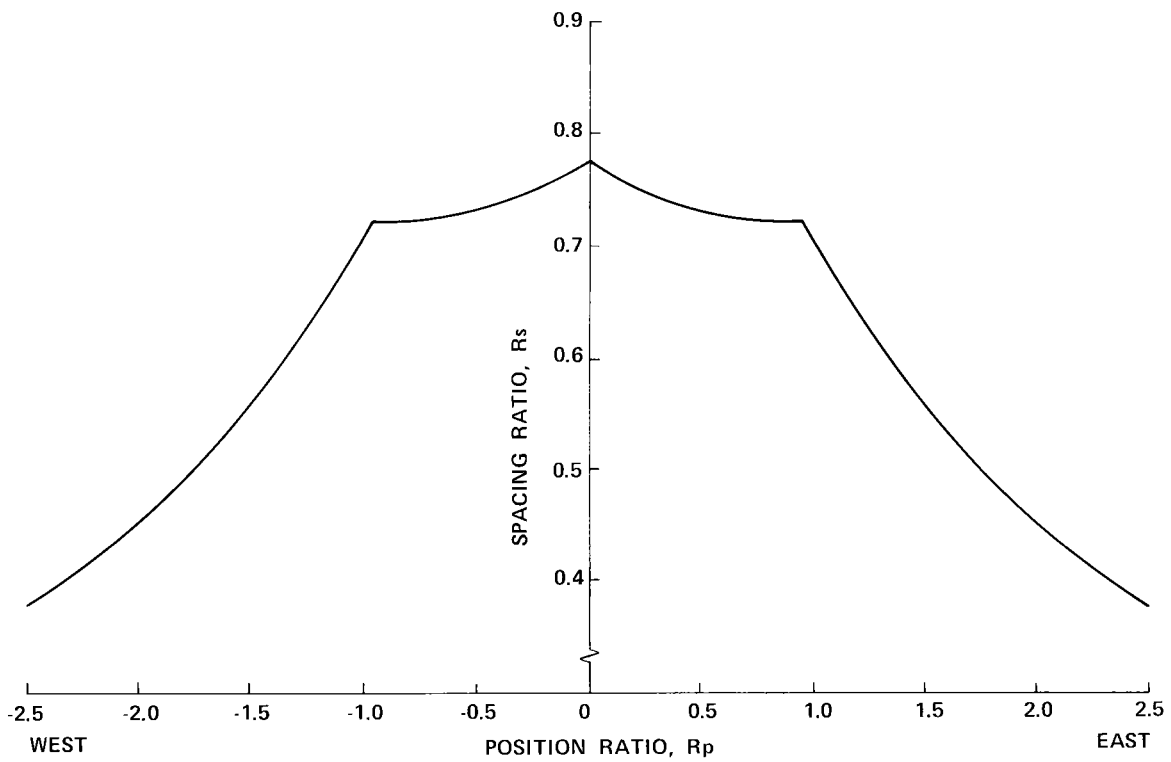


Figure 3-18. Nonuniform Field West-East Mirror Spacing Ratio for No Shadowing or Blocking Between 9:00 a.m. and 3:00 p.m. on June 21

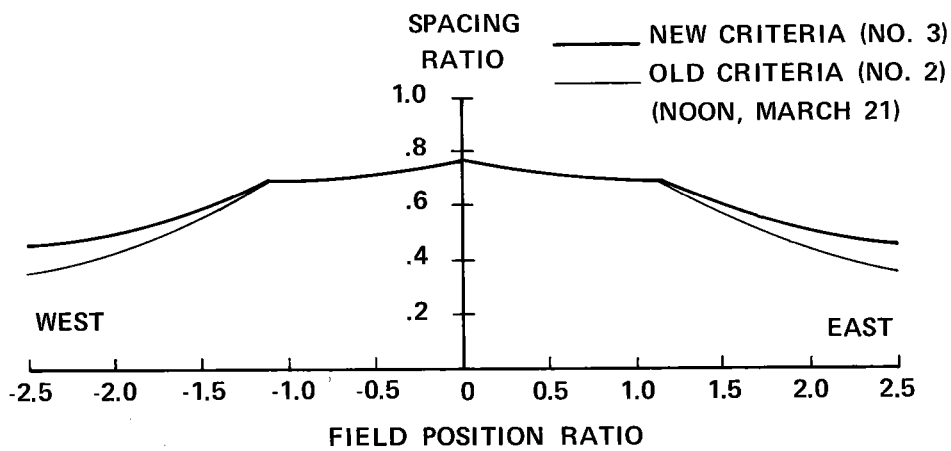


Figure 3-19. East-West Spacing Ratio Criteria for Field Number 3

spacing has been decreased for the outer heliostats to achieve a shrinking of the field at some cost in obscurations. Figure 3-20 shows the percent of area overlap that exists at 9:00 a.m., June 21 with this heliostat spacing.

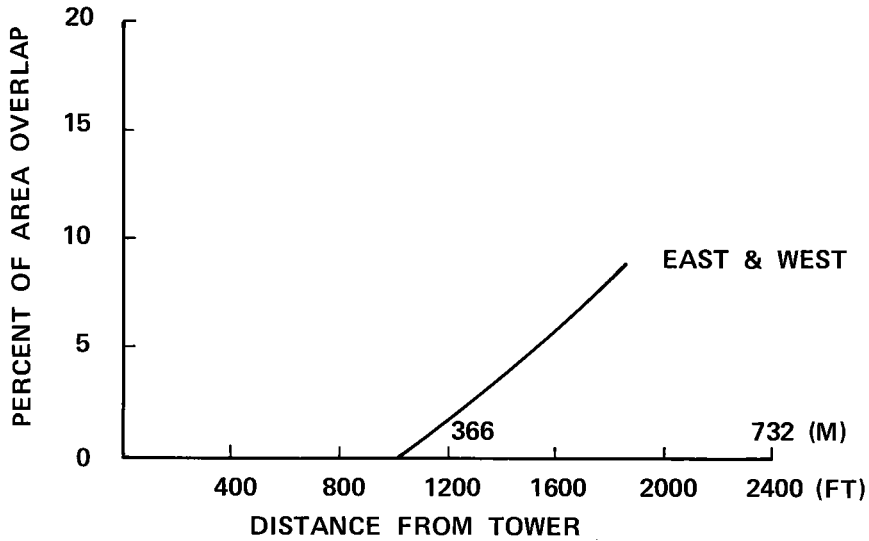


Figure 3-20. Percent of Area Overlap, East-West, Field Number 3

Nonuniform Field Design

The field criteria quantified above were used in the computer simulation to define the locations of the heliostats in the field. The three nonuniform fields were used to define field sizes and shapes consistent with the system power specification. Once these characteristics were defined based on the peak time-point (noon, March 21), the field performance of other timepoints was examined. In some cases, flux maps at the aperture and on the cavity walls were generated on the computer software.

Field Number 1. Figure 3-21 shows the field that was derived from the appropriate criteria and spacing geometry discussed above. It is a relatively large field (1219 m by 1036 m [4000 ft by 3400 ft]) and, as desired, exhibits essentially no obscurations throughout the year. The average ground cover is 0.27. Tables 3-2 and 3-3 list the field characteristics and the aperture sizes associated with this field. Annual energy for this field (all four cavities) is approximately  $530 \times 10^3$  MWh. Heliostats on the outer edge of this asymmetric field each provide similar peak performance--approximately 20 kW per heliostat.

Table 3-2  
 HELIOSTAT FIELD NUMBER 1--FIELD CHARACTERISTICS \*

QUADRANT	RADIUS m (ft)	NUMBER OF HELIOSTATS	POWER MWth
North	792 (2600)	2828	78
South	427 (1400)	1506	33
East	518 (1700)	1527	38
West	518 (1700)	<u>1527</u>	<u>38</u>
Totals		7388	187

\* Based on the following.

Average ground cover = 0.27  
 Tower height = 213 m (700 ft)  
 Cut out radius = 85 m (280 ft)

Table 3-3  
 HELIOSTAT FIELD NUMBER 1--RECEIVER CHARACTERISTICS \*\*

QUADRANT	CAVITY DIAMETER m (ft)	APERTURE		POWER MWth
		DIAMETER m (ft)	AREA m <sup>2</sup> (ft <sup>2</sup> )	
North	24 (78)	8.5 (28)	57 (616)	78
South	12 (39)	6.7 (22)	35 (380)	33
East	15 (49)	6.7 (22)	35 (380)	38
West	15 (49)	6.7 (22)	35 (380)	38

\*\* Based on the following.

All cavities 12 m (39 ft) high  
 Average ground cover = 0.27  
 Tower height = 213 m (700 ft)  
 Cut out radius = 85 m (280 ft)

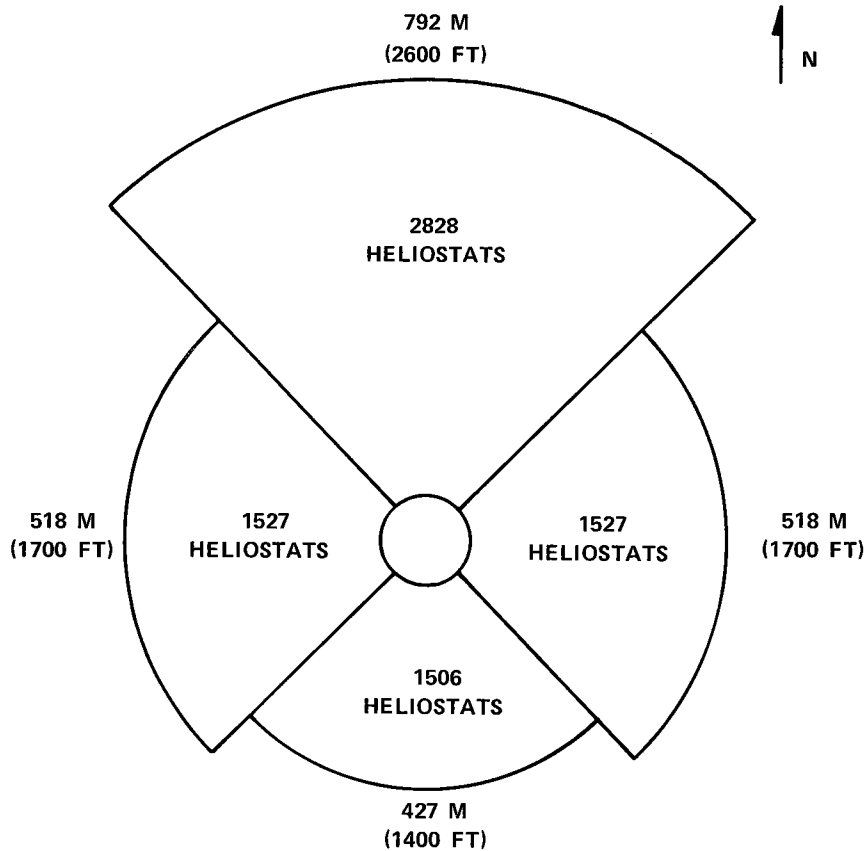


Figure 3-21. Heliostat Field Number 1

Field Number 2. Figure 3-22 shows the field that was derived from the appropriate criteria and spacing geometry discussed above. Field Number 1 is also shown (dashed) for comparison. This field represents a 28 percent savings in field area and requires essentially the same number of heliostats to meet the peak power specification. The average ground cover is 0.36. Table 3-4 lists the field characteristics and the aperture sizes associated with this field.

Field Number 3. Figure 3-23 shows the heliostat field that was derived from the appropriate criteria and spacing geometry. Field Number 1 is also shown (dashed) for comparison. This heliostat field represents a 39 percent saving in land area over Field Number 1.

Baseline Heliostat Field. The baseline heliostat field is shown in Figure 3-24. This field was derived from Field Number 3 by requiring equal effectiveness of all

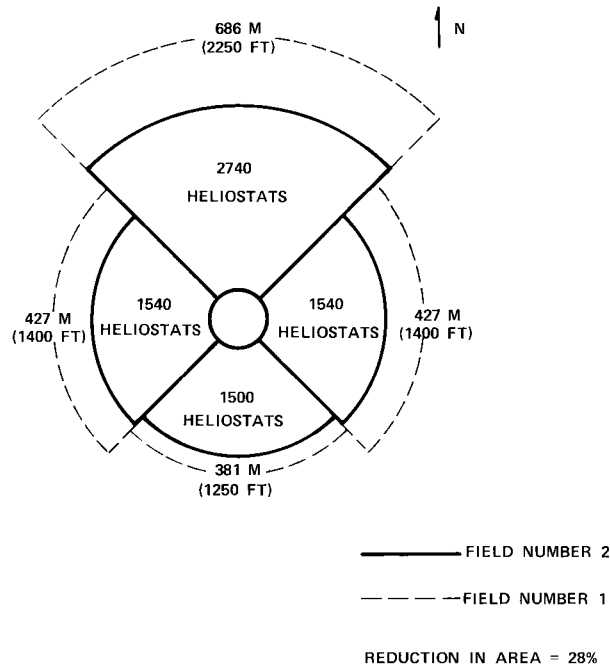


Figure 3-22. Heliostat Field Number 2

Table 3-4  
HELIOSTAT FIELD NUMBER 2--CHARACTERISTICS \*

QUADRANT	RADIUS m (ft)	NUMBER OF HELIOSTATS	POWER MWth
North	686 (2250)	2740	78
South	381 (1250)	1500	33
East	427 (1400)	1540	38
West	427 (1400)	<u>1540</u>	<u>38</u>
Total		7320	187

\* Based on the following.

Average ground cover = 0.36

Tower height = 213 m (700 ft)

Cut out radius = 85 m (280 ft)

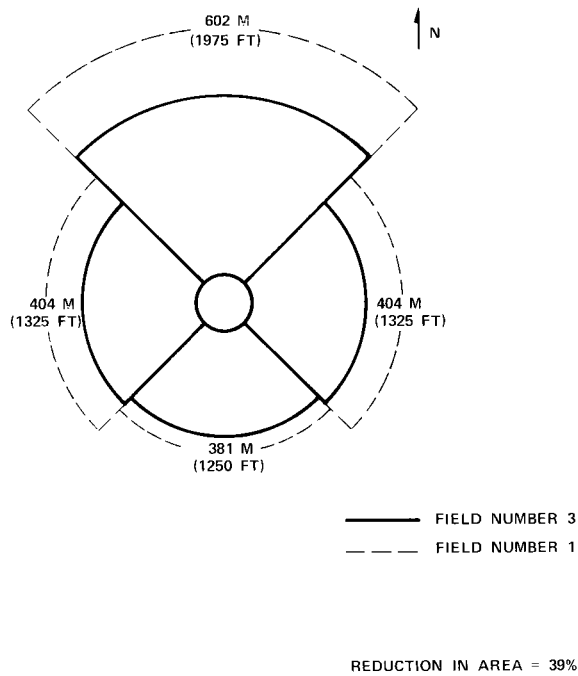


Figure 3-23. Heliostat Field Number 3

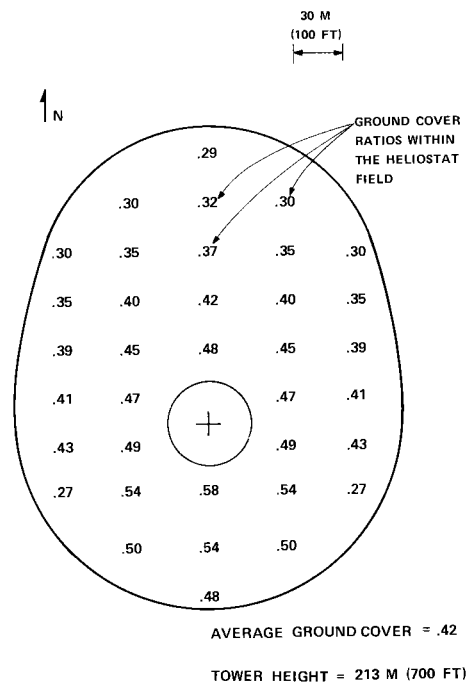


Figure 3-24. Plan View of Baseline Design Heliostat Field

mirrors on the perimeter of the field. The characteristics of this baseline field are given in the following tabulation.

Land Area	650,000 m <sup>2</sup> (6,993,000 ft <sup>2</sup> )
Cut out radius	85 m (280 ft)
Average ground cover	0.42
Tower height	213 m (700 ft)
Number of Heliostats	6990

Field performance characteristics are given in Tables 4-1, 4-2, and 4-3.

#### Baseline Field Analysis

The baseline field was analyzed by Black & Veatch to size the four receiver cavities based on the power from the field quadrants at solar noon on March 21. This analysis was also used to determine the aperture sizes which resulted in the maximum system efficiency. Direct incident flux maps on the interior surfaces (both heat transfer surfaces and inert surfaces) of the cavities were calculated for use as input in a detailed cavity heat-balance analysis. The results of this analysis are contained in two subsections of Section 4, "Cavity Heat Exchanger Design" and "Cavity Performance."

## Section 4

### RECEIVER CAVITY AND HEAT EXCHANGER DESIGN

There are no precedents for the design of a high-temperature, air-cooled heat exchanger to convert redirected solar power to thermal power. Therefore, the first phase of the design procedure was to determine the criteria which this heat exchanger must satisfy. These criteria are:

- The operating stresses in the heat exchanger must be well below a conservative estimate of the allowable stresses of the materials at operating temperature in an oxidizing environment.
- The overall efficiency of the heat exchanger must be as high as possible.
- The heat exchanger must have sufficient operational flexibility to function properly during daily and annual variation in the sun's position and during partial cloud cover conditions.
- The heat exchanger must raise air, at about 140 psia, to about 1950°F with a total pressure loss below 5 psi.

At each major design decision point, these criteria were used to select the most suitable alternative. This section describes for each major design decision the alternatives and the rationale (including analytic methodology) used in selecting among the alternatives.

#### FUNDAMENTALS OF HIGH-TEMPERATURE, CAVITY-TYPE HEAT EXCHANGERS

Prior to developing the conceptual baseline design of the receiver, a significant effort was expended in a preliminary analysis of the fundamental physical relationships which govern the performance of a high-temperature, cavity-type heat exchanger.

#### Important Parameters

While the cavity receiver must satisfy criteria such as fabricability, reliability, and operational flexibility, these criteria will be a strong function of the materials and heat transfer geometry. The cavity efficiency, however, has been

shown to be a strong function of two parameters and a very weak function of all other parameters. The two important parameters are (1) the ratio of heat transfer area to aperture area and (2) the heat transfer surface efficiency. In this preliminary analysis, the details of the heat exchange surface were not considered. Instead, each cavity surface is modeled as a smooth surface. The two parameters are defined as follows.

- Area Ratio--The area ratio,  $R$ , is the ratio of the heat transfer surface area to the aperture area. The heat transfer surface area is calculated as the total area of those cavity surfaces on which heat transfer devices will be located. The area ratio,  $R$ , is a single number.
- Heat Transfer Surface Efficiency--The heat transfer surface efficiency is calculated by considering an imaginary surface which is placed in front of the actual heat transfer surface. The heat transfer surface efficiency,  $\eta_{HT}$ , is defined by the following equation.

$$\eta_{HT} = \frac{\phi_{ON} - \phi_{OFF}}{\phi_{ON}} \quad (4-1)$$

Where  $\phi_{ON}$  is the total flux, from all sources, crossing the imaginary surface toward the heat transfer surface; and  $\phi_{OFF}$  is the total flux, from all sources, crossing the imaginary surface outward from the heat transfer surface. The heat transfer surface efficiency is, by this definition, that fraction of the power incident on a portion of the heat transfer surface which is absorbed by the heat transfer fluid in that portion of the heat transfer surface. This surface efficiency is a function of the location in the cavity. It is also a strong function of the detailed heat transfer surface geometry.

#### Cavity Efficiency

The results of the preliminary analysis are as follows.

- The cavity efficiency is a very weak function of the incident radiation flux distribution.
- The cavity efficiency is a very weak function of the shape of the cavity.
- The cavity efficiency is a strong function of the average value of the heat transfer surface efficiency,  $\bar{\eta}_{HT}$ , but is a very weak function of the manner in which that heat transfer surface efficiency varies throughout the cavity.
- The cavity efficiency is a strong function of the area ratio,  $R$ . This is because for the power leaving any portion of the cavity interior, the fraction of that power lost through the aperture decreases as  $R$  increases. The size and location of inert surfaces have very little effect on the cavity efficiency. Inert surfaces

are those which do not have coolant flow but, at equilibrium, reflect and reradiate all the power which they receive.

- If the weak functional dependences of the cavity efficiency are neglected, the cavity efficiency,  $\eta_C$ , can be accurately estimated using the following formula.

$$\eta_C = \frac{R \cdot \bar{\eta}_{HT}}{R \cdot \bar{\eta}_{HT} + (1 - \bar{\eta}_{HT})} \quad (4-2)$$

This relationship is shown graphically in Figure 4-1. Examination of this figure shows that the cavity efficiency can be increased by increasing the average heat transfer surface efficiency or by increasing the ratio of heat transfer surface area to aperture area.

- It will be shown later in this section that fabricability and reliability considerations will place an upper limit on the heat transfer surface efficiency. Therefore, if the cavity efficiency is to be improved, it must be by improving the area ratio. Since an increase in the heat transfer surface area increases the size, weight, and cost of the receiver, this area ratio is best increased by reducing the aperture area. The proper sizing of the aperture area is a difficult problem, since any reduction in aperture area increases cavity efficiency but decreases the total power into the aperture. The proper aperture sizes were calculated and will be discussed later in this section.
- Other methods of increasing cavity efficiency were considered. One method was to cover the aperture with a glass-like substance which is opaque to long-wavelength radiation but translucent to almost all of the solar spectrum. This would create a "greenhouse" effect. The analysis showed that significant improvement in cavity efficiency was possible only for cavities with an initial low efficiency. For an efficient cavity, the reflective losses at the aperture far outweighed the "greenhouse" effect.

#### HEAT TRANSFER SURFACE CANDIDATE MATERIALS

Those materials which might have proved suitable for the heat transfer surface include both metals and high-temperature ceramics. This section discusses the preliminary candidate materials and the rationale behind the selection of the final candidate materials.

##### Metals

Because conventional, large-scale gas turbines have turbine inlet gas temperatures of about 1038°C (1900°F), it is desirable to heat the compressed air to this temperature range. Some portion of the heat transfer surface will, therefore, have a temperature approaching 1093°C (2000°F). Because of this very high operating temperature, only nickel-base and cobalt-base superalloys were considered. These include the following.

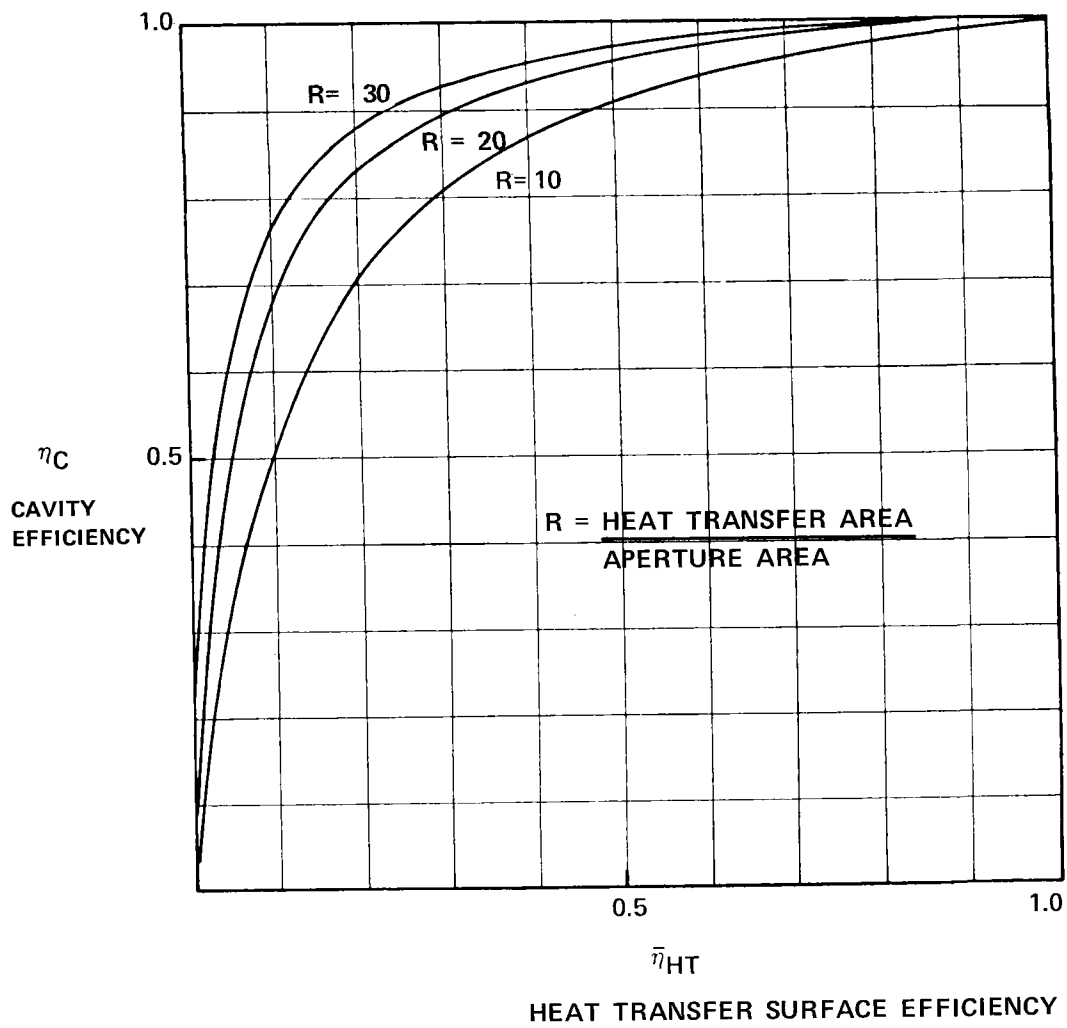


Figure 4-1. Estimated Cavity Efficiency

- Inconel 600
- Inconel 617
- Inconel 800
- Haynes 188
- Hasteloy X

All of these materials experience a rapid decrease in creep rupture strength as the operating temperature increases above 871°C (1600°F). Even with the relatively low gas pressure used in this system, and the assumption that the incident radiation was distributed as favorably as possible, analysis showed that none of the candidate metals had operating stresses below their estimated values for 100,000-hour creep rupture failure. When the anticipated incident flux distribution and the necessity for a safety factor are considered, none of the candidate metals are suitable for heating compressed air above 732°C (1350°F). Since the cycle efficiency would be significantly reduced by this low operating temperature, metals were rejected as a suitable heat transfer surface material.

#### Ceramics

Because of their high allowable temperatures and comparatively high yield strengths, ceramics are obvious candidates for consideration for a high-temperature heat exchanger. The uncertainties regarding ceramics for this application are resistance to thermal shock, resistance to thermal fatigue, and suitability of fabrication and joining techniques.

Georgia Tech prepared a large table of material properties for those ceramics which might be suitable for a high-temperature heat exchanger. This table is shown in Appendix A. All of the materials in this table have some properties which are required for high-temperature operation. The list of suitable ceramics was reduced to three by consideration of the following properties.

- Allowable Stress
- Thermal Conductivity
- Thermal Expansion
- Operating Temperature Limit
- Capital Cost
- Commercial Availability
- Fabricability
- Available Joining Techniques

The three final candidate ceramics were silicon carbide, cordierite, and alumina.

## HEAT TRANSFER SURFACE GEOMETRIES

Two fundamentally different heat transfer surface geometries were considered. This section describes and discusses the two geometries and their respective advantages and disadvantages. The methodology used to analyze these two geometries, the results of those analyses, and the rationale for the selection of the recommended geometry will be presented in subsequent sections.

### Tube-Type Geometry

The obvious, and most straightforward, heat transfer geometry is a tube-type configuration. This is shown in Figure 4-2. In this configuration, thin-walled tubes are placed inside the cavity where they will be heated, not only by direct incident flux, but also by flux which was reflected or reradiated from other portions of the cavity. The coolant, compressed preheated air in this system, is forced through the tubes where it is convectively heated. The tubes will be arranged in banks with spaces between the tubes. An inert ceramic surface will be placed behind the bank of tubes in order to reflect and reradiate flux onto the backs of the tubes and thereby minimize circumferential flux variation.

The tube-type geometry has the following advantages.

- The high-temperature ceramic materials are manufactured in tube form in a wide range of diameters and wall thicknesses. The ceramic sheets to be used as the inert back walls are also commercially available.
- Extensive field erection will not be required because the ceramic components of the tube-type geometry are available in fairly large pieces.
- The failure of a single tube will not require the receiver to be removed from service because the air will flow through many tubes in a parallel flow arrangement.
- The methods of analysis which will be used are known to yield valid results because the geometry is similar to that used in conventional, radiant heat exchangers. This will decrease the required factor of safety and, consequently, the capital cost.

The tube-type geometry has the following disadvantages.

- It is impossible, in practice, to maintain a circumferentially uniform flux on the tubes; therefore there will be tensile thermal stresses in the tube walls. Ceramics are much weaker in tension than in compression.
- High-temperature, high-pressure ceramic joints have not been required by existing systems; consequently methods of producing joints of this type have not been investigated in depth. Although

the vendors of ceramic tubes express confidence in producing joints that will satisfy the requirements of this system, no such joints have a proven performance record.

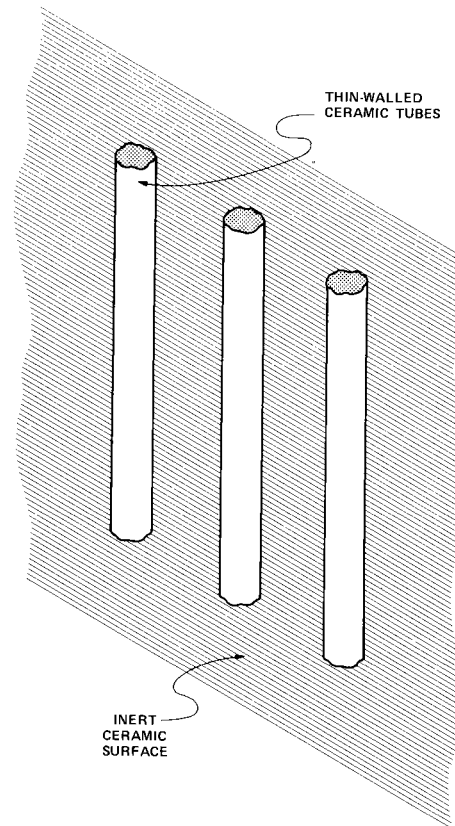


Figure 4-2. Tube-Type Heat Transfer Surface Geometry

#### Extended Surface Geometry

The extended surface geometry is shown in Figure 4-3. In this geometry, there is a large surface, called the web, which is convex when viewed from the gas side. The web has a large number of small holes, each of which acts as the base of a hollow finger which extends into the gas flow path. A portion of the radiation striking the heat transfer surface will enter the fingers. Each finger, acting as a tiny cavity, will trap that radiation and be heated. The gas will be heated by convection as it flows across the outside of the fingers.

The extended surface geometry has the following advantages.

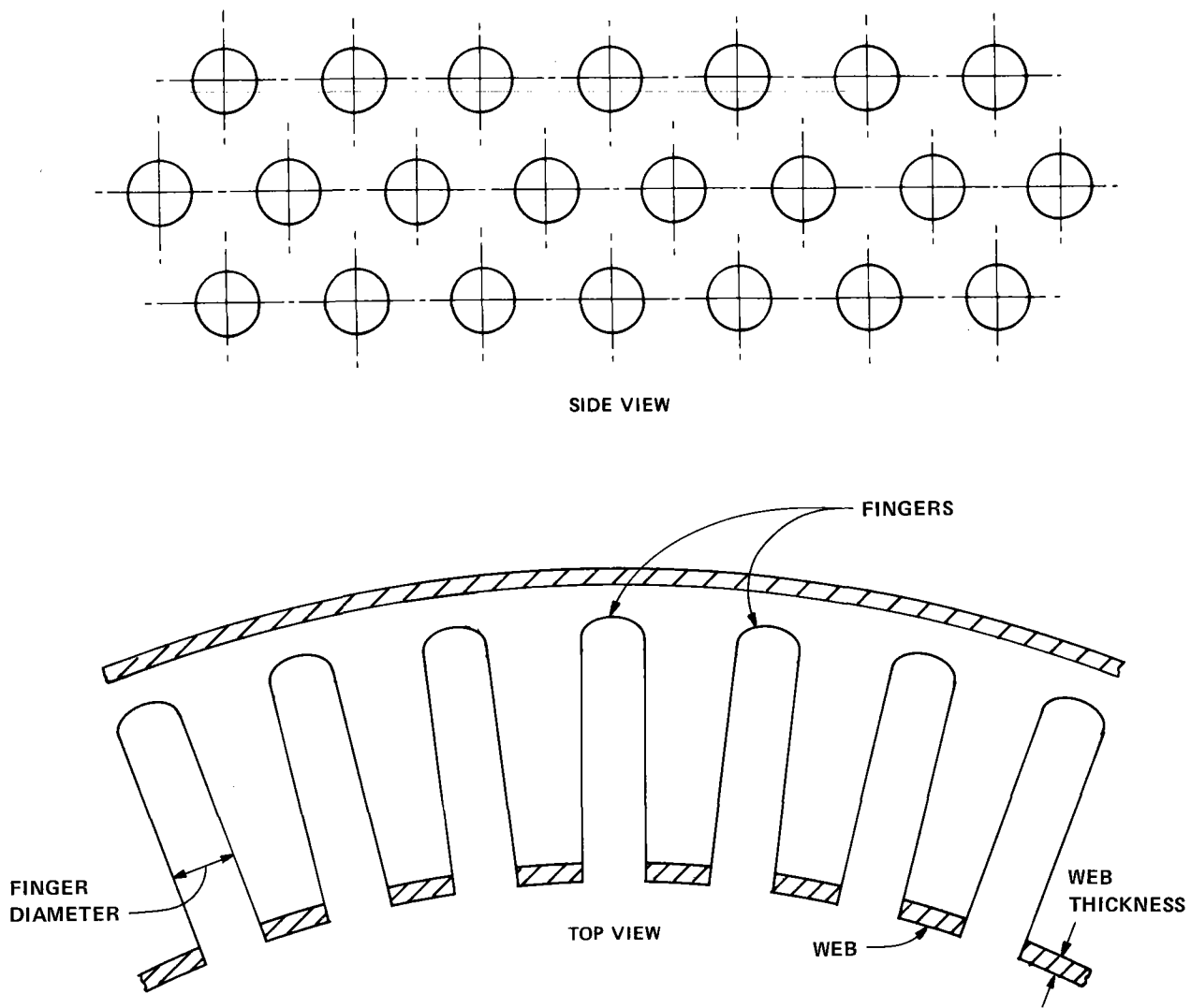


Figure 4-3. Extended Surface Heat Transfer Geometry

- The web-finger arrangement will be in compression from the internal air pressure because the coolant is external to the heat transfer surface. It should be possible to design the receiver in such a manner that the total stress anywhere in the web or fingers is compressive.
- The joints between sections of the web, and the joints between the web and the fingers, will be in compression because of the pressure of the external coolant. This should simplify the joining techniques.

The extended surface geometry has the following disadvantages.

- Neither the fingers nor the web sections are commercially available. Special orders would be required.
- This geometry would probably require extensive field erection, utilizing highly skilled labor.
- Although the heat transfer surface is in compression, the cavity shell is in tension. The construction of a pressure vessel of the size required for this system is an exceedingly difficult task. A preliminary estimate of the thicknesses required indicated a total receiver shell mass of approximately 1.8 million kg (4 million pounds).
- The detailed analyses of this geometry would be very complex because the configuration is irregular. These analyses would, of necessity, require some engineering approximations. The results of these analyses would, therefore, require a larger factor of safety than would be required for a more simple geometry.

#### HEAT TRANSFER SURFACE DESIGN ANALYSIS

For each of the two geometries, there is a preferred design. That design is the one which best satisfies the criteria on page 4-1. In order to determine the preferred design for each of the two geometries, to select the better of those two designs, and predict the performance of that better design, a detailed analysis of each of the two geometries was performed. This section describes the analytic methodology used and the results of the analyses.

##### Analytic Methodology

The approaches used in studying the two geometries were similar with regard to the assumptions made, the equations developed, and the method of solving those equations.

In both cases, a unit area of the heat transfer surface was considered. It was assumed that the unit areas adjacent to the unit being studied were identical with that unit area. This is justified because the temperature and flux gradients at

the microscopic level (within the unit area) are orders of magnitude larger than the gradients of the average temperature and average flux at the macroscopic level (among unit areas). The unit area of heat transfer surface, whether a portion of the web-finger arrangement or a few tube segments, was broken into about fifty small areas. The fluxes and temperature on each small area were assumed to be constant across that small area. A further assumption was made that both reflection and reradiation will be Lambertian in nature. With these assumptions, it was possible to formulate a system of nonlinear equations which have as unknowns only the temperatures of the small areas. These equations include the effects of reflection, reradiation, convection, and conduction. Because the adjacent unit areas were assumed identical to the unit area being studied, the radiative and conductive effects of those adjacent unit areas were included without increasing the number of variables in the equation set. Because it was possible to invert the radiative interaction matrices in closed form, infinite-order reflections were included. The equation set was solved iteratively using a matrix version of the Newton-Raphson technique. Convergence was very rapid, and unconditionally stable with regard to variation of any independent parameter.

The convective interaction between the ceramic and the gas was modeled using accepted correlations. The thermal and mechanical stresses were calculated using the classical theory of elasticity. The gas thermodynamics were based on an ideal gas model.

### Results of Analyses

Tube-Type Geometry. For each of the two geometries, a large number of parametric studies were conducted. These studies yielded a large body of data which, because of the large number of varied parameters, is not conveniently presentable in either graphical or tabular form. This section presents the qualitative conclusions of these quantitative analyses. The results of the analysis of the tube-type geometry are as follows.

- The gas convective-cooling coefficient is a very weak function of tube diameter. For developed turbulent flow, which this system requires for effective heat transfer, the convective coefficient is proportional to the tube diameter raised to the one-fifth power. If this weak dependence is neglected, the analytic results for the tube-type geometry are independent of tube diameter.
- The tube wall thickness affects the thermal stress, the pressure stress, and the amount of thermal conduction around the tube circumference. This thermal conduction was found to have a very

small effect on the analytic results, being completely overshadowed by the radiative heat transfer. The major contribution to the maximum stress in the tubes was found to be the temperature variation around the tube circumference. The thermal stress caused by the temperature difference through the tube wall was small because that temperature difference was small, on the order of 1°C (1.8°F). The temperature drop between the outside of the tube and the coolant was almost entirely across the boundary layer film. Therefore, the stress and temperature levels and distributions are almost independent of tube wall thickness. Since the tubes are thin-walled, and because the wall thickness is not an important parameter, the tubes can be modeled as having no wall thickness. This approximation causes little inaccuracy and results in a single value for tube diameter.

- The geometry can be uniquely specified by two dimensionless numbers since the results are almost independent of tube diameter and wall thickness. One is the ratio of tube spacing to tube diameter (S/D) and the other is the ratio of the offset of the tubes from the back wall to the tube diameter (O/D). The distances D, S, and O are defined in Figure 4-4.
- For a broad range of fluid and flux parameters, the minimum total stress in the tubes was found to occur for an S/D ratio of about 3:1. If the tubes are placed closer than this, not enough energy passes between the tubes to effectively heat the back sides of the tubes. This results in large thermal stresses. If the tubes are placed much farther apart than this, there is no effective mechanism to heat the sides of the tubes, which then run colder than the front and back. This also causes large thermal stresses. A typical result is shown in Figure 4-5 for silicon carbide tubes with an O/D ratio of 2:1, an air temperature of 704°C (1300°F), and a convective-cooling coefficient of 170 W/m<sup>2</sup> °C (30 Btu/h-ft<sup>2</sup>-°F). It should be noted that, for an incident flux of 225 kW/m<sup>2</sup>, the maximum tensile stress for an O/D ratio of 3:1 is about 34 mPa (5 Ksi), which is less than one-half of the minimum estimate of the allowable stress for silicon carbide at temperatures up to 1316°C (2400°F).
- The maximum tensile stress was found to be a function of the O/D ratio. The minimum stress value was calculated for an O/D ratio of 1:1. However, care must be taken with this result. For large (5:1) values of O/D, the analysis did not include sufficient adjacent areas to assure accuracy. For small (1:1) values of O/D, the small areas into which the unit area was subdivided were too large with respect to the distances between them to assure accuracy. The optimum O/D ratio is probably near 1:1 but further analysis will be required in detailed design.
- Silicon carbide and cordierite have similar thermo-optical and thermomechanical properties. The temperature and stress results for these two materials were very similar. Alumina has a high

thus  
MAX  
ALLOW

is  
2X225=450  
↑?

See  
4-13

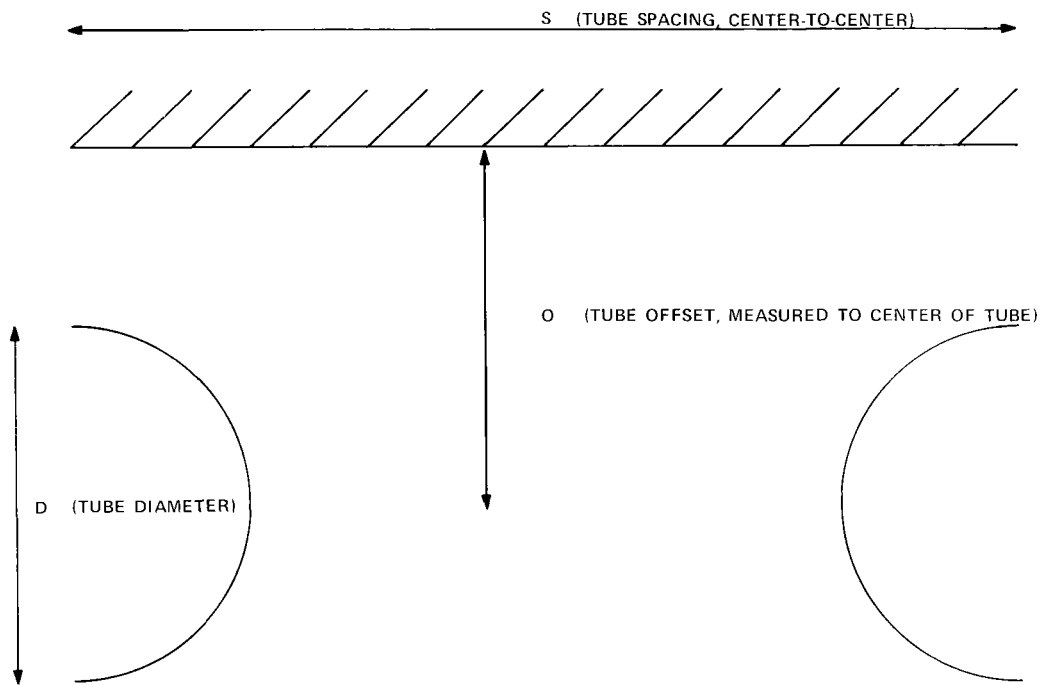


Figure 4-4. Tube-Type Receiver Layout

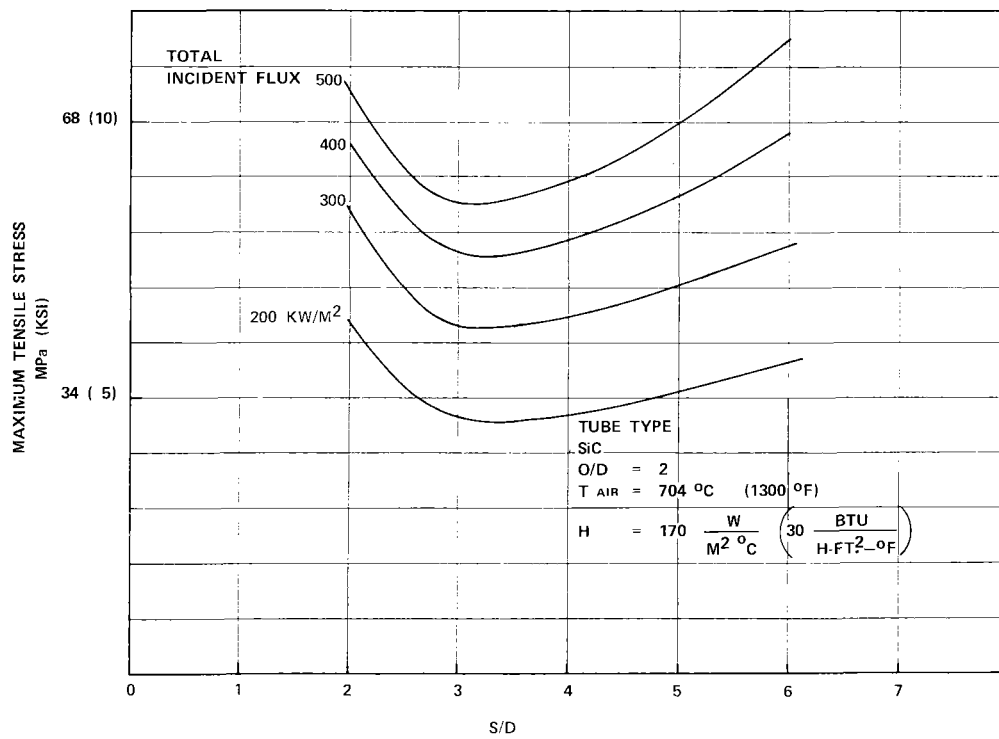


Figure 4-5. Tube Stresses as a Function of Design Parameters

coefficient of thermal expansion, a low thermal conductivity, and a low allowable stress, when compared with either silicon carbide or cordierite. The ratio of maximum stress to allowable stress was approximately twice as great for alumina as for the other two materials.

- Both the temperature and stress results were found to be insensitive to the thermo-optical material properties and to the incident flux distribution.
- The preliminary analyses, described earlier in this section, indicated that the total incident flux onto the heat transfer surface will not vary much from its average value. An average value of  $225 \text{ kW/m}^2$  appears to be optimum. Below this value, the heat transfer surface efficiency decreases. Above this value, the heat transfer surface efficiency increases very slowly and the maximum tube temperature continues to rise. An average total incident flux of  $225 \text{ kW/m}^2$  provides an average heat transfer surface efficiency which is about as high as is consistent with an S/D ratio of 3:1. For an average total incident flux of  $225 \text{ kW/m}^2$ , the average heat transfer surface efficiency is about 0.43. The maximum allowable value of total incident flux, based on material stress and temperature limits, is about  $450 \text{ kW/m}^2$ . The cavity was designed for an average total incident flux of  $225 \text{ kW/m}^2$  and will have a peak total incident flux below  $375 \text{ kW/m}^2$ .

Extended Surface Geometry. The results of the analysis of the extended surface geometry are as follows.

- Since the compressed air will be flowing across many banks of fingers, neither the pressure drop nor the convective heat transfer coefficient will be affected by the manner in which the banks of fingers are arranged with respect to each other. Rather, these parameters will depend only on the number of fingers and the spacing between nearest fingers. Therefore, an arrangement of the fingers in a hexagonal, close-packed array was chosen as the optimum layout.
- Since the pressure drop in the receiver impacts the cycle efficiency, the finger spacing is determined by trading off pressure drop against convective efficiency. An analysis of a single finger showed that the length of a finger should not exceed five times the diameter of a finger. For longer fingers, that length beyond five diameters contributes to the pressure drop in the gas, but does not materially aid in heat transfer.
- For a finger L/D ratio of 5:1, the spacing between fingers is governed by pressure drop considerations. It was found that, for fingers placed closer than two diameters between centers, the pressure drop in the receiver approached ten percent of inlet pressure to the receiver. Therefore, the extended surface which was used in the analysis was a hexagonal, close-packed finger array with a spacing between fingers equal to two finger diameters.

- The minimum web thickness, from structural strength and fabricability considerations, appeared to be about one inch. For this web thickness, the maximum total incident flux was limited to about 200 kW/m<sup>2</sup> by the value of the thermal stress in the web. For this value of total incident flux, the average heat transfer surface efficiency was calculated to be 0.23.
- Because the thermal stress calculation in the web was approximate, owing to the complicated geometry, a limiting case was analyzed in which the web thickness was permitted to approach zero. Although this could not be constructed, it did determine a relationship between total incident flux and heat transfer surface efficiency which was not limited by thermal stress considerations. With this very thin web, the upper limit on incident flux is determined by the temperature in the web material. With an assumed web temperature limit of 1316°C (2400°F), the highest obtainable average heat transfer surface efficiency was calculated to be 0.27.

#### SELECTION OF HEAT TRANSFER SURFACE GEOMETRY

The tube-type geometry was selected over the extended surface geometry for the following reasons.

- The extended surface receiver would be larger, heavier, and more expensive than the tube-type receiver. In order to have a receiver cavity efficiency of 0.92, the tube-type geometry requires an area ratio of 15:1 while the extended surface would require an area ratio of about 31:1.
- The tube-type receiver can be fabricated, using existing technology, from commercially manufactured materials. In addition, the tube-type receiver would require less field erection than an extended surface receiver.
- The only advantage of the extended surface geometry was negated because a tube-type geometry which yielded low thermal stresses was found.
- The extended surface was inferior to the tube-type geometry, even when limiting case analyses were used. If fabricability and structural considerations were included in the extended surface analysis, the extended surface could only suffer in terms of its performance. Further, because of the complexity of the extended surface geometry and the degree of approximation required in its analysis, a larger factor of safety would be required to ensure reliability. This could only increase the size, weight, and capital cost of the receiver.

The principal problem anticipated for the tube-type geometry is identification of ceramic-ceramic and ceramic-metal joining techniques which are suitable for fabrication of large cavities; these techniques should include field erection and field maintenance capabilities.

## MATERIALS SELECTION

Three candidate ceramic materials were identified earlier in this section as silicon carbide, cordierite, and alumina. The tube-type geometry was also established as the preferred heat transfer surface geometry. In this section, the rationale for the selection of the design material and design alternate material will be presented.

Alumina was eliminated as a candidate because of the thermal stress considerations already described. It can be seen from Appendix B and the earlier discussion of "Tube-Type Geometry" that the thermo-optical and thermomechanical properties, and the associated performance characteristics, are similar for cordierite and silicon carbide. Therefore, the selection between the two materials was based on other considerations.

Both ceramics are commercially available from various suppliers. The Carborundum Company of Niagara Falls, New York is a well-recognized manufacturer of silicon carbide and Coors Porcelain Company manufactures cordierite. Both companies routinely produce tubing, but current manufacturing techniques impose restrictions on lengths, diameters, and wall thicknesses available. Coors can supply cordierite tubes up to 15 cm (6 inches) in diameter, wall thicknesses of 0.3 to 0.6 cm (1/8 to 1/4 inch), and lengths up to 183 cm (6 feet). The 183-cm (6-foot) length limitation is due to kiln constraints, and could be increased to 3.0 m (10 feet) if the market demand warranted the conversion of the cordierite firing process to another kiln. Carborundum can provide silicon-carbide tubes 1.5 to 1.8 m (5 to 6 feet) in length with wall thicknesses of nominally 0.6 cm (1/4 inch). Tube diameters up to 20 cm (8 inches) are reasonable.

There is little experience in the joining of ceramic tubes at the temperature and pressure conditions of interest in this program. As a result, significant effort will be required to develop a satisfactory means of linking tubes to form the final heat exchanger configuration. It is felt that cordierite can best be joined using a sauerisen cement and a collar to enclose the butt-type joint. The required cement characteristics may be difficult to achieve, and the collars may result in unacceptable stress concentrations. Cordierite, can, at present, be molded into the geometries required by the heat exchanger.

Connection of silicon-carbide tubes is approached in a different manner. Tubes can be butt "welded" together, but air leakage through the joints could be a problem.

A problem common to all ceramic joints is the nonuniformity of the tube materials; that is, the fabrication techniques used on ceramic tubing make it difficult to hold tight tolerances, and diamond machining is very costly. The joining method must also be compatible with field erection of the heat exchanger.

Based on the currently available joining and fabrication techniques, and the amount of available data for the two materials, silicon carbide was selected as the candidate design material and cordierite as the alternative design material. A compendium of information on silicon carbide, written by the Carborundum Company, is contained in Appendix E.

As additional experimental data become available, this material selection will be reviewed to ensure that the choice of the design material reflects the latest available information.

#### CAVITY HEAT EXCHANGER DESIGN

After the tube-type geometry was selected, and silicon carbide was selected as the design material, the receiver cavities were subjected to more detailed design. This section describes the specific type of tube geometry, the sizing rationale and results of the sizing analysis, and the exterior structure of the cavities.

##### U-Tube Design

A U-tube design, as shown in Figure 4-6, was selected as the baseline heat exchanger design. This geometry has the following advantages.

- Thermal stresses will be minimized because the tubes are free to expand in a longitudinal direction, and free to bend in a lateral direction.
- The ceramic-metal joints will not be highly stressed because the tubes are free to expand longitudinally, and because these joints are not subjected to direct flux.
- The total expansion of each of the two legs will be almost equal since the cold leg of the U-tube is longer than the hot leg. This will minimize the lateral bending in the plane of the U-tube and reduce the stresses on the tube-to-duct joints.
- The top portion of the U-tube can be located above the cavity ceiling, if the bend of the U-tube is found, by subsequent analysis, to be highly stressed by a nonuniform flux pattern. If this modification were to occur, it would then be possible to lightly

springload the U-tube in its longitudinal direction, thereby simplifying the design of the joints between tube sections.

- The legs will exert a stabilizing effect on each other, reducing the effects of hot spots, because the hot and cold legs will alternate around the receiver perimeter. Further, the local value of heat transfer surface efficiency will be very nearly uniform across the heat transfer surface which increases cavity efficiency.
- The hottest air temperatures will occur at the base of the cavity where the total flux will have its lowest value.

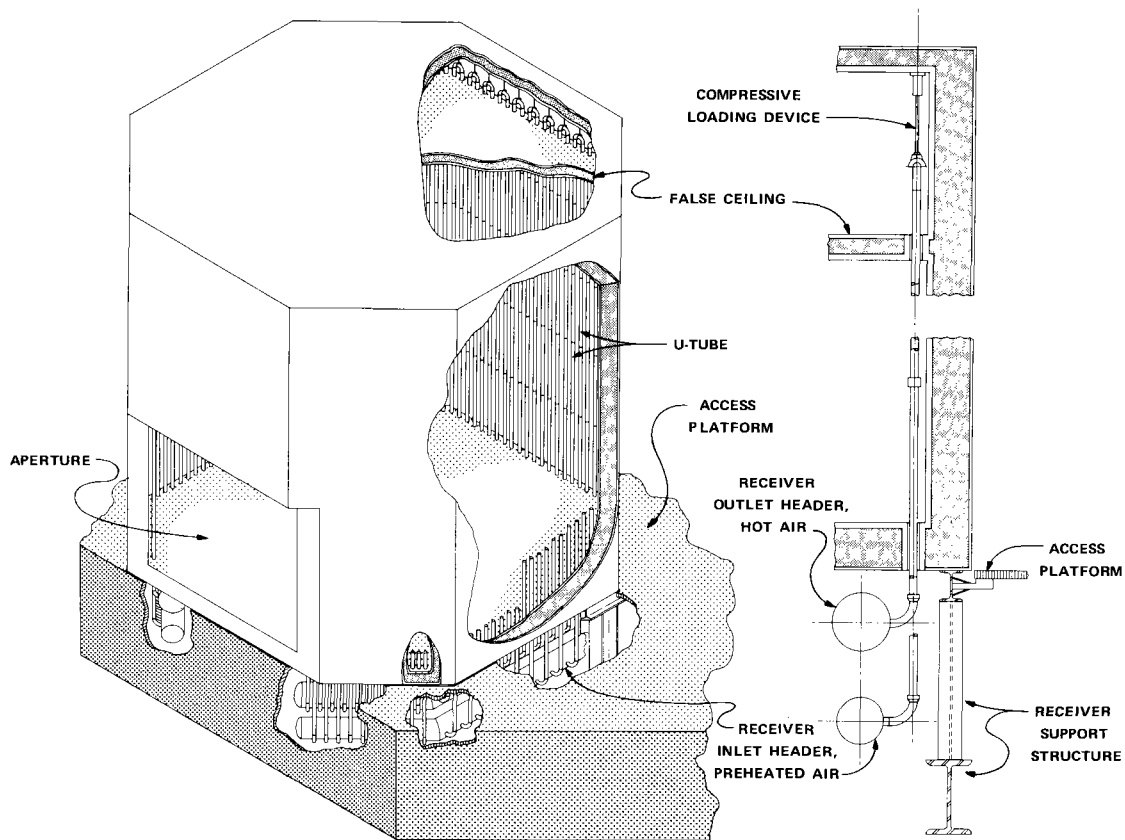


Figure 4-6. Cutaway of Tube-Type Cavity Receiver/Heat Exchanger

#### Cavity Sizing

The four receiver cavities will not be equal in size, because the different portions of the heliostat field will reflect different amounts of solar-thermal energy as a function of time of day and day of year. All four cavities will have the same height, 12.2 m (40 feet). This permits the U-tubes in the cavities to be standardized both in length and number of segments.

This standardization minimizes the design analysis effort and offers a possible cost reduction from mass-production techniques. The differences among the cavities will be manifested in different perimeters and different aperture sizes.

The cavities were sized by analyzing the power from the four sections of the heliostat field at solar noon on March 21. The cleanly redirected power from the field sections, at that timepoint, is listed in Table 4-1.

Table 4-1  
CAVITY SIZE ANALYSIS, BASED ON FOUR SECTIONS OF  
HELIOSTAT FIELD AT NOON, MARCH 21

FIELD SECTION	MWt
North	69
South	33
East	41
West	41

The heat exchanger tube size was selected by analyzing the pressure drop in the tubes. If the pressure drop is too large, there will be a significant reduction of thermodynamic-cycle efficiency. If the pressure drop is too small, unbalanced flow with all of the associated problems such as tube starvation, hot spots, and tube burnout will occur. A receiver pressure drop of about 4 psi was selected as an optimum value. The resulting tube size was 4 inches inside diameter. The diameters of the cavities and the number of U-tubes per cavity are listed in Table 4-2.

The apertures were sized by mapping the flux, in the aperture plane, at solar noon on March 21. Analysis showed that the best aperture, in terms of maximizing the product of aperture efficiency and cavity efficiency, was that aperture drawn through the  $125 \text{ kW/m}^2$  isopleth. For the baseline heliostat field, these isopleths were very nearly circular; the apertures were approximated as circles. The aperture sizes are listed in Table 4-3.

Table 4-2  
CAVITY DIAMETERS AND NUMBER OF U-TUBES PER CAVITY

CAVITY	DIAMETER (m) *	NUMBER OF U-TUBES
North	19.7	88
South	10.2	42
East	12.3	52
West	12.3	52

\* Although the cavities would be octagonal, for ease of construction, they were modeled as right circular cylinders.

Table 4-3  
CAVITY APERTURE DIAMETERS, BASED ON ANALYSIS  
AT NOON, MARCH 21

CAVITY	APERTURE DIAMETER (m)
North	8.23
South	6.40
East	6.71
West	6.71

#### Receiver Housing

Because there was concern about conductive losses through the cavity walls, a detailed analysis of the wall insulation design was carried out. The design criteria were that the insulation be commercially available and that the total conductive loss be less than one percent of the cavity throughput with the conservative value of 1316°C (2400°F) as an inside wall temperature. These criteria were satisfied with a three-layer composite. The materials and their thicknesses are listed in Table 4-4.

Table 4-4  
RECEIVER HOUSING MATERIALS AND THICKNESSES

LAYER	MATERIAL	THICKNESS (cm)
Inside (hot)	EP Ceramic Firebrick	9
Middle	JM-HT Banroc	21
Outside (cold)	Diatomaceous Earth	3

The cavity structural enclosure design was addressed only at a conceptual level. Sufficient analysis was performed to ensure that no significant problems were present, and to ensure that sufficient volume, weight, and cost were included in the baseline design. A conceptual drawing of the cavity structural enclosure is shown in Appendix F.

#### CAVITY PERFORMANCE

The relationships presented in the first part of this section of the report were based on averaging techniques. While these relationships can be used to accurately estimate cavity efficiency, the averaging techniques preclude the use of these relationships to calculate the distribution, within the cavity, of flux levels and material temperatures. Therefore, a detailed cavity analysis was performed. This section describes the results of that detailed analysis.

#### Detailed Cavity Performance

This section presents the results of the detailed cavity analysis for the north-facing cavity.

Figures 4-7 and 4-8 show the maps of direct incident solar radiation on the wall and ceiling of the north cavity at solar noon on March 21. It is clear that the direct incident flux is highly nonuniform on the heat transfer surface, having a zero value over about one-half the wall area. These flux maps were used as input to the detailed cavity analysis computer software.

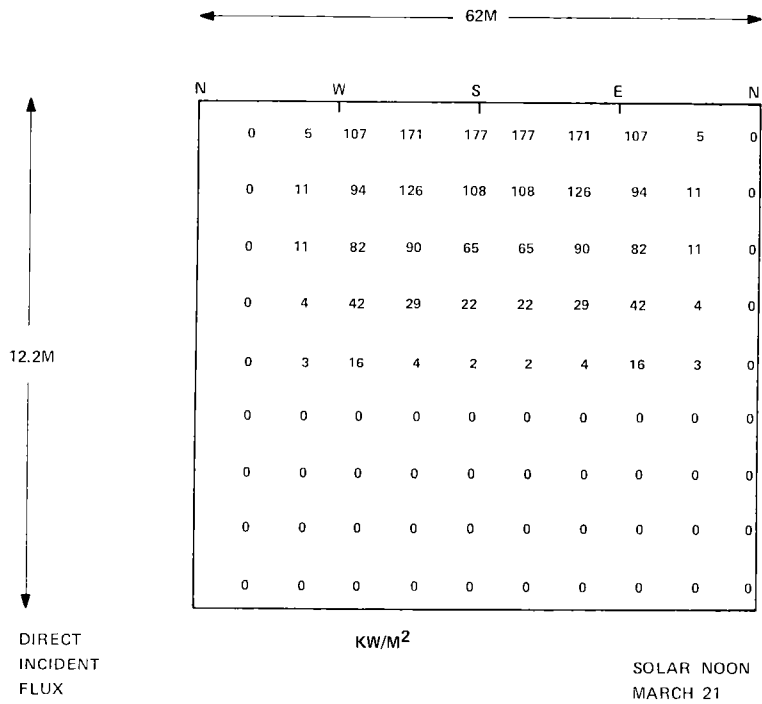


Figure 4-7. North Cavity Wall Flux Map

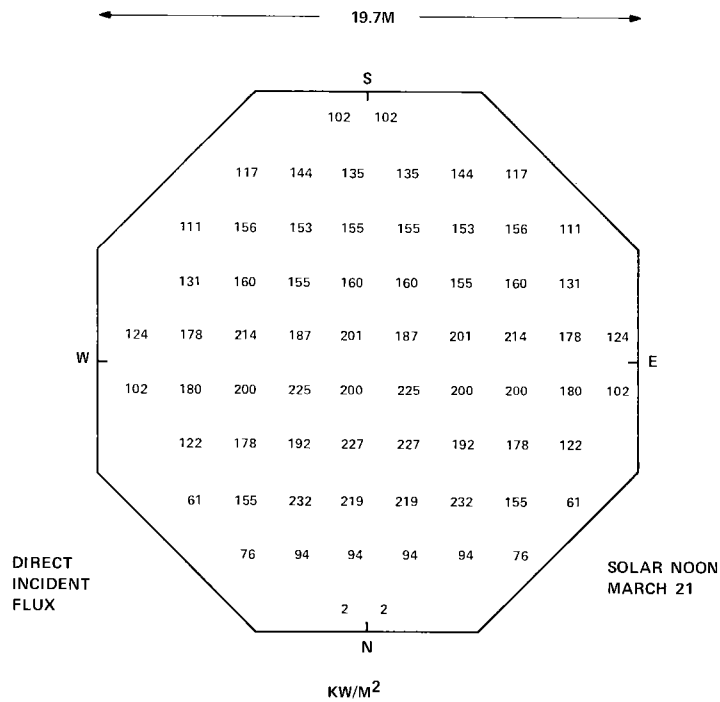


Figure 4-8. North Cavity Ceiling Flux Map

Figure 4-9 shows the map of total incident flux (including all reflected and reradiated flux) on the heat transfer surface. It is clear that the total flux is much more uniform than the direct incident flux. This is in accordance with the assumptions and results presented earlier in this section of the report. A coarser grid is used in the detailed cavity analysis than in the flux analysis in order to limit the number of independent variables.

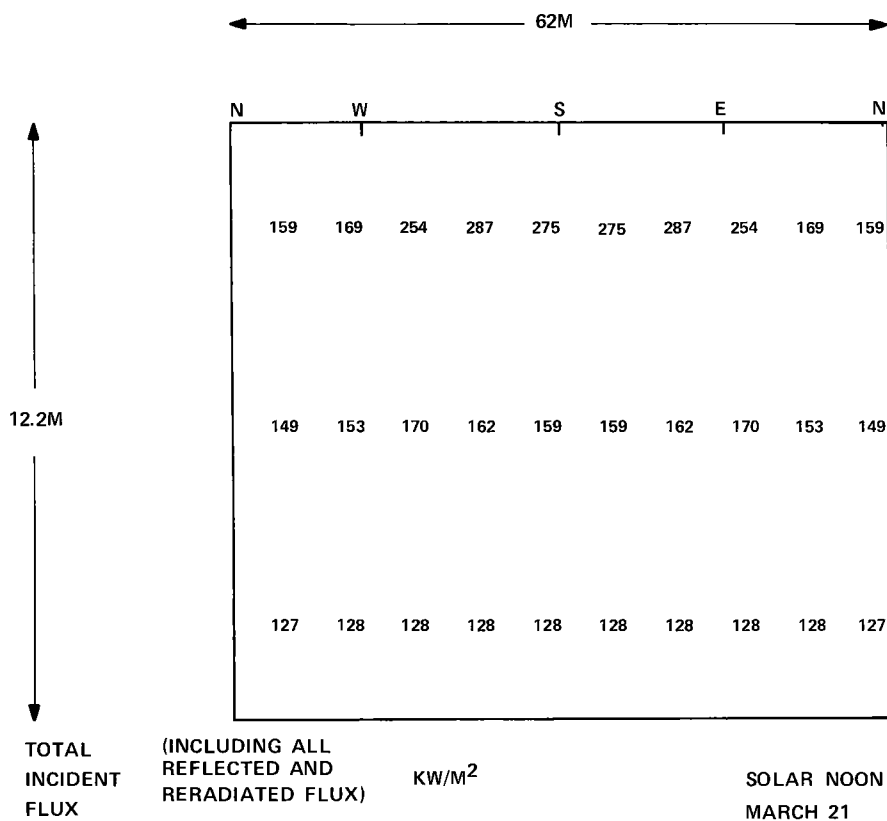


Figure 4-9. North Cavity Wall Flux Map

Figure 4-10 shows the map of absorbed flux on the heat transfer surface. The important result is that the average absorbed flux on each vertical panel, shown below the map, is very uniform around the receiver circumference. This indicates that the required air flow in the U-tubes will be almost uniform, minimizing control problems and possible hot spots.

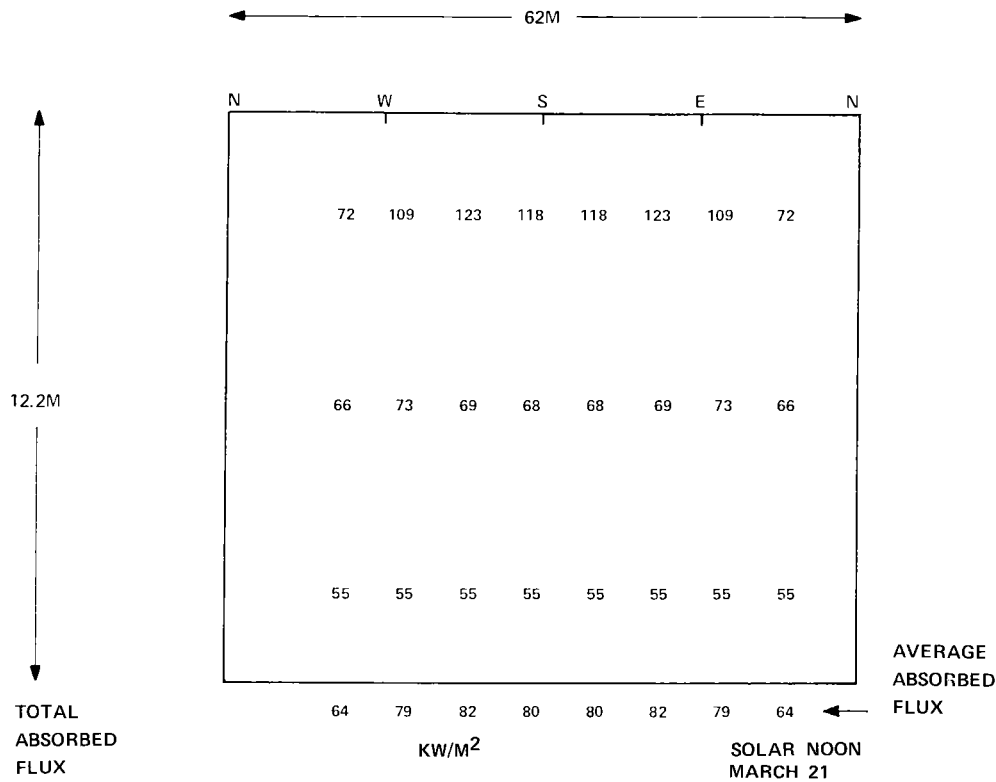


Figure 4-10. North Cavity Wall Flux Map

Figure 4-11 shows the map of maximum tube temperature on the heat transfer surface. These temperatures are well below the limiting temperatures for the final candidate materials, about 1316°C (2400°F).

#### Cavity Efficiency

For the four cavities previously specified, the efficiencies as estimated by the relationship discussed under "Cavity Efficiency" earlier in this section are given in Table 4-5.

A detailed analysis of the north cavity calculated an efficiency for the north cavity of 0.89. This correlation is close enough to reinforce the validity of the relationships developed from the averaging techniques previously given.

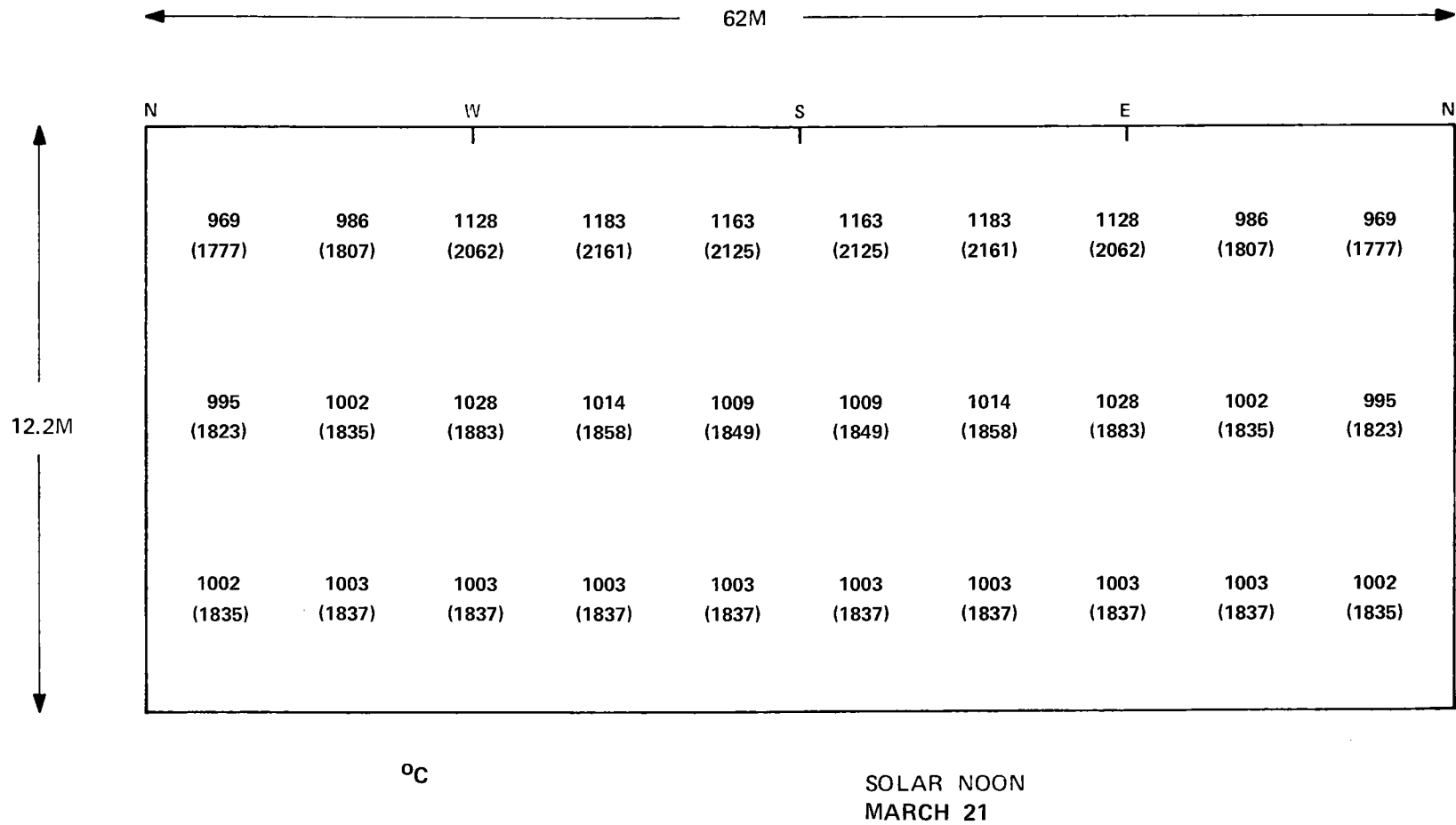


Figure 4-11. North Cavity Maximum Tube Temperature

Table 4-5  
CAVITY EFFICIENCIES

CAVITY	CAVITY EFFICIENCY
North	0.90
South	0.88
East	0.89
West	0.89

It is important to realize that while the cavity efficiencies are not as high as were anticipated, (0.92), these values are not discouraging at this point in the system design. The entire design of the receiver heat transfer surface was based on minimizing the material stresses, maximizing the reliability of the system, and ensuring sufficient heat transfer to operate the thermodynamic cycle. When more complete data are available regarding the thermal-cycling properties of the materials and the allowable stresses, it will be possible to iterate the design of the heat transfer surface to improve cavity efficiency.

For example, the S/D ratio of the tubes could be decreased below 3:1. This decrease would raise the heat transfer surface efficiency. Since the gas velocity in the tubes must be kept high to ensure turbulence and effective heat transfer, the number of tubes would not be reduced. Rather, the total heat transfer area would be reduced. This reduction would increase the fraction of the direct incident flux which strikes the heat transfer surface, which will slightly increase cavity efficiency. Further, this reduction will reduce the size, weight, and capital cost of the receiver. A preliminary estimate of the effect of a change in S/D ratio from 3:1 to 2:1 is that it would increase the cavity efficiency by about 0.21. Figure 4-5 shows that this reduction in spacing would also increase the maximum tensile stress in the tubes. For this reason, the heat transfer surface design iterations will require better material data than are, at present, available.

#### Transient Effects

There are two distinct types of transient impacts to which the cavity receiver must react. The first is the slow transient caused by the apparent motion of the solar disk. The effect of this motion is to alter the distribution of the direct incident flux on the cavity surfaces. This transient will have very little effect on the performance of the cavity. This can most easily be seen by comparing the flux distributions of Figures 4-7 and 4-9. These figures demonstrate that the circum-

ferential variation of total flux is much less than the circumferential variation of direct flux. Therefore, as the direct incident flux pattern slowly rotates around the circumference of the cavity, the total flux pattern will change even more slowly.

The second type of transient is a sudden change in the level of the direct incident flux. This could be caused by cloud cover or by a control malfunction in the heliostat field. If the flux level were to suddenly decrease, the cavity thermal inertia would maintain the turbine gas inlet temperature for a short time. As that gas inlet temperature drops, the load-carrying capacity of the turbine is reduced. As the gas inlet temperature continues to drop, the generator output will be reduced. Finally, the power output of the turbine will equal the power required by the compressor and the generator will be fully disconnected from the power grid. At that point in time, the unit will begin to lose speed. Until that point in time, however, the volume flow through the receiver will remain constant. During this transient, the maximum rate of temperature decrease in the heat transfer material is calculated to be about 100°C/minute (180°F/minute). Although the control system or the buffer storage system, if activated, would decrease the airflow through the cavity, the scenario described is that one which would cause the maximum rate of temperature decrease for the heat transfer surface material.

If the flux were to suddenly increase from zero to its maximum value and, due to a control system malfunction, no air were flowing through the cavity, the rate of temperature increase would be as large as is possible. With this sudden flux increase, the maximum rate of temperature increase is calculated to be about 400°C/minute (700°F/minute). Further, the cavity temperature would increase until it reached a temperature of about 1871°C (3400°F). It is clear that the cavity will not withstand this sudden sustained flux increase inasmuch as the limiting temperature of SiC and cordierite is approximately 1316°C (2400°F).

However, this situation is no different than exists for modern steam boilers which will not withstand firing temperatures without water flowing in the tubes. One other transient to which the cavity will be subjected is the nighttime cooldown. If the cavity is equipped with insulated aperture doors, the cooldown during a sixteen hour night was calculated to be from about 1093°C (2000°F) to about 371°C (700°F).

## Section 5

### HEAT EXCHANGER TUBE TESTS AND EVALUATION

#### TEST PHILOSOPHY AND OBJECTIVES

In order to more accurately determine the material properties of prospective ceramic heat exchanger materials and to validate the analytical model used to predict material temperatures and convective-cooling coefficients, a series of experimental tests were designed and conducted. The objectives of these tests were as follows.

- Determine the thermo-optical properties of the selected ceramic materials at the temperature of application.
- Verify the validity of the analytical model used to predict material temperatures and heat transfer parameters.
- Test the resistance of the heat exchanger U-tube configuration, joints, and materials to thermal cycling.

#### SUMMARY OF CONCLUSIONS

The results of the tests performed to achieve the above listed objectives are summarized as follows.

- The measured thermo-optical properties of samples of the Carborundum Company's KT silicon carbide and Coors Porcelain Company's CD-1 cordierite were found to be in good agreement with previous measurements on similar materials of this composition. Prior to the thermo-optical measurements, the test samples were thermally cycled in an oxidizing atmosphere to simulate material surface aging in diurnal, heat exchanger operation.
- The analytically predicted material temperatures and heat transfer parameters were corroborated by experimental testing. The analytical model is a valid representation of the actual physical phenomena.
- At the time heat exchanger U-tube configuration testing was begun, only the secondary material candidate (cordierite) was available. Conclusions drawn from tests on this material are as follows.
  - Tapered compression seals are a workable method of making ceramic-to-metal connections for the conditions achieved to date (0.38 MPa and 1200°C [55 psia and 2200°F]).

- Sleeve-type joints of cordierite are unsatisfactory.
- Cordierite tubes, as supplied, are unsatisfactory for continuous use at or above the test conditions achieved to date (0.38 MPa and 1200°C [55 psia and 2200°F]).

The primary test candidate (silicon carbide) was unavailable for testing in a U-tube configuration during the course of this contract. However, near the end of the contract period, joined silicon-carbide tubes suitable for testing in the required configuration became available; the test results and conclusions for this material will appear in a subsequent report (EPRI Project RP 475-2).

#### THERMOOPTICAL PROPERTY DETERMINATION

The thermo-optical properties of the candidate ceramic materials were determined by the TRW Systems Group, Thermo-Physical Properties Branch, Redondo Beach, California. The spectral directional reflectance,  $\rho_\lambda$ , of a sample of the Carborundum Company's KT silicon carbide was measured at various angles of incidence,  $\theta$ , at three specimen temperatures. Because the physical properties of cordierite prevented heating of the sample in the TRW test equipment, the spectral directional reflectance of a sample of the Coors Porcelain Company's CD-1 cordierite was measured only at room temperature and at a near-normal angle of incidence.

Testing of the specimens at near-room temperature with various angles of energy incidence was performed using a Gier Dunkle Heated Cavity Reflectometer. Testing at elevated temperatures and at near-normal angles of incidence was performed using a TRW Paraboloid Reflectometer.

A sample of the spectral directional reflectance measurement test results is shown in Figure 5-1. The complete set of test data is contained in Appendix B along with a more detailed description of the test procedures and equipment. Table 5-1 is a summary of the spectral directional reflectance\* tests performed on samples of cordierite and silicon carbide.

#### VERIFICATION OF ANALYTICAL METHODOLOGY

Experimental tests using straight ceramic tube sections were designed and conducted to verify that the mathematical model developed for analysis and design of the heat

---

\*  $\rho = 1 - \epsilon$ ;  $\alpha = \epsilon$ .

DIRECTIONAL SPECTRAL REFLECTANCE

CUSTOMER CODE NO. :

TRW DESIGNATION: S/N 122-76

MATERIAL: Silicon Carbide, .020 in. thick

ANGLES

POLAR,  $\theta = 15^\circ$  from Sample Normal

AZIMUTHAL,  $\varphi = \text{Arbitrary}$

MEASUREMENT

INSTRUMENTS

Spectral Directional Reflectance

Heated Cavity Reflectometer

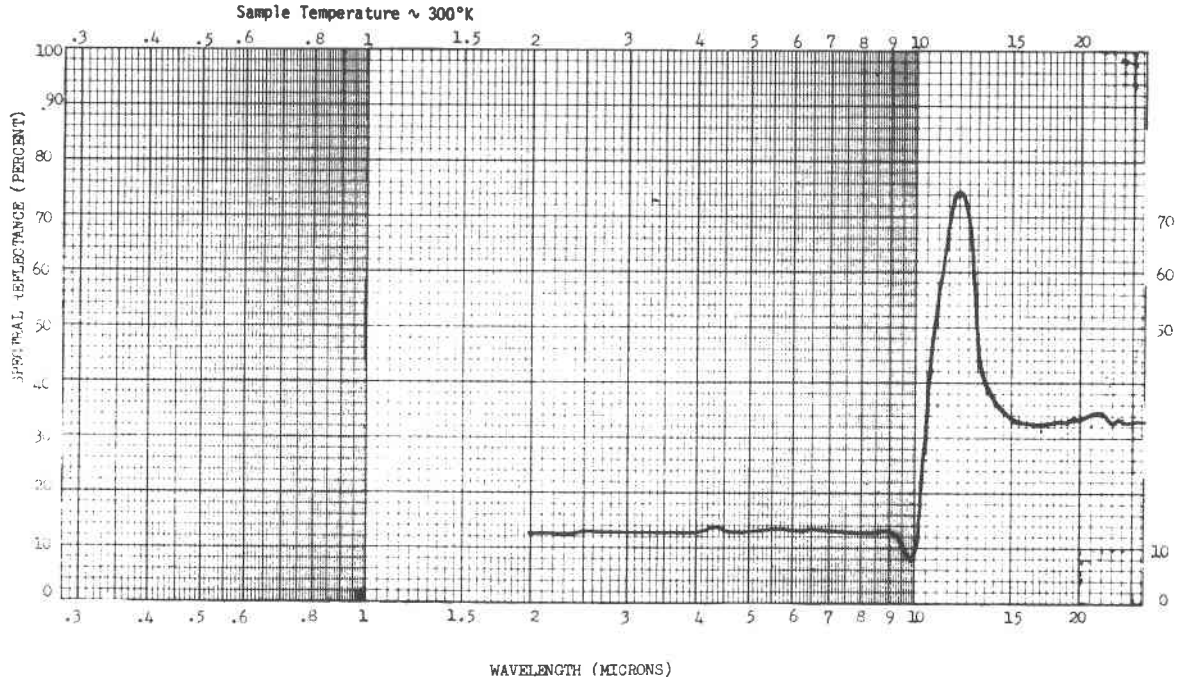


Figure 5-1. Directional Spectral Reflectance

Table 5-1

EMITTANCE OF CORDIERITE AND SILICON CARBIDE

SAMPLE MATERIAL	SAMPLE TEMPERATURE		ANGLE OF EMITTANCE ( $\theta$ )	DIRECTIONAL EMITTANCE ( $\epsilon_\theta$ )	HEMISPHERICAL EMITTANCE ( $\epsilon$ )
	°C	(°F)			
Cordierite	30	(85)	15°	0.85	0.81
Silicon Carbide	30	(85)	15°	0.68	0.67
Silicon Carbide	30	(85)	30°	0.69	--
Silicon Carbide	30	(85)	45°	0.69	--
Silicon Carbide	30	(85)	60°	0.68	--
Silicon Carbide	30	(85)	72°	0.62	--
Silicon Carbide	880	(1600)	9°	0.87	0.83
Silicon Carbide	1100	(2000)	9°	0.90	0.85

exchanger was, in fact, representative of the actual physical phenomena. Testing was performed at the Engineering Experiment Station, Georgia Institute of Technology, Atlanta, Georgia.

#### Experiment Setup

Testing was performed on tubes manufactured of the Carborundum Company's KT silicon carbide, on tubes manufactured of the Coors Porcelain Company's CD-1 cordierite, and on tubes manufactured of transparent fused silica.

The test apparatus consisted of a modified C-shaped bank of fused-quartz infrared lamps; three coplanar, parallel, ceramic tubes mounted side by side; and a flat, fused-silica foam reflector. The three ceramic tubes were placed between the infrared lamp bank and the fused-silica foam reflector. This arrangement of tubes, reflector, and lamp bank simulated an array of parallel heat exchanger tubes, the design configuration selected for the heat exchanger baseline design (Section 4). The test apparatus is pictured in Figure 5-2, minus the fused-silica foam reflector.

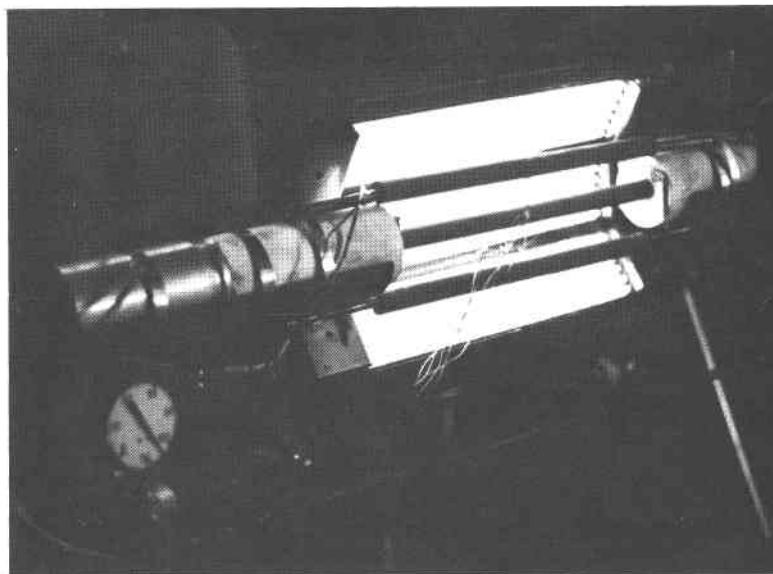


Figure 5-2. Photograph of Single-Tube Test Apparatus

### Test Procedure

The center ceramic tube contained a flow of preheated, compressed air. The two side tubes are dummy tubes, present to provide the proper radiative interchange. The two dummy tubes were cooled with ambient air such that their surface temperatures were nominally equal to the surface temperature of the center tube. The three tubes were irradiated by the fused-quartz infrared lamps, simulating anticipated operating conditions in the heat exchanger baseline design. Flux incident onto the center tube was nominally  $200 \text{ kW/m}^2$  ( $6.34 \times 10^4 \text{ Btu/h-ft}^2$ ).

### Data Acquisition

The temperature of the compressed air was monitored at the inlet and the outlet of the center ceramic tube, as were the airflow rate and pressure. Temperature measurements were made using thermocouples. Flow measurements were made using tapered-tube float-type Brooks Rotameters.

Surface temperatures of the ceramic tubes were measured using thermocouples and an infrared pyrometer. Five thermocouples were attached to the surface of the center tube around the midpoint of the tube. One thermocouple was attached to the surface of one of the dummy tubes at the tube's midpoint. A Barnes IT-7 infrared pyrometer was aimed at the surface of the center tube at the tube's midpoint and was filtered to exclude radiant energy coming directly from the fused-quartz infrared lamps or energy reflected by the ceramic tubes or by the fused-silica foam reflector.

The flux level of the quartz lamp bank was determined using a Hy Cal Asymptotic Calorimeter (Model C-1300-A-60-072, Serial No. 48425). The flux was measured at various positions and distances from the lamp bank, both with and without the fused-silica foam reflector and the three ceramic tubes in place.

### Test Results

Validation of the analytic model was achieved by entering various measured test data into the analytical model and comparing the resulting computed values of temperature variation and the convective heat transfer coefficient to the experimentally measured values. Measured values of inlet air temperature, inlet air pressure, mass flow rate, incident flux, test geometry and material properties were entered into the analytical model. With these data as input, the analytic model predicted the temperature variation around the tube and the interior convective heat transfer coefficient.

Table 5-2 shows experimentally and analytically determined values of the interior convective heat transfer coefficient for four test cases. Figure 5-3 shows the experimentally and analytically determined temperature variation around the tube for one test case.

Table 5-2  
CONVECTIVE HEAT TRANSFER COEFFICIENT

CASE	EXPERIMENTAL		ANALYTIC	
	$\text{kW/m}^2\text{-}^\circ\text{C}$	( $\text{Btu/h-ft}^2\text{-}^\circ\text{F}$ )	$\text{kW/m}^2\text{-}^\circ\text{C}$	( $\text{Btu/h-ft}^2\text{-}^\circ\text{F}$ )
1	0.21	(37)	0.20	(35)
2	0.30	(52)	0.28	(49)
3	0.42	(74)	0.39	(68)
4	0.70	(123)	0.53	(94)

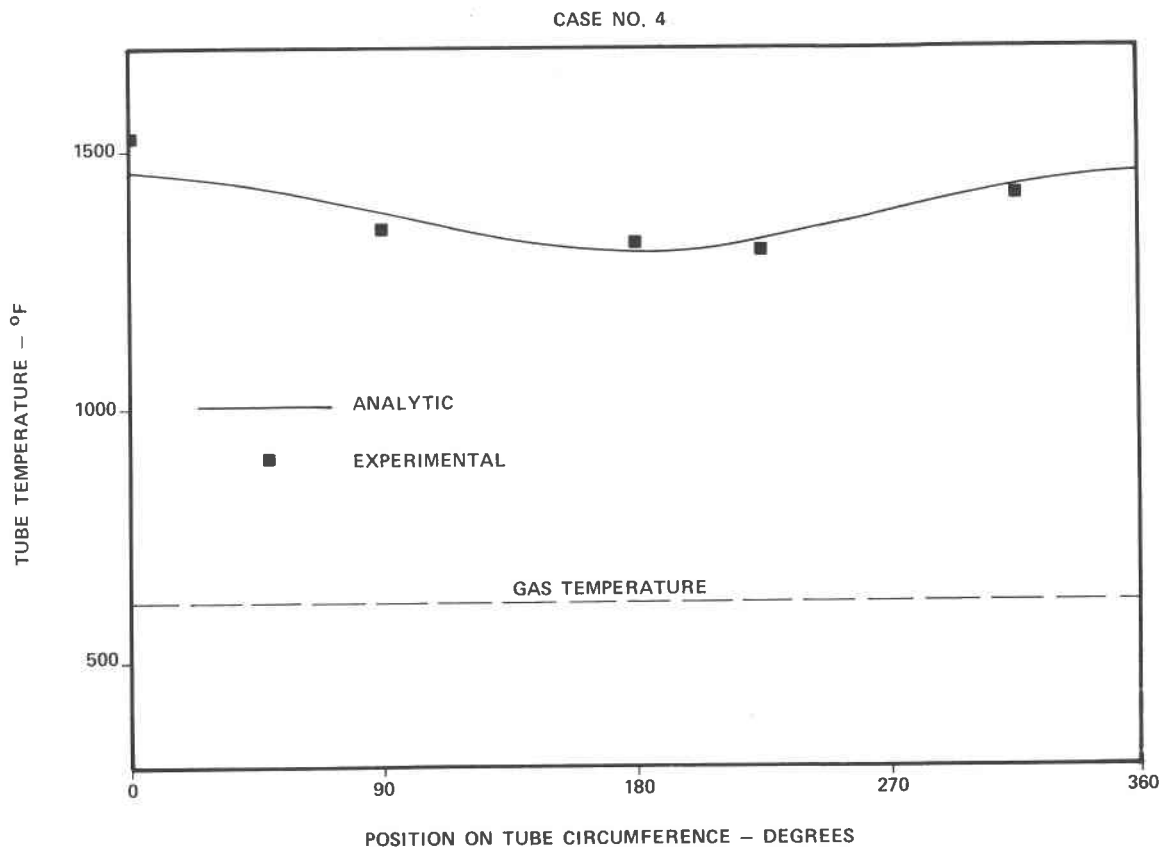


Figure 5-3. Comparison of Experimental and Calculated Temperature Distributions on Single Tube

## Conclusions

As can be seen in Table 5-2 and in Figure 5-3, agreement between the analytically determined values and the experimentally determined data is good. It was concluded that, based on the comparison with experimentally determined data, the analytic model is a valid representation of the actual physical phenomena.

Test data are contained in Appendix C, along with a more detailed description of the test procedures and equipment.

## HEAT EXCHANGER CONFIGURATION TESTING

To obtain data on the integrity of ceramic-to-ceramic and ceramic-to-metal joints, the resistance of tubes and joints to thermal cycling, and the longitudinal and circumferential variation of temperature along a U-tube, a series of experiments was designed and conducted. Testing was performed at the Engineering Experiment Station, Georgia Institute of Technology, Atlanta, Georgia.

### Thermal-Cycling Resistance

Determination of the resistance of the heat exchanger U-tube configuration and joints was achieved by subjecting a specimen to the anticipated thermally-induced stress levels and monitoring its response. By recording material temperature at various points along the U-tube, as well as the inlet and outlet air conditions, and by observing the mode of failure (if any), a test of the performance of the U-tube configuration and joint designs under thermal cycling similar to that expected in actual, daily operation was performed.

### Experiment Design

Tests on the heat exchanger U-tube configuration were performed using a 100-kW lamp array in conjunction with a reflecting cavity, simulating the operating environment of the actual heat exchanger. The diameter and length of the ceramic tubes used in testing were selected to be compatible with the available facility and budget limitations and to facilitate handling.

Because the governing heat transfer relations involve parameters in a nonlinear manner, a scale-model test can only duplicate either the mechanical or the heat transfer relationships. Because the heat transfer relationships had been duplicated for the validation of the analytical model, U-tube tests were designed to duplicate the mechanical aspects of the heat exchanger configuration. (thermally-induced stresses in the tubes and joints).

### Experiment Setup

The test apparatus was designed to accept U-tubes having a nominal diameter of 5.1 cm (2 in) and a U-bend with a centerline radius of curvature of 7.6 cm (3 in). Overall height of the U-tube was equal to 121.9 cm (48 in).

The U-tube is situated in a cavity defined by sheets of diffusely reflecting fused-silica foam. The cavity is 40.6 cm (16 in) wide by 16.2 cm (6 in) deep and 121.9 cm (48 in) in height.

The cavity is closed by a quartz lamp bank containing 84 fused-quartz infrared lamps, each rated at 1.6 kW (5500 Btu/h) of power at 230 volts. The fused-quartz lamp bank is track-mounted to permit access to the U-tube within the cavity.

Figure 5-4 shows the test apparatus with a cordierite U-tube in position and with the quartz lamp bank retracted from the cavity.

### Test Procedure

Compressed air was preheated and introduced into the inlet of the U-tube. The U-tube was then irradiated with the bank of fused-quartz infrared lamps, providing a nominal incident heat flux onto the U-tube of  $200 \text{ kW/m}^2$  ( $6.34 \times 10^4 \text{ Btu/h-ft}^2$ ). This arrangement simulated thermally-induced stress levels expected in the heat exchanger baseline design.

### Data Acquisition

During testing, the temperature, pressure, and flow rate of the compressed air were monitored at the inlet and outlet of the U-tube assembly. These data were taken using equipment similar to that utilized previously during the analytic model validation tests, as previously described in this section.

In addition to these data, the surface temperatures on the U-tube were monitored by means of attached thermocouples. One thermocouple was placed near the U-tube inlet, two were placed circumferentially at a point upstream of the U-bend, one was attached to the U-bend, four thermocouples were placed circumferentially at a point downstream of the U-bend, and one was attached to the tube near the U-tube exit.

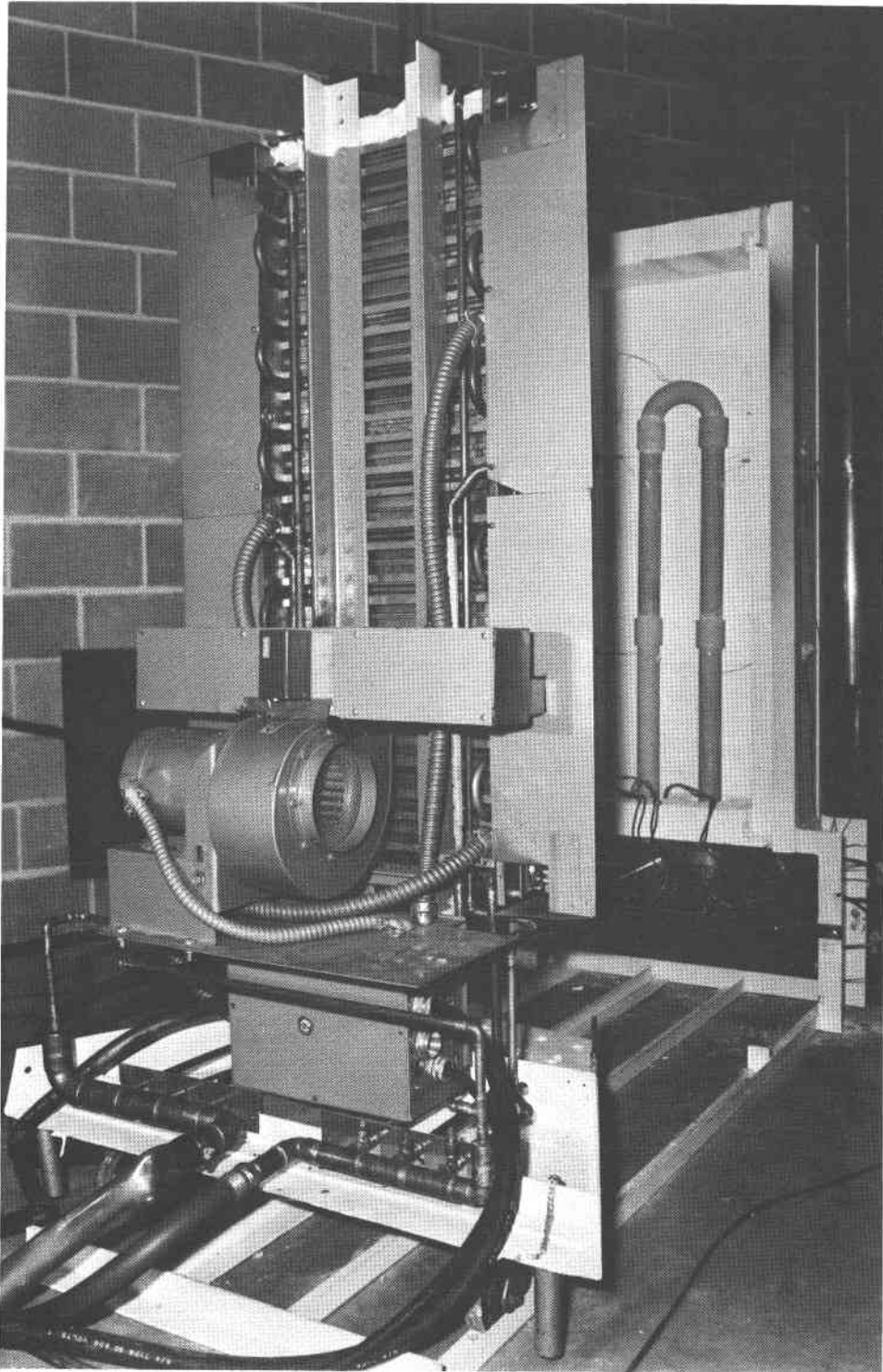


Figure 5-4. Photograph of the Heat Exchanger U-Tube Test Apparatus

The above data were recorded for each thermal cycle (heat up - cool down). During thermal cycling, the maximum inlet air temperature was 290°C (550°F); the maximum pressure 0.38 MPa (55 psia). Generally, the tubes were heated until the surface temperature nominally equalled 1100°C (2000°F) and then allowed to cool to 480°C (900°F). Thermal cycling of the U-tube was repeated until the U-tube failed. Determining the mode of failure and examining the recorded data provided information on the resistance of the heat exchanger U-tube configuration and joints to thermal cycling.

#### Test Specimen

An earlier survey of ceramic materials identified silicon carbide as the primary candidate. However, at the time the test apparatus became operational, tubes made of silicon carbide in the required size had not yet been delivered. As a result, testing of the secondary material candidate, cordierite, was undertaken.

The cordierite U-tube was assembled from four straight tube segments and one semicircular tube segment. All segments were joined using external sleeves, also made of cordierite. The sleeves are cemented onto the tube segments using either Sauereisen cement No. 78 or No. 8. Sleeves with and without interior shoulders were used, though not at the same time.

Because of the difficulty encountered in using Sauereisen cement No. 8 during the assembly of the first test specimen, it was utilized to make only one ceramic-to-ceramic joint. Sauereisen cement No. 78 was utilized exclusively from then on for the assembly of cordierite U-tubes.

The completed cordierite U-tube was attached to the air inlet and air outlet headers of the test apparatus via tapered compression seals. The tapered compression seals were formed by sliding loosely fitting flanges with tapered recesses onto the ends of the U-tube. The tapered recesses were then filled with a mixture of chopped asbestos fiber and sodium silicate. When the flanges were bolted to mating fixtures on the headers, the asbestos fiber was tightly compressed against the tube, forming a compression seal. The sodium silicate, upon drying, formed an adhesive bond.

#### Thermal-Cycling Test Results

Testing was initiated on three U-tubes made of cordierite. The first U-tube was assembled using sleeves having an interior shoulder. On the fourth thermal cycle,

this tube failed at the sleeve on the inlet side of the U-bend, cracking horizontally into two pieces along the interior shoulder line. The second U-tube was assembled with sleeves having no interior shoulder. This tube survived seven thermal cycles before failing at the sleeve on the inlet side of the U-bend. The third U-tube was assembled with sleeves having no internal shoulders and a 1/8-inch wall thickness, half the previous sleeve wall thickness. The straight tube segment above the inlet of the U-tube failed on the first thermal cycle. This segment, which had survived 11 thermal cycles in the first two assemblies, failed along vertical mold parting lines which had developed into microcracks during thermal cycling.

During testing of the second cordierite U-tube, one of the tapered compression seals blew out. The seal failure was precipitated by creep in the bolts retaining the flange. The problem was eliminated by replacing the bolts with water-cooled bolts made of stainless steel.

#### Conclusions

As a result of thermal cycling the cordierite U-tubes, it was concluded that sleeve joints of cordierite are unsatisfactory and that cordierite tubes, as supplied, are unsatisfactory for the intended application. Because the fault that precipitated the failure of the seal was corrected, tapered compression seals are judged to be a workable method of achieving ceramic-to-metal connections for conditions achieved to date (0.38 MPa and 1200°C [55 psia and 2200°F]).

Tubes of silicon carbide (the primary material candidate) in the required dimensions became available for testing on June 25, 1976, too late for inclusion in this report. Test results for the silicon-carbide tubes will be included in a later report (EPRI Project RP 475-2).

## Section 6

### GAS TURBINE SELECTION, INTERFACES, AND HYBRID OPERATION

Solar power systems must be compatible with existing turbomachinery if solar-thermal power generation is to be a commercially viable, near-term energy alternative. The development of a new turbine system requires an investment of several hundred million dollars and 10 to 15 years of effort. Furthermore, domestic turbine manufacturers have indicated to Black & Veatch that significant market demand is a prerequisite to any turbine development program, regardless of the availability of external program funding. Therefore, even the eventual availability of a special gas turbine for solar power is questionable, since large-scale solar concept applications have yet to be demonstrated.

It follows that this solar-thermal power system design is based upon an existing, commercially available gas turbine. This conceptual design effort includes provisions for interfacing the turbine with the central solar receiver, and for allowing hybrid turbine operation utilizing fossil fuels during periods of reduced solar insolation or solar outage. This hybrid capability results in the avoidance of the problems inherent in current thermal storage designs.

#### OBJECTIVES

The primary objective of the turbine selection process was to identify a commercially available gas turbine unit with a high cycle efficiency that was adaptable to the central receiver solar concept. Subsequent to the identification of such a unit, it was necessary to establish the interest of the manufacturer in the proposed solar application, and to conceptually design the necessary turbine/receiver interfaces.

An overview of the interface objectives is as follows.

- Utilize existing turbomachinery with a minimum of adaptive modifications
- Operate with high thermodynamic-cycle efficiency

- Operate from solar, fossil, or a combination of both heat sources
- Minimize heat and pressure losses in the ducting
- Provide access to all turbine, cavity, and piping components
- Retain turbine reliability

The turbine selection was made based upon the first two objectives, with due consideration given to the inherent requirements of hybrid operation.

#### GAS TURBINE SELECTION

There are many open-cycle gas turbines on the commercial market today. A turbine acceptable for reference in the baseline conceptual design will be identified in this section.

##### Simple vs. Regenerative Cycle

The simple and regenerative ideal Brayton cycles are depicted schematically in Figure 6-1. It can be seen that the regenerative cycle is an enhancement of the simple-cycle gas turbine, with a resultant increase in cycle efficiency. As the companion temperature-entropy diagrams illustrate, the regenerative cycle employs an air-to-air heat exchanger to extract waste heat from the turbine exhaust and to add this heat to the compressor discharge. The utilization of waste heat reduces the amount of heat that must be added to the cycle (heat required in the process between states 2a and 3 is less than heat in process 2 - 3); this reduction of cycle external thermal-energy requirements increases the thermodynamic-cycle efficiency.

The addition of the regenerator to the basic Brayton cycle has consequences beyond improvements in cycle efficiency. The cost of a regenerative-cycle turbine is greater than a simple-cycle machine. A regenerative turbine, which accounts for less than 15 percent of the estimated total open-cycle, solar-thermal system cost, costs approximately 30 percent more than the simple-cycle unit, while demonstrating an efficiency increase on the order of 15 percent. Inasmuch as the heliostat field is the major system cost component, and its size, for a given system power level, is directly related to cycle efficiency, there is a strong economic incentive to select an efficient turbine cycle.

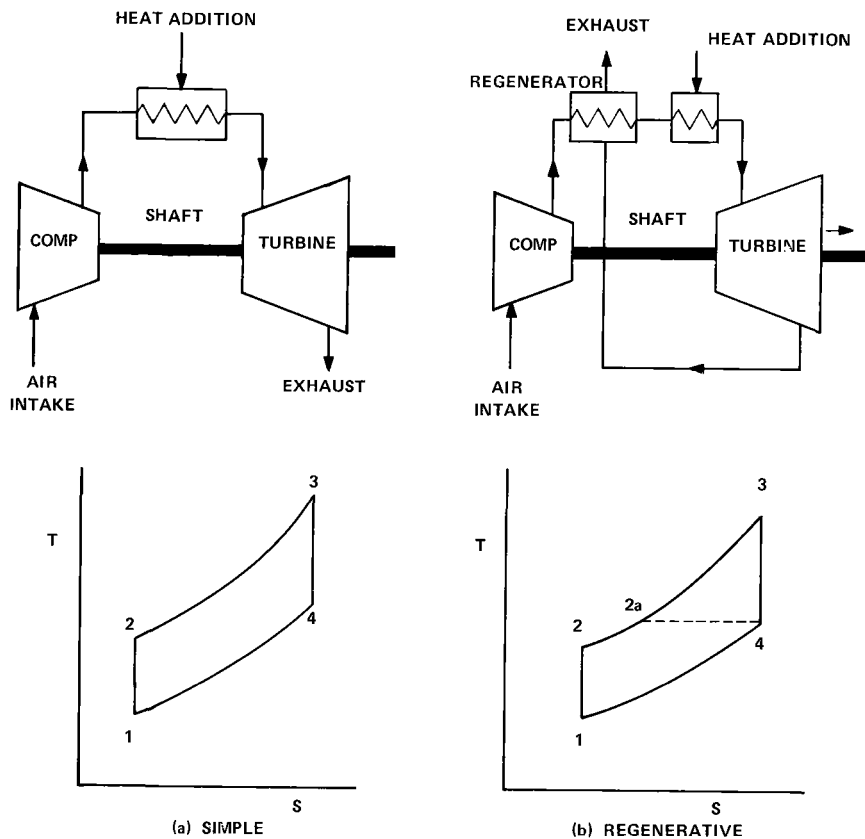


Figure 6-1. Simple and Regenerative, Ideal Brayton Cycles

The operating characteristics of a regenerative unit differ somewhat from a simple cycle. Due to the thermal inertia of the regenerator mass, the regenerative turbine cannot, on a regular basis, be started as rapidly as a simple-cycle turbine. This is a pertinent consideration in peak load applications, but should not be of great significance in the intermediate load applications projected for solar-thermal plants. The power rating of a given turbine is reduced slightly with the addition of a regenerator due to the additional pressure drops within the regenerator (see discussion under "Calculation of Cycle Efficiency").

Based on opportunities for higher system efficiency and reduced total system cost, the regenerative-cycle gas turbine was selected for application in this solar-thermal concept.

#### Calculation of Cycle Efficiency

The performance of a gas turbine is influenced by many factors. In order to evaluate the sensitivity of turbine performance to the various influencing factors,

a computer model was developed. This model characterized turbine performance in terms of specific work output and thermal efficiency. The following parameters were considered.

- Ambient conditions
- Turbine inlet temperature
- Compression ratio
- Regenerator effectiveness
- Turbine and compressor efficiencies
- Pressure losses within the cycle

It is particularly important that the final three parameters be considered for they are among the more prominent factors which differentiate a real gas turbine from an ideal one. The significance of these characteristics can be seen on Figure 6-2. The effects of the compressor and turbine inefficiencies and the pressure drops within the cycle are, in essence, to increase the amount of work that the cycle must do to sustain itself, while simultaneously reducing the ability of the cycle to do that self-sustaining work. In other words, because the work required to drive the compressor is more than one-half the gross output of the turbine, the net output of the cycle is very sensitive to losses within the cycle.

Thermal efficiency is obviously a concern in turbine design. This term describes the amount of energy that must be added to the cycle in order to extract useful work from the machine. Denoting work as  $W$ ,

$$\text{Thermal Efficiency} = \frac{\text{Net Work Output}}{\text{Heat Input}} = \frac{W_{\text{turbine}} - W_{\text{compressor}}}{\text{Heat Input}} \quad (6-1)$$

The second important turbine characteristic is net specific work output. This term quantifies the amount of net cycle work that is available for each pound of working fluid (air) that flows through the machine.

$$\text{Specific Net Work Output} = \frac{W_{\text{turbine}} - W_{\text{compressor}}}{\text{Air Mass Flow}} \quad (6-2)$$

Because turbines are essentially constant volume flow machines, the capacity of a given unit depends upon the net specific work term. Since machine cost increases with physical size, turbine designers strive to maximize net specific work in order to reduce machine size, and thus cost.

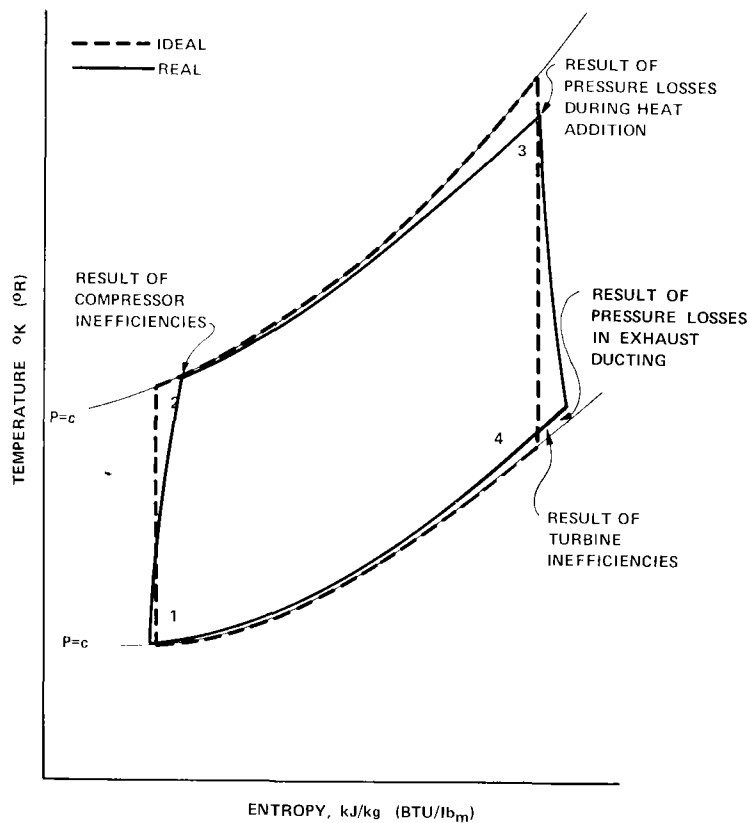


Figure 6-2. Comparison of an Ideal Brayton Cycle to the Real Gas Turbine Cycle

The two graphs of Figure 6-3 were obtained by exercising the previously described gas turbine performance computer software. The graphical results shown are typical outputs of parametric runs. It can be readily observed that both turbine cycle efficiency and net specific work output are improved by increasing the turbine inlet temperature. It can also be seen that the pressure drop incurred by the working fluid (air) during the heat addition process is an important cycle performance consideration; increasing the pressure drop from 0.014 MPa to 0.042 MPa (2 to 6 psi) had a significant impact on the cycle efficiency. While interpreting these graphs, it should be realized that nominal values, representative of existing equipment performance, were used for turbine adiabatic efficiency, compressor adiabatic efficiency, and regenerator effectiveness. However, due to the simple nature of the model, it was necessary to ignore loss mechanisms such as turbine cooling air requirements. As a result of these simplifications, the turbine performance curves of Figure 6-3 should be considered indicative of performance trends rather than specific performance predictions.

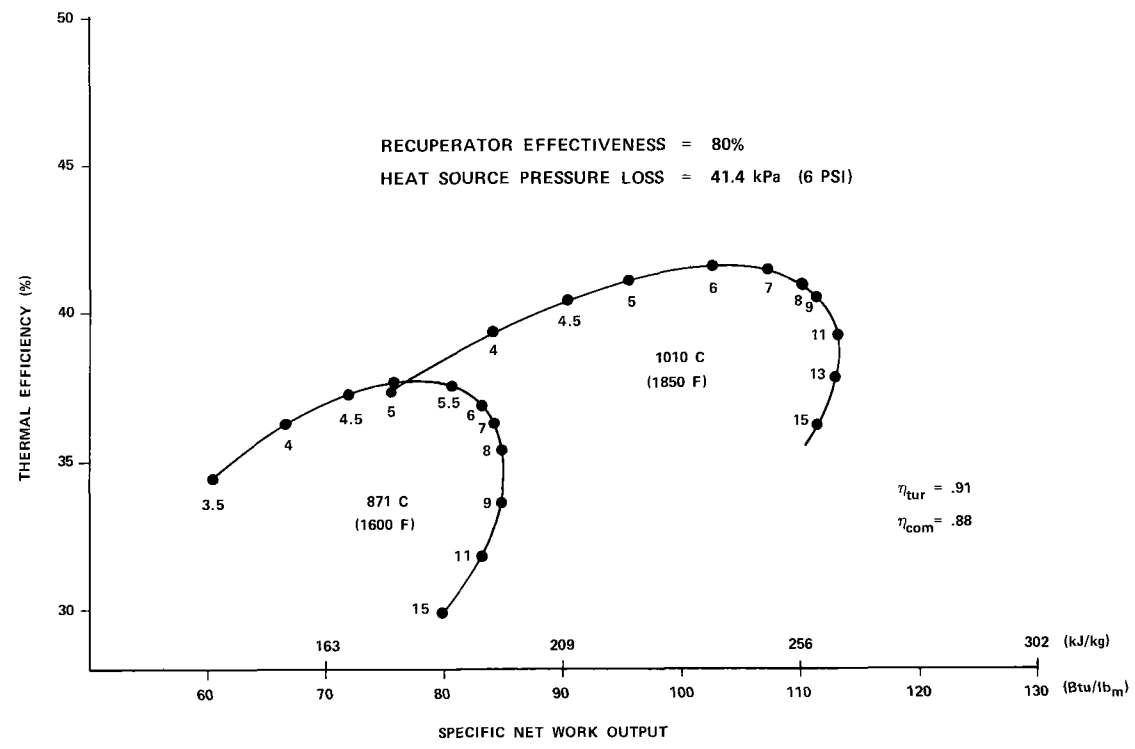
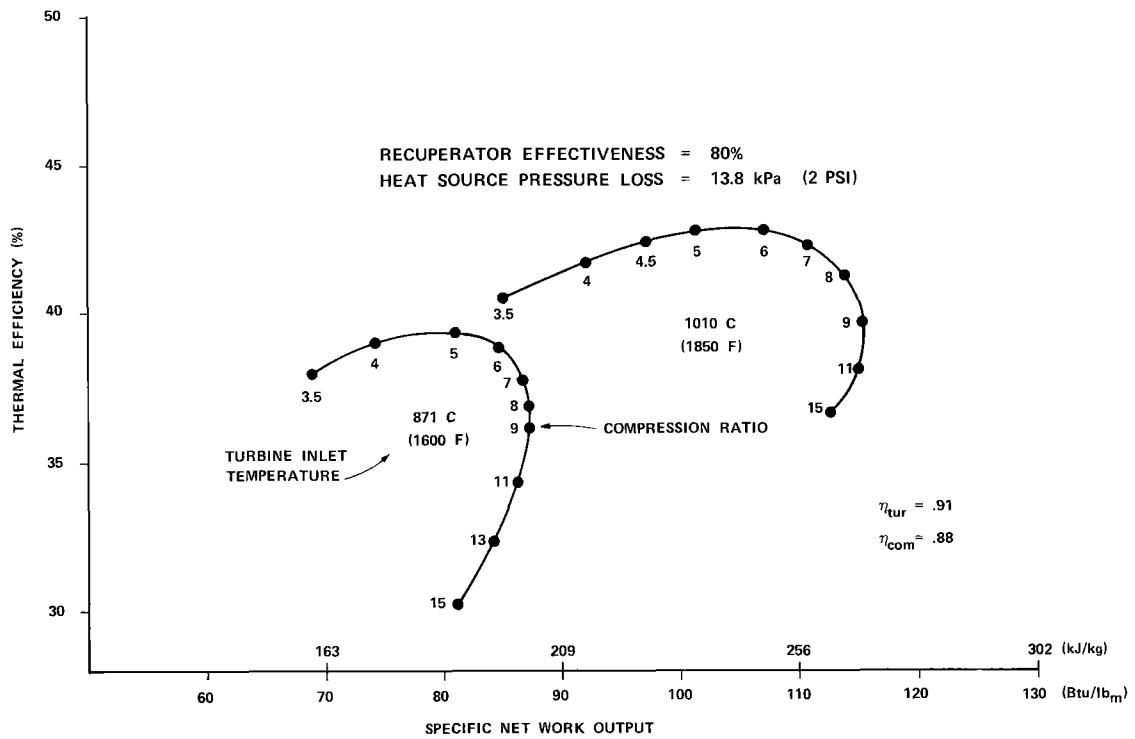


Figure 6-3. Regenerative Gas Turbine Performance

Based on this analysis, it is possible to draw two general conclusions that influence the solar heat exchanger and turbine interfaces conceptual design process. Those conclusions are as follows.

- There is an incentive to have a high air temperature at the solar heat exchanger outlet for ducting to the turbine inlet. Air temperatures in the 1038°C to 1093°C (1900 to 2000°F) range are consistent with current gas turbine technology.
- Pressure drops through the solar heat exchanger and the turbine interfacing network should be minimized to maintain high cycle efficiency.

It is also possible to gain some insight as to how cycle compression ratios are chosen. For a heat source pressure drop of 0.042 MPa (6 psi), nominally typical of existing machines, the knee of the performance curve occurs around an 8:1 to 9:1 compression ratio. It follows that the turbine designer might select such a compression ratio as a compromise between the design objectives of high cycle thermal efficiency and high net specific work output (and thus reduce machine specific cost).

#### Selection of Commercial Baseline Turbine

The General Electric regenerative Frame 7 heavy-duty gas turbine has been selected as the commercial baseline turbine. This decision was reached after surveying the turbines currently available, and visiting both General Electric and Turbodyne. Westinghouse does not offer a regenerative turbine for utility use and, as concluded earlier in this section, the regenerative cycle was an important aspect of this system design. The Turbodyne GT-110 unit was attractive because its external combustor design had the potential to lend itself well to central receiver interfaces. However, Turbodyne indicated that a regenerative machine for utility use was not planned, and that solar adaptive modifications to the turbine might not be possible due to their licensing agreements with Brown, Boveri and Company of Switzerland.

The General Electric MS 7001R, Model B, nominally rated at 60 MWe with a 1066°C (1950°F) peak turbine inlet temperature is adaptable to the proposed solar-thermal central receiver concept. This unit has, at present, a guaranteed thermal efficiency of 37 percent (system net), and this value will increase as simple cycle-proven equipment improvements are incorporated into future models of the regenerative turbine. This turbine system, pictured in Figures 6-4 and 6-5, has a compression ratio of 9.3:1. It utilizes ten combustor pods located within the regenerative turbine combustion wrapper that circumferentially encloses the compressor-turbine interface. A complete MS 7001R package power plant weighs approximately 800,000 kg (880 tons).

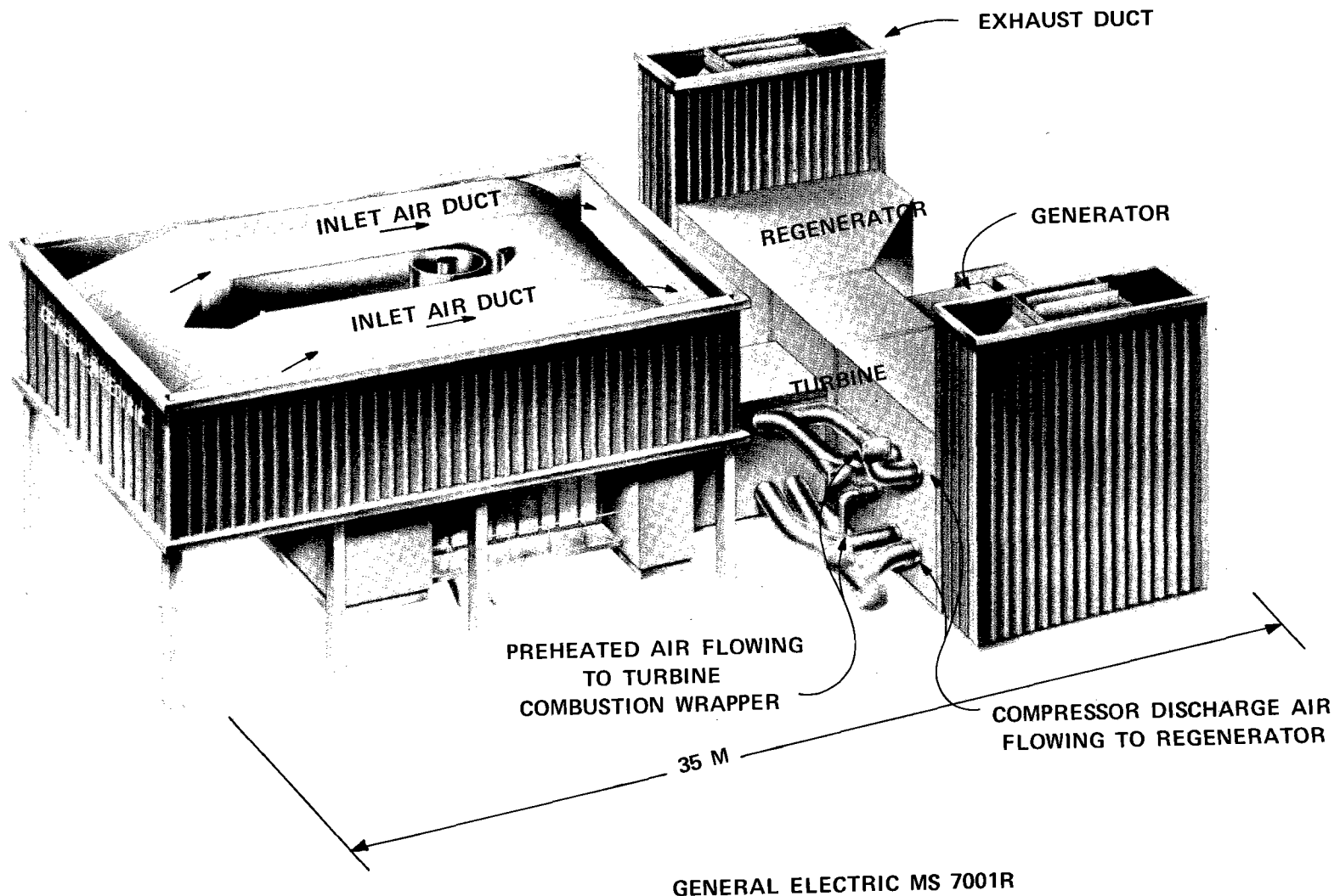


Figure 6-4. Orientation Photograph of MS 7001R

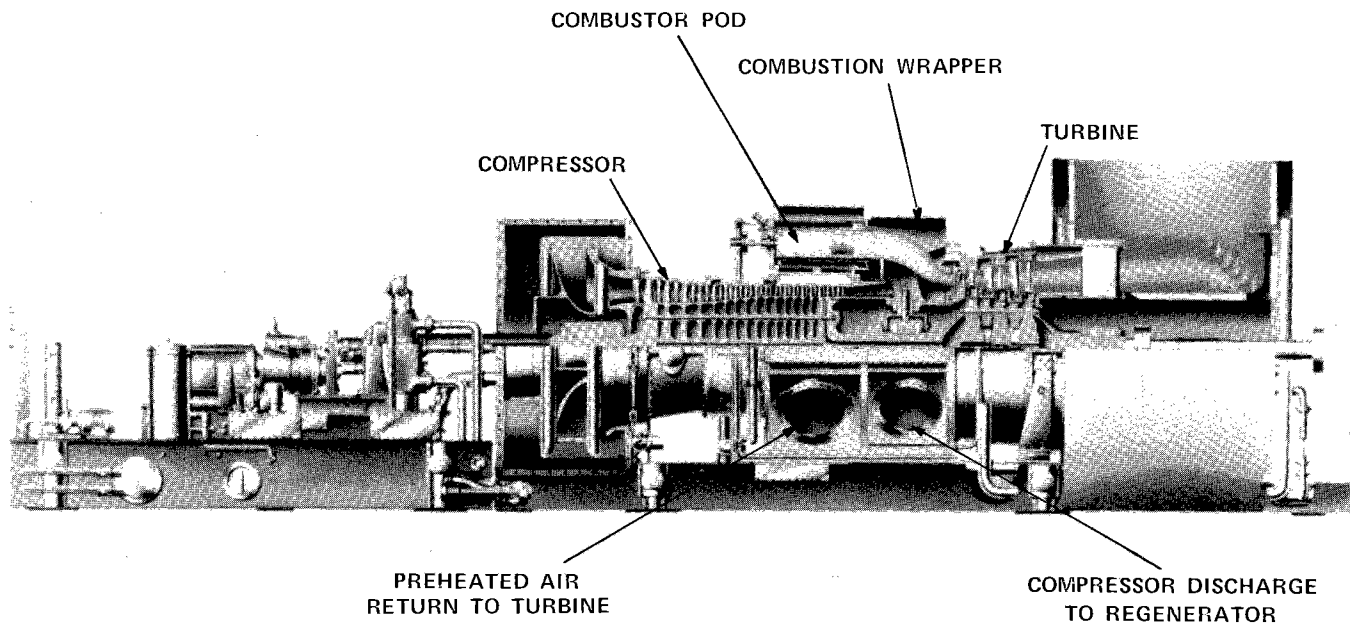


Figure 6-5. Cutaway of MS 7001R

As a result of Black & Veatch personnel visiting Schenectady, N.Y. and Greenville, S.C., General Electric expressed considerable interest in our program concept. Subsequent discussions identified two primary problem areas relative to turbine/receiver interfacing.

- The combustion wrapper of the regenerative MS 7001R normally receives preheated air from the regenerators. This comparatively cool, 482°C (900°F), air is used to shield the combustion wrapper and combustors from the high temperatures associated with combustion. Because the solar central receiver concept requires that the solar heat addition process occur outside the turbine unit, the air is already at temperature, 1038°C (1900°F), when it enters the combustion wrapper. This high air temperature precludes its use as a coolant for the wrapper and associated surfaces, as is done in normal turbine operation.
- The transition from solar to fossil fuels

The first concern requires that some means of cooling the combustion wrapper surfaces be provided. Alternatively, a thermal barrier protecting the metal surfaces from exposure to high temperatures could be developed. The solar to fossil fuel transition presents an unusually complex combustion initiation and control situation. General Electric suggested that this problem should best be avoided in a solar demonstration program. They suggested adopting an "either/or" operating mode in which the unit would be temporarily (15 to 30 minutes) shut down when changing from one energy source to another.

It is significant to note that each turbine manufacturer contacted indicated that development of a new turbine, or major changes to existing equipment, were probably beyond their current interests; sales of existing machines with minor modifications are of interest. Available resources are limited and, therefore, a highly probable market demand must exist in order to justify the dedication of those resources to nontrivial, application-specific developments. The extent of required modifications to the existing combustion system have yet to be determined, and so no absolute assessment of manufacturer interest has been made.

#### Potential Choice of Small, 2- to 3-MWe Pilot Plant Turbine

In order to facilitate the development and demonstration of the solar-thermal open-cycle gas turbine concept, consideration was given to identifying a turbine suitable for a pilot plant program. The Solar Division of International Harvester manufactures such a turbine, the 2.7-MWe regenerative Centaur shown in Figure 6-6. The standard design of the machine utilizes an external combustor and a turbine inlet

temperature of 899°C (1650°F); cycle efficiency is nominally 32 percent. After several visits to their facilities in San Diego, it appears that the Centaur could be adapted to a solar-thermal application with a reasonable degree of effort. The principal adaptive requirements would include additional air ducting to convey hot air from the central receiver to the turbine inlet, and a control scheme to coordinate solar and fossil fuel utilization. This latter requirement might well require modification of the combustor system as well.

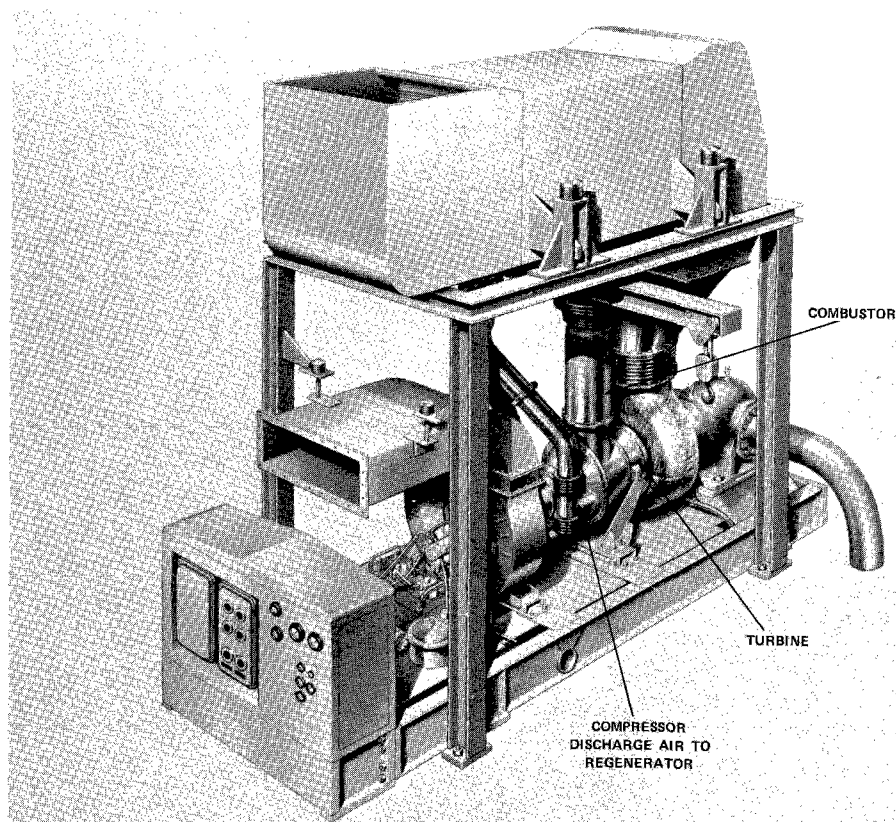


Figure 6-6. Orientation Picture of Solar Centaur

#### HYBRID OPERATION

Due to the variable nature of insolation, utility standards of unit reliability and availability could not be met by a solar-thermal turbine whose sole operating mode utilized solar energy directly. A hybrid operation capability would permit the system to operate independently of weather conditions and daylight hours.

## Objectives

The open-cycle gas turbine hybrid operation capability is intended to increase the reliability and availability of the solar-thermal power system. It does so by fulfilling the missions of both a buffer storage subsystem and a long-term storage subsystem. Buffer storage allows power generation to continue during short-term (30 minutes) solar interruptions such as passing cloud coverage; it would permit the system to be shut down in an orderly fashion during extended solar outages. Long-term storage is intended to provide an energy source during non-daylight hours.

The hybrid system concept utilizes the combustion of fossil fuel to satisfy both buffer and long-term storage requirements. During periods of solar outage, fossil fuels would be burned and the power system would operate as a conventional gas turbine. During periods of reduced insolation, solar energy and fossil fuel would be used simultaneously, and in variable proportions, to provide the necessary thermal inputs to the gas turbine.

The specific objectives of a hybrid, open-cycle gas turbine design are as follows.

- Enable turbine generator to produce rated electrical power continuously
- Allow hybrid operation of unit with fossil fuel while utilizing all available insolation
- Provide operational flexibility to the solar-electric system
- Utilize existing technology in the system concept, when possible
- Retain turbine reliability
- Minimize system complexity

## Arrangement Options and Choice

The fossil fuel combustors and the solar heat exchangers could be placed in either a series or parallel arrangement as shown in the simplified schematic of Figure 6-7. The hybrid system conceptual design must also consider whether the fossil fuel combustion process should occur internal or external to the turbine shell. Therefore, four heat source arrangements are possible.

- Series, internal
- Series, external
- Parallel, internal
- Parallel, external

The series arrangement permits the fossil fuel combustion process to perform an air temperature augmentation function. Enough fuel is burned so that the cumulative air temperature rise through both heat sources results in the desired turbine inlet temperature. Alternatively, the parallel arrangement assumes that air will exit either heat source at the desired turbine inlet temperature. This equal exit temperature philosophy is desirable in that it eliminates the downstream temperature equalization problems that would be present if the heat source exit temperatures were unequal. It may also reduce the difficulties associated with ducting air to the turbine from the solar cavities. It appears reasonable to expect that a piping network designed to convey air at a uniform 1038°C (1900°F) would be less complex than one designed to duct an airstream with nonuniform temperatures.

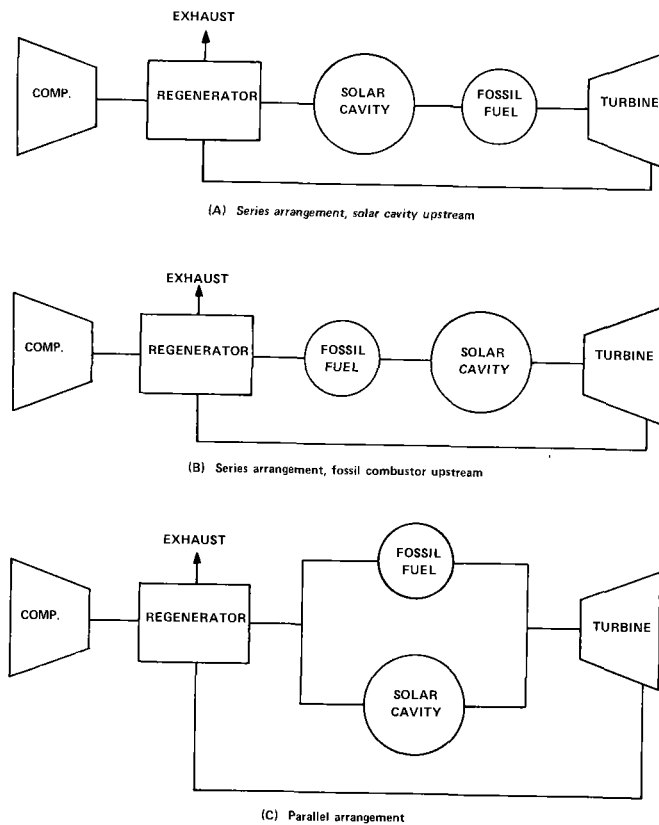


Figure 6-7. Possible Heat Source Arrangements

Before evaluating the relative merits of the respective system arrangements, the requirements of the hybrid concept were considered. A listing and discussion of these requirements follow.

- Allow solar-fossil fuel changeover without generation interruption
- Minimize heat addition process pressure drop
- Rate of fossil heat addition must be controllable
- Airflow through heat sources must be controllable

A solar-fossil fuel changeover without interrupting power generation is necessary if this solar power system is to be viable from a utility viewpoint. Neither the capacity nor the reliability of a generating unit can acceptably be subject to the variable and unpredictable influences of cloud coverage and other environmental effects. The pressure loss through the heat addition process should be low because the efficiency of the turbine cycle is sensitive to this parameter, as described earlier in this section. If the power plant is to operate in a fossil fuel displacement mode by taking maximum advantage of available solar energy, the rate of fossil fuel combustion must be variable. Ideally, the system should be capable of operating at a fixed generation capacity on either solar or fossil heat inputs, each of which could vary in a complementary fashion from 0 to 100 percent. The final requirement is that airflow through the heat sources must be modulated. Inasmuch as the lower-bound solar inputs to a receiver cavity are only controllable to a degree, reducing the air mass flow through the cavity heat exchanger will be the air temperature governing mechanism under low-level insolation conditions. It follows that airflow through the combustors will necessarily vary in response to solar cavity airflow fluctuations.

Airflow control through the fossil fuel combustors is of great importance. Turbine manufacturers (GE, Turbodyne, Solar) have preliminarily stated that fuel combustion cannot be initiated in existing combustors when the turbine is operating at full speed, a necessary conceptual design capability if power generation is not to be interrupted by fuel changeovers. Normal turbine startup procedures initiate combustion when the machine has reached 20 percent of rated speed. As such, the conditions for normal combustion initiation are significantly dissimilar from those present in the combustors at 100 percent rated speed, and it is a 100 percent speed light-off capability that is desired for hybrid operation. It may be possible to develop or adapt combustors with this 100 percent capability, but turbine manufacturers have indicated to Black & Veatch that extensive study would be

required to resolve that question. Accordingly, for the purposes of this conceptual design program, it was deemed prudent to develop a hybrid operation scheme that would provide a more conventional combustion environment for light-off.

In light of these requirements and considerations, the alternative heat source arrangements can be evaluated. If solar and fossil heat sources are to be in a series arrangement, with the combustors located within the turbine shell as is common practice, the solar heater must be upstream of the combustor. This is necessary because modification of either the combustor transition components or the hot gas path leading to the turbine inlet from the combustor would constitute a major turbine design change, which is unacceptable. Furthermore, passing combustion products through the solar heat exchanger would be poor practice, even if it could be located downstream of the combustor.

With the solar cavity preceding the combustor in the series arrangement, another problem develops. During periods in which the power system is operating in the solar mode, the temperature of the air entering the combustor would be nominally 1038°C (1900°F). Conventional combustors are not capable of enduring such extreme temperatures. Existing gas turbine combustor designs utilize the relatively cool regenerator discharge air, 482°C (900°F), to protect metal components from the high combustion temperatures. This cooling air would not be readily available if the solar heat exchangers were operating upstream of the combustor. Therefore, ceramic combustors are a prerequisite development for a series arrangement of the solar and fossil heat source. Ceramic combustor development is not compatible with the objective of utilizing existing technology and hence, a series arrangement of heat sources is not attractive.

A parallel heat source arrangement has many desirable features. Cool air is available at the combustor inlet to permit conventional combustor materials and cooling techniques to be employed. Airflow to various heat sources can be modulated as necessary with conventional valves because of the low air temperature. Pressure drops associated with parallel network arrangements are inherently less than in series arrangements; this permits higher cycle efficiencies. Because modifications to turbine transition ducting and hot gas path are not acceptable, as discussed earlier, it becomes necessary for both the solar and fossil heat sources to be located external to the turbine shell. This permits the standard combustors to be removed from the unit, and the subsequent reassignment of this space to a receiving area for the externally heated air (refer to "Conceptual Design/Performance,"

discussed later in this section). Furthermore, since both types of heat sources will be external to the turbine, the control of and access to these components will be enhanced.

Clearly, the use of external, parallel path, solar and fossil heat sources is desirable. This arrangement facilitates the utilization of existing equipment and technology. It should also help to ensure the operational reliability and feasibility of the system.

#### Adaptability of Baseline Turbine to Hybrid Operation

The baseline turbine for this conceptual design, the GE MS 7001R, is compatible with the hybrid operation concept and with the arrangement choice (see previous discussion in this section under "Arrangement Options and Choice"). An adaptive concept that is responsive to the constraints listed below has been developed. The objectives are as follows.

- Turbine modifications should be minimized
- Combustor light-off requirement should be considered
- Combustor cooling air should be provided
- Pressure and heat losses should be minimized
- Control of heat addition process by source is necessary
- Simultaneous use of solar and fossil heat sources is necessary

The conceptual design of the hybrid system, described in "Conceptual Design/Performance," requires a valving and ducting network to permit regenerator discharge air to be directed to the proper solar cavities, or to the combustors. Since this can be done external to the turbine frame, the modifications do not significantly impact the turbine manufacturing process. It is also necessary for the combustors to have a light-off capability with the turbine operating, and to have a large turndown ratio so that heat addition within the combustor can be varied. To restate the turndown requirement, the hybrid operation concept demands that airflow through the combustor be a highly controlled variable. Existing heavy-duty gas turbine combustors encounter a relatively constant, uncontrolled airflow. As a result, combustor designs have not included turndown as an important consideration. Development of a combustor which can operate effectively with significantly varying airflow is necessary. Alternatively, heat source airflow could be varied in discrete amounts rather than on a continuum basis. This could be done by installing, for example, 10 relatively small combustors that would be individually brought on-line as required.

These system concepts have been preliminarily reviewed by personnel of the General Electric Gas Turbine Products Division. They have acknowledged that some innovative designs would be required to achieve the desired combustor performance, but the problems are not insurmountable. Their initial judgment was that hybrid operation could be achieved using a network of the standard-size combustors, but that they would not be quite standard because of the incorporation of a pilot combustion stage. This pilot stage would be added to the standard combustor to facilitate ignition at full turbine speed. It is possible, but not probable, that the use of the pilot stage would permit ignition without reducing airflow through the combustor.

If the pilot stage approach is adopted, it is estimated that it would operate at approximately 10 to 20 percent of the normal combustor heat. Additional study would be required to determine whether pilot operation would necessarily be continuous, or if it could be activated only when needed. The transition from solar to fossil fuel, utilizing fuel flow on a ramp function, is estimated to require approximately one minute. It is not anticipated that reliability would be a problem.

The open-cycle gas turbine solar-electric system concepts have also been reviewed by Solar personnel. It appears that the Solar Centaur can also be adapted to the solar-thermal power system using the proposed interfacing system, including some modification of the combustor.

#### Conceptual Design/Performance

The conceptual design of the hybrid solar-electric open-cycle gas turbine is shown schematically on Figure 6-8. The four solar cavity heat exchangers are in a parallel path arrangement with two fossil fuel combustors. Valves are provided on both inlet and outlet sides of all heat sources to allow the selective modulation of airflow to the various components, and to permit the isolation of components from the remainder of the power system. This isolation capability will facilitate equipment repairs without compromising power system availability. Furthermore, it will permit selective solar cavity operation in response to insolation conditions, and prevent combustion products from backflowing into an inoperative cavity.

Pictures of the standard MS 7001R were shown on Figures 6-4 and 6-5. It should be noted that two ducts lead from each side of the combustion wrapper, which accepts the compressor discharge, to the regenerators located on either side of the turbine.

Compressed air flows into the regenerator via these ducts, passes through the regenerator, and is then discharged into a pipe which returns the preheated air to the regenerative, combustion wrapper. Finally, the preheated air flows into the combustors mounted within the wrapper.

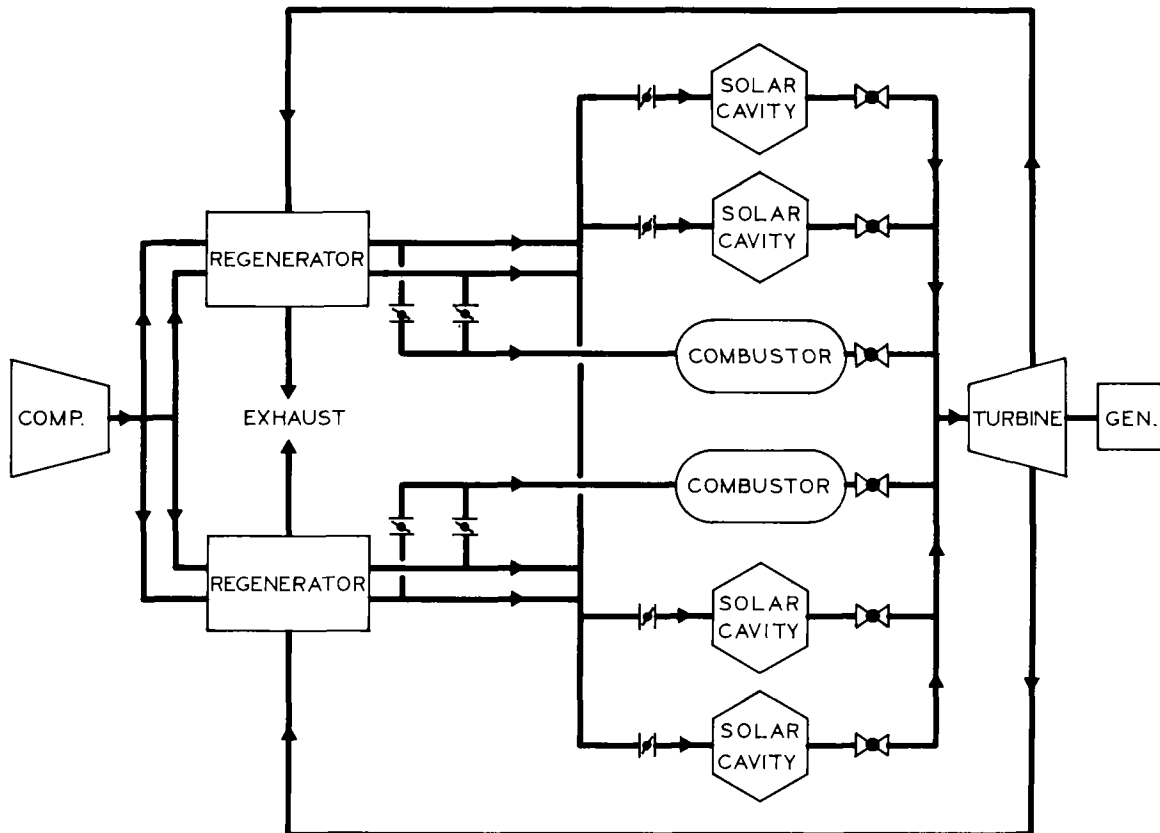


Figure 6-8. Flow Diagram of the Solar-Powered Open-Cycle Gas Turbine with Hybrid Operation Capability

The conceptual baseline design interrupts normal MS 7001R operation at this point. The preheated air is discharged into a new ducting network which includes the parallel path arrangement of external combustors and solar cavity heat exchangers (refer to Figure 6-8). After the network valving has selectively directed air through the proper heat source for heating to design temperatures, the air must be ducted back to the turbine in a fashion that does not require significant modifications to the basic turbine frame. This turbine interface ducting will be described later in this section.

The specific design of the external combustors is beyond the scope of this study. However, a number of preliminary performance estimates have been made, and issues requiring further study and evaluation have been identified. As mentioned earlier in this section, it is anticipated that the transition from solar to fossil fuel could be made without generation interruption utilizing the described hybrid concept, and that it could be done in approximately one minute. Such a system would not adversely affect the basic turbine unit, nor would it require substantial turbine modifications.

The effects of repeated thermal cycling on the combustors required for this concept are unknown. In gas turbines operating at present, thermal cycling of combustors and other hot gas path components is, of course, an important consideration. Thermal cycling impacts the expected life of equipment, and it is particularly critical in a combustion system because of the extreme temperatures and the high rates of temperature change. Manifestations of thermal cycling in the conventional GE combustors have been as follows.

- Distortion in the combustor liner
- Louver cracking in the combustor liner
- Wear at crossfire tube and transition-piece fits

The lives of gas turbine parts are strongly influenced by the following.

- Type of fuel
- Starting frequency
- Load cycle
- Environmental conditions
- Maintenance procedures

A detailed investigation of combustor operation and design would be necessary to predict the cyclic combustor performance.

An assessment of the most desirable number and type of combustors should be the product of a definitive study by a turbine manufacturer. The conceptual design proposes the use of two external combustors, Figure 6-9, similar to those currently in use by Turbodyne. By minimizing the number of combustors, the ducting and system control problems should be reduced. The space requirements atop the concrete support tower should also be reduced by using a small number of combustors. More than one combustor was needed, it was felt, because it would lessen the combustor turndown requirements as well as enhance system reliability. It was assumed that

two such combustors would be acceptable. On the other hand, General Electric has expressed a preference for a system that utilizes their "standard," ten MS 7001R combustor pod approach. This scheme appears to require an unacceptably complex valve and duct network and, as such, was not incorporated in the baseline conceptual design.

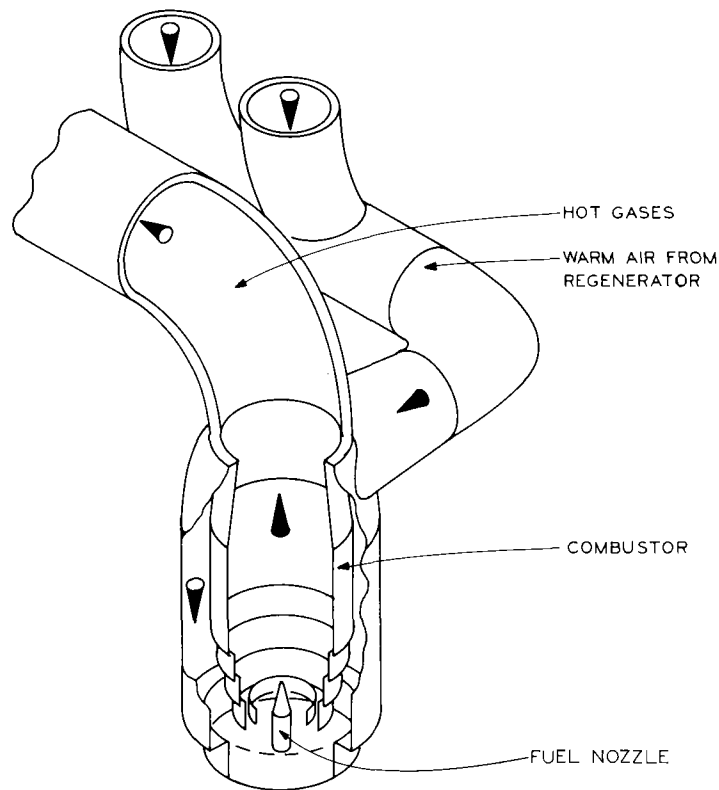


Figure 6-9. External Combustor Subsystem (Conceptual)

Either combustor scheme is compatible with the basic hybrid system operation concept. Both schemes require some degree of combustor development and/or modification. An evaluation of the performance potential, development effort, and cost of the respective concepts should be undertaken in detailed design. At present, however, the logic of using a small number of relatively large combustors is appealing, and as such, this approach is incorporated into the baseline conceptual design pending definitive study.

## INTERFACE DUCTING

Separate and distinct pieces of equipment comprise the central-receiver, solar-thermal power generation system. In order for the system to operate, a means of linking the system components together must be provided. This permits the thermodynamic process of heat-to-power conversion to function. A conceptual design of the necessary interfaces is developed in this section.

### Objectives

The interface ducting must link the turbine unit with the solar and fossil heat sources located external to the machine. Air at approximately 0.96 MPa (140 psia) and 482°C (900°F) must be conveyed from the regenerator discharge connections to the combustor and solar cavity heat exchanger inlets. Valves to control this air-flow are included in the ducting. Air at the nominal conditions of 0.96 MPa (140 psia) and 1038°C (1900°F) will be discharged from the various heat sources when they are in an operating mode. This high-temperature fluid must be conveyed to the inlet connections on the turbine frame. In the event of a turbine trip, energy inputs to the turbine must be curtailed instantly to prevent turbine overspeed. Therefore, provisions must be made for diverting solar cavity discharge air away from the turbine; the thermal inertia of the cavity necessitates this while, conversely, the instant shutoff nature of fuel flow eliminates the bypass requirements on combustors. The objectives of the ducting conceptual design effort follow.

- Insulation against heat loss
- Containment of hot, pressurized air
- Arrangement for low pressure drop
- Valving for hybrid operation

The mass flow rate of air for a nominal 60-MWe gas turbine is on the order of two million pounds per hour.

### Requirements

Pressurized air at 482°C (900°F) must be ducted to the various heat source inlets with a minimal loss in fluid pressure. It follows that the piping network performing that function should be designed to withstand the hoop stress, temperature, and thermal expansion conditions associated with that activity. The flow areas should also be large enough to pass the required air mass without excessive flow velocities, since pressure losses increase with the square of flow velocity.

Chrome-moly pipes, 81 cm (32 inches) in diameter with a one-quarter-inch wall thickness, connected to each of the four regenerator discharge ports are capable of satisfying these requirements. The outer surfaces of these pipes would be thermally insulated to minimize heat losses. Thermal expansion of the pipes would be absorbed in a restrained bellows.

These preheated air ducts cannot be dedicated to individual heat sources if operational flexibility of the system is to be ensured. To permit the distribution of air among the four solar cavities in response to insolation conditions, there must be a common flow path through at least a part of the route to the cavities (refer to Figure 6-8). In order to maintain a constant air velocity (nominally 30 m/sec [100 fps]), this common flow path pipe would require a diameter of 1.65 m (65 inches). Downstream of the common path, the airflow would again diverge into four separate lines, each serving a single solar cavity.

Valves to modulate the airflow among the various solar cavities and fossil fuel combustors are required. Since the flow conditions are moderate (0.97 MPa [140 psia], 482°C [900°F]), conventional valves can be used. Posi-Seal International, Inc. commonly fabricates low-leakage, wafer-type valves for the power industry in the size range of interest for this application. Low leakage is a necessary characteristic to permit isolation of system components. The establishment of allowable leakage rates and proper valve sizes, as well as sizing the ducts themselves, would be an aspect of detailed system design. For conceptual design purposes, a 32-inch valve is assumed.

After passing through the heat sources and achieving a nominal temperature of 1038°C [1900°F), another series of pipes ducts the air to the turbine. In principle, this piping network is similar to that which supplies air to the heat sources; an isolation valve is provided, along with a section of common airflow path to enhance system operating flexibility. Because of the higher air temperatures, the internal airflow area must be increased to 1.07 m (42 inches) in order to maintain a nominal air velocity of 30 m/sec (100 fps). The containment and valving of this hot air is complex, however, because of the 1038°C (1900°F) temperature. This temperature results in substantial metal strength reductions and thus, conventional duct and valve designs are not applicable.

### High-Temperature Ducting Design/Test

The high-temperature ducting concept should meet the same objectives as mentioned earlier in this section. To do so, the following requirements must be satisfied.

- Withstand internal pressure
- Insulate duct wall from the 1038°C (1900°F) airflow
- Maintain air cleanliness

Furthermore, the turbine combustion wrapper, which will receive the hot air, is not normally exposed to 1038°C (1900°F) air. Some means of protecting this wrapper from excessive temperatures must be considered. Ideally, some protection mechanism applicable to both the high-temperature ducts and the regenerative wrapper should be developed.

Throughout the conceptual design process, conventional materials have been utilized whenever possible. Conventional materials, including the superalloys, do not, however, have adequate strength at 1038°C (1900°F) to contain 0.97 MPa (140 psia) in the duct sizes of interest. Therefore, either temperature-resistant materials such as ceramics must be used in fabricating the pipes, or a method to protect metal pipes from the high air temperatures must be developed. The relatively large duct sizes required, and the lack of experience in the ceramic industry with large components, are persuasive considerations in designing a reliable duct network. Accordingly, it was decided to use metal ducts, with an internal thermal barrier to prevent the metal temperatures from exceeding 482°C (900°F).

Cooling techniques to limit metal temperatures are commonly used in gas turbine hot gas paths; transpiration cooling and air films are examples of the methods used. However, the vast amounts of surface area involved in the duct network preclude the use of these costly and complex techniques.

Alternatively, a thermal barrier between the high-temperature air and the metal pipe could be constructed of conventional insulating materials. Such a design should consider the following.

- Erosion of insulation subject to attack by the high velocity airstream
- Thermal expansion of pipe
- Prevention of pressure differentials on insulation

Insulation surface erosion must be prevented not only to eliminate insulation maintenance problems, but also to avoid damage to the turbine blades by entrained particulate matter. The thermal expansion characteristics of a system subjected to thermal cycling are a necessary consideration so that unacceptable material stress levels do not result. Because insulating materials have relatively low rupture and crushing strengths, it is imperative that the hoop stresses in the duct system be transmitted to the metal pipe.

The conceptual design of the high-temperature air ducts is shown on Figure 6-10. The innermost insulation is a 5-cm (2-inch) layer of Eagle-Picher ceramic block. The inner surface is coated with a high-temperature cement-type binder material that is intended to be erosion resistant. Behind the ceramic block would be 7.5 cm (3 inches) of Eagle-Picher PV Supertemp. This two-layer insulation system should be sufficient to induce a very substantial temperature differential between the 1038°C (1900°F) airstream and the metal pipe; calculations indicate that the pipe metal temperature would be nominally 371°C (700°F). This low temperature would permit the use of carbon steel pipes with a nominal wall thickness of 1 cm (0.33 inch). A 2.5 cm (1 inch) layer of Eagle-Picher Tab-Lock insulation on the pipe outer surface would further reduce system heat losses, and help to protect personnel from exposure to hazardous temperatures. This combination of three insulating materials reduces the outer surface temperature of the ducts to approximately 150°C (300°F). It also limits the thermal losses within the extensive high-temperature duct network to 1 percent of the power system thermal rating. It is reasonable to expect that a similar layered-insulation approach could be used to protect the turbine combustion wrapper from the high-temperature air it will be receiving from the heat sources. A detailed analysis would be required to assess its impacts on turbine operation.

The insulating materials could be supplied as preformed pieces to expedite installation in a commercial plant. Standard installation techniques over impalling pins, with occasional support rings, are anticipated to be adequate. The binder coating would be applied to the ceramic blocks during the manufacturing process. After installation, the discontinuous nature of the insulation blocks would allow air pressure to easily penetrate the insulation, and thus eliminate pressure differential difficulties. Depending on the heat transfer characteristics of the insulation at points of discontinuity, support rings, and impalling pins, the use of a more temperature-resistant pipe metal may be justified; a chrome-moly steel could be used in lieu of carbon steel.

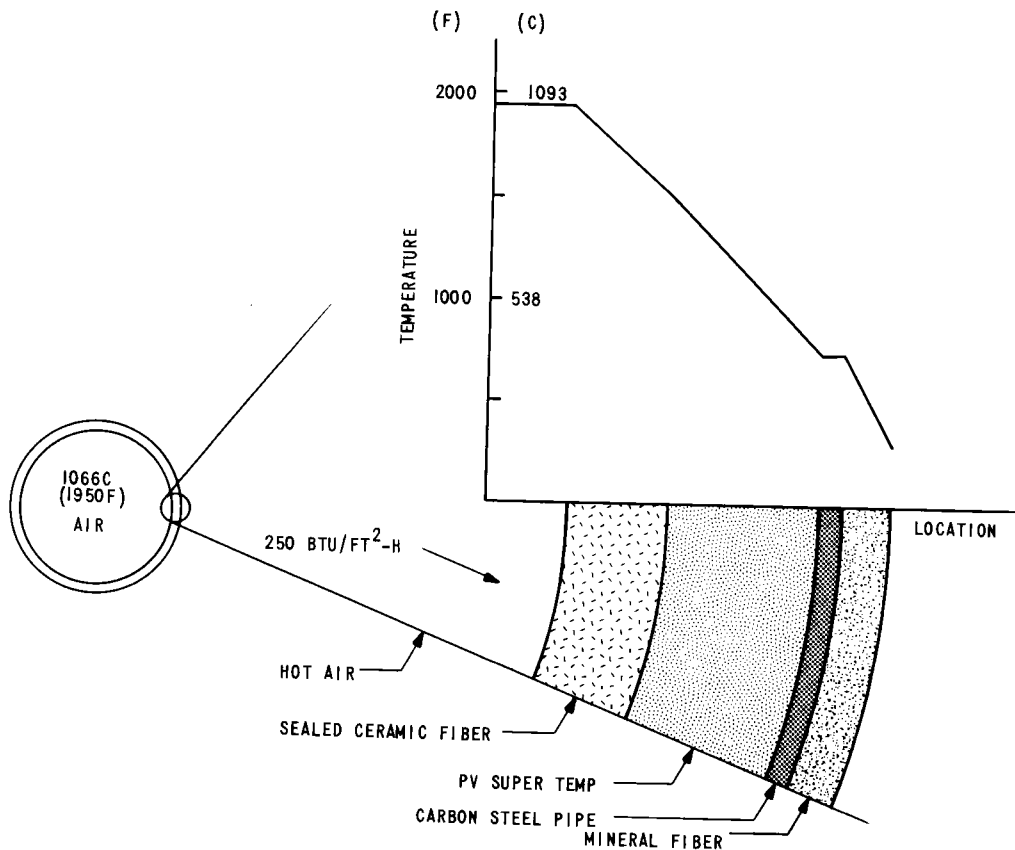


Figure 6-10. Hot Air Duct Insulation

A sample of the ceramic block insulation with binder coating has been incorporated in the heat exchanger configuration test setup at Georgia Tech. It should be possible to get a preliminary indication of the insulation's erosion resistance during the heat exchanger cyclic test, but no data are available at present.

#### High-Temperature Isolation Valve Design

The high-temperature valves will operate in a binary, on/off fashion. Their purpose will be component isolation, rather than both flow control and component isolation, as required of the heat source inlet valves. It will also be necessary for the valves to perform an emergency turbine bypass function previously described. Under emergency conditions, airflow to the turbine must be interrupted rapidly to prevent overspeeding of the unit. It is desirable to interrupt this airflow downstream of the solar cavities because it ensures that cooling air will continue to pass through the heat exchangers; cavity overheating during

the heliostat field defocusing process would thus be prevented. As such, the valves must be capable of venting the normal throughput, or a yet to be determined fraction thereof, to the atmosphere.

The high-temperature valve arrangement must be capable of the following.

- Operating with 1038°C (1900°F) and 0.97 MPa (140 psia) air
- Withstanding exposure to combustion products
- Shutting off flow with low leakage
- Passing design airflow with low pressure drop
- Venting air to atmosphere instantly for emergency turbine bypass

A valve capable of meeting these requirements does not exist at present. Black & Veatch identified AiResearch Manufacturing Company of Arizona as an organization experienced in high-temperature valve design. Historically, AiResearch has supplied valves for aircraft and missile high-temperature applications.

Subsequent to a meeting between Black & Veatch and AiResearch personnel, AiResearch submitted a technical proposal for a high-temperature isolation and emergency bypass valves study program. This study program would address the broad issues of valve configuration and functions, fabrication materials, critical parts analysis, maintenance, operational performance, and cost. Primary study efforts would be directed toward a bench-model test-size valve, with scaling factors provided to develop data on commercial-size valves. The program outputs would include a layout drawing complete with dimensions, materials, processes, and information necessary to draw detailed parts. Cost predictions, scaling factors, and scheduling information would also be delivered.

#### Turbine Interface Layout

Conceptual layouts of the gas turbine, central receiver and interface ducting have been developed throughout this program. They are shown on the successive figures that follow, for both the 60-MWe commercial system and the 2.7-MWe pilot plant.

A perspective view of the commercial-size central receiver showing the relative locations of the four solar cavities and the turbine enclosure can be seen on Figure 6-11. A cutaway elevation view in Figure 6-12 illustrates the ducting network linking the system components. The combustors located beneath the MS 7001R turbine unit are also shown on this figure. The fossil fuel combustors

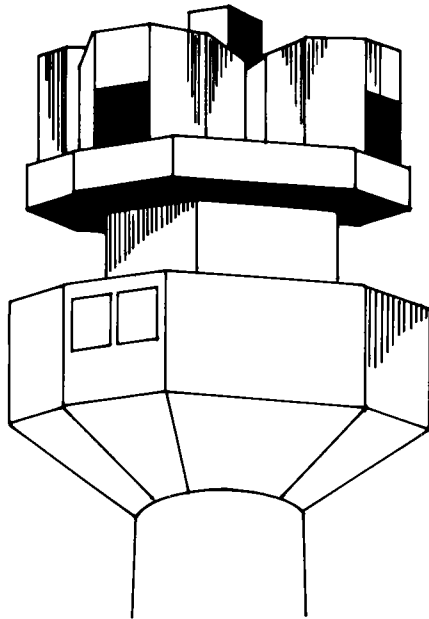


Figure 6-11. Perspective View of Receivers and Turbine Enclosure Atop the Tower

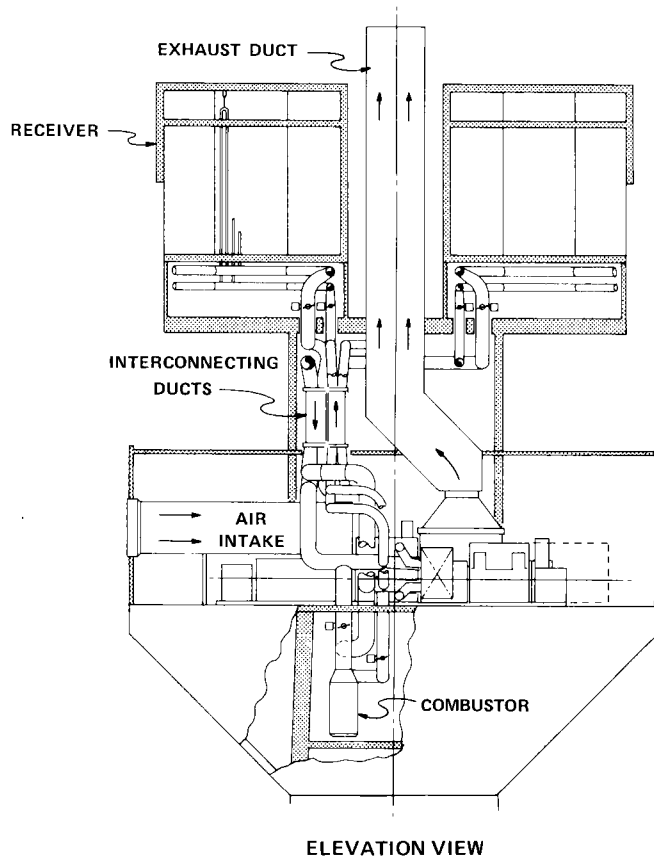


Figure 6-12. Elevation View of the Receiver/Turbine/Combustor System Arrangement

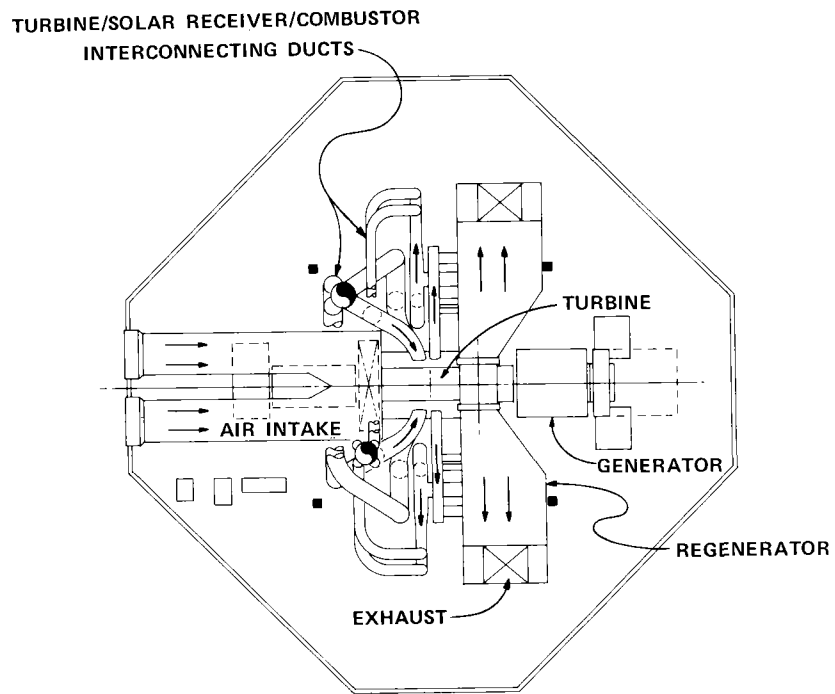


Figure 6-13. Turbine Operating Floor--Plan View

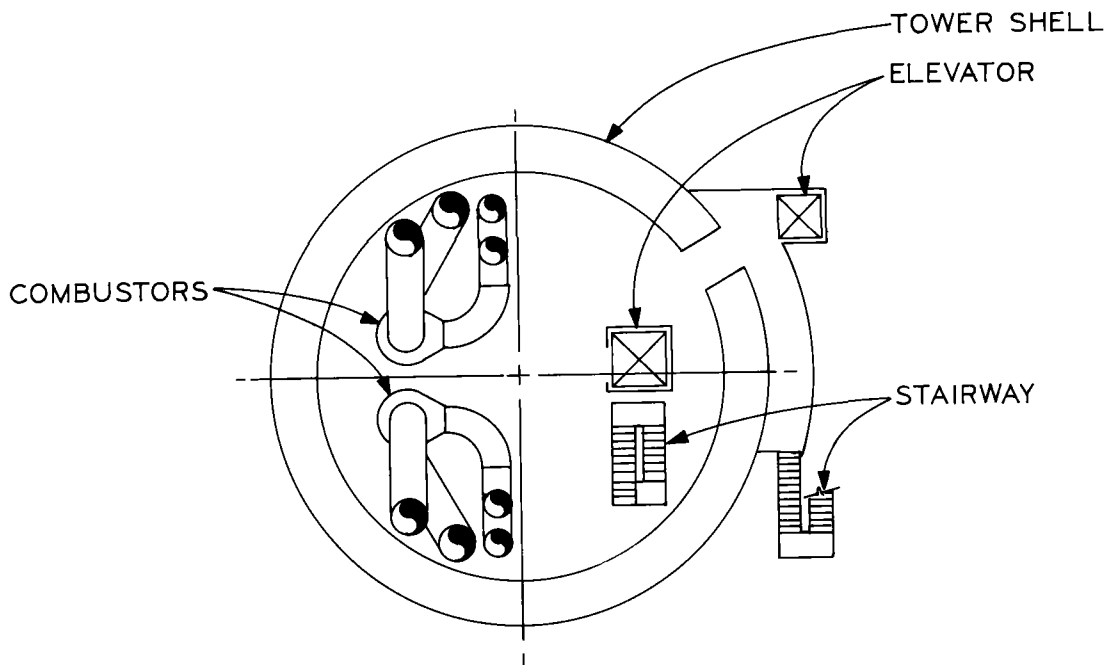


Figure 6-14. External Combustor Operating Floor--Plan View

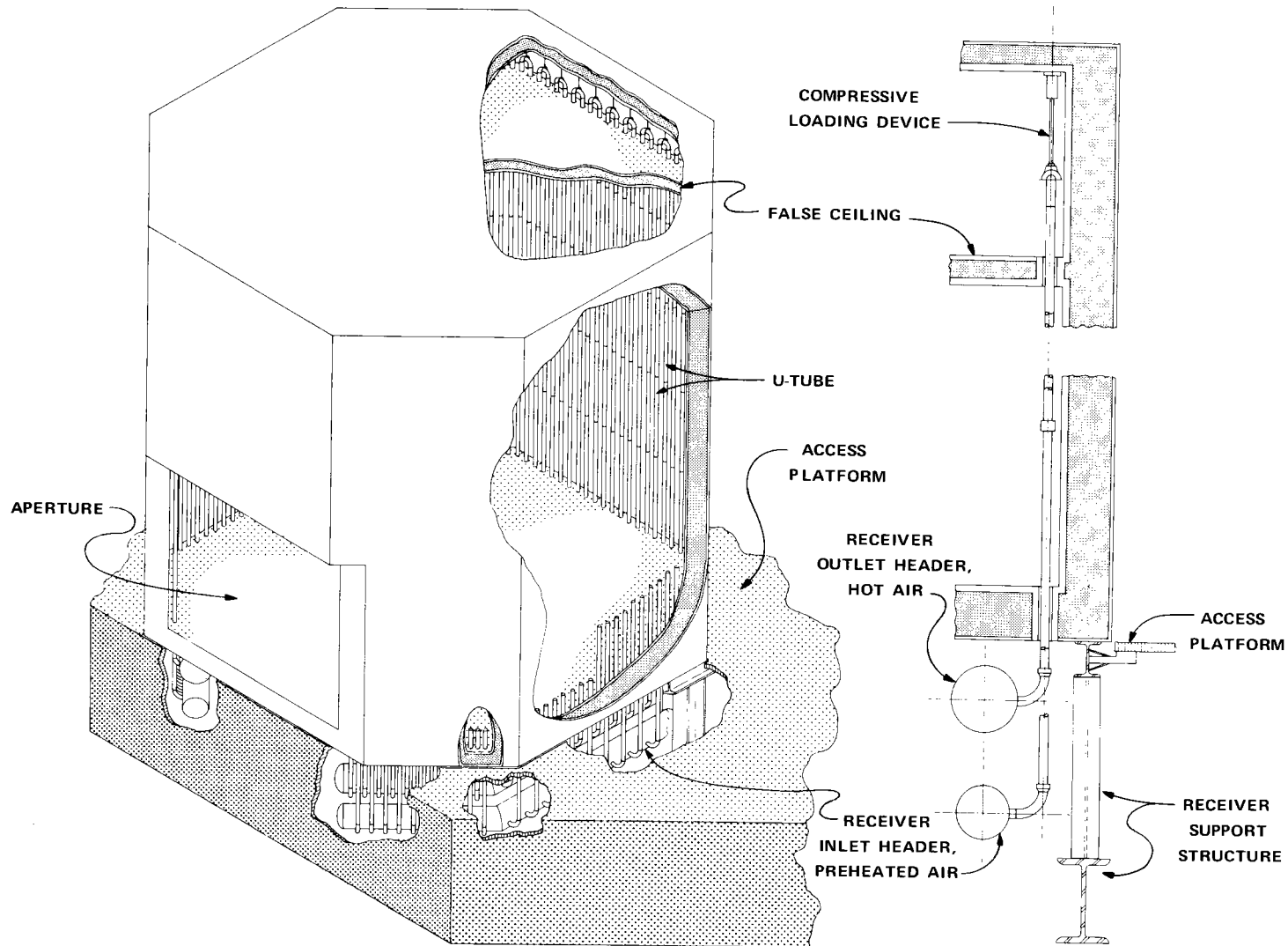


Figure 6-15. Cutaway of Tube-Type Cavity Receiver/Heat Exchanger

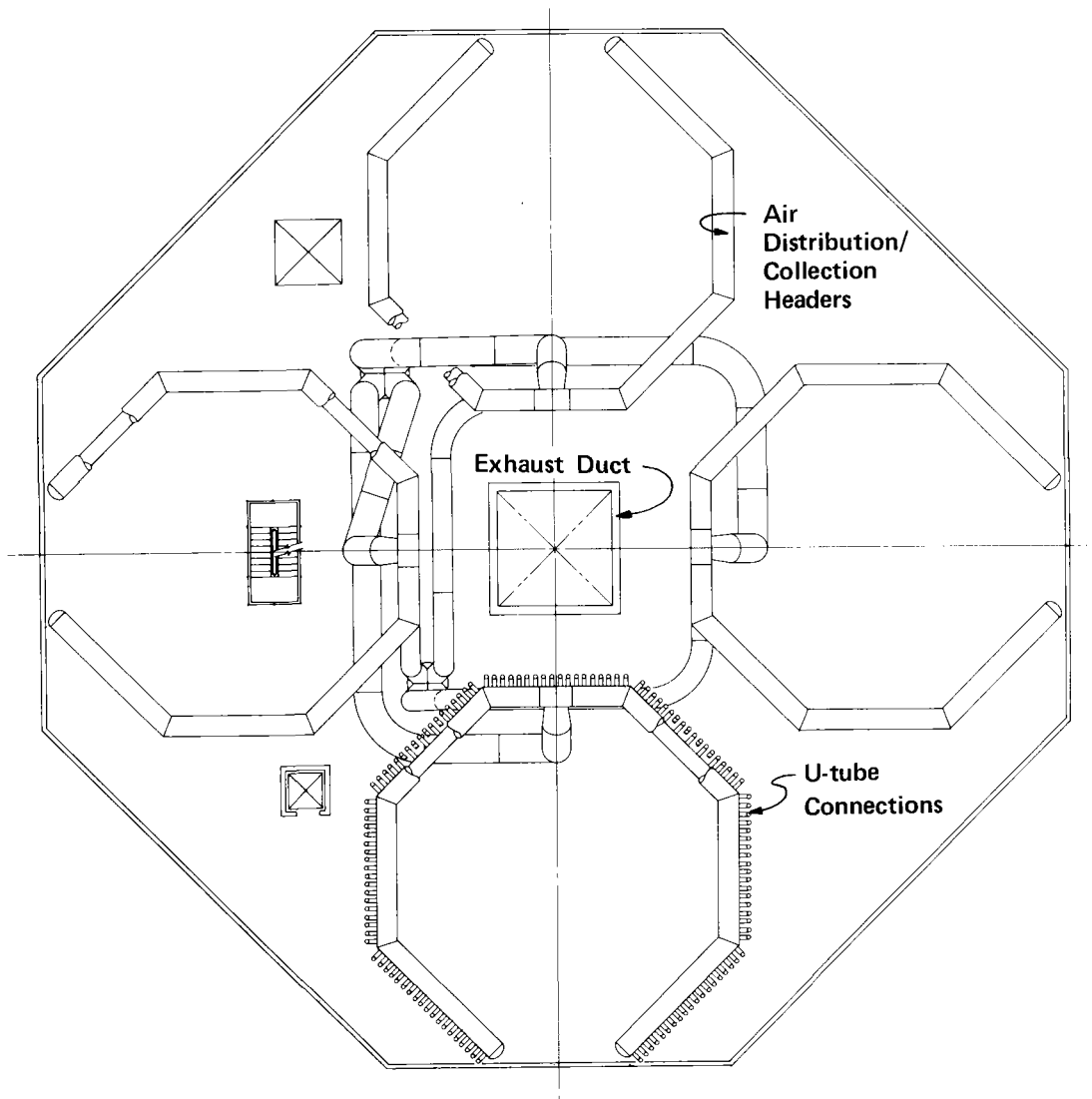


Figure 6-16. Plan View of the Cavity Receiver's Interfacing Piping  
Beneath the Cavity Support Structure

are positioned within the concrete tower shell, and in close horizontal proximity to the regenerator discharge connections and to the turbine inlet ports. Plan views of the turbine operating floor and the buffer/storage combustor floor are shown respectively in Figures 6-13 and 6-14. As one progresses toward the top of the central receiver, Figures 6-15 through 6-17 are of interest. Pictured in Figure 6-15 is a cutaway of a receiver cavity. The connection of the U-tube legs to the manifolds can be seen. Similarly, the inset graphically represents the locations of the cold and hot air manifolds; the hot manifold is positioned above the cold one so that the hot U-tube leg is shorter than the cold leg. Differential thermal expansion of the respective legs is thereby minimized. Figure 6-16 illustrates the air distribution manifolds that supply warm air to, and accept hot air from, the solar heat exchangers. The lower manifold pictured in Figure 6-16 includes the extension elbows for connecting the manifold to the individual heat exchanger U-tubes. The turbine exhaust duct passes up the center of the platform between the cavities and air ducts. A plan view of the cavity structure can be found on Figure 6-17. A lower cavity cutaway reveals the individual U-tubes dispersed about the cavity inner perimeter.

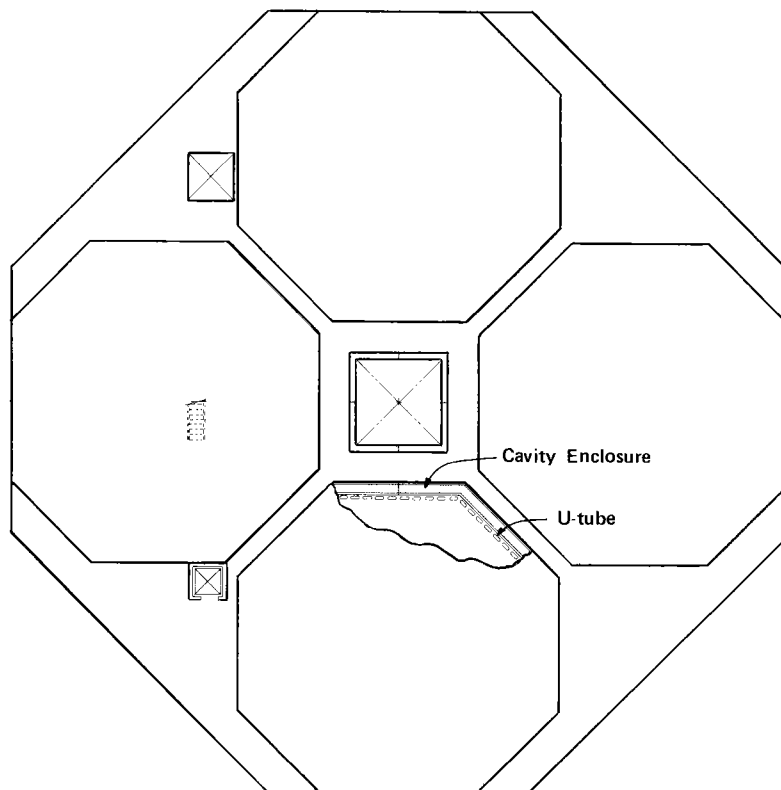


Figure 6-17. Plan View of the Cavity Receiver Arrangement Atop the Tower

The difficulties of interfacing the existing MS 7001R gas turbine with the solar-unique aspects of the system have been resolved to the point of conceptual design. No insurmountable problems have been identified. Detailed design will be required to verify insulation techniques, to specify flow distribution characteristics, and to resolve the problems inherent with the thermal expansion of ducting components. Additional analysis is required to analyze system configurations with regard to system cost, performance, and reliability. Development work is necessary in the areas of valving, combustors, and controls prior to the construction of this solar-thermal, open-cycle, gas turbine system. Depending on the assessed reliability of the solar cavity, it might be possible to eliminate the high-temperature isolation valve from the interface system requirements.

A less rigorous conceptual design of 2.7-MWe pilot plant turbine interfaces has been completed. The proposed turbine for the pilot plant is the Solar Centaur, pictured on Figure 6-6. It can be seen that this turbine has a single combustor, and it is normally mounted external to the turbine frame. As a result, the adaptation of this turbine to the central receiver is less complex than with a commercial-size machine. Figure 6-18 is a drawing of how the Centaur might be modified for solar-thermal applications. The combustor pod is moved upward from its normal position to provide room for a lateral pipe branch. Within this branch, the hot air from the solar heat exchanger and/or combustor would combine into a single flow for turbine inlet. The recuperator would also probably need to be elevated to provide additional combustor space. As in the case of the GE MS 7001R, no modifications to the turbine proper are required. It would perhaps be desirable to modify the recuperator so that preheated air could be removed from both top and bottom ports as shown. At present, only the bottom port exists. Combustor modification to permit full-speed ignition is probable.

As in the commercial plant, heat source inlet control valves (not visible on Figure 6-18) are required to modulate airflow in response to insolation conditions. High-temperature valves for component isolation and emergency turbine-trip control are needed, as is a high-temperature duct system. However, the Solar Centaur currently operates at a nominal turbine inlet temperature of 900°C (1650°F) (cycle efficiency is reduced as a result: 0.32 versus 0.37 for the MS 7001R). This is more within the operating regimes of the superalloys and thus, these pilot plant valving and ducting problems can be conquered more readily.

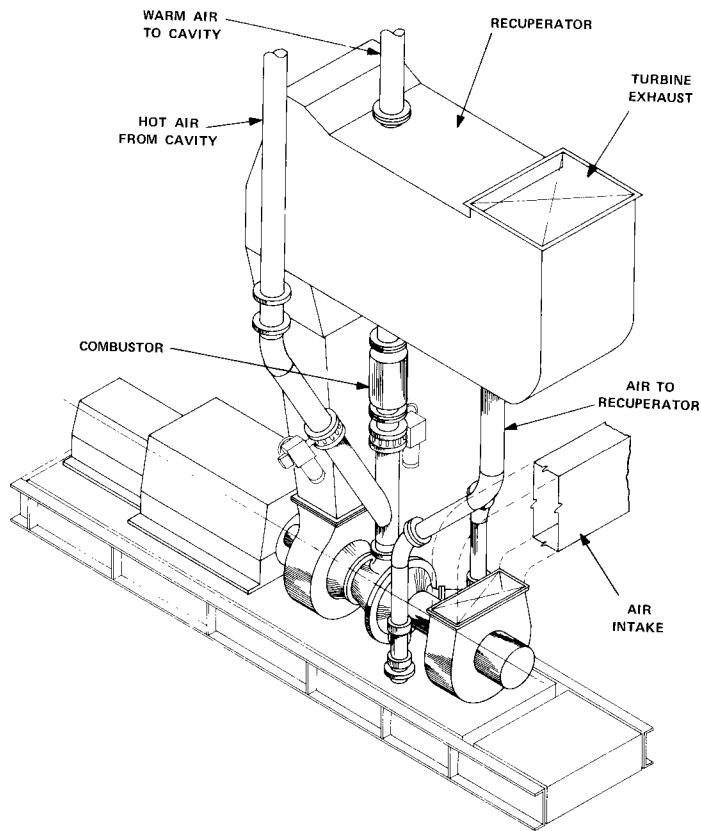


Figure 6-18. Perspective of the Turbine/Central Receiver Interface Piping

## Section 7

### RECEIVER TOWER DESIGN

The central receiver must be elevated well above ground level due to the performance characteristics of a heliostat field. The importance of low pressure drops in the airflow path of the turbine system was established in Section 6. Since airflow pressure drop is a function of path length (among other considerations), it is desirable to minimize the distance between the central receiver and turbine. Furthermore, Section 6 described the difficulties associated with ducting high-temperature air from the solar heat exchangers to the turbine. Therefore, both the solar cavities and the turbine generator unit will be located atop a support tower. Support tower and platform design will be preliminarily addressed in this section.

#### REQUIREMENTS AND DESIGN CHOICES

Although tower design was not a primary concern within the scope of this program, Black & Veatch made a preliminary tower system design evaluation to verify the feasibility of the turbine-tower concept. The receiver support tower should satisfy the following requirements.

- Height consistent with heliostat field optics
- Resistance to wind and seismic loads
- Turbine support platform
- Receiver cavity mounted above turbine
- Personnel access to the tower top
- Permit installation and maintenance of equipment atop the tower

Receiver height was established in Section 3 subsequent to a trade-off analysis between increased heliostat field performance and increased tower cost for taller towers. The tower and the structures atop it must be able to withstand the forces and accelerations that will be generated by wind loading and seismic activity. The turbine support platform must be of adequate strength to accept the static and dynamic loads of the turbine generator set; adequate space for the turbine interfaces and maintenance must also be provided. The General Electric MS 7001R

regenerative unit is about 35 m (116 feet) long in its standard configuration, and weighs about 800,000 kg (880 tons). The four receiver cavities must be mounted above the turbine. The cavity support area will be on the order of 38 m (125 feet) across the faces. The cavities and ancillary devices are estimated to weigh approximately 700,000 kg (1.5 million pounds); the cavity pedestal design will include a structural steel frame to support these loads. As in any operating system, provisions for personnel access must be made, and a means for installing and servicing equipment atop the tower must be an aspect of the tower design.

This combination of requirements can be best satisfied by a steel-reinforced concrete tower, and two structural steel platforms for supporting the turbine and receiver cavities. The reinforced concrete tower extends from the subterranean mat to just beneath the turbine platform as a continuous, hollow, tapered column. The structural steel turbine support platform rests directly upon the top of this column. A steel space frame extends upward from the turbine platform to provide the support areas required by the cavities and interconnecting duct network.

The arrangement of the support tower, tower mat, turbine support platform, and cavity support platform are shown schematically on Figure 7-1. Additional drawings of the various structures may be found in Appendix F. A more detailed examination of tower structure features and pertinent design criteria can also be found in Appendix F.

A suitable framing system has been identified, but the design of the support floors has been conceptual only. A detailed design of the major structural components is necessary to determine the size of the members shown in the various drawings. Rigorous dynamic analysis is also required to predict tower response under seismic activity conditions.

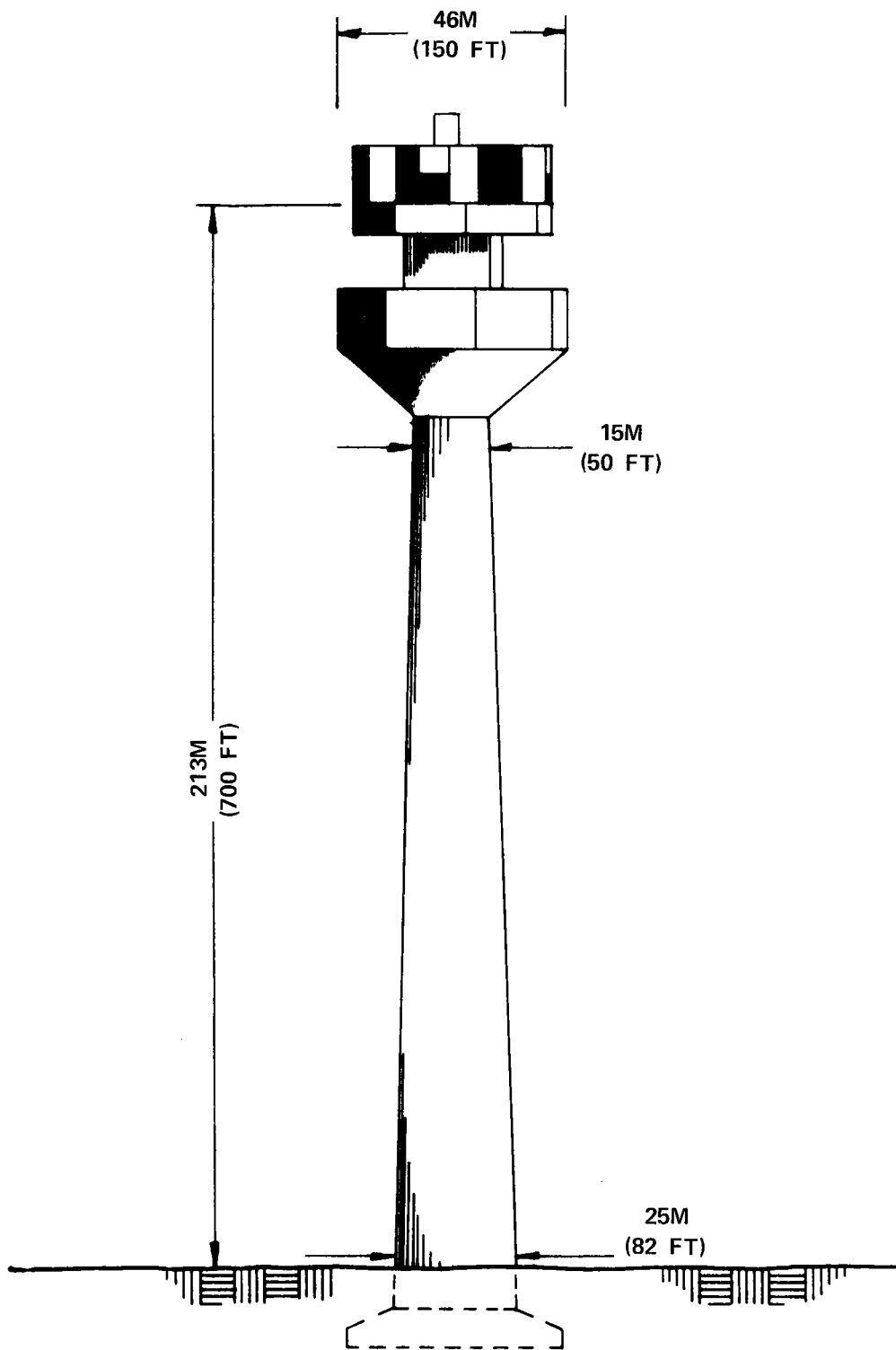


Figure 7-1. Open-Cycle Gas Turbine Support Tower

## Section 8

### SYSTEM COSTS

The technical aspects of solar-thermal power generation utilizing an open-cycle gas turbine have been addressed thus far in this report. In this section, the capital costs of the solar-electric power system will be considered. Furthermore, estimated costs for busbar electricity will be developed, and the entire system compared with the EPRI Strawman. All costs are in 1976 dollars.

#### COLLECTOR/CONCENTRATION SUBSYSTEM

The cost of the collector/concentrator includes the following major components.

- Land
- Heliostats
  - Installation, alignment, calibration
  - Foundations
  - Frame
  - Mirror
  - Motors
  - Batteries
  - Controlling computer
  - Control and power cable network
- Fencing

It will be assumed that grading of the land to permit heliostat installation is not necessary, and that it is possible to purchase a tract of land in the desired heliostat field configuration. It is also assumed that ground surface treatment to prevent excessive dust levels is not required. Prudent system design suggests that a buffer area surrounding the heliostat field will be necessary (30 m [100 feet] assumed) as well as a 2-m (6-foot) perimeter fence.

Land costs are assumed to be \$800/acre. Since the design of heliostats and their ancillary equipment is beyond the scope of this study, a range of heliostat system cost estimates will be utilized. It was felt that values of \$75, \$100,

and  $\$125/\text{m}^2$  of mirror area might adequately bracket the mid-range and long-range costs of complete heliostat systems. It was assumed that the heliostat cost includes all installation costs and the necessary control devices. Using the heliostat field specified in "Baseline Heliostat Field" in Section 3, the estimated cost of the collector/concentration subsystem is  $\$19,702,000$ , if heliostat systems can be purchased for  $\$75/\text{m}^2$ . The costs are tabulated on Table 8-1.

Table 8-1  
ESTIMATED COLLECTOR/CONCENTRATOR SUBSYSTEM COSTS (1976 DOLLARS)

	QUANTITY	COSTS (\$)		\$/kW*
Land @ $\$800/\text{acre}$	168 acres	135,000		
Fencing @ $\$8/\text{ft}$	9300 feet	75,000		
Heliostats @ $\$75/\text{m}^2$	259,888 $\text{m}^2$	19,492,000		
@ $\$100/\text{m}^2$	259,888 $\text{m}^2$	25,989,000		
@ $\$125/\text{m}^2$	259,888 $\text{m}^2$	<u>32,486,000</u>		
Total Direct Estimated Cost		19,702,000	$\$75/\text{m}^2$	358
		26,199,000	$\$100/\text{m}^2$	476
		32,696,000	$\$125/\text{m}^2$	594

\*Based on a 55-MWe turbine capacity at the 854-m (2800-ft) elevation of Inyokern, California (including tower).

#### HEAT TRANSFER SUBSYSTEM

The heat transfer subsystem is, to a large degree, composed of ceramic materials in configurations, and in amounts, unlike those in existing equipment. Consequently, there is very little experience to draw upon when estimating the cost of this subsystem. Cost projections by Carborundum were used as the basis for estimating ceramics-related costs. Other major components of the subsystem include insulating materials, cavity structural enclosures and radiation shields; these costs were generated using manufacturers' data in conjunction with Black & Veatch experience. However, it is again noteworthy that these structures involve highly unique features, and thus costing information is difficult to generate at the conceptual design level. The estimated costs of the solar cavities and the pertinent unit prices are presented in Table 8-2.

Table 8-2  
ESTIMATED HEAT TRANSFER SUBSYSTEM COSTS (1976 DOLLARS)

	QUANTITY	COST (\$)	\$/kw
Heat Exchanger	4		
Silicon-Carbide Tubing	21,060 ft	3,020,000	
Silicon-Carbide U-bends	234	82,000	
SiC to SiC Joints	4212	1,685,000	
SiC to Metal Joints	468	187,000	
Reflecting Panels	32,600 ft <sup>2</sup>	<u>652,000</u>	
Subtotal		5,626,000	102
Cavity Enclosures			
Steel		1,400,000	
Insulation	42,000 ft <sup>3</sup>	1,100,000	
Aperture Doors	4	320,000	
Platform and Walkways	--	<u>45,000</u>	
Subtotal		2,865,000	52
Air Header Extension Elbows			
Hot Air	234	550,000	
Warm Air	234	<u>110,000</u>	
Subtotal		660,000	12
Radiation Shields	5000 ft <sup>2</sup>	<u>720,000</u>	<u>13</u>
Total Direct Estimated Cost		9,871,000	179

\* Based on a 55-MWe turbine capacity at the 854-m (2800-ft) elevation of Inyokern, California (including tower).

Total estimated direct cost of the heat transfer subsystem is \$9,871,000.

#### ELECTRIC POWER GENERATION SUBSYSTEM

The electric power generation subsystem includes all the equipment necessary to convey and convert thermal energy supplied by the solar cavity (heat transfer subsystem) into electrical energy suitable for transmission into the utility distribution grid. The fossil fuel combustors are also considered to be a part of this subsystem. The major components of this subsystem are as follows.

- Open-cycle, regenerative gas turbine
- Auxiliary turbine equipment, including starting motor
- Electric generator
- Electrical transformers and switchgear
- Turbine control system, including selective heat source operation logic
- External combustors
- Ducting network linking gas turbine to heat sources, including support hangers
- Exhaust ducting
- Valves
- Fossil fuel storage and pumping equipment

Price data on this equipment were based on inputs from General Electric, AiResearch, Posi-Seal International, Eagle-Picher, Ingersol-Rand, and the Black & Veatch estimating group.

The total direct estimated cost of the electric power generation subsystem is \$14,540,000 as presented on Table 8-3.

#### RECEIVER TOWER SUBSYSTEM

The receiver tower subsystem consists of the equipment and structure necessary to support and erect the electric power generation and heat transfer subsystems. This subsystem includes the following.

- Tower mat
- Steel-reinforced concrete tower
- Structural steel space frame for receiver support
- Structural steel turbine platform
- Turbine platform enclosure
- Rail hoist for turbine installation

The cost estimates are based upon pricing data from M.W. Kellogg Company, and Black & Veatch experience with power plant chimneys. A listing of these cost estimates may be found on Table 8-4. It should be emphasized that tower costs are very sensitive to design specifications. Inasmuch as rigorous computer analysis is required to develop a tower design compatible with the load-carrying requirements of this concept in the seismic activity zone associated with Inyokern, California, this cost estimate should only be interpreted as an indication of receiver tower costs.

Table 8-3

## ESTIMATED ELECTRIC POWER GENERATION SUBSYSTEM COSTS (1976 DOLLARS)

	QUANTITY	COST (\$)	\$/kW <sup>*</sup>
Turbine			
General Electric MS 7001R Package Power Plant	1	7,500,000	
Turbine Installation	--	1,500,000	
Control System Enhancement	--	300,000	
External Combustors	2	400,000	
Exhaust Ducting	200 ft	500,000	
Electrical Feed to Substation	1	700,000	
Transmission Substation	1	<u>900,000</u>	
Subtotal		11,800,000	215
Heat Source Interface Ducting			
To Heat Sources	1200 ft	500,000	
From Heat Sources	1200 ft	<u>1,100,000</u>	
Subtotal		1,600,000	29
Interface Valving			
To Heat Sources	6	150,000	
From Heat Sources	6	<u>750,000</u>	
Subtotal		900,000	16
Fossil Fuel Supply			
Piping and Valves	1500 ft	80,000	
Surge Tank	1	6,000	
Pumps	2	24,000	
Storage Tanks, 180,000 gal Capacity	2	120,000	
Unloading Station	1	<u>10,000</u>	
Subtotal		<u>240,000</u>	<u>4</u>
Total Estimated Direct Cost		14,540,000	264

\* Based on a 55-MWe turbine capacity at the 854-m (2800-ft) elevation of Inyokern, California (including tower).

Table 8-4

ESTIMATED RECEIVER SUPPORT SUBSYSTEM COSTS (1976 DOLLARS)

	COST (\$)	\$/kW <sup>*</sup>
Tower Mat	1,600,000	
Tower	4,300,000	
Structures Atop Tower	2,100,000	
Turbine Enclosure	275,000	
Rail Hoist	<u>1,000,000</u>	
Total Direct Estimated Cost	9,275,000	169

\*Based on a 55-MWe turbine capacity at the 854-m (2800-ft) elevation of Inyokern, California (including tower).

The total direct estimated cost of this subsystem is \$9,275,000.

BALANCE OF PLANT SUBSYSTEM

There are many support facilities that are necessary for the operation of a power plant. Included in the general balance of plant would be the following major items.

- Turbine room crane
- Elevators and ladders
- Platforms and walkways
- Office and maintenance facilities
- Control room
- Site work--roads, parking, sewage, lighting
- Miscellaneous electrical construction
- Miscellaneous piping
- Water system
- Fire protection

The power plant cost-estimating experience of Black & Veatch was used as the basis for developing these costs. The costs are tabulated in Table 8-5.

Table 8-5  
ESTIMATED BALANCE OF PLANT COSTS (1976 DOLLARS)

	COST (\$)	\$/kW <sup>*</sup>
Turbine Room Crane	100,000	
Elevators, Ladders, and Platforms	500,000	
Office, Control Room, Maintenance Facilities	500,000	
Site Work	500,000	
Miscellaneous Electrical Construction	500,000	
Miscellaneous Piping	300,000	
Fire Protection	100,000	
Water System	<u>100,000</u>	
Total Estimated Direct Cost	2,600,000	47

<sup>\*</sup> Based on a 55-MWe turbine capacity at the 854-m (2800-ft) elevation of Inyokern, California (including tower).

The total direct estimated cost of this subsystem is \$2,600,000.

#### SYSTEM CAPITAL COST SUMMARY

The total capital cost of the solar thermal power system is a composite of the subsystem costs previously presented in this section. A summary of these costs is displayed in Table 8-6.

The total capital investment required for an open-cycle gas turbine solar-electric system with a hybrid operation capability is \$74,048,000, assuming complete heliostat systems are available for \$75/m<sup>2</sup> of mirror area. For the nominal plant rating of 60 MWe, the cost is \$1,234/kWe. If the cost is based upon the actual predicted performance (55 MWe) of the open-cycle gas turbine plant located at Inyokern, California, at noon on March 21, investment is \$1,346/kWe.

Table 8-6

60-MWe OPEN-CYCLE GAS TURBINE SOLAR-ELECTRIC SYSTEM ESTIMATED  
COST SUMMARY (1976 DOLLARS)

	COST (\$)	\$/kW <sup>*</sup>
Collector/Concentrator Subsystem @ \$75/m <sup>2</sup>	19,702,000	358
Heat Transfer Subsystem	9,871,000	179
Electric Power Generation Subsystem	14,540,000	264
Receiver Tower Subsystem	9,275,000	169
Balance of Plant	<u>2,600,000</u>	<u>47</u>
Total Direct Cost	55,988,000	1,017
Contingency and Spare Parts (5%)	2,800,000	51
Indirect Costs (10%)	<u>5,600,000</u>	<u>102</u>
Total Capital Investment (1976)	64,388,000	1,170
Interest During Construction (15%)	<u>9,660,000</u>	<u>176</u>
Total Cost at Commercial Operation	74,048,000	1,346

\* Based on a 55-MWe turbine capacity at the 854-m (2800-ft) elevation of Inyokern, California (including tower).

## COMPARISON WITH EPRI STRAWMAN CAPITAL COST

Capital costs per kilowatt are presented in Table 8-7 in the standard format recommended by EPRI for central receiver systems. This format permits comparison with the EPRI strawman 100-MWe, central receiver system. For this comparative purpose, a 100-MWe, open-cycle, gas turbine, central-receiver system is assumed to consist of two, 50-MWe modules. The costs per kilowatt of each of these modules were taken to be equal to those developed for the 55-MWe baseline design. The cost savings of colocating the two modules was estimated to be less than 5 percent, which is within the accuracy of the total cost estimate.

The cost of heliostats, assuming they are being made in production quantities, is difficult to estimate at this time. Because of the significant impact of this cost element on the total system cost, a \$60/m<sup>2</sup> to \$125/m<sup>2</sup> range of heliostat costs was utilized to calculate the costs per kilowatt quoted in Table 8-7. The

Table 8-7  
POWER PLANT COST ESTIMATES CENTRAL RECEIVER CONCEPT

	EPRI STRAWMAN	OPEN-CYCLE GAS TURBINE
Collector Area (km <sup>2</sup> )	1.0	0.43
Storage Time (h)	6	6
Account	\$/kWe	\$/kWe
Land	2	2
Structures and Facilities	44	45
Heliostats *	600	284-591
Central Receiver/Tower/Heat Exchanger	95	348
Storage/Tanks	180	4 **
Turbine Plant Equipment	80	231
Electric Plant Equipment	21	29
Miscellaneous Plant Equipment	4	4
Allowance for Cooling Towers	20	
Total Direct Cost	1,046	947-1,254
Contingency Allowance and Spare Parts Allowance (5%)	52	47-63
Indirect Costs (10%)	105	95-125
Total Capital Investment (1976)	1,203	1,089-1,442
Interest During Construction (15%)	180	163-216
Total Cost at Yr of Comm'l Opn.	1,383	1,252-1,658

\* Collector Cost - Strawman, \$60/m<sup>2</sup>  
                   - Open Cycle, \$60-\$125/m<sup>2</sup> range

\*\* Fossil fuel system

lower figure corresponds to the strawman heliostat cost and the upper figure was set to bracket projected costs of present-day heliostat designs.

Several items in the comparison bear special mention. First, the open-cycle gas turbine plant is basically a hybrid plant, using fossil fuel to fire the turbine combustors during periods of solar outage. Therefore, the amount of storage available is established by the capacity of the fuel storage tanks. For this system design, fuel tanks of adequate capacity for 6 hours of storage operation each day for a period of 12 days were provided. Hence, the storage "time" is listed as 6 hours. The storage/tanks account is much less for the open-cycle plant than for the strawman because of the reduced complexity of oil storage tanks versus thermal storage devices.

Second, the accounts for land, structures and facilities, and electric plant equipment are roughly the same for the strawman plant and the open-cycle gas turbine (OCGT) plant. However, the receiver/tower/heat exchanger account is considerably larger for the OCGT, due mainly to the costs of mounting the turbine at the top of the tower and the new technology required for the high-temperature heat exchanger.

Turbine plant equipment is about three times larger for the OCGT. The heliostat account favors the OCGT because of its energy storage concepts. Part of this difference is due to installation of the turbine aboveground, modification for external combustors and hybrid operation, and the more intricate interface ducting required between receiver and turbine. On the other hand, the strawman figure for this account, \$80/kWe, appears unduly low. Steam turbine prices alone account for about \$67/kWe at the 100-MW level, with substantial additional costs for feedwater heaters, steam piping, pumps, steam condenser, and cooling towers.

#### COMPARISON WITH EPRI STRAWMAN PERFORMANCE

The annual efficiency performance of this hybrid system, subdivided into pertinent loss mechanisms for the major subsystems, is shown in Figure 8-1. Heliostat field performance is impaired by three factors: (1) mirror surface foreshortening, (2) heliostat shadowing and blocking, (3) mirror reflectivity losses. Aperture efficiency and cavity efficiency collectively describe the central receiver's capability to capture redirected solar energy and to subsequently affect a heat exchange process with the working fluid of the gas turbine. There are minor

system performance losses due to thermal and pressure losses in the interfacing network that links the central receiver to the turbine. No losses are encountered in the energy storage subsystem because the hybrid nature of the solar-thermal open-cycle concept permits the turbine to operate at the same level of effectiveness regardless of whether the heat source is solar energy or fossil fuel.

The solar-related subsystems convert 49.3 percent of the incoming solar energy into usable thermal energy. The General Electric MS 7001R regenerative gas turbine, with an estimated annual thermal efficiency of 36 percent, is coupled with the solar subsystems to give an overall system efficiency of 17.8 percent.

For comparison purposes, the dashed line on Figure 8-1 represents the performance of the EPRI strawman.

The strawman comparison requires that the performance of the open-cycle, gas turbine, solar-electric system be calculated on an annual average basis. The heliostat field design methodology described in Section 3 utilized timepoints to establish the heliostat field layout and performance characteristics. The timepoint selected for heliostat field final design was solar noon on March 21. At this design timepoint, the system performance betters the 17.8 percent annual average performance shown on Figure 8-1, primarily due to improved heliostat field performance characteristics. The efficiency train at solar noon on March 21, shown on Figure 8-2, displays an overall system efficiency of 21.7 percent.

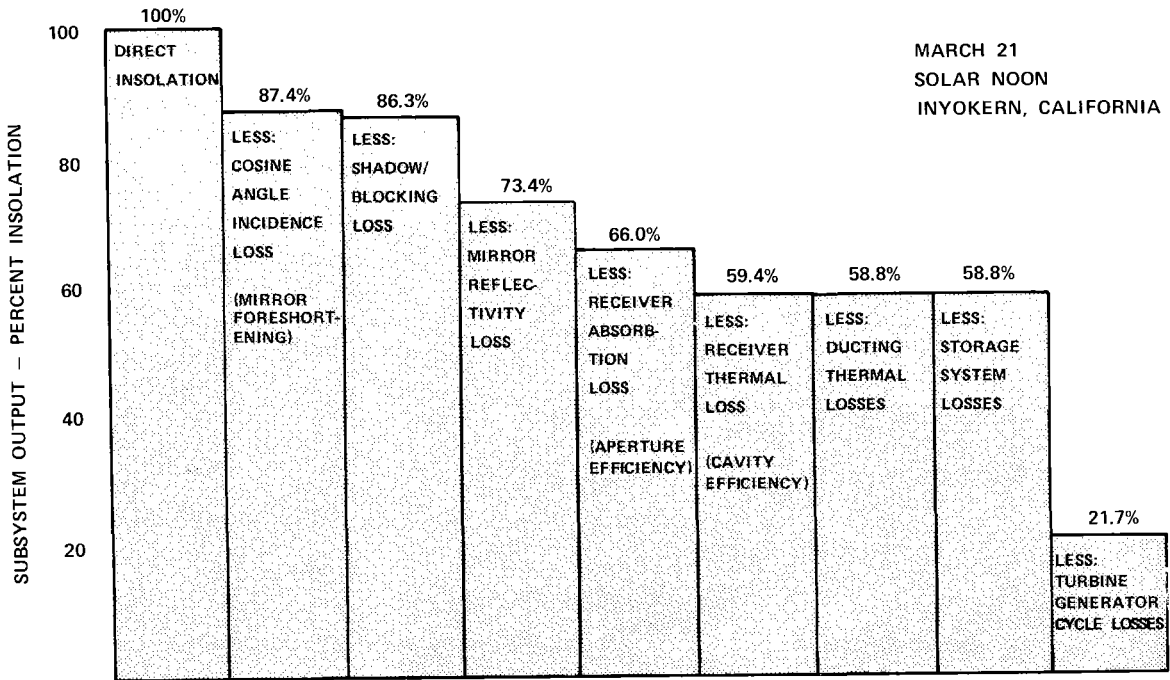


Figure 8-1. Solar-Thermal, Hybrid Open-Cycle Gas Turbine System Performance

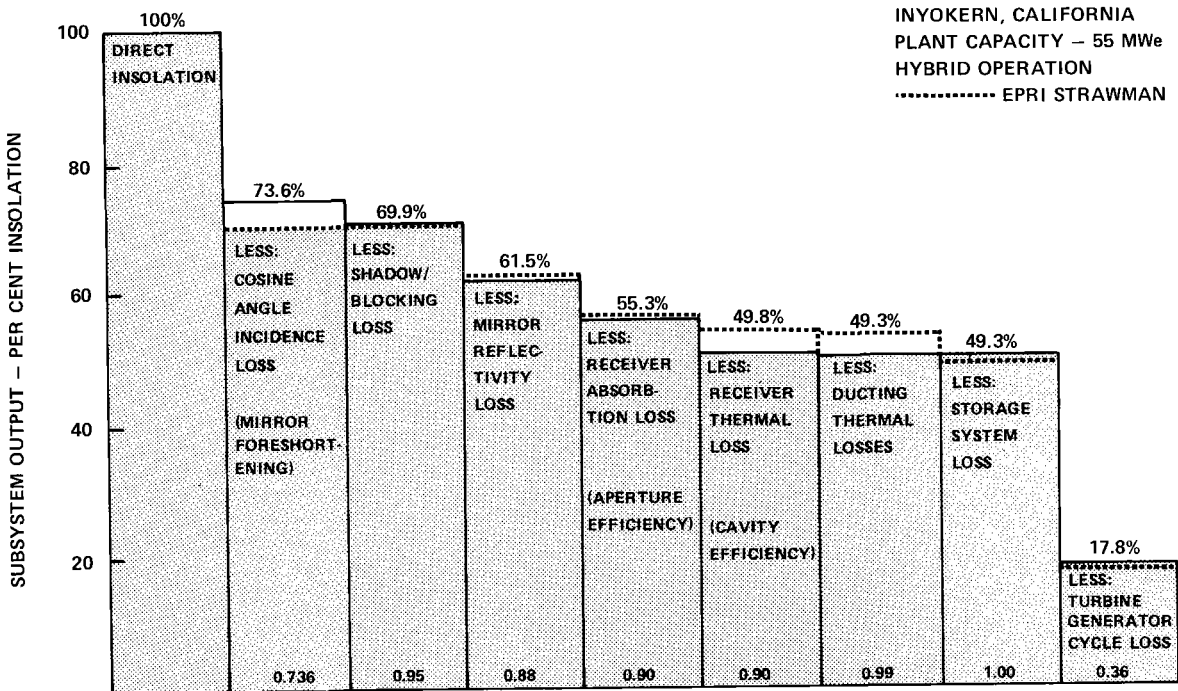


Figure 8-2. Baseline System Performance

## Section 9

### BENCH-MODEL RECEIVER

Following the successful completion of the conceptual design of a commercial-scale plant, the next logical step is to design, fabricate, and test a bench-model of the critical subsystems. The most critical subsystem is the high-temperature, cavity receiver. This section describes the design, estimated costs, and test plan for a 1-MWt bench-model receiver.

#### BENCH-MODEL RECEIVER DESIGN

In order for a bench-model to be a valid simulation of a prototype, it must be very similar with respect to the important, or critical, parameters. For the high-temperature cavity receiver, those critical parameters are as follows.

- Overall Cavity Shape--A drastic change in the basic cavity shape would lead to total incident flux patterns and cavity efficiencies which are not representative of the prototype.
- Dimensionless Tube Parameters--Since the total stress in the tubes has been shown to be a strong function of the S/D and O/D ratios, these ratios should be the same as those in the prototype. The L/D ratio of the tubes is not significant. The buckling loads, the natural frequencies, and the bending stresses of the tubes are all functions of the L/D ratio, but none in a linear manner. Further, the functional dependences are such that these parameters cannot be simultaneously duplicated in a bench-model.
- Convective-Cooling Coefficient--The tube temperatures, tube stresses, and cavity efficiency are strong functions of the magnitude of the convective-cooling coefficient.
- Gas Temperature Rise--The total incident flux pattern, the cavity efficiency, and the material stresses are all dependent upon the alternating hot and cold legs of the U-tubes around the cavity perimeter. Unless the temperature differences are as in the prototype, this simulation will be invalid.
- Pressure Drop--Proper distribution of air among the U-tubes is necessary for the receiver to function reliably. The method of control of this air distribution will be strongly influenced by the pressure drop.

With these critical parameters in mind, a preliminary analysis of a bench-model design was carried out. The results are given in the following tabulation for both a 400-kWt and a 1-MWt bench-model.

Table 9-1  
RESULTS OF BENCH-MODEL DESIGN PRELIMINARY ANALYSIS

	400 kWt	1 MWt
Cavity Radius	0.8 m (2.5 ft)	1.5 m (5.0 ft)
Cavity Diameter	1.5 m (5.0 ft)	3.0 m (10.0 ft)
Cavity Height	1.1 m (3.5 ft)	1.5 m (5.0 ft)
Tube Inside Diameter	1.3 cm (0.5 in.)	2.5 cm (1.0 in.)
Tube Spacing	3.8 cm (1.5 in.)	7.6 cm (3.0 in.)
Tube Length	2.1 m (7.0 ft)	3.0 m (10.0 ft)
Number of U-tubes	50	48
Average Gas Velocity	30 m/s (100 ft/sec)	60 m/s (200 ft/sec)
Reynolds Number	30,000	100,000
Pressure Drop	0.007 MPa (1 psi)	0.014 MPa (2 psi)
Inlet Gas Temperature	482°C (900°F)	482°C (900°F)
Outlet Gas Temperature	1038°C (1900°F)	1038°C (1900°F)
Inlet Gas Pressure	0.97 MPa (140 psia)	0.97 MPa (140 psia)
Convective-Cooling Coefficient		519 W/m <sup>2</sup> -°C (90 Btu/h-ft <sup>2</sup> -°F)

The Reynolds number for the 400-kWt bench-model is only 30,000. For the tube sizes and roughnesses with which we are dealing, this represents flow which is more nearly laminar than fully turbulent. No convective-cooling coefficient is shown because no satisfactory algorithm exists for this flow regime. Because of the Reynolds number and the small tube diameter, a bench-model below 1 MWt does not appear practical. The Reynolds number for the 1-MWt bench-model indicates, while not fully turbulent, a highly developed turbulent flow. Any significant increase in tube size would reduce the Reynolds number to an unacceptable value.

It should be clearly understood that these design results are preliminary. The actual design of the bench-model will be strongly impacted by the specifics of the test facility. Also, a great deal of iteration is necessary. For example, the

analysis indicated a convective-cooling coefficient of  $519 \text{ W/m}^2\text{-}^\circ\text{C}$  ( $90 \text{ Btu/h-ft}^2\text{-}^\circ\text{F}$ ). This is about 50 percent higher than in the prototype. This would cause the bench-model to have a higher efficiency, higher thermal stresses, and cooler material temperatures than the prototype.

## Section 10

### PROJECT CONCLUSIONS AND DEFINITION OF FUTURE DEVELOPMENT NEEDS

The major conclusions supported by the program accomplishments reported in this document are:

- The conceptual design of a commercial-size, open-cycle, gas turbine, solar-electric plant with overall conversion efficiencies of 21.7 and 17.6 percent for the design timepoint and the annual average, respectively, has been completed utilizing state-of-the-art methods and hardware. Highlights of the design include the following features.
  - A 360° heliostat field was chosen because it resulted in lower total heliostat-tower costs, lower tower height, and higher receiver efficiency. The baseline heliostat field was oval in shape, with the tower south of center and a nonuniform heliostat ground cover.
  - Four independent cavities, each facing a 90° sector of the 360° heliostat field, were chosen to constitute the central receiver because turbine/receiver interface ducting was simplified while overall efficiency and system operational flexibility was enhanced.
  - The receiver cavity/heat transfer surface was designed as a series of vertical U-tubes because of ease of erection, simple component replacement, and low operating stresses. Silicon carbide and cordierite were selected as the U-tube design and back-up materials, respectively, because of thermal and mechanical properties, resistance to thermal shock, resistance to oxidation, fabricability, commercial availability, and cost.
  - The General Electric MS 7001R gas turbine, nominally rated at 60 MWe, was selected for the conceptual baseline design. It is possible to develop a turbine/receiver conceptual interface design which enhances system operational flexibility and reliability (for both solar energy and fossil fuel operation) while minimizing the need for adaptive turbine modifications.
  - A structural steel space frame, for supporting the turbine and receiver, located atop a steel-reinforced concrete support tower, was identified as the best receiver tower design because cost was minimized and erection flexibility was enhanced.
- The validity of the analytical methodology utilized in the prediction of receiver/heat transfer performance and stress levels was experimentally verified by a series of tests. Receiver designs based on these analysis techniques can be developed with confidence.

- A concept was developed that allows hybrid turbine operation from either solar energy or fossil fuels, or a combination of both, so that power generation is not subject to fluctuation due to the intermittent and variable nature of available sunlight. This hybrid operation capability enables the solar-electric power plant to be a source of reliable power to serve peak loads and qualifies the operating utility to receive a demand capacity credit for the plant.
- The projected cost, in 1976 dollars, of the open-cycle, solar-electric system ranges from \$1250/kW to \$1660/kW, depending upon the cost of the heliostat field system (\$60-\$125/m<sup>2</sup>).

#### FUTURE DEVELOPMENT REQUIREMENTS AND RECOMMENDATIONS

There are three hardware developments which are required for the successful operation of this system concept. The required developments are;

- A high-temperature solar heat exchanger that utilizes high-temperature ceramic tubes (silicon carbide). Sufficient testing has been performed to demonstrate that existing SiC tubing can be utilized. A reliable ceramic-ceramic joint compatible with field erection practices is a major item requiring serious research effort.
- High-temperature isolation valves and internally insulated metal ducting that are capable of carrying 1038°C (1900°F) air at velocities of 38 m/s (125 ft/sec).
- External combustors for regenerative gas turbines configured so that hybrid operation is both flexible and easily controlled. This development appears to be limited to design modifications rather than serious redesign of the existing turbomachinery.

It is recommended that a timely and logical program plan be pursued toward the final objective of demonstrating a commercial-size, open-cycle, solar-electric system. The conceptual design herein constitutes the first step of such a program plan. The recommended next step in the open-cycle, solar-electric system development is the design, fabrication, and test of a 1-MWt high-temperature cavity/heat exchanger, the least conventional component of the solar-electric system.

Appendix A  
POTENTIAL CERAMIC MATERIALS  
FOR HEAT EXCHANGER APPLICATIONS

Table A-1

THERMOPHYSICAL PROPERTIES OF SELECTED REFRACTORY MATERIALS

Property	Material		Material		Material		Material		Material		Material		Material		Material		Material		Material		Material		Material		Material		Material		Material	
	SiC	Al <sub>2</sub> O <sub>3</sub>	Co <sub>3</sub> O <sub>4</sub>	Si <sub>3</sub> N <sub>4</sub>	B <sub>4</sub> C	Graphite	HfB <sub>2</sub>	ZrB <sub>2</sub>	ZrC	ZrO <sub>2</sub>	TaC	TiC	TiN	MoSi <sub>2</sub>	SiO <sub>2</sub>	Pyroceram	Mullite	Beryllium Oxide	Reference											
Density (gm/cc)	3.10	3.93	2.51	3.2	2.3	2.22	11.20	6.10	6.80	5.61	15.6	4.92	5.43	6.24	2.24	2.6	3.16	3.01												
Porosity (%)	0	2.0	0.03												0			1.00												
Maximum Working Temperature (°F x 10 <sup>2</sup> )	42	35			55	54.3				40	36.3	27	40	18				32.7												
Inert Atmosphere	30	35			25.5						18							36												
Oxidizing Atmosphere																														
Flexural Strength (psi x 10 <sup>3</sup> )	27	30	12.2	19.6	15.5	4		29	30	26	64	124	34	50	36		40	7.8												
@ 70° F	22	20		26	2.2	5	13		20	9	70	33	7.9	26	7		7.9	13												
@ 2000° F																														
Tensile Strength (psi x 10 <sup>3</sup> )		37	15.9	15.9	0.4	2.2	13		23	20	50	68		22	22		15	9												
@ 70° F		33				2.5	13		12	9	2.9	40		43	5.5		15	10												
@ 2000° F																														
Compressive Strength (psi x 10 <sup>3</sup> )	150	150	33.6	75	45	4.9	13		238	300		190	185				200	9												
@ 70° F		50				6	13			150							50													
@ 2000° F																														
Elastic Modulus (psi x 10 <sup>6</sup> )	56	57		8.0	12.46	1.65	13	37	69	25	78	45	36	58	17.2		56	7.9												
@ 70° F	54	54		8.0		1.70	13			23				40	17.8		53	8												
@ 1000° F	51	48		8.0		1.80	13			20				40			50	9												
@ 2000° F																														
Thermal Conductivity (Btu/in/hr.ft <sup>2</sup> .°F)					106	750	12			12		138	168	230	23		819	6.12												
@ 500° F mean	720	111								2.11		64	75	325	22		580	8.12												
@ 1000° F mean	465	70							240	15		44	61	187	11		190	8.12												
@ 1500° F mean	250	53							240	15		30	71	120	11		131	8.12												
@ 2000° F mean		44			86	380	11.12		240	17																				
Mean Specific Heat (70°-2000° F)	0.34	0.25		0.25	0.03	0.32	12	0.08	0.16	0.12	0.14	0.05	0.17	0.20	0.12		0.30	7.8												
70°-2000° F	1.12	0.15		0.03	12	12		9	9	9	9	9	9	9	16		15	9.12												
Coefficient Thermal Expansion (in/in°F x 10 <sup>-6</sup> )	3.6	3.85	1.6	4.1					3.2	0.7	2.2	4.1		4.33	2.0															
70° F-500° F	1.2	10	12	16					16	12	16	9.12		2.16	15															
70° F-1000° F	1.17	10	12	16					16	12	16	9.16		2.16	15															
70° F-1500° F	1.7	10	12	16					16	12	16	9.16		2.16	15															
70° F-2000° F	1.7	10	12	16	0.42				16	12	16	9.16		2.16	15															
Total Emittance	0.65	0.77	0.82			0.84	4								0.63		0.62	12												
500° F	0.70	0.62	0.73			0.85	4								0.72		0.72	12												
1000° F	0.79	0.49	0.66			0.85	4								0.55		0.60	12												
1500° F	0.86	0.46	0.62			0.85	4								0.48		0.62	15												
2000° F										0.25	5																			
Spectral Emittance	0.18	0.89								0.22	5							0.21	8											
70° F	0.71	0.33								0.41	2.5							0.21	8											
2000° F																														

A-2

Table A-1 (Cont.)  
THERMOPHYSICAL PROPERTIES OF  
SELECTED REFRACTORY MATERIALS

References

1. "'KT' Silicon Carbide," Brochure No. A-1716-A, Carborundum Company.
2. P.T.B. Shaffer, High Temperature Materials - No. 1 Materials Index, Plenum Press (1964).
3. M. E. Tyrkell, G. V. Gibbs and H. R. Shell, "Synthetic Cordierite," Bulletin 594, Bureau of Mines (1961).
4. C. D. Spears, "Some Problems in Emittance Measurements at the Higher Temperatures and Surface Characterization," Measurement of Thermal Radiation Properties of Solids, NASA-SP-31 (1963).
5. R. L. Cox, "A Technique for Measuring Thermal Radiation Properties of Translucent Materials at High Temperatures," Ibid 4.
6. W. A. Clayton, "A 500° to 4500°F Thermal Radiation Test Facility for Transparent Materials," Ibid 4.
7. J. E. Hove and W. C. Riley, Ceramics for Advanced Technologies, John Wiley & Sons (1966).
8. E. Ryshkewitch, "Beryllium Oxide Ceramics: Processes, Properties and Applications," AFML-TR-65-378 (May 1966).
9. J. R. Hague, et al., Refractory Ceramics for Aerospace: A Materials Selection Handbook, The American Ceramic Society (1964).
10. W. H. Gutzen, Alumina as a Ceramic Material, The American Ceramic Society (1970).
11. J. M. Akridge, "Thermal Conductivity of Refractory Material," Letter Report BFR-62-32, Applied Physics Lab (1962).
12. G. W. Wolf and V. L. Orne, "Thermal Properties of Solids," E9R-12073, Vought Astronautics (1959).
13. The Industrial Graphite Engineering Handbook, Union Carbide Corporation (1970).
14. Y. S. Touloukian, Editor, Thermophysical Properties of High Temperature Solid Materials - Volume 4: Oxides and Their Solutions and Mixtures - Part I: Simple Oxide Compounds and Their Mixtures, The McMillan Co.
15. L. K. Eliason and G. C. Zellner, "A Survey of High Temperature Ceramic Materials for Radomes," ML-TDR-64-296 (September 1964).
16. A. Goldsmith, T. E. Waterman, and H. J. Hirschhorn, "Thermophysical Properties of Solid Materials: Volume IV: Cermets, Intermetallics, Polymeric, and Composites," WADC-TR-58-476 (November 1960).
17. The Reactor Handbook: Volume 3: Materials, Section I General Properties, U. S. Atomic Energy Commission (February 1955).
18. Materials Handbook, Corning Glass Works (1961).

Appendix B

MEASUREMENT OF THE RADIATIVE PROPERTIES  
OF TWO MATERIALS: SILICON CARBIDE AND CORDIERITE

This appendix was authored for Black & Veatch  
by G. L. Brown of the TRW Thermophysics Laboratory.

## Appendix B

### MEASUREMENT OF THE RADIATIVE PROPERTIES OF TWO MATERIALS: SILICON CARBIDE AND CORDIERITE

#### INTRODUCTION

The spectral directional reflectance,  $\rho_\lambda$ , of a sample of silicon carbide has been measured at various angles of incidence,  $\theta$ , and three specimen temperatures. Similar data have been taken on a cordierite specimen at one, near-normal, angle of incidence and at near-room temperature (300°K). This is a part of the work requested in Georgia Institute of Technology Engineering Experiment Station Purchase Order Number 16-Q-20-100-A1757-76-61500. This work has been performed by the TRW Systems Group Thermophysics Laboratory on specimens supplied by Georgia Institute of Technology.

#### METHOD OF MEASUREMENT

Two methods have been used to determine spectral reflectance: one for measurements with the specimen at near-room temperature ( $\sim 300^\circ\text{K}$ ); the other for measurements at elevated temperatures (up to  $1370^\circ\text{K}$ ). For near-room temperature measurements at various angles of energy incidence, the Gier Dunkle Heated Cavity Reflectometer (Reference B-1) was used. For measurements at elevated temperatures and at near-normal ( $9^\circ$ ) angles of energy incidence, the TRW Paraboloid Reflectometer (Reference B-2) was used.

Both instruments use what is termed the "reciprocal" method of reflectance measurement. That is, the specimens are irradiated uniformly and hemispherically with infrared energy, and that energy which is reflected from the specimen within a narrow solid angle and at a specified angle from the specimen normal is detected. A more direct method of measurement would be to irradiate the specimen with a narrow beam of energy at a specified angle from the sample normal and collect all of the energy reflected from the specimen, regardless of the angle of reflection. To collect this reflected energy would require an integrating sphere or an optical system which collects and focuses the energy on a radiant detector. Lack of a

sphere coating which is highly reflecting and diffuse in the infrared to 26 microns precludes the use of an integrating sphere. Since the most sensitive radiant detectors are generally areally sensitive, use of a collection and focussing system would create many uncertainties.

The "reciprocal" method has been shown theoretically and experimentally to be equivalent to the direct method and is the technique used almost exclusively in the field.

#### RESULTS

The near-normal ( $15^\circ$ ), room-temperature ( $300^\circ\text{K}$ ) spectral directional reflectance of the cordierite specimen is shown in Figure B-1. Similar data for the silicon-carbide specimen is shown in Figure B-2. Figures B-3 through B-6 show reflectance data for the silicon-carbide sample at higher angles of energy incidence up to  $72^\circ$  from the sample normal.

The near-normal ( $9^\circ$ ) spectral directional reflectance of the 0.020-inch thick silicon-carbide specimen at temperatures of  $1150^\circ\text{K}$  and  $1370^\circ\text{K}$  are given in Figures B-7 and B-8. Similar data for the 0.080-inch thick silicon-carbide specimen at  $1370^\circ\text{K}$  are given in Figure B-9.

#### REFERENCES

- B-1 R. B. Dunkle, et al., "Heated Cavity Reflectometer for Angular Reflectance Measurements," Progress in International Research on Thermodynamics and Transport Properties, American Society of Mechanical Engineers, pp. 541-567 (1962).
- B-2 B. E. Newnam, E. E. Luedke, and J. T. Bevans, "High Temperature Reflectance Measurements with the Paraboloid Reflectometer," AIAA Paper 68-25, AIAA 6th Aerospace Sciences Meeting, January 1968.

Table B-1

## EMITTANCE OF CORDIERITE AND SILICON-CARBIDE SPECIMENS

TRW S/N	SAMPLE DESCRIPTION	MEASUREMENT INSTRUMENT	SAMPLE TEMPERATURE (°K)	ANGLE OF EMITTANCE $\theta$ (1)	DIRECTIONAL EMITTANCE $\epsilon_{\theta}$ (2)	HEMISPHERICAL EMITTANCE $\epsilon_H$ (3)
121-76	Cordierite (.202")	HCAR <sup>(4)</sup>	300°K	15°	0.85	0.81
122-76	Silicon Carbide (.020")	HCAR	300°K	15°	0.68	0.67
122-76	↓	↓	↓	30°	0.69	--
122-76				45°	0.69	--
122-76				60°	0.68	--
122-76				72°	0.62	--
122-76				PBR <sup>(5)</sup>	1150°K	9°
122-76	↓	↓	↓	9°	0.90	0.85
123-76				Silicon Carbide (.080")	1370°K	9°

(1) The angle of emittance corresponds to the angle at which the spectral reflectance data were taken, since  $\epsilon_{\lambda, \theta} = 1 - \rho_{\lambda, \theta}$  for opaque solids. The angle is measured from the sample normal.

(2) The directional emittance is the ratio of the energy emitted by the specimen at angle  $\theta$  and temperature,  $T_s$ , to that emitted by a black body at the same angle and temperature.

(3) Hemispherical emittance values were found using the correlations between normal and hemispherical emittance shown in Figure 13-15 of Heat and Mass Transfer by Eckert and Drake (2nd Edition, McGraw-Hill, New York, 1959).

(4) Heated Cavity Absolute Reflectometer

(5) Paraboloid Reflectometer

DIRECTIONAL SPECTRAL REFLECTANCE

ANGLES

CUSTOMER CODE NO.:

POLAR,  $\theta = 15^\circ$  from Sample Normal MEASUREMENT

Spectral Directional  
Reflectance

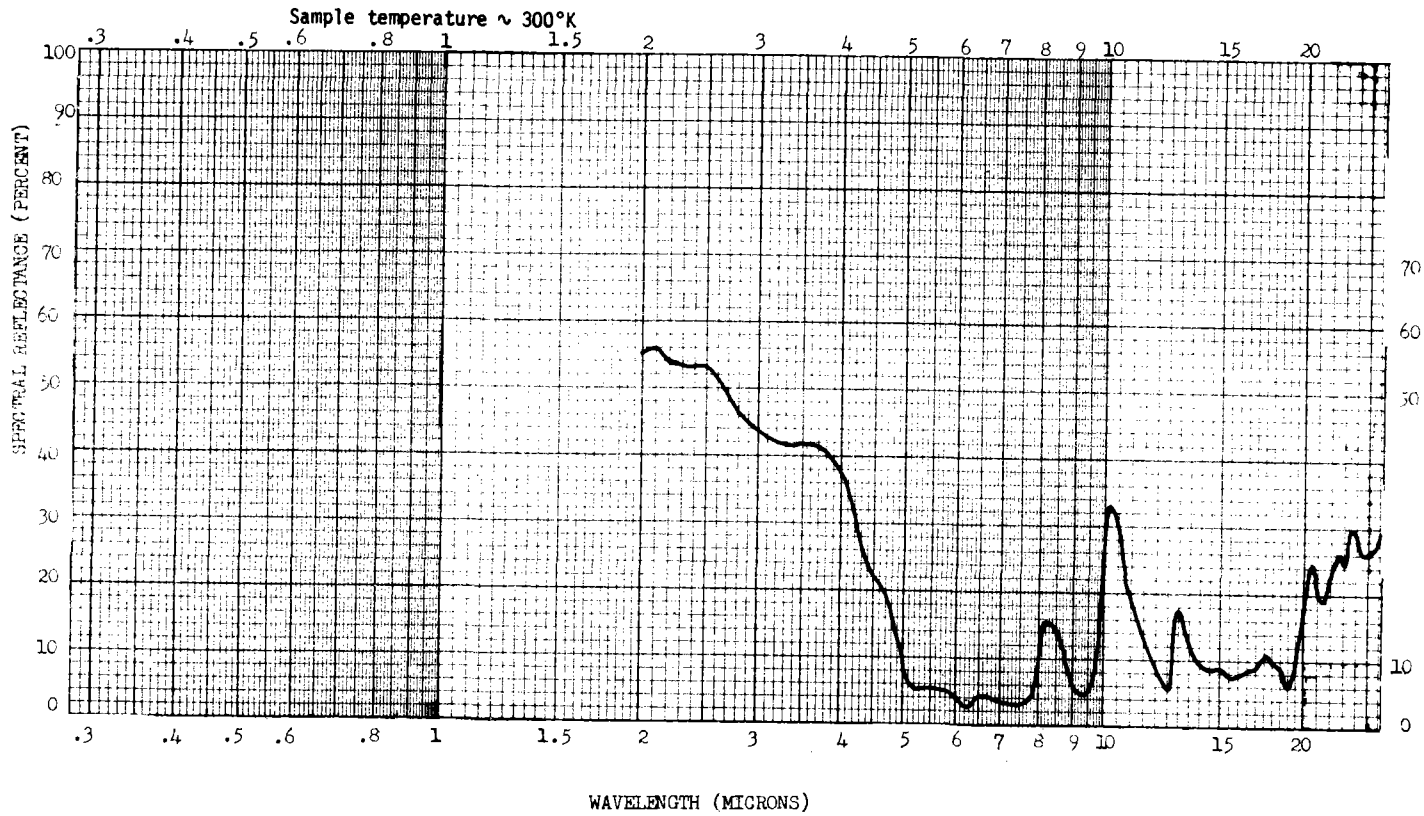
TRW DESIGNATION: S/N 121-76

AZIMUTHAL,  $\phi = \text{Arbitrary}$  INSTRUMENTS

Heater Cavity

MATERIAL: Cordierite, .020 in. thick

Reflectometer



B-5

Figure B-1. Directional Spectral Reflectance

DIRECTIONAL SPECTRAL REFLECTANCE

ANGLES

CUSTOMER CODE NO.:

POLAR,  $\theta = 15^\circ$  from Sample Normal

MEASUREMENT

Spectral Directional Reflectance

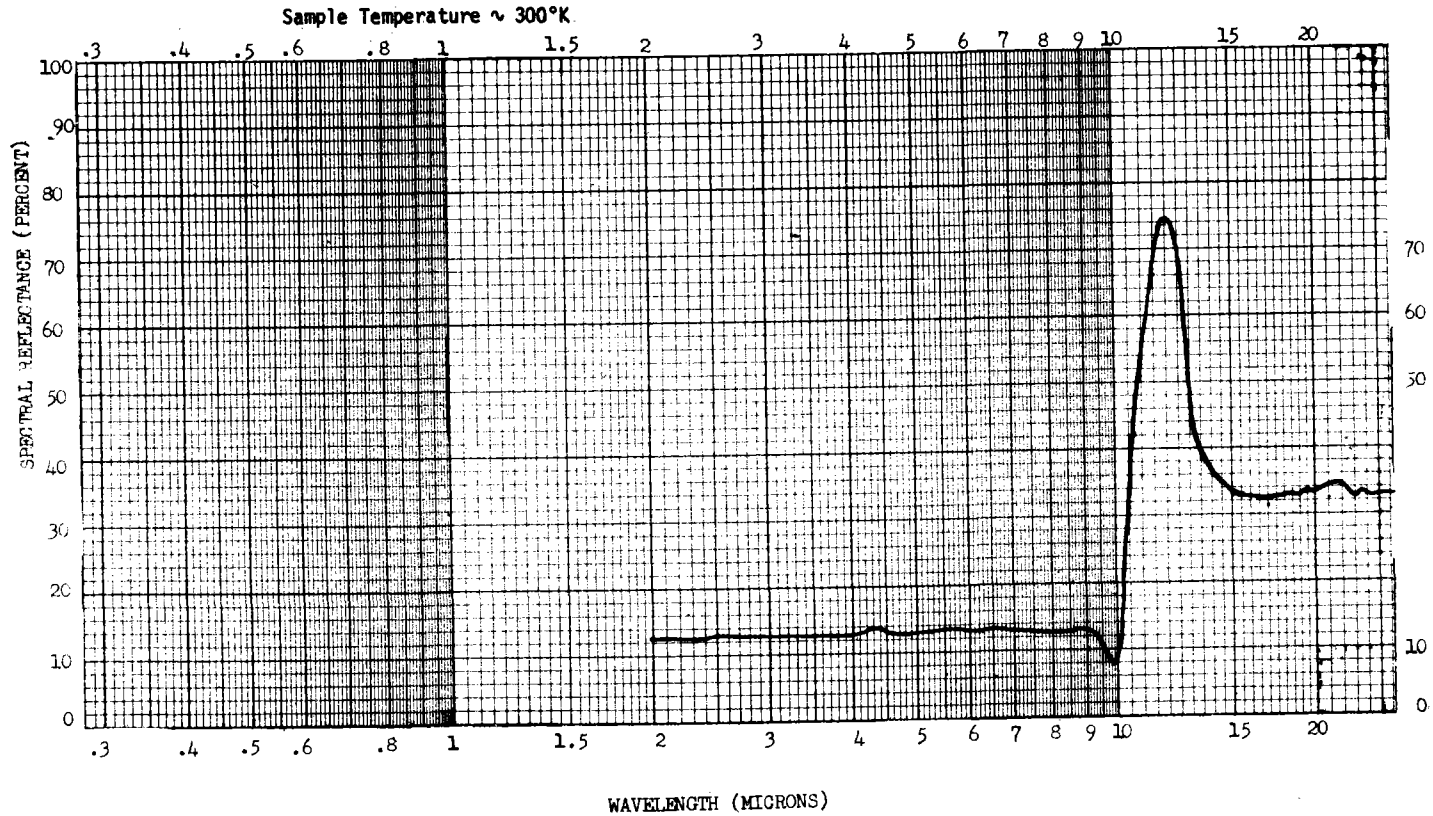
TRW DESIGNATION: S/N 122-76

AZIMUTHAL,  $\varphi = \text{Arbitrary}$

INSTRUMENTS

Heated Cavity Reflectometer

MATERIAL: Silicon Carbide, .020 in. thick



B-6

Figure B-2. Directional Spectral Reflectance

## LKAB:s Experimental Blast Furnace and Pellet Development

Hallin, Mats<sup>1</sup>  
 Hooey, Lawrence<sup>1</sup>  
 Sterneland, Jerker<sup>1</sup>  
 Thulin, Dag<sup>2</sup>

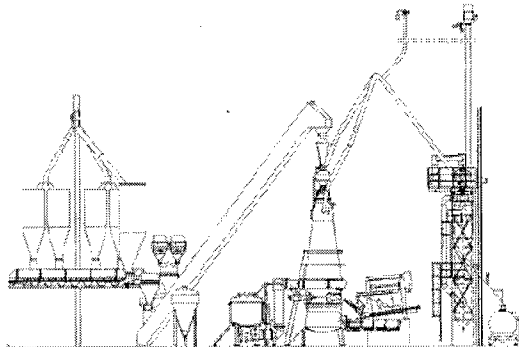
LKAB <sup>1</sup>Luleå(Sweden) <sup>2</sup>Brussels(Belgium)

LKAB:s experimental blast furnace with a hearth diameter of 1.2m and a working volume of 8.2m<sup>3</sup> produces appr. 35 tonnes of hot metal/day and, not the least, valuable information.

The furnace is used for the evaluation of burden materials and combinations as well as modified or new blast furnace operational concepts and equipments.

9 campaigns ranging from 6 to 11 weeks have been performed since the startup in 1997.

### OVERVIEW OF THE FURNACE



The furnace is equipped with systems for injecting pulverised coal, oil and other injection materials. All typical equipment required by commercial blast furnaces is included. The general specifications and working parameters are shown below:

Working volume	8.2 m <sup>3</sup>
Hearth diameter	1.2 m
Working height	5.9 m
3 Tuyeres, diameter	54 mm
Top pressure	up to 1.5bar
Injection	coal, oil, slag formers
Blast volume	up to 2000 Nm <sup>3</sup> /h
Blast heating	pebble heaters
Max. blast temp.	1300°C
Furnace crew*	5/shift
	*excluding sampling/research staff
Tapping volume	c. 1.5 t/tap
Tap time	5-15 min
Fuel rate	c. 500kg/t hot metal

Burden probes are installed at the tuyere level and in the lower and upper shaft. There is one inclined probe the bosh area. All probes are equipped with a gas collecting and temperature measuring head. The shaft probes and the inclined probe may also be used heads to collect material samples from the furnace.

At the end of a campaign the furnace is quenched by nitrogen and after cooling, excavated. Material samples from a net pattern are then retrieved for each layer. Software has been developed to show the sampling points in 3D and enable the researcher to move around in the furnace environment and select any sample to get detailed information, such as mineralogical images.

When it comes to evaluating the results from the experimental blast furnace operation, the following criteria have been found relevant:

- Permeability and its variation during operation, measured as the burden resistance  $PV_{bosh} = (Blast\ pr.^2 - Top\ pr.^2) / (Bosh\ gas\ vol.)^{1.7} \cdot const.$
- Gas utilisation and its stability,  $\eta_{CO} = CO_2 / (CO + CO_2)$ , as from top gas analysis.
- Burden descent rate and its stability, calculated from stock rod information.
- Top gas temperature and its stability.
- Stability in hot metal composition.

### LKAB BLAST FURNACE PELLETS

The LKAB olivine pellets, KPBO, was introduced nearly 20 years. Because the olivine pellets softened and melted at considerably higher temperatures than the previously used types of pellets, it was possible to reduce fuel consumption in blast furnaces operating with 100% pellets. For the first time better operating results were achieved with pellets than with sinter in terms of productivity and fuel rate.

In recent years the main focus has been to develop a pellet designed to have softening and melting properties that work well with sinter. The criteria have been stability in material decent, burden permeability and gas utilisation.

Thanks to the experimental blast furnace, LKAB has now launched a new blast furnace pellet specially designed for operation with sinter. The new product, KPBA, an acid pellet with quartzite as main additive, has been in regular use in European steel works for more than a year.

### LKAB Blast Furnace Pellets

		KPBO	KPBA
Fe	%	66.6	67.1
SiO <sub>2</sub>	%	2.05	2.3
CaO	%	0.46	0.55
MgO	%	1.55	0.52
Al <sub>2</sub> O <sub>3</sub>	%	0.22	0.22

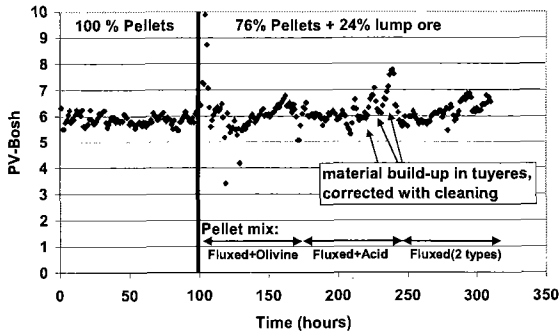
The improved operational stability experienced in the experimental blast furnace with the new pellet in a mixed burden has been confirmed in a commercial blast furnace, c f the standard deviations:

Burden: 54% sinter, 23% fluxed pellets and 23%KPBO/KPBA

	LKAB exp BF (1.2m)		Bremen No 2 BF (12m)	
	KPBO	KPBA	KPBO	KPBA
etaCO %	45.7	47.2	48.1	48.6
Std dev, etaCO %	2.9	0.7	2.4	2.1
PV bosh	6.6	6.7	6.7	6.7
Std dev, PV bosh	0.25	0.17	0.81	0.66

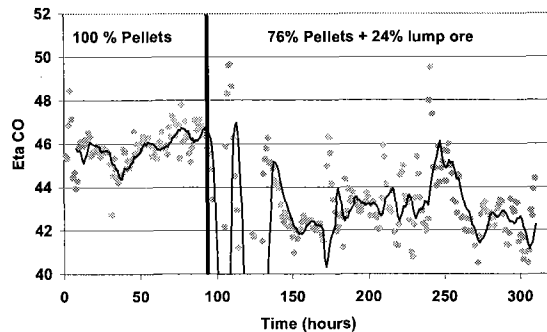
### PELLETS AND LUMP ORE

In many instances there are not necessarily any immediately visible changes despite large changes in burden mix. An example, the change in burden resistance PV-bosh with the introduction of a 24% goethitic lump ore into a 100% pellet burden, is shown below:



The trial consisted of a change from 100% LKAB olivine pellets to lump ore (c. 24%) mixed with a commercial fluxed pellet (c. 23%) and the balance being LKAB olivine, acid or experimental fluxed pellets. Despite of large differences in properties between 100% pellet operation and the mixtures pellets and lump ore, the furnace did not show a drastic change in resistance to gas flow.

However, this grade of goethitic lump ore has shown to have a pronounced effect on the blast furnace that can be related to reducibility. The figure below shows the change in gas utilisation with the introduction of lump ore into the burden:



The total fuel rate increased by over 20 kg/tonnes of hot metal due to the addition of 24% lump ore. Analyses of shaft probe samples showed correspondingly that the reduction extents of lump ore were substantially lower than pellets.

Further investigation is necessary to determine the effects on the relationships between hot metal silicon content and PV-bosh, gas utilisation or top gas temperature, for example.

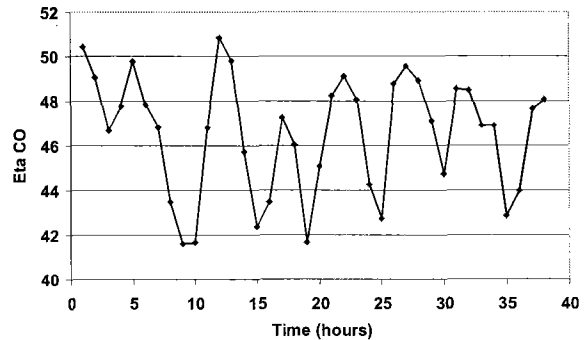
### RELIABILITY OF LABORATORY TESTS

A common laboratory scale test for evaluating the physical condition of pellets during high temperature reduction is swelling, but is the test result always reliable?

A certain experimental pellet showed extreme swelling and cracking after reduction in a blast furnace shaft, a phenomena not seen in the standard laboratory swelling test.

On the other hand, a small amount of sulphur added to the gas in the swelling test did cause the catastrophic swelling behaviour to the same pellet type. However sulphur compounds, as well as other potentially important trace components, are not included in the standard swelling test, or any standard tests, thus severely limiting the tests' reliabilities.

The behaviour of this experimental pellet type in the experimental blast furnace is shown below. The furnace went through cycles of rapid reduction, high etaCO peaks, followed by poor gas distribution and burden descent. Once the burden slipped rapid charging occurred, followed by rapid reduction and swelling and so on.



### CONCLUSIONS - PROSPECTS

The LKAB experimental blast furnace has proved to be a realistic evaluation tool to simulate the complex nature of a commercial blast furnace operation.

The know-how accumulated, and accumulating will contribute to the development of blast furnace burden materials, operational concepts and equipments.

DIRECTIONAL SPECTRAL REFLECTANCE

CUSTOMER CODE NO.:

TRW DESIGNATION: S/M 122-76

MATERIAL: Silicon Carbide, .020 in. thick

ANGLES

POLAR,  $\theta = 30^\circ$  from Sample Normal

AZIMUTHAL,  $\phi =$  Arbitrary

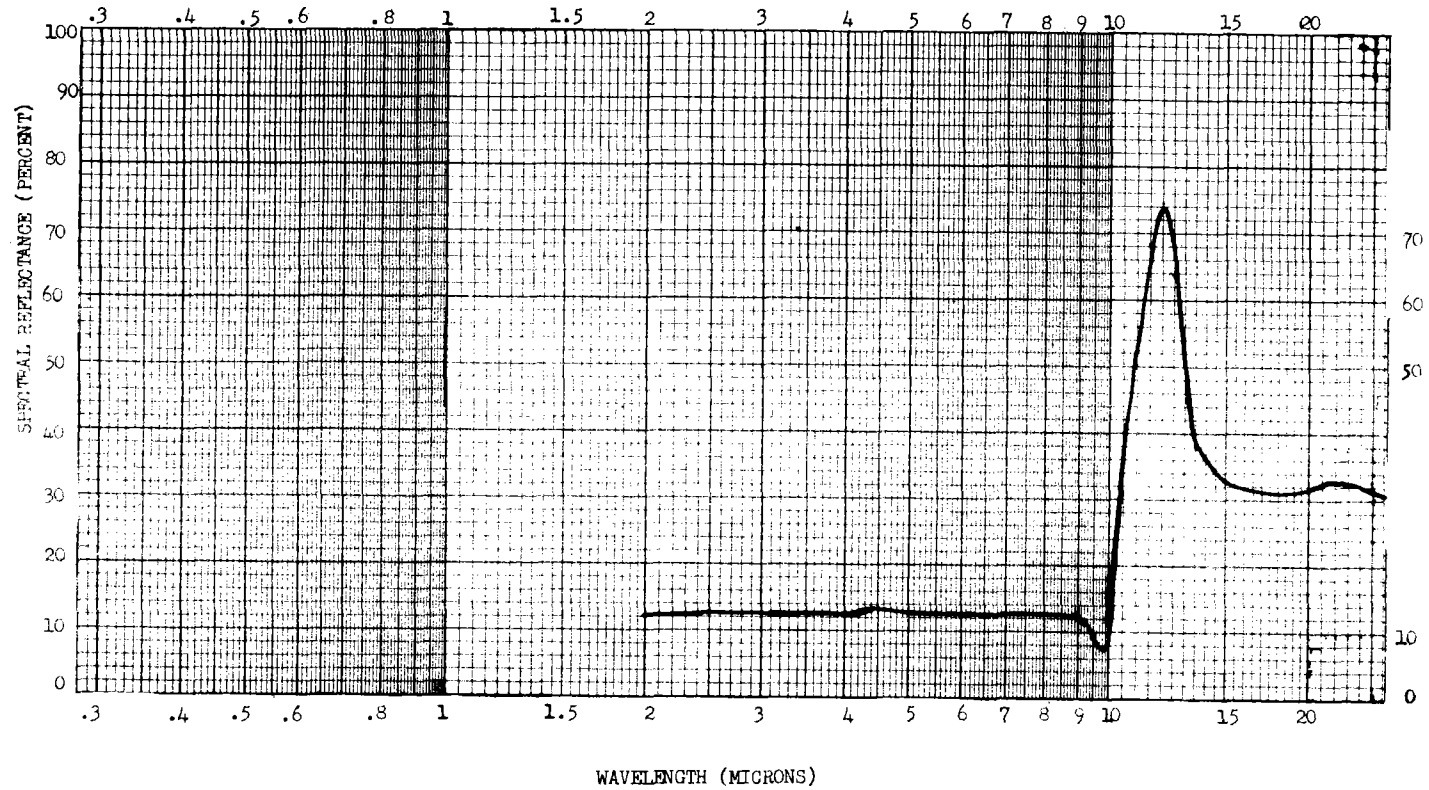
MEASUREMENT

INSTRUMENTS

Spectral Directional Reflectance

Heated Cavity Reflectometer

Sample Temperature  $\sim 300^\circ\text{K}$



B-7

Figure B-3. Directional Spectral Reflectance

DIRECTIONAL SPECTRAL REFLECTANCE

CUSTOMER CODE NO.:

TRW DESIGNATION: S/N 122-76

MATERIAL: Silicon Carbide, .020 in. thick

ANGLES

POLAR,  $\theta = 45^\circ$  from Sample Normal

AZIMUTHAL,  $\varphi =$  Arbitrary

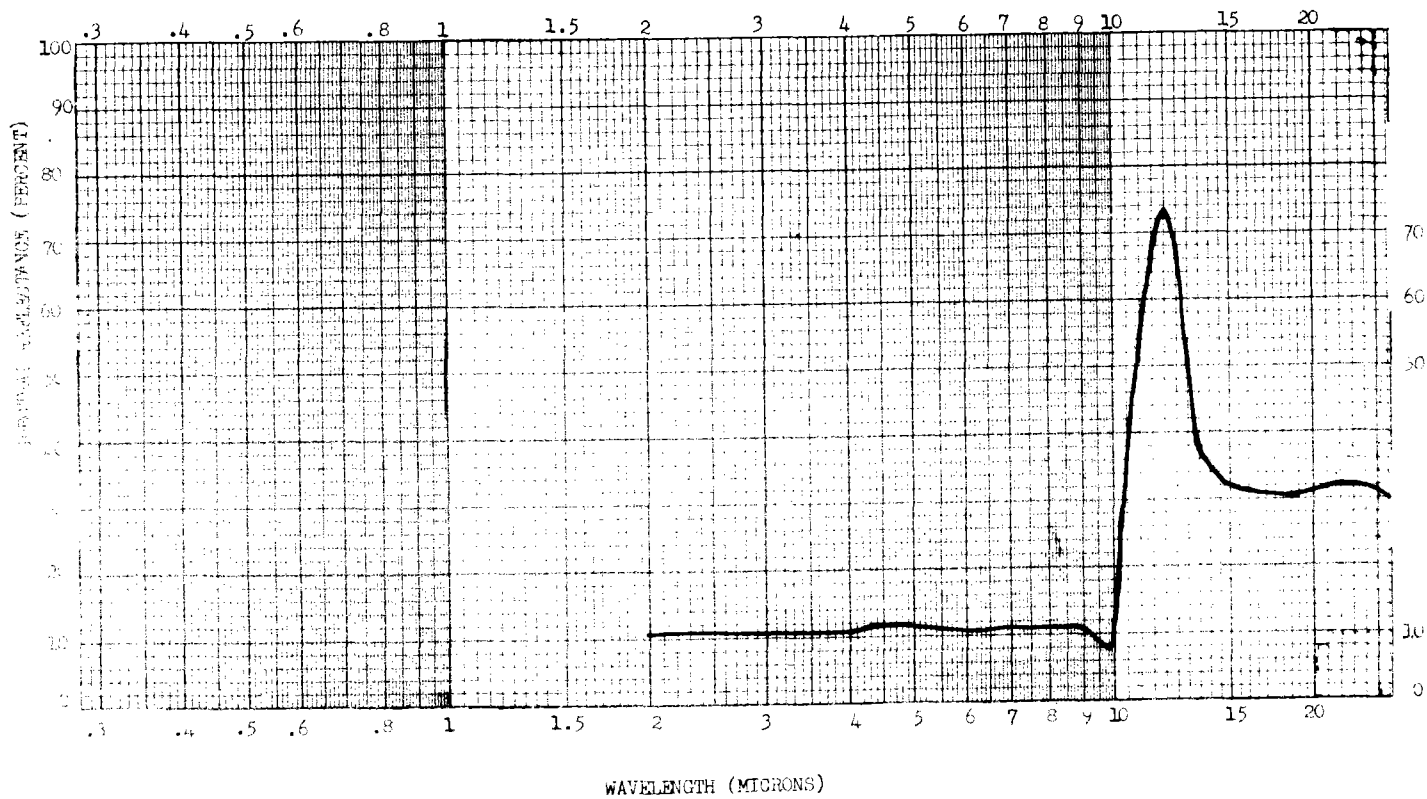
MEASUREMENT

INSTRUMENTS

Spectral Directional Reflectance

Heated Cavity Reflectometer

Sample Temperature  $\sim 300^\circ\text{K}$



B-8

Figure B-4. Directional Spectral Reflectance

DIRECTIONAL SPECTRAL REFLECTANCE

CUSTOMER CODE NO.:

TRW DESIGNATION: S/N 122-76

MATERIAL: Silicon Carbide, .020 in. thick

ANGLES

POLAR,  $\theta = 60^\circ$  from Sample Normal

AZIMUTHAL,  $\varphi =$  Arbitrary

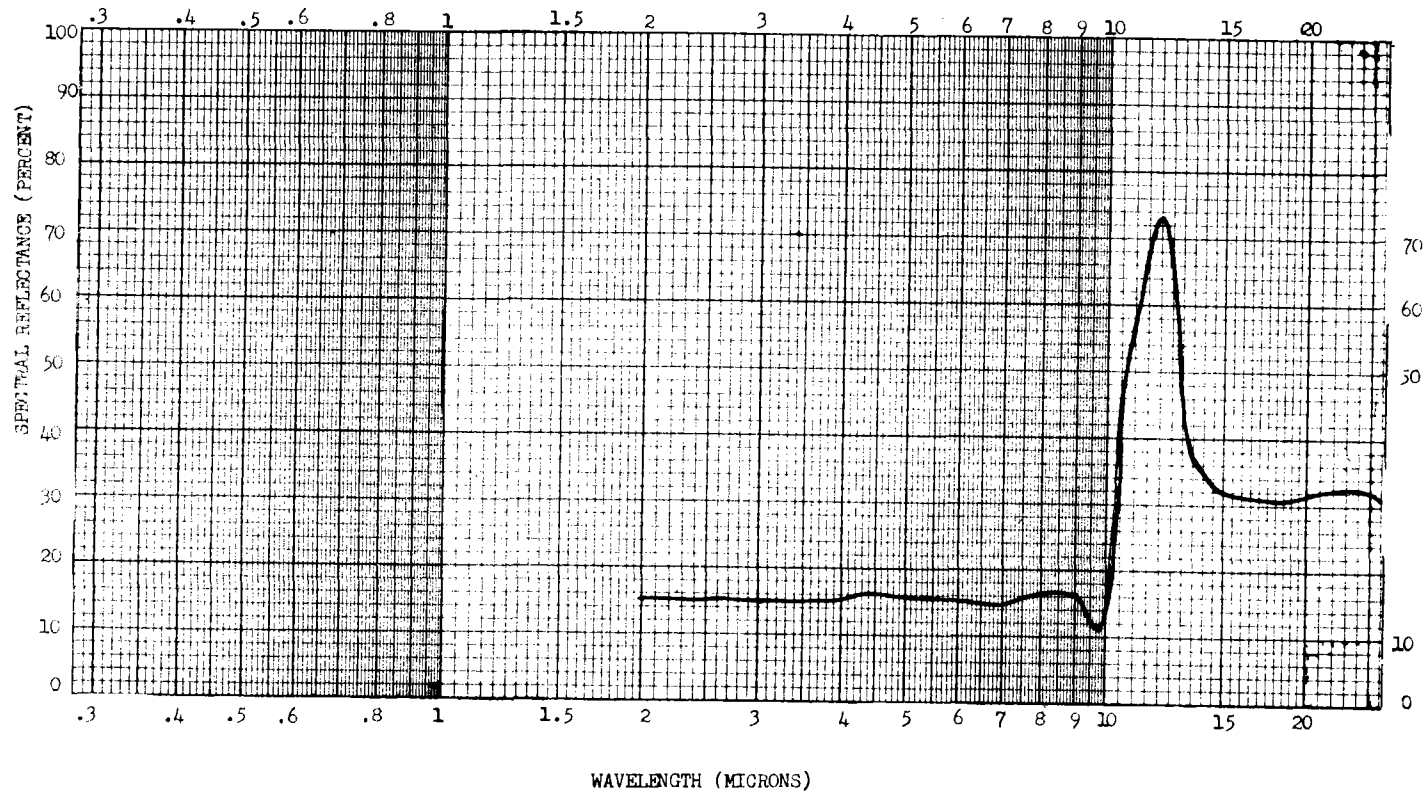
MEASUREMENT

INSTRUMENTS

Spectral Directional Reflectance

Heated Cavity Reflectometer

Sample Temperature  $\sim 300^\circ\text{K}$



B-9

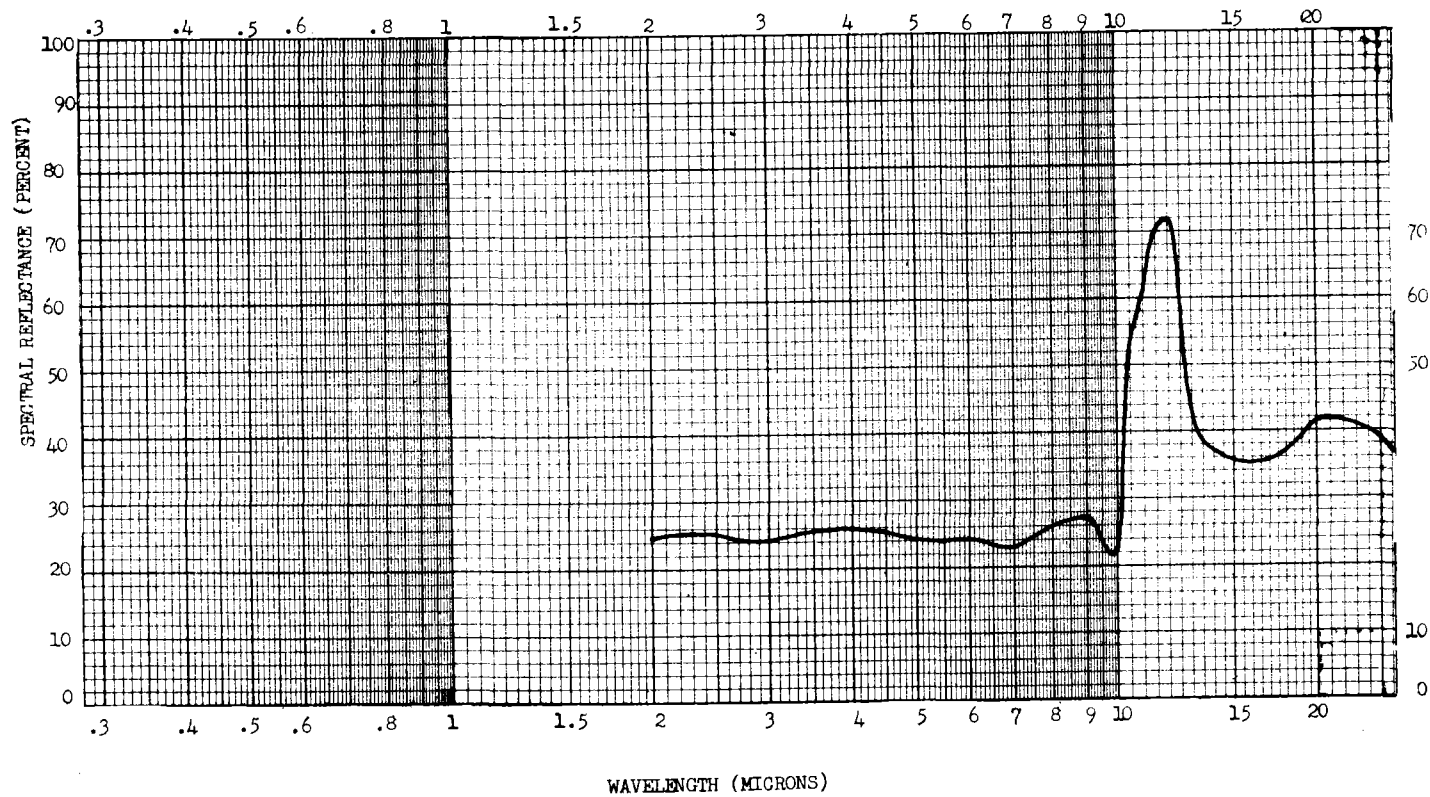
Figure B-5. Directional Spectral Reflectance

DIRECTIONAL SPECTRAL REFLECTANCE

CUSTOMER CODE NO. :  
TRW DESIGNATION: S/N 122-76  
MATERIAL: Silicon Carbide

ANGLES  
POLAR,  $\theta = 72^\circ$  from Sample Normal  
AZIMUTHAL,  $\varphi =$  Arbitrary

MEASUREMENT  
INSTRUMENTS  
Spectral Directional  
Reflectance  
Heated Cavity  
Reflectometer



B-10

Figure B-6. Directional Spectral Reflectance

DIRECTIONAL SPECTRAL REFLECTANCE

CUSTOMER CODE NO.:

TRW DESIGNATION: S/N 122-76

MATERIAL: Silicon Carbide, .020 in, thick

ANGLES

POLAR,  $\theta = 9^\circ$  from Sample Normal

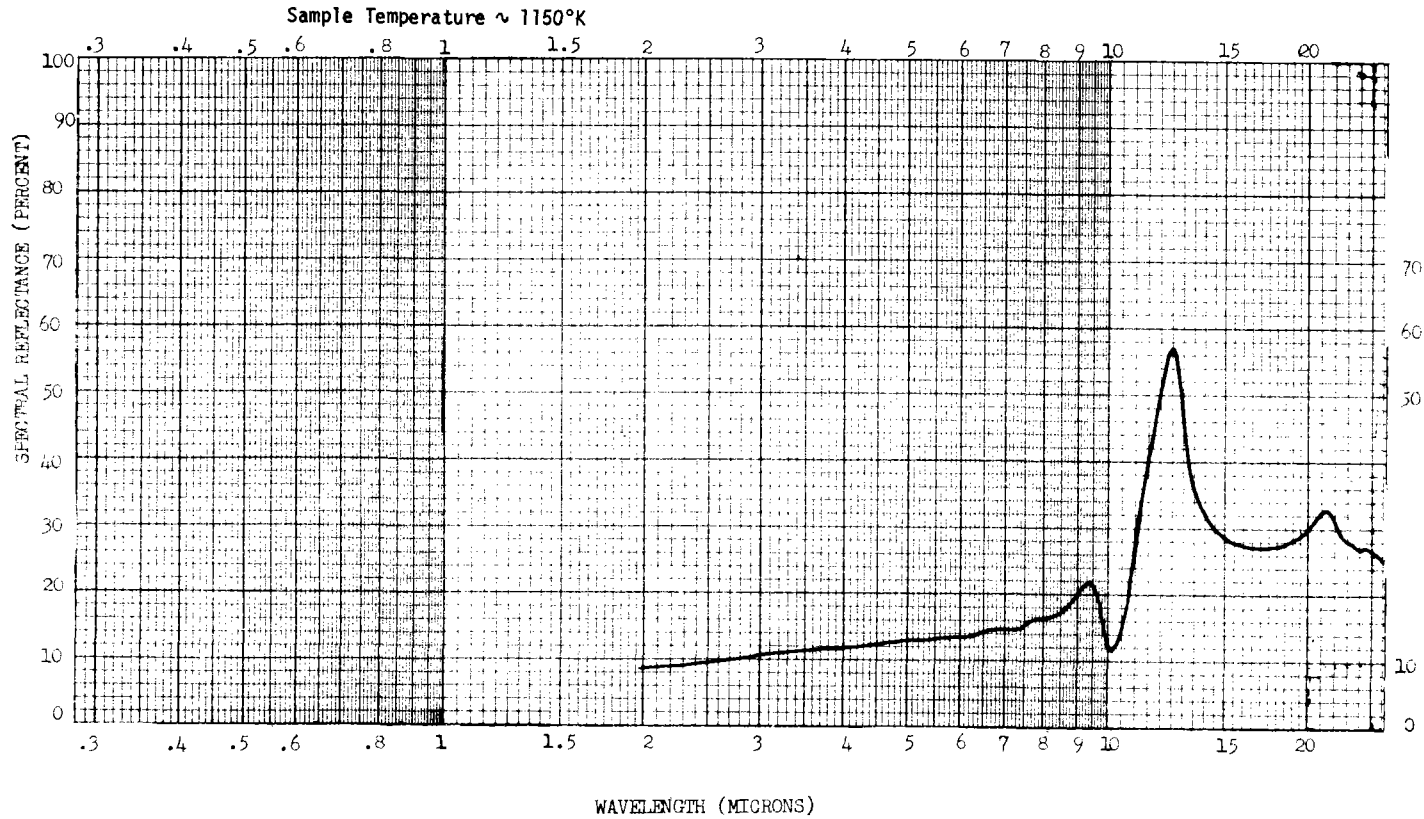
AZIMUTHAL,  $\phi =$  Arbitrary

MEASUREMENT

INSTRUMENTS

Spectral Directional Reflectance

Paraboloid Reflectometer



B-11

Figure B-7. Directional Spectral Reflectance

DIRECTIONAL SPECTRAL REFLECTANCE

CUSTOMER CODE NO.:  
TRW DESIGNATION: S/N 122-76  
MATERIAL: Silicon Carbide, .020 in. thick

ANGLES  
POLAR,  $\theta = 9^\circ$  from Sample Normal  
AZIMUTHAL,  $\phi = \text{Arbitrary}$

MEASUREMENT  
Spectral Directional Reflectance

INSTRUMENTS  
Paraboloid Reflectometer

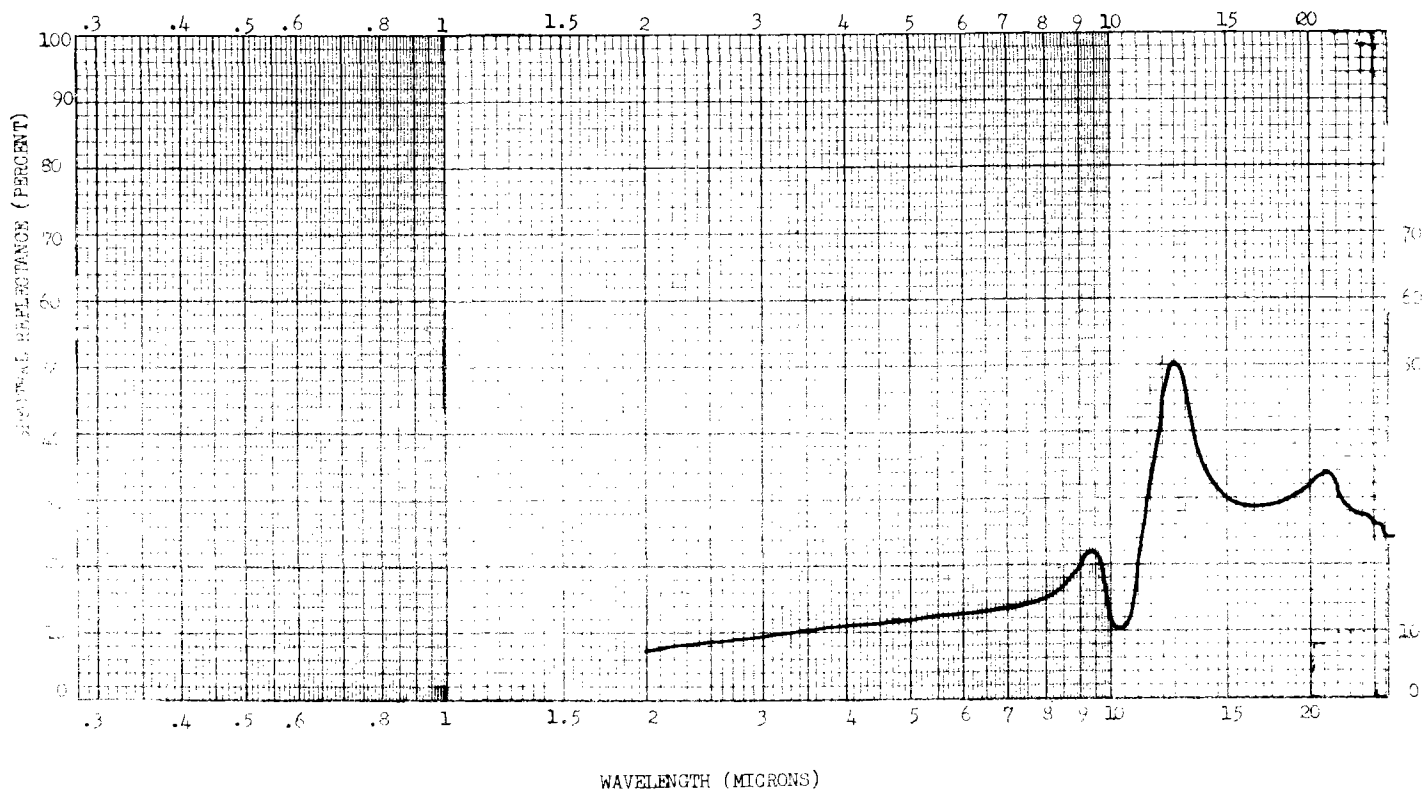


Figure B-8. Directional Spectral Reflectance

DIRECTIONAL SPECTRAL REFLECTANCE

CUSTOMER CODE NO.:

TW DESIGNATION: S/N 123-76

MATERIAL: Silicon Carbide, .080 in. thick

ANGLES

POLAR,  $\theta = 9^\circ$  from Sample Normal

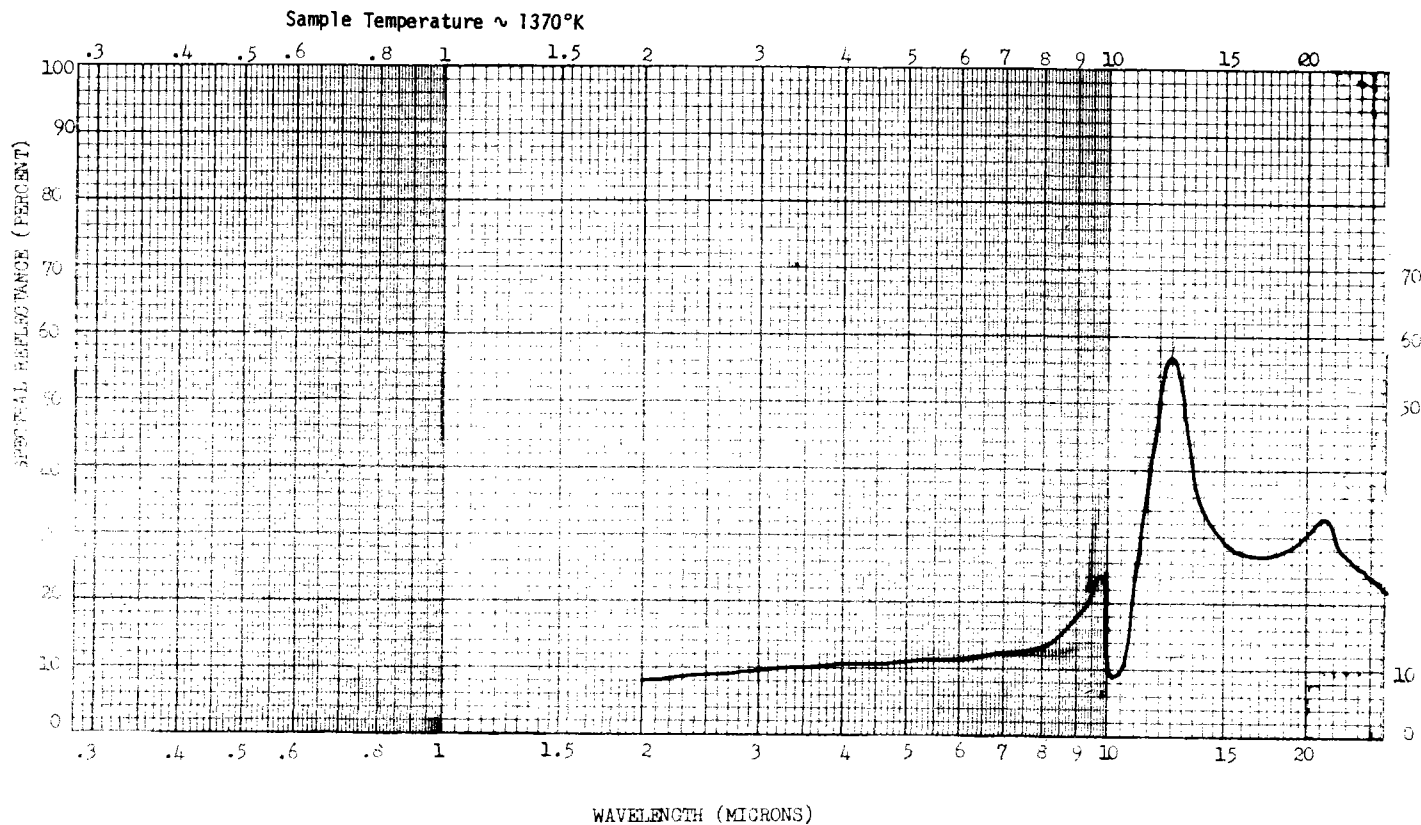
AZIMUTHAL,  $\varphi = \text{Arbitrary}$

MEASUREMENT

Spectral Directional Reflectance

INSTRUMENTS

Paraboloid Reflectometer



B-13

Figure B-9. Directional Spectral Reflectance

Appendix C

EXPERIMENTAL VALIDATION OF THE  
ANALYTICAL HEAT TRANSFER MODEL

This Appendix was authored for Black & Veatch by J. N. Harris  
of the Engineering Experiment Station, Georgia Institute of Technology.

## Appendix C

### EXPERIMENTAL VALIDATION OF THE ANALYTICAL HEAT TRANSFER MODEL

#### INTRODUCTION

To facilitate the analysis and design of the receiver/heat exchanger, a mathematical model representative of the actual physical phenomena was developed by Black & Veatch. In order to verify that the analytical model was indeed a valid representation of the actual physical phenomena, experiments using straight ceramic tube sections were designed and conducted. These tests were performed at the Engineering Experiment Station, Georgia Institute of Technology, Atlanta, Georgia.

#### EXPERIMENT SETUP

Testing was performed using tubes manufactured of the Carborundum Company's KT silicon carbide, tubes manufactured of the Coors Porcelain Company's CD-1 cordierite, and tubes manufactured of transparent fused silica.

The test apparatus consisted of a modified C-shaped bank of fused-quartz infrared lamps; three coplanar, parallel, ceramic tubes mounted side by side; and a flat fused-silica foam reflector. The three ceramic tubes were situated between the infrared lamp bank and the fused-silica foam reflector. This arrangement of tubes, reflector, and lamp bank simulated an array of parallel heat exchanger tubes, the design configuration selected for the heat exchanger baseline design (Section 4). The test apparatus is pictured in Figure C-1, minus the fused-silica foam reflector.

The bank of infrared lamps consisted of three water-cooled modules, each containing six fused-quartz infrared lamps. Each quartz lamp was rated at 1.6 kilowatts (5500 Btu/h). The three modules were arranged in a modified C-shape (semihexagon) so as to concentrate the radiant energy.

The bank of ceramic test tubes consisted of three, one-inch (outside diameter) ceramic tubes, each 16 inches in length. The tubes were placed coplanar, side by side, and parallel to each other, spaced on 2-1/2-inch centerlines. The center

tube was the tube under test; the two tubes to either side were dummy tubes, present only to provide representative radiative interchange.

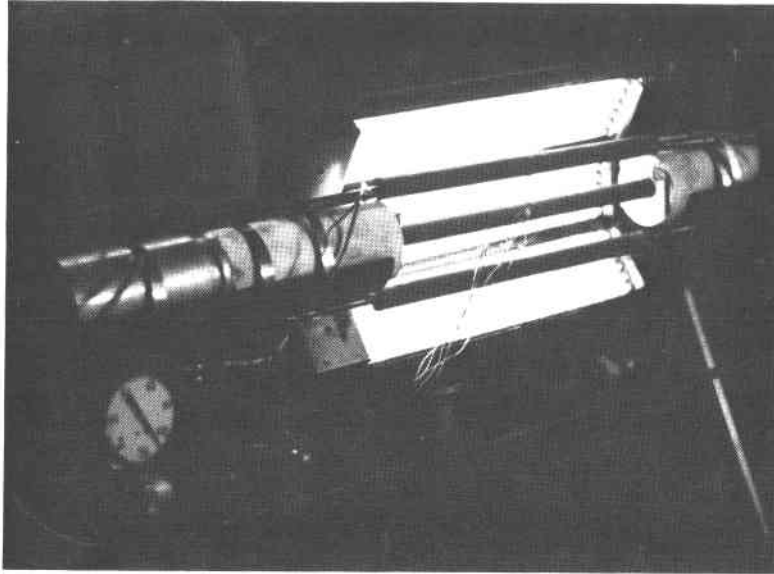


Figure C-1. Photograph of Single-Tube Test Apparatus Without Reflector in Place

The reflector consisted of a single flat sheet of fused-silica foam.

These three components were arranged such that the three ceramic tubes were situated between the infrared lamp bank and the fused-silica foam reflector. The reflector was placed parallel to the three tubes, 1-3/4 inches from the tubes' centerlines. The lamp bank was situated such that the distance from the centerline of the middle tube to the front surface of the quartz lamp bank was 3 inches. The distance from the centerlines of the dummy tubes to the lamp bank was 2-1/2 inches.

#### TEST PROCEDURE

The center ceramic tube contained a flow of preheated, compressed air. The two side tubes or dummy tubes were only present to provide the proper radiative interchange of energy. These tubes contained flows of ambient air sufficient to cool their surface temperature to be nominally equal to the surface temperature of the center

tube. The three tubes were irradiated by the infrared lamp bank, inducing thermal stresses at levels expected for the heat exchanger baseline design. Flux incident onto the center tube was nominally  $200 \text{ kW/m}^2$  ( $6.34 \times 10^4 \text{ Btu/h-ft}^2$ ). The flow diagram for the test apparatus is shown in Figure C-2.

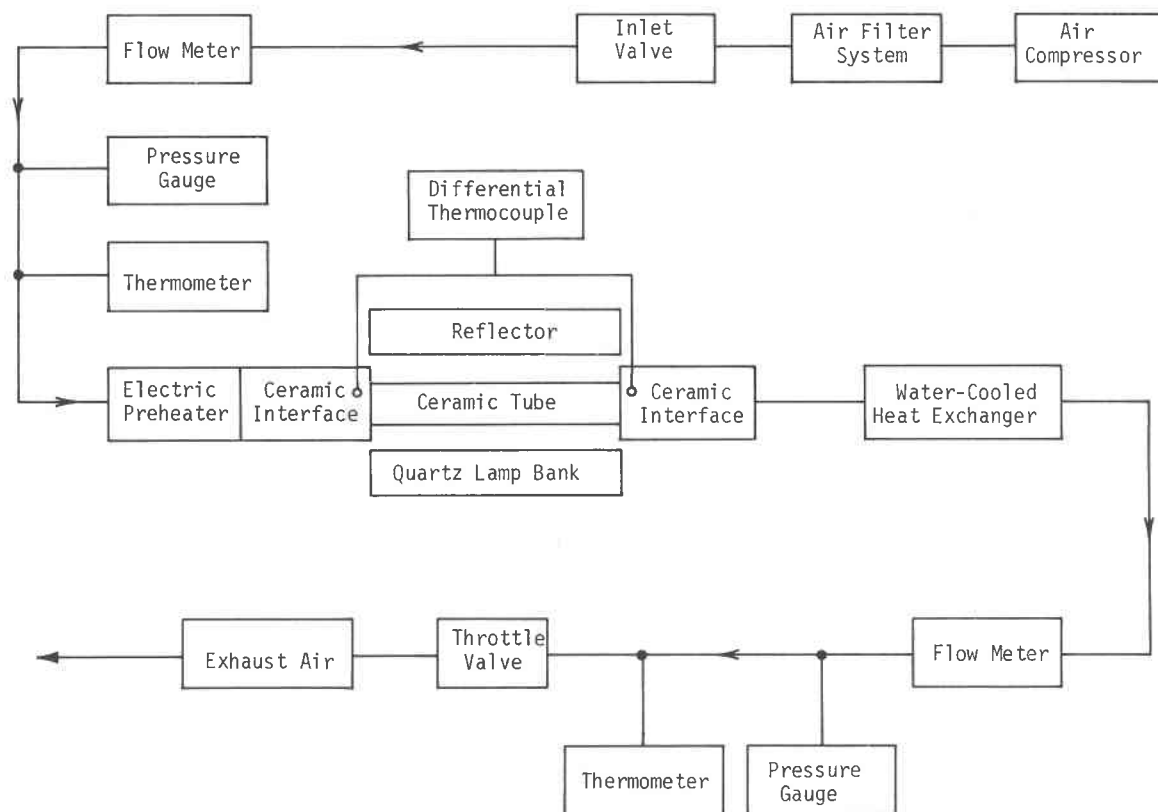


Figure C-2. Flow Diagram for Single-Tube Test Apparatus

Inlet air to the center tube was filtered and supplied to the test apparatus at an operating pressure of 160 psig. Two conventional gate valves, one at the inlet to the test apparatus and one at the exhaust, regulated pressure and flow rate through the center ceramic test tube.

The temperature of the inlet air was controlled by an electric preheater. The electric preheater had a maximum (nominal) power level of 5.4 kW ( $1.84 \times 10^4 \text{ Btu/h}$ ) and was manually controlled by a variable auto-transformer. The preheater also served as the interface between the test apparatus and the center ceramic test tube. The electric preheater is shown in cross section in Figure C-3.

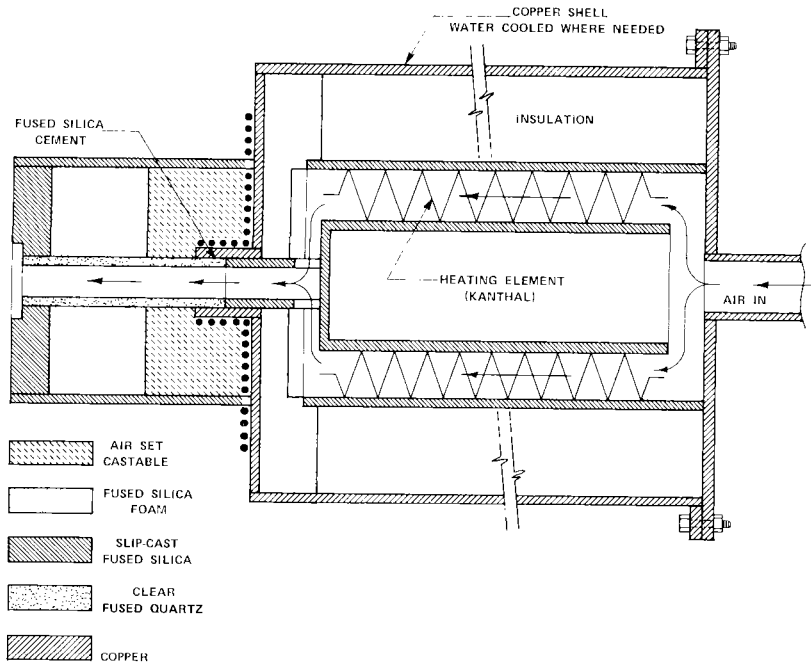


Figure C-3. Electric Preheater-Ceramic Interface

At the exhaust end of the ceramic test tube, the tube was supported by an "output interface," shown in cross section in Figure C-4. The joints between the preheater and the ceramic tube and between the ceramic tube and the output interface (exhaust end support) were butt joints. A force exerted by a pneumatic cylinder on the output interface and transferred to the center ceramic tube was sufficient to seal the two butt joints. The output interface was free to slide in its support cradle while transmitting the pneumatic cylinder's force to the ceramic tube. In this way, the center ceramic tube was free to elongate due to thermal expansion while the seals at the two butt joints were maintained.

Heated air exiting the ceramic tube was passed through an exhaust cooler, a water-cooled heat exchanger. The exhaust cooler was a modified Heatron Capacity Booster, originally designed to transfer heat from the suction line to the liquid line in a refrigeration system.

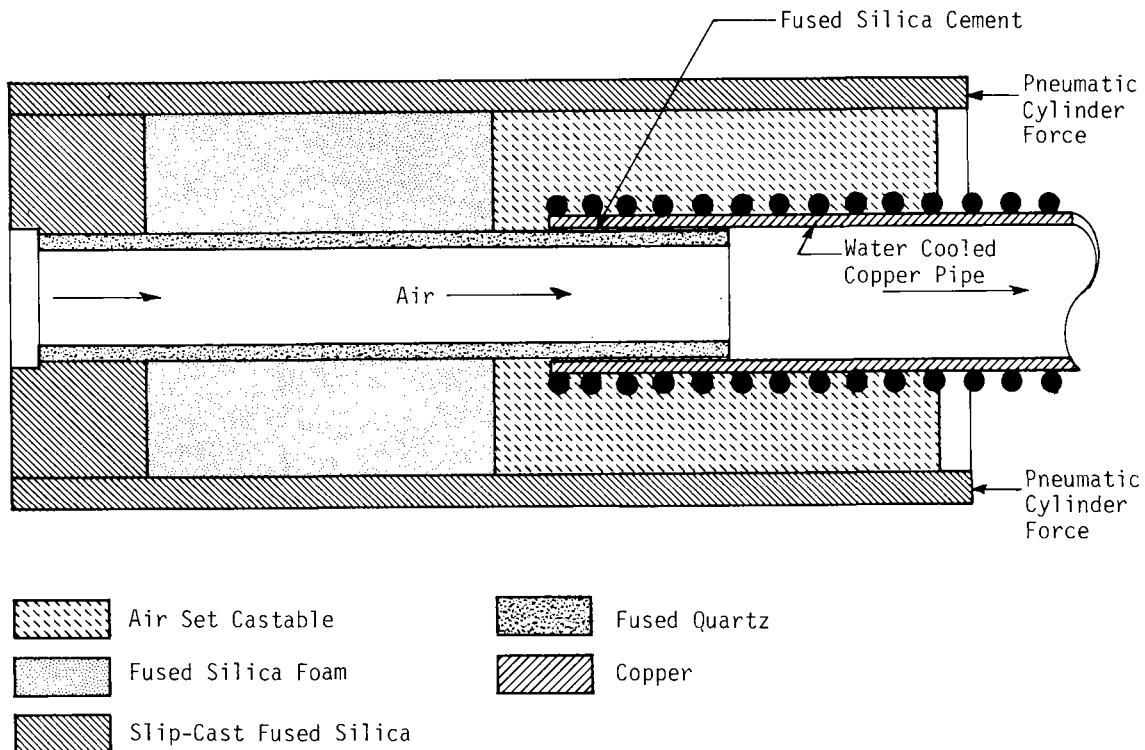


Figure C-4. Output Interface

#### DATA ACQUISITION

The temperature of the compressed air was monitored at the inlet and the outlet of the center ceramic tube, as were the airflow rate and pressure. Temperature measurements were made using thermocouples. Flow measurements were made using tapered-tube float-type Brooks Rotameters.

Surface temperatures of the ceramic tubes were measured using thermocouples and an infrared pyrometer. Five thermocouples were attached to the surface of the center tube circumferentially around the tube's midpoint. One thermocouple was attached to the surface of one of the dummy tubes at the tube's midpoint. A Barnes IT-7 infrared pyrometer was aimed at the surface of the center tube at the tube's midpoint and was filtered to exclude radiant energy coming directly from the fused-quartz lamps or energy reflected by the ceramic tubes or by the fused-silica foam reflector. The radial location of the six thermocouples located at the midpoint of the respective tubes and the position of the aimpoint of the infrared pyrometer are indicated in Figure C-5.

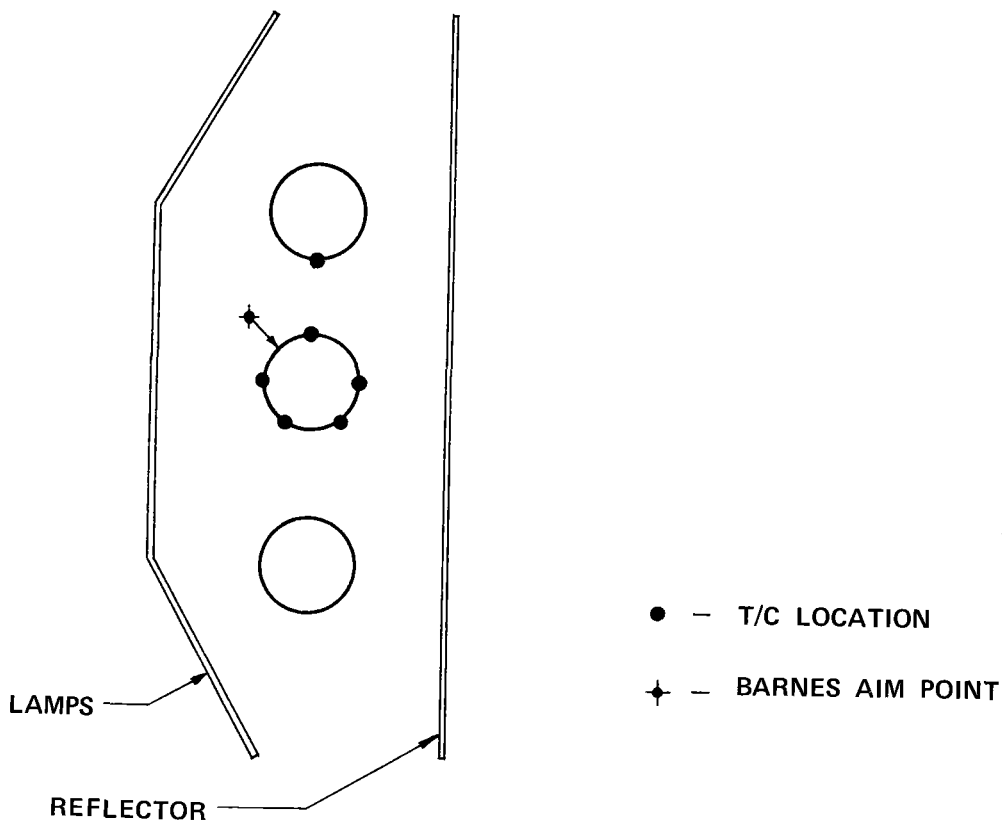


Figure C-5. Diagram of Tube Surface Thermocouple (T/C) Locations

The flux level of the fused-quartz lamp bank was determined using a Hy Cal Asymptotic Calorimeter (Model C-1300-A-60-072, Serial No. 48425). The flux was measured at various positions and distances from the lamp bank. Positions where flux measurements were taken are indicated in Figure C-6.

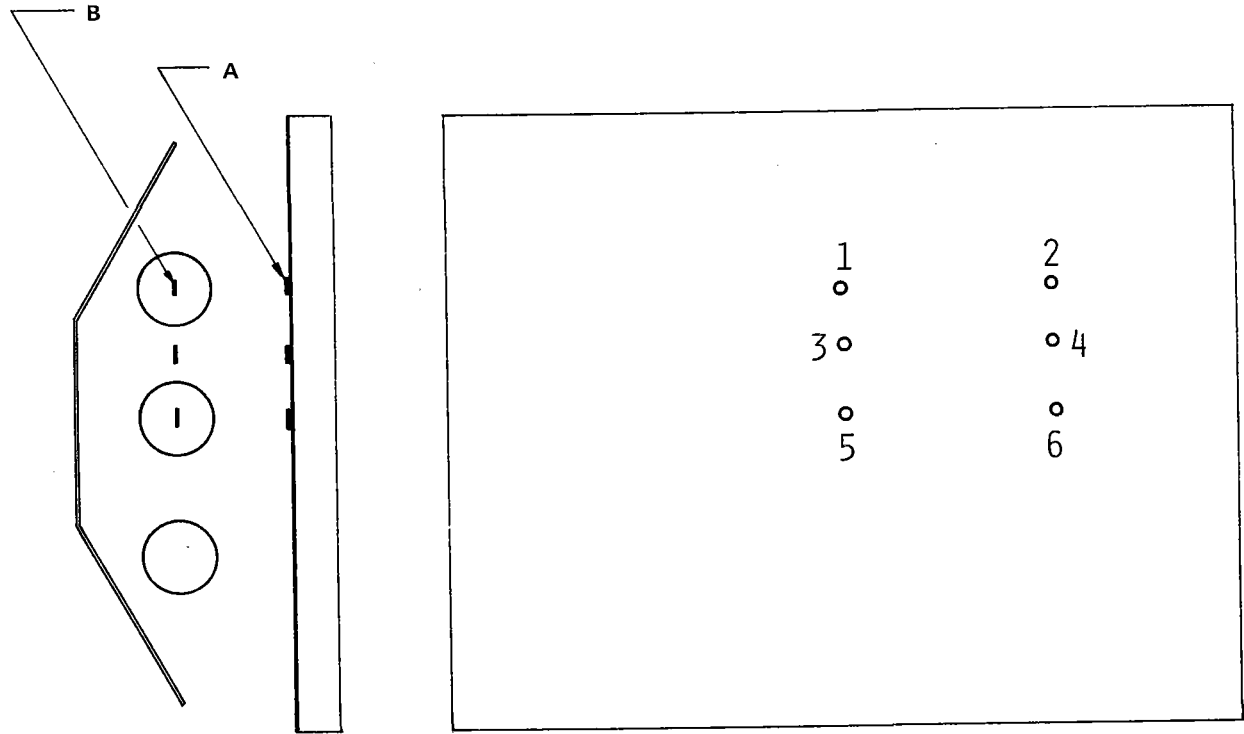
#### TEST RESULTS

Tests were performed using ceramic tubes made of silicon carbide, tubes made of cordierite, and tubes made of fused silica.

#### Flux Level Measurements

Prior to testing, the flux levels achieved by the infrared lamp bank at the tube surfaces and at the reflector surface were mapped under conditions simulating expected, actual conditions as closely as possible. Data was obtained using a Hy Cal Engineering Model C-1300-A-160-072 Asymptotic water-cooled calorimeter.

### CALORIMETER POSITIONS



○, | — SENSOR

A = SENSOR SURFACE FLUSH WITH INSIDE SURFACE OF REFLECTOR, ALL TUBES IN PLACE

B = SENSOR SURFACE APPROXIMATELY AS SHOWN, TOP TUBE REMOVED FOR POSITIONS 1 AND 2, CENTER TUBE REMOVED FOR POSITIONS 5 AND 6.

Figure C-6. Diagram of Heat Flux Sensor Locations

All flux measurements were made with the fused-silica foam reflector in place. To provide electrical and water cooling leads for the calorimeter, one-inch diameter holes were drilled in the fused-silica foam reflector at the positions shown in Figure C-6. All positions except the one in use for the calorimeter were closed with fused-silica plugs during actual flux measurements. The sensor portion of the calorimeter, for each test position, was located as shown in Figure C-6.

Heat flux measurements were made at the six reflector positions with the fused-quartz infrared lamps operating at 280 volts and with air (800°F, ambient pressure) flowing at 12 cfm (input to the preheater) through the center ceramic tube. Ambient air was flowing through the dummy tubes at a rate to bring the surface temperatures of the dummy tubes nominally to the same value as that of the center tube. Flux measurements at the upper dummy tube (Positions 1B, 2B - Figure C-6) and at the middle tube (Positions 5B, 6B - Figure C-6) were made with those respective tubes removed. Flux measurements at points between the two tubes were made with the ceramic tubes in position and with air flowing through them. The energy flux data obtained is summarized in Table C-1.

Table C-1  
MEASURED FLUX LEVELS

CALORIMETER POSITION	FLUX LEVEL	
	$\text{kW/m}^2$	(Btu/h-ft <sup>2</sup> )
1A	145	(46,000)
2A	124	(39,300)
3A	136	(43,100)
4A	118	(37,400)
5A	134	(42,500)
6A	110	(34,900)
1B	232	(73,500)
2B	196	(62,100)
3B	191	(60,500)
4B	110	(34,900)
5B	211	(66,900)
6B	171	(54,200)

### Silicon-Carbide Tube Tests

Data was obtained under many different inlet air conditions with silicon-carbide tubes installed in the facility. Initially, the dummy tubes were not cooled. However, due to concern that the dummy tubes would become hotter than and radiate excessive energy to the tube under test, it was decided to cool the dummy tubes. These tubes were cooled, with unrestricted ambient air, to a surface temperature nominally equal to the surface temperature of the center tube. The fused-quartz infrared lamps were operated at 280 volts and the fused-silica foam reflector was in position. The data obtained from tests with silicon carbide are listed in Table C-2. Flow rates are given in actual cfm at the specified pressures and 23°C (74°F).

As noted in Table C-2, five data points are for a different silicon-carbide tube than the rest of the data. The original tube was broken during installation of a new thermocouple. This tube replacement afforded the opportunity to compare two similar tubes and check repeatability of the data.

### Cordierite Tube Tests

Cordierite tubes were installed and tested in the same manner as the silicon-carbide tubes. In all tests, the lamps were operated at 280 volts and the dummy tubes were air-cooled. The data obtained from tests with cordierite tubes are summarized in Table C-3. Flow rates are given in actual cfm at the specified pressures and 23°C (74°F).

### Fused-Silica Tube Tests

A clear fused-silica tube was coated on the inside with a homogeneous dark gray coating composed of a 4 weight percent (w/o) nickel oxide, 65 w/o fused-silica slip, 13 w/o Ludox AS colloidal silica and 18 w/o fused silica (325-mesh). The coating was dried and fired onto the tube by heating it to 730°C (1350°F). The tube was installed and tested under the same conditions as the cordierite tubes with the following differences. Because of the difficulty in attaching thermocouples to the tube surface, surface temperature of the fused-silica tube was monitored with a Barnes IT-7 pyrometer only. Silicon-carbide tubes were used for dummy tubes, and their surface temperatures were held as close as possible to the surface temperatures obtained under similar conditions during the silicon-carbide tube tests. The data obtained from tests with the fused-silica tube are tabulated in Table C-4. Flow rates are given in actual cfm at the specified pressures and 23°C (74°F).

Table C-2

## HEAT TRANSFER DATA FOR SILICON-CARBIDE TUBE

PRESSURE IN TUBE (psig)	PREHEATER OUTPUT (F)	AIR FLOW (cfm)	TUBE SURFACE TEMPERATURE (F)							TEMPERATURE RISE ACROSS TUBE (F)	NOTES*
			BARNES IR PYROMETER	T/C							
				1	5	10	15	20	8		
100	1,500	3	--	1,783	1,794	1,703	1,737	1,703	1,681	70	1
100	520	12.3	1,250	1,576	1,426	1,389	1,381	1,487	--	240	
60	500	19.7	1,300	1,490	1,340	1,312	1,303	1,402	--	254	
60	500	19	1,475	--	--	--	--	--	--	262	
60	500	18	1,250	1,525	1,350	1,318	1,307	1,415	1,591	240	1
60	500	12	1,375	1,615	1,560	1,460	1,415	1,505	1,590	250	1, 2
60	500	8	1,450	1,660	1,590	1,525	1,460	1,525	1,590	275	1, 2
30	500	19	1,600	--	--	--	--	--	--	337	
30	500	19	1,375	1,615	1,545	1,460	1,385	1,460	1,615	240	1, 2
30	500	18.7	1,450	1,616	1,514	1,481	1,472	1,569	--	331	
15	500	19	1,725	--	--	--	--	--	--	394	
15	500	19	1,425	1,545	1,615	1,540	1,445	1,505	1,635	274	1, 2
15	500	18.7	1,550	1,701	1,634	1,591	1,580	1,678	--	391	
0	500	45	1,650	--	--	--	--	--	--	338	
0	500	21	1,810	1,760	1,715	1,672	1,625	1,751	--	427	
0	500	21	1,550	1,710	1,658	1,590	1,480	1,525	1,620	330	1, 2

\* Notes:

(1) Dummy tubes air cooled.

(2) Different SiC tube under test.

Table C-3

## HEAT TRANSFER DATA FOR CORDIERITE TUBE

PRESSURE IN TUBE (psig)	PREHEATER OUTPUT (F)	AIR FLOW (cfm)	TUBE SURFACE TEMPERATURE (F)							TEMPERATURE RISE ACROSS TUBE (F)
			BARNES IR PYROMETER	T/C						
				1	5	10	15	20	8	
100	480	8.0	1,000	1,276	1,201	1,179	1,254	1,426	1,244	124
100	500	3.6	1,150	1,437	1,361	1,361	1,405	1,514	1,276	242
60	425	18	1,000	1,329	1,318	1,148	1,222	1,372	1,297	115
60	500	12	1,100	1,437	1,361	1,244	1,308	1,481	1,351	242
60	500	8.3	1,150	1,503	1,448	1,329	1,372	1,525	1,308	176
30	500	18	1,150	1,437	1,394	1,286	1,340	1,459	1,415	153
15	500	18	1,350	1,536	1,536	1,394	1,426	1,503	1,525	202
0	500	17	1,500	1,658	1,647	1,818	1,525	1,636	1,580	265
30	800	8.1	1,625	1,681	1,626	1,481	1,525	1,681	1,569	185
15	800	8.0	1,650	1,715	1,681	1,525	1,558	1,715	1,591	244
0	800	7.9	1,750	1,760	1,715	1,569	1,591	1,738	1,591	306

Table C-4  
HEAT TRANSFER DATA FOR FUSED-SILICA TUBE

PRESSURE IN TUBE (psig)	PREHEATER OUTPUT (F)	FLOW (cfm)	SURFACE TEMPERATURE BARNES I.R. PYROMETER (F)	TEMPERATURE RISE ACROSS TUBE (F)
100	500	7.4	1,200	287
100	500	3.3	1,375	449
60	420	18	1,125	218
60	500	12	1,125	240
60	500	7.8	1,150	285
30	490	18	1,200	286
15	490	18	1,300	327
0	500	18	1,475	385

#### ANALYTICAL MODEL VALIDATION

Validation of the analytical model was achieved by inputting various measured test data to the analytical model and comparing the resulting calculated values (circumferential temperature variation and the convective heat transfer coefficient) to the experimentally measured values. The measured values of inlet air temperature, inlet air pressure, mass flow rate, incident flux, test geometry, and material properties were put into the analytical model. With this data input, the analytical model correctly predicted the temperature variation around the tube and the interior convective heat transfer coefficient.

Table C-5 presents a comparison between the interior convective heat transfer coefficients calculated from experimental data and those predicted by the analytical model for four test cases. The agreement is excellent for Cases 1, 2, and 3, and good for Case 4.

The comparison between the measured and analytically predicted temperature distributions around the center tube for four test cases is presented in Figures C-7 through C-10. The agreement is acceptable in Case 1 and excellent in Cases 2, 3, and 4. The differences between the experimental and analytical results for Case 1 are believed to be caused by excessive radiative energy losses due to the elevated tube temperature.

Table C-5  
CONVECTIVE HEAT TRANSFER COEFFICIENT

CASE	EXPERIMENTAL		ANALYTICAL	
	$\text{kW/m}^2\text{-}^\circ\text{C}$	$\text{Btu/h-ft}^2\text{-}^\circ\text{F}$	$\text{kW/m}^2\text{-}^\circ\text{C}$	$\text{Btu/h-ft}^2\text{-}^\circ\text{F}$
1	0.21	(37)	0.20	(35)
2	0.30	(52)	0.28	(49)
3	0.42	(74)	0.39	(68)
4	0.70	(123)	0.53	(94)

CONCLUSIONS

As can be seen in Table C-5 and in Figures C-7 through C-10, agreement between the analytically determined values and the experimentally measured data is good. It was concluded that, based on the comparison to experimentally determined data, the analytical model is a valid representation of the actual physical phenomena.

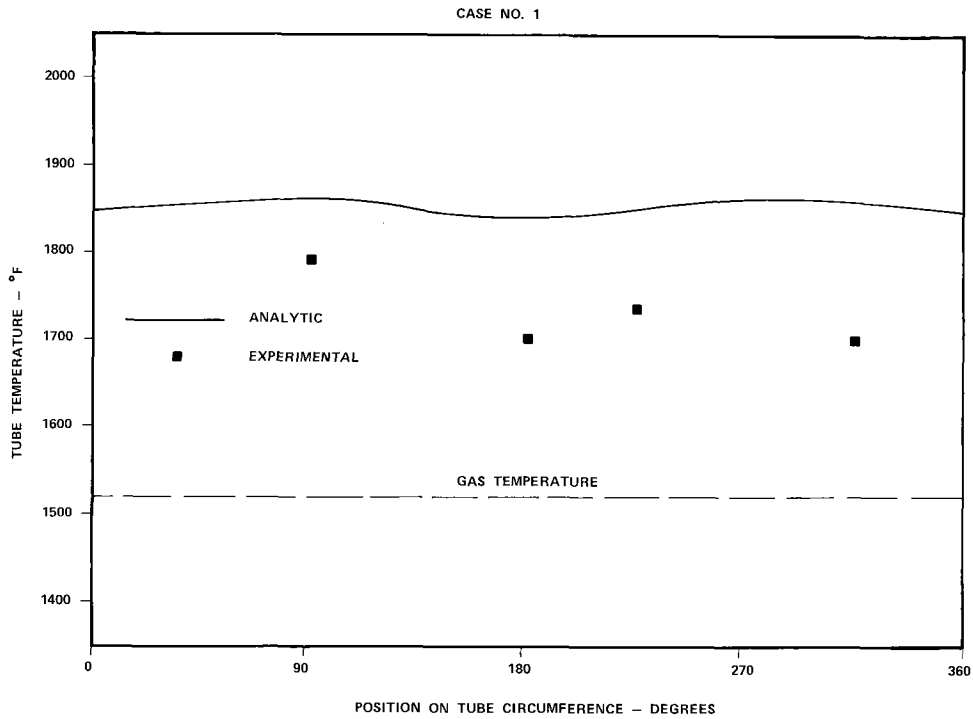


Figure C-7. Comparison of Experimental and Calculated Temperature Distributions on Single Tube

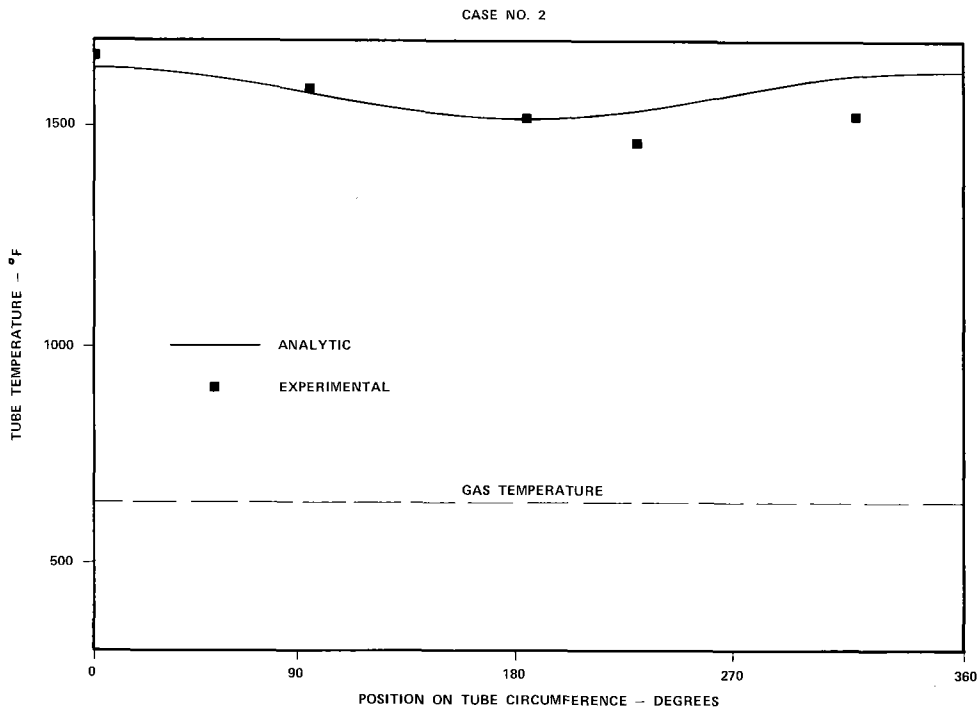


Figure C-8. Comparison of Experimental and Calculated Temperature Distributions on Single Tube

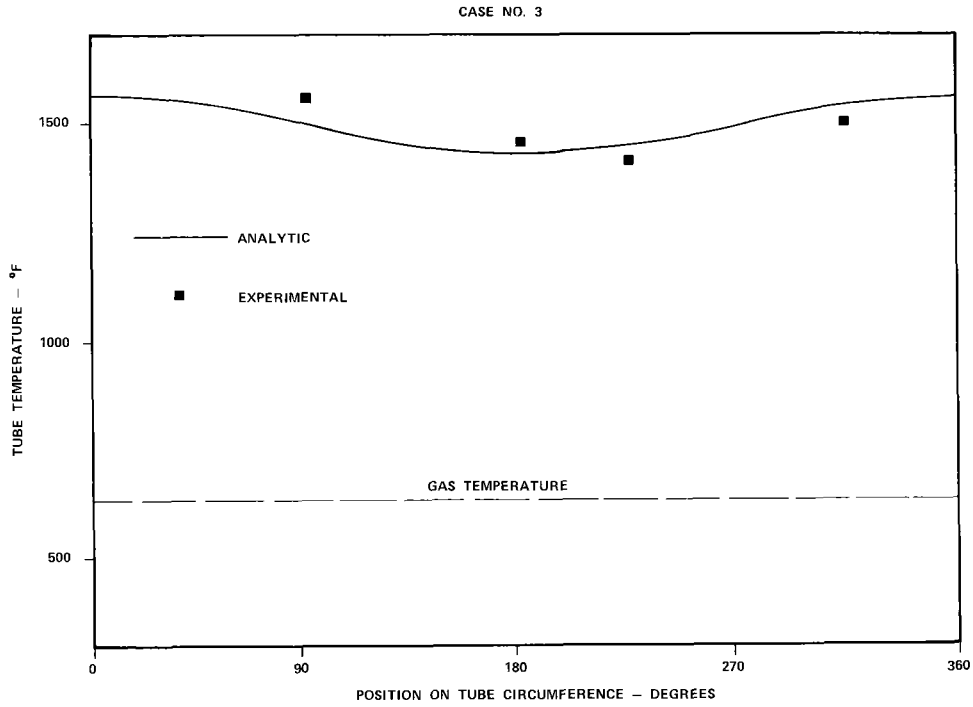


Figure C-9. Comparison of Experimental and Calculated Temperature Distributions on Single Tube

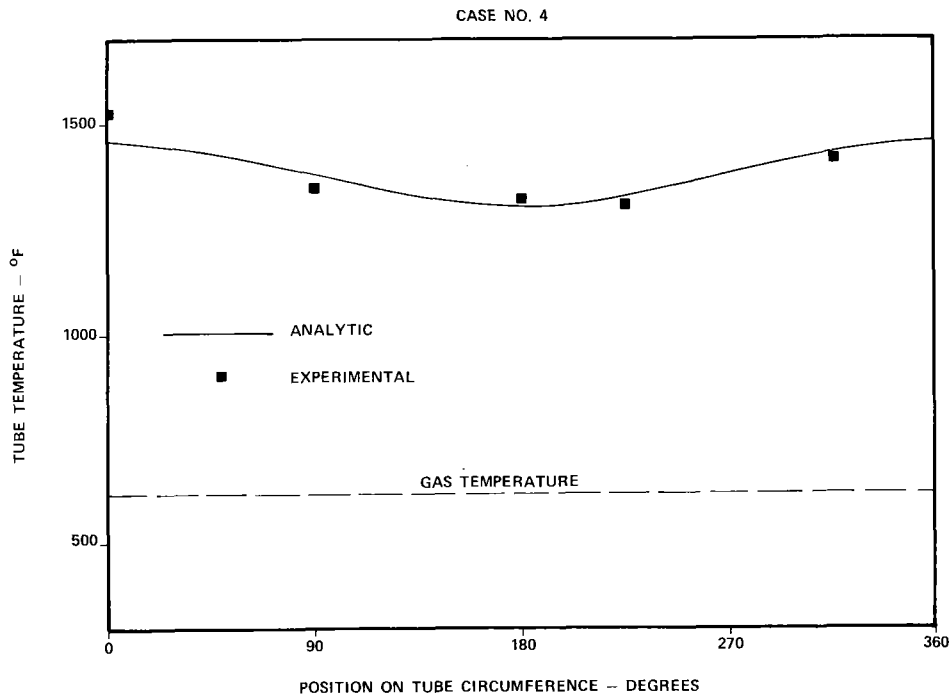


Figure C-10. Comparison of Experimental and Calculated Temperature Distributions on Single Tube

Appendix D

THERMAL-CYCLE TESTING OF THE  
HEAT EXCHANGER U-TUBE CONFIGURATION

This Appendix was authored for Black & Veatch by J. N. Harris  
of the Engineering Experiment Station, Georgia Institute of Technology.

## Appendix D

### THERMAL-CYCLE TESTING OF THE HEAT EXCHANGER U-TUBE CONFIGURATION

#### INTRODUCTION

To obtain data on the integrity of ceramic-to-ceramic and ceramic-to-metal joints, the resistance of tubes and joints to thermal cycling, and the longitudinal and circumferential variation of temperature along a heat exchanger U-tube, a series of experiments was designed and conducted. Testing was performed at the Engineering Experiment Station, Georgia Institute of Technology, Atlanta, Georgia.

#### TESTING METHODOLOGY

A determination of the heat exchanger U-tube configuration/joint failure resistance was achieved by subjecting a U-tube specimen to the anticipated thermally-induced stress levels and monitoring the resulting responses. By recording circumferential, surface temperature variations at various points along the U-tube, by monitoring the inlet and outlet air conditions, and by observing the mode of failure (if any), a test of the performance of the U-tube under thermal-cycling conditions similar to those expected in actual, daily operation was performed.

#### EXPERIMENT DESIGN

Tests on the heat exchanger U-tube configuration were performed using a 100-kW lamp array in conjunction with a reflecting cavity. This experimental setup simulated the expected operating environment of the actual heat exchanger. The diameter and length of the ceramic tubes used in testing were selected to be compatible with the available facility and budget limitations and to facilitate handling.

Because the governing heat transfer relations involve parameters in a nonlinear manner, a scale-model U-tube test can only duplicate either the mechanical or the heat transfer relationships. Because the heat transfer relationships had been duplicated during the validation of the analytic model, U-tube tests were designed to duplicate the mechanical aspects of the heat exchanger configuration (thermally-induced stresses in the tubes and joints).

## EXPERIMENT SETUP

The test apparatus consisted of an open rectangular cavity, a bank of fused-quartz infrared lamps, and a ceramic U-tube. The bank of infrared lamps was track-mounted such that it could be retracted from the cavity, permitting access to the U-tube located within. The test apparatus is pictured in Figure D-1, with a U-tube in position in the cavity and with the lamp bank retracted from the cavity.

The fused-quartz infrared lamp bank was a water-cooled module containing 84, 41-cm (16-in) long lamps. Each fused-quartz infrared lamp was rated at 1.6 kW (5500 Btu/h) at 230 volts. The infrared lamp bank is pictured in Figure D-2.

The test apparatus had been designed to accept U-tubes having a nominal outer diameter of 5.1 cm (2 in). The parameter  $S/O$ , the ratio of the centerline to centerline spacing ( $S$ ) of the U-tube's vertical legs to the U-tube's outer diameter ( $D$ ), was 3:1. The U-bend had a centerline radius of curvature of 7.6 cm (3 in). Overall height of the U-tube was 121.9 (48 in).

The open rectangular cavity was defined by flat sheets of fused-silica foam. Because the fused-quartz infrared lamps were conveniently available in lengths of 41 cm (16 in), the cavity was 41 cm (16 in) in width. The height of the cavity was adequate to accommodate a U-tube specimen, 121.9 cm (48 in). With the parameter  $O/D$ , the ratio of the spacing between the back cavity wall and the U-tube's centerline ( $O$ ) to the U-tube's outer diameter ( $D$ ), set equal to 1:1 and with the parameter  $S/D$  set equal to 3:1, a cavity depth of 15 cm (6 in) was analytically determined to result in thermally-induced tube stresses nearly equal to those calculated for the baseline design. The cavity is pictured in Figure D-3 with U-tube in position. Figure D-4 is a horizontal cross section of the reflecting cavity showing the relative positions of the infrared lamp bank and the U-tube.

Control of the test apparatus was via four, 460-volt, 100-amp, three-phase, silicon-controlled rectifiers (SCR's). One SCR was employed to power the air preheater. The other three each powered 28 of the 84 fused-quartz infrared lamps. The control panel was wired with latching relays and an alarm system to automatically shut down and remain off (until manually reset) if a heating overload occurred. The system also shut down if a momentary power failure occurred.

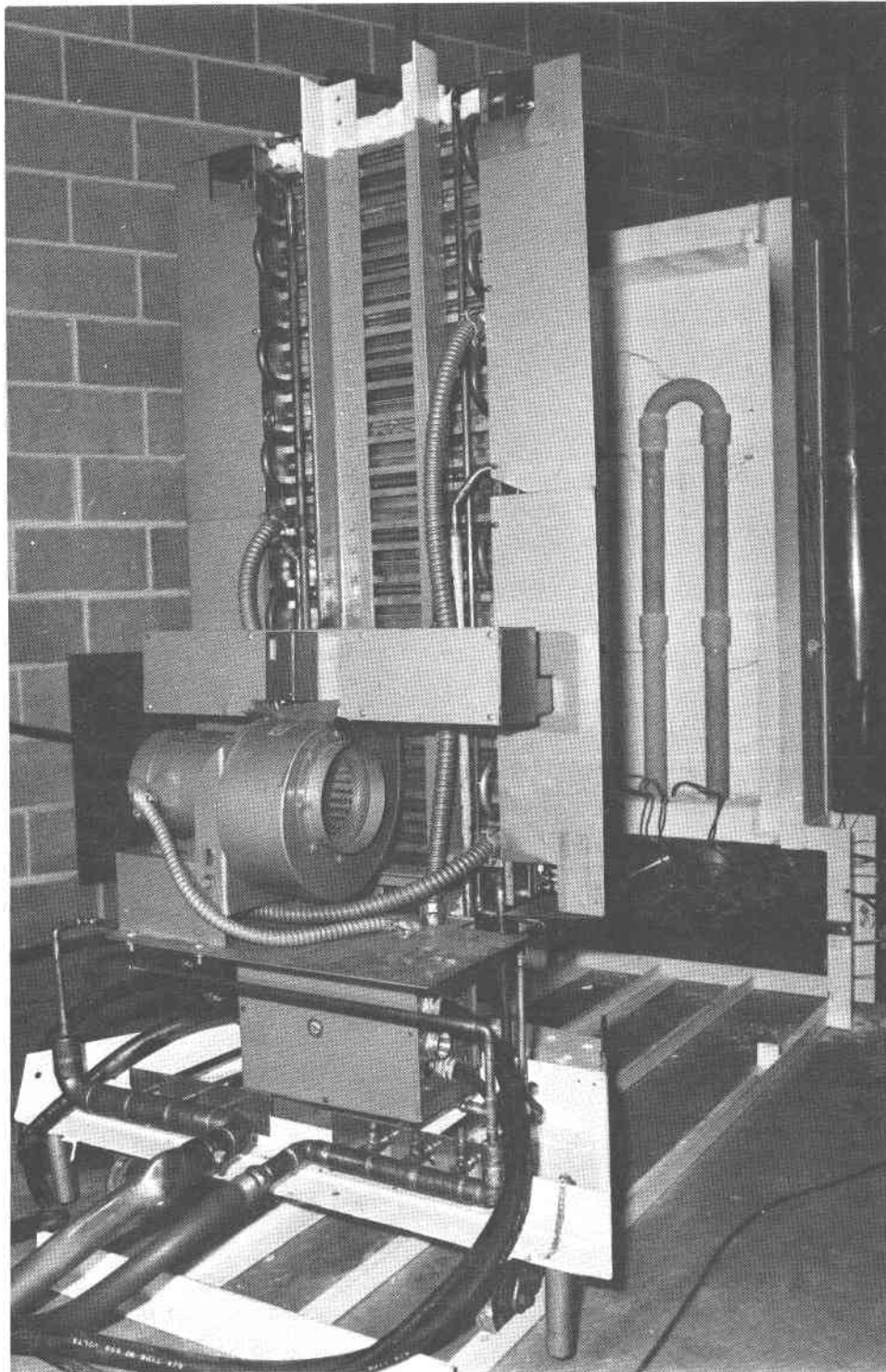


Figure D-1. U-Tube Configuration, Thermal-Cycle Test Apparatus

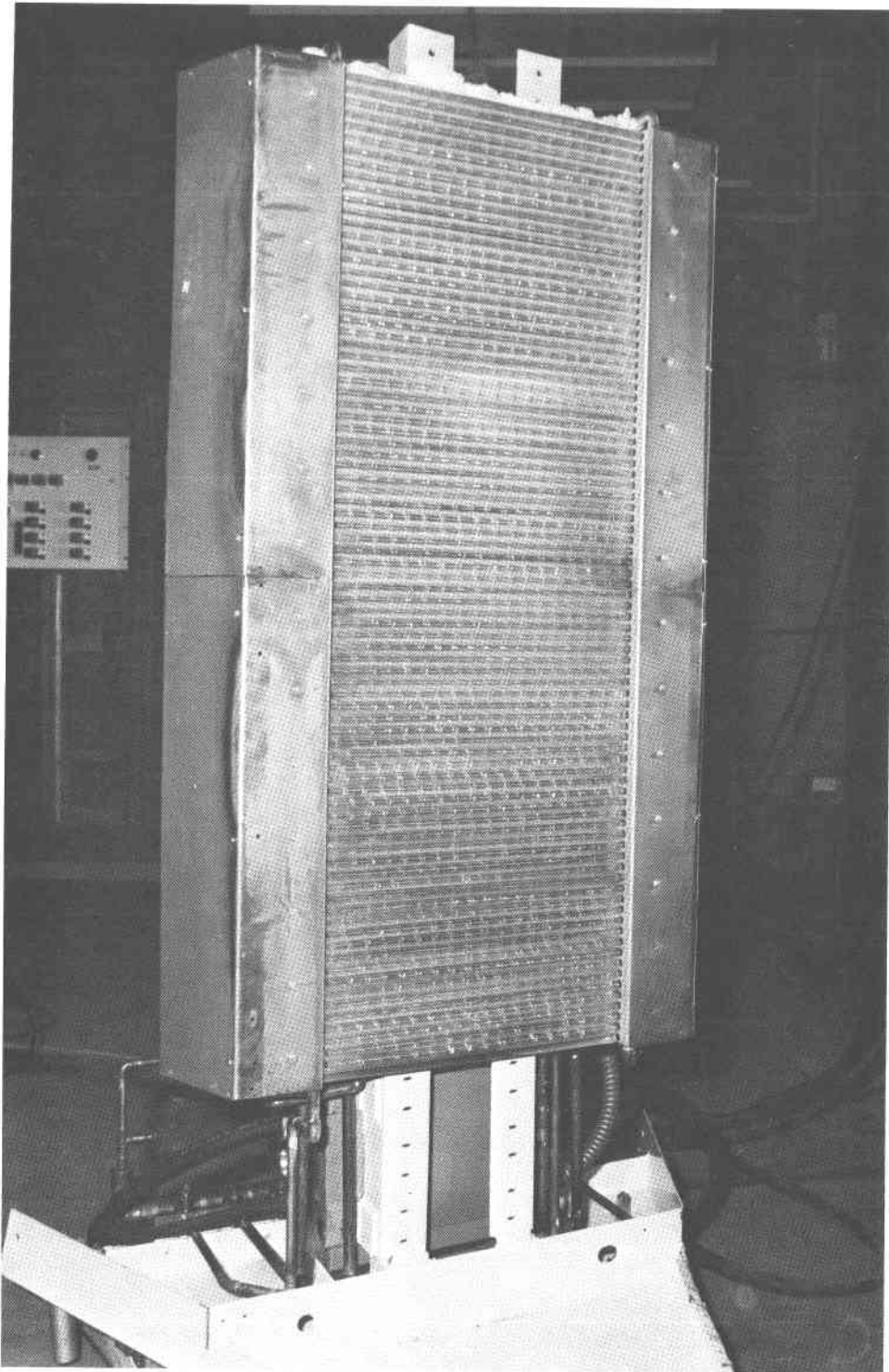


Figure D-2. Front View of Lamp Module

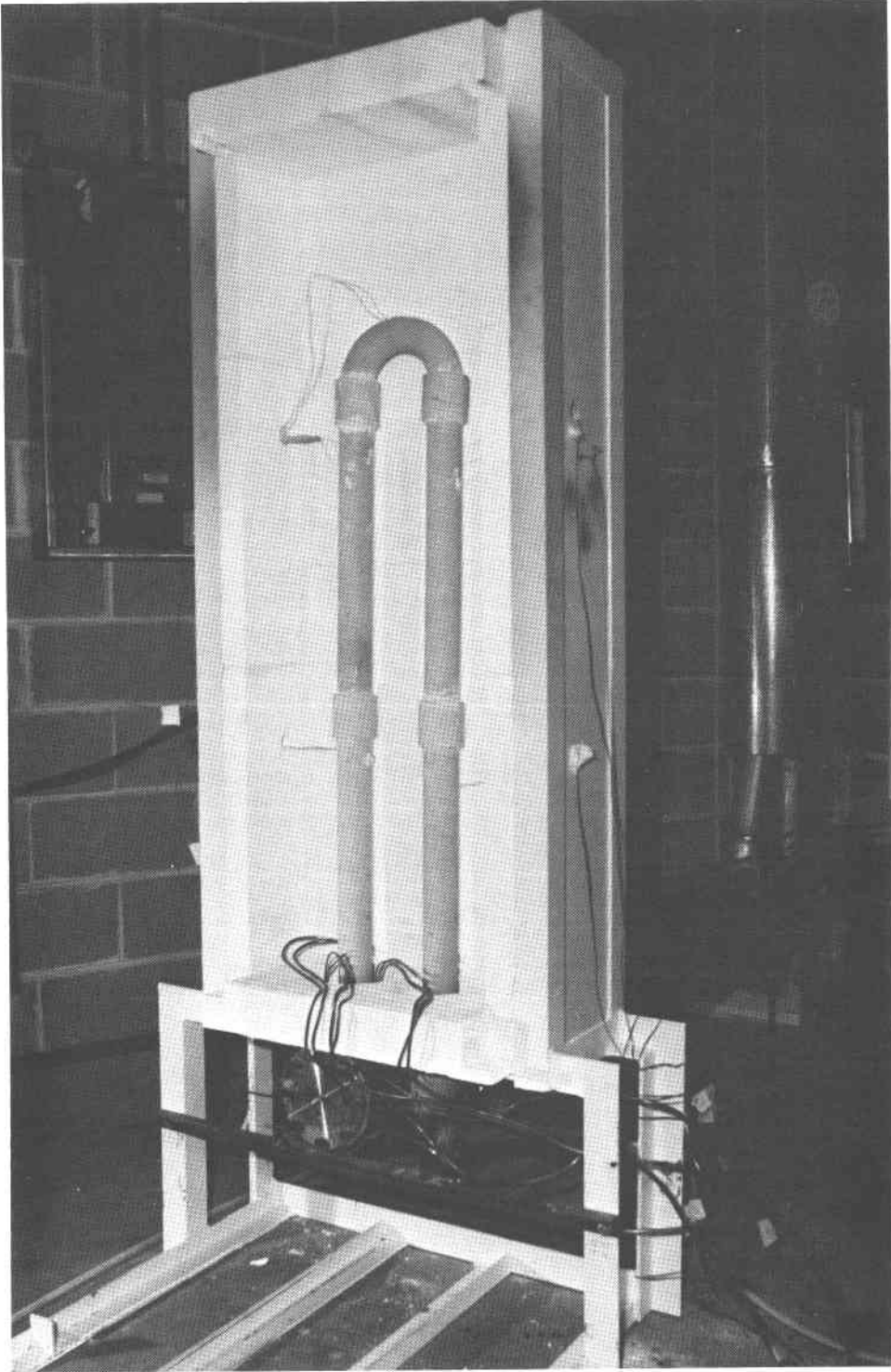


Figure D-3. Reflecting Cavity of Thermal-Cycle Test Facility with Tube in Place

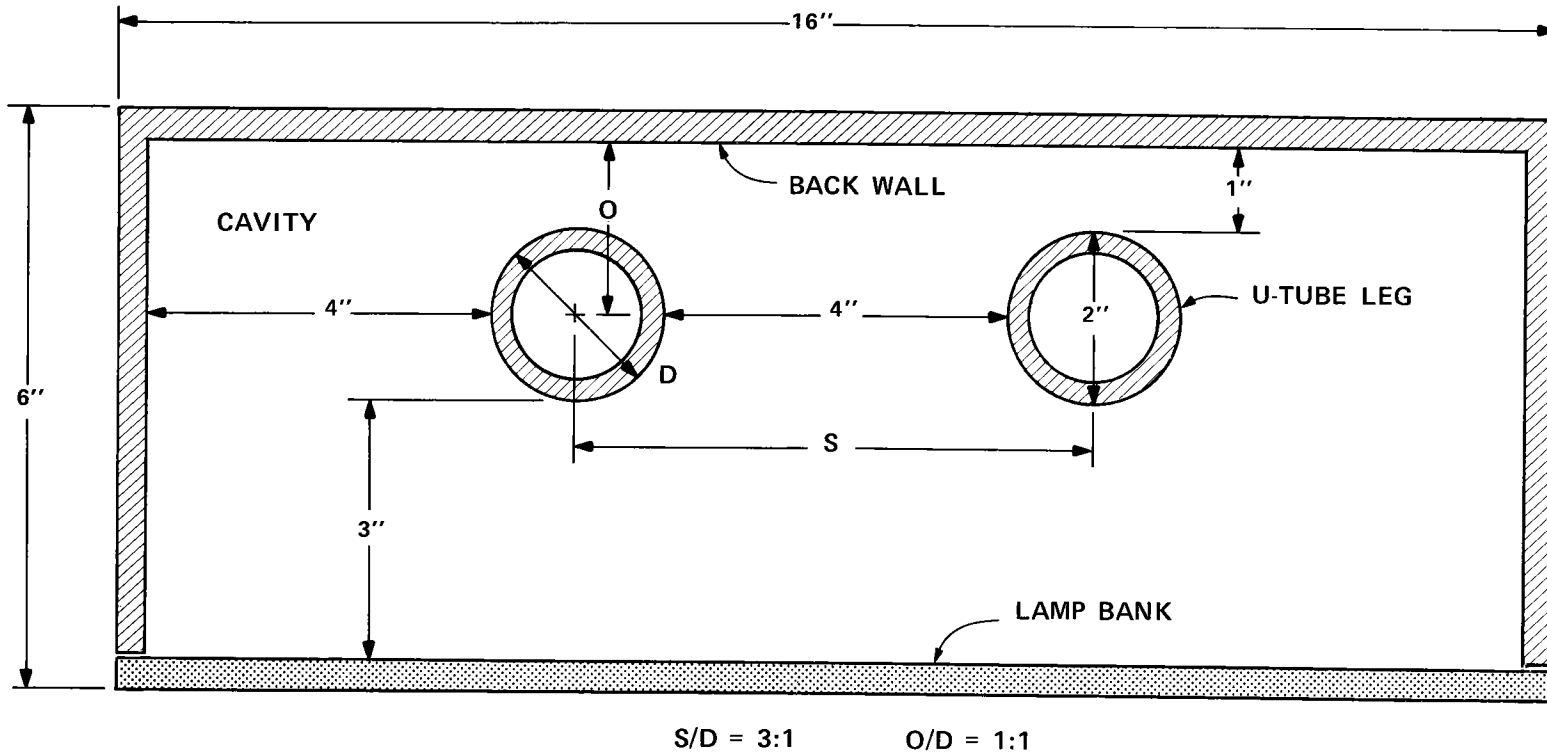


Figure D-4. U-Tube Thermal-Cycling Experiment Configuration

## TEST PROCEDURE

Compressed air was preheated and introduced into the inlet of the ceramic U-tube. The U-tube was then irradiated with the bank of fused-quartz infrared lamps, providing a nominal incident heat flux onto the U-tube of  $200 \text{ kW/m}^2$  ( $6.34 \times 10^4 \text{ Btu/h-ft}^2$ ). This arrangement simulated the thermally-induced stress conditions expected in the baseline heat exchanger design. The heated air exiting the ceramic U-tube passed through a water-cooled, critical-flow orifice and then expanded into a muffler. From the muffler, the air was ducted to outside the building. A cross section of the hot-side header showing the water-cooled, critical-flow orifice is shown in Figure D-5.

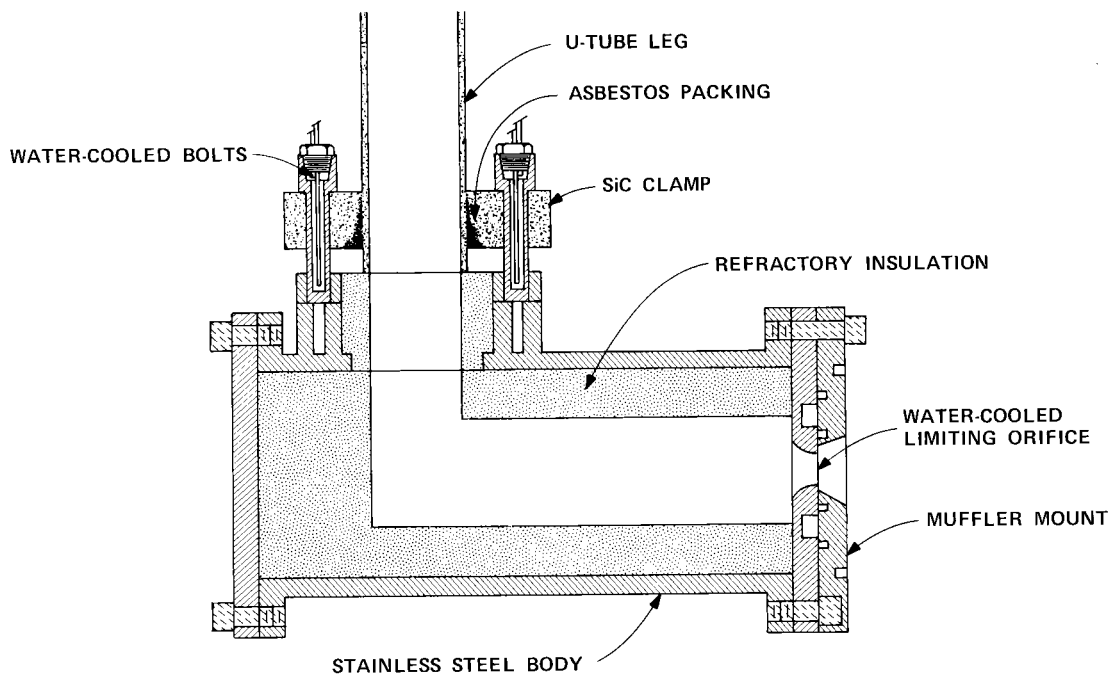


Figure D-5. Hot-Side Header for Thermal-Cycle Test Apparatus

## DATA ACQUISITION

During testing, the temperature, pressure, and flow rate of the air were monitored at the inlet and outlet of the U-tube assembly. Temperature measurements were made using thermocouples. Flow measurements were made using tapered-tube float-type Brooks Rotameters.

In addition to these data, the surface temperatures on the U-tube were monitored by means of attached thermocouples. One thermocouple was placed near the U-tube inlet, two were placed circumferentially at a point upstream of the U-bend, one was attached to the U-bend, four thermocouples were placed circumferentially at a point downstream of the U-bend, and one was attached to the tube near the U-tube exit.

The above data were recorded for each thermal cycle (heat up--cool down). During thermal cycling, the maximum inlet air temperature was 290°C (550°F); the maximum pressure 0.38 MPa (55 psia). Generally, the tubes were heated until the surface temperature nominally equalled 1100°C (2000°F) and then allowed to cool to 480°C (900°F). Thermal cycling of the U-tube was repeated until the U-tube failed. Determining the mode of failure and examining the recorded data provided information on the resistance of the heat exchanger U-tube configuration and joints to thermal cycling.

#### TEST SPECIMEN

An earlier survey of ceramic materials identified silicon carbide as the primary material candidate. However, at the time the test apparatus became operational, tubes made of silicon carbide in the required size had not been delivered. As a result, the testing of the secondary material candidate, cordierite, was undertaken.

A cordierite U-tube was assembled from four straight tube segments and one semi-circular tube segment. All segments were joined using external sleeves, also made of cordierite. The sleeves are cemented onto the tube segments using either Sauereisen cement No. 78 or No. 8. Sleeves with and without interior shoulders were used, though not at the same time. A cross section of a typical cordierite sleeve having an interior shoulder is shown in Figure D-6.

Because of the difficulty encountered in using Sauereisen cement No. 8 during the assembly of the first test specimen, it was utilized to make only one ceramic-to-ceramic joint. Sauereisen cement No. 78 was utilized exclusively from then on for the assembly of cordierite U-tubes.

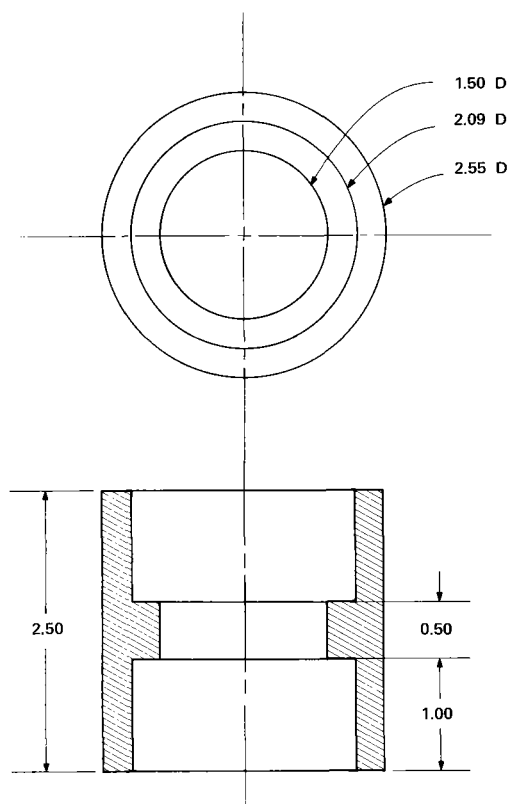


Figure D-6. Cross Section of Cordierite Sleeve with Interior Shoulder

In all, three cordierite U-tubes were assembled and tested. However, all U-tubes were assembled using the same four straight tube segments. At the completion of testing on a U-tube, the sleeve joints were cut off such that the straight tube segments could then be utilized for construction of the next specimen. The removal of the sleeve joints, however, shortened the straight tube segments such that each assembled U-tube specimen was shorter than the preceding.

A completed cordierite U-tube was attached to the air inlet and air outlet headers of the test apparatus via tapered compression seals (ceramic-to-metal joints). The tapered compression seals were formed by sliding loosely fitting flanges with tapered recesses onto the ends of the U-tube. The tapered recesses were then filled with a mixture of chopped asbestos fiber and sodium silicate. When the flanges were bolted to mating fixtures on the headers, the asbestos fiber was tightly compressed against the tube, forming a compression seal. The sodium silicate, upon drying, formed an adhesive bond. A cross section of a ceramic-to-metal tapered compression seal can be seen in Figure D-5.

Erection of a U-tube proceeded as follows. First, two straight tube segments were attached to the inlet and outlet headers via tapered compression seals. Second, another straight tube segment was attached on top of each of the first two tube segments via cordierite sleeves and Sauereisen cement No. 78. Third, these two two-segment lengths of tube were joined together with a cordierite U-bend, again via sleeves and cement. The assembly of the U-tube while in place in the test apparatus was felt to minimize any mechanical stresses.

#### TEST RESULTS

The first cordierite U-tube tested was assembled using sleeves having interior shoulders. After each thermal cycle, the infrared lamp bank was retracted from the cavity and the U-tube was inspected. On the fourth cycle, the U-tube failed; the cordierite sleeve on the inlet side of the U-bend cracked completely into two pieces. Failure was horizontal and just below the interior shoulder. The air inlet conditions on the fourth cycle were 0.20 MPa (29 psia) and 288°C (550°F). The tube surface temperature had reached 843°C (1550°F) at the time of failure and the exit air temperature had attained 627°C (1160°F).

Pertinent test data for the four thermal cycles of the first specimen are given in Table D-1.

During disassembly of the first U-tube, shallow exterior cracks were found in the straight tube segments paralleling the area where the mold parting lines had been ground off the tubes.

The second cordierite U-tube was assembled using the straight tube segments from the first U-tube and using sleeves having no interior shoulders. After the first thermal cycle [inlet air pressure 0.20 MPa (29 psia) and inlet air temperature 288°C (550°F)], the sleeve on the exhaust side of the U-bend developed a crack which was subsequently repaired successfully with Sauereisen cement No. 78.

During installation of a higher capacity flow meter, the second through the fifth thermal cycles were performed without flowing air (lamps only). During these cycles, the U-tube was heated to a nominal temperature of 1100°C (2000°F) and allowed to cool to a normal temperature of 480°C (900°F).

Table D-1

## THERMAL-CYCLE TEST DATA ON FIRST CORDIERITE U-TUBE

CYCLE	INLET AIR PRESSURE	INLET AIR TEMPERATURE	TIME OF HEAT-UP	EXIT AIR TEMPERATURE	MAXIMUM SURFACE TEMPERATURE
NUMBER	MPa (psia)	°C (°F)	MINUTES	°C (°F)	°C (°F)
1	0.16 (23)	27 (80)	9	502 (935)	738 <sup>*</sup> (1360)
2	0.20 (29)	104 (220)	18	538 (1000)	704 <sup>*</sup> (1300)
3	0.20 (29)	232 (450)	10	516 (960)	704 <sup>*</sup> (1300)
4 <sup>**</sup>	0.20 (29)	288 (550)	20	627 (1160)	843 <sup>*</sup> (1550)

\* Tube surface cooled to ambient [27°C (80°F)] between cycles.

\*\* Sleeve on inlet side of U-bend failed.

The sixth thermal cycle was performed with inlet air at 0.38 MPa (55 psia) and 275°C (525°F) with a flow rate of 300 kg/h (11 lb/min). The tube surface attained 1200°C (2200°F) and the exit air temperature achieved 627°C (1160°F). During the sixth thermal cycle, the tapered compression seal on the exhaust end of the U-tube blew out. Failure of the seal was attributed to creep in the bolts retaining the flange. The U-tube was removed, the seal repaired, and the U-tube reinstalled. Creep was eliminated by the use of water-cooled bolts made of stainless steel.

Pertinent test data for the seven thermal cycles of the second cordierite U-tube are given in Table D-2.

Failure of the sleeves was attributed to excessive thermal stresses in the 0.64 cm (0.25 in) thick sleeve walls. In an effort to reduce stress levels, the third cordierite U-tube was assembled using sleeves having a wall thickness of 0.34 cm (0.125 in). The straight tube segments used twice previously were again used for assembly. Thermal cycling was initiated with inlet air at 0.48 MPa (70 psia) and a temperature of 277°C (530°F) with a flow rate of 300 kg/h (11 lb/min). At 15-1/2 minutes after the start of the first cycle, the straight tube segment on the inlet side of the U-tube exploded. Exit air temperature had attained 538°C (1000°F).

#### CONCLUSIONS

As a result of thermal cycling the cordierite U-tubes, it was concluded that sleeve joints of cordierite are an unsatisfactory means of coupling cordierite tubes and that cordierite tubes, as supplied, are unsatisfactory for the intended application. Because the fault that precipitated the failure of the seal was corrected, tapered compression seals are judged to be a workable method of achieving ceramic-to-metal connections for conditions achieved to date (0.38 MPa and 1200°C [55 psia and 2200°F]).

Tubes of silicon carbide (the primary material candidate) in the required dimensions became available for testing on June 25, 1976, too late for inclusion in this report. Test results for the silicon-carbide tubes will be included in a later report (EPRI Project RP 475-2).

Table D-2

## THERMAL-CYCLE TEST DATA ON SECOND CORDIERITE U-TUBE

CYCLE	INLET AIR PRESSURE	INLET AIR TEMPERATURE	MASS FLOW	TIME OF HEAT-UP	EXIT AIR TEMPERATURE	MAXIMUM SURFACE TEMPERATURE	TIME OF COOL-DOWN	MINIMUM SURFACE TEMPERATURE
	MPa (psia)	C (F)	kg/h (lb/min)	MINUTES	C (F)	C (F)	MINUTES	C (F)
1*	0.20 (29)	274 (525)	--	6	524 (975)	829 (1525)	N/A	27 (80)
2	0.10 (14.7)	--	0	27	--	1067 (1950)	7	482 (900)
3	0.10 (14.7)	--	0	5.5	--	1067 (1950)	7.5	460 (860)
4	0.10 (14.7)	--	0	9.5	--	1099 (2010)	7.5	482 (900)
5	0.10 (14.7)	--	0	9	--	1071 (1960)	--	27 (80)
6**	0.38 (55)	274 (525)	300 (11)	8	246 (475)	218 (425)	N/A	N/A
6 <sup>+</sup>	0.38 (55)	274 (525)	300 (11)	21	627 (1160)	1216 (2220)	--	27 (80)
7 <sup>++</sup>	0.38 (55)	213 (415)	300 (11)	4	277 (530)	399 (750)	N/A	27 (80)

\* Sleeve on exhaust side of U-bend cracked.

\*\* Preheated air flow only (no lamps).

<sup>+</sup> Lamps turned on. Tapered compression seal failed at end of cycle.

<sup>++</sup> Sleeve on inlet side of U-bend failed.

Appendix E

SUITABILITY OF SiC FOR HIGH-TEMPERATURE  
SOLAR COLLECTOR/HEAT EXCHANGERS

This Appendix was authored for Black & Veatch by Dr. Edwin H.  
Kraft of The Carborundum Company Research and Development Division.

## Appendix E

### SUITABILITY OF SiC FOR HIGH-TEMPERATURE SOLAR COLLECTOR/HEAT EXCHANGERS

#### INTRODUCTION

The choice of a material for use in high-temperature structures must take into consideration several important aspects of materials. Elevated temperatures such as those envisioned in the solar collector/heat exchanger impose severe oxidation, thermal expansion, heat transfer and joining requirements. The temperatures and physical size of the apparatus impose significant thermal and mechanical stresses. Cost and availability are critical factors due to the large amount of materials required.

Silicon carbide is an excellent candidate for applications such as this because of its combination of high strength at high temperatures, low thermal expansion, high thermal conductivity, oxidation resistance and the abundance of constituent elements. There are now basically two types of pressureless, sintered SiC ceramics which could be used for high-temperature applications. The first is reaction-sintered SiC such as Super KT which is a high performance material processed similar to KT SiC which has been available for nearly 20 years. The second is sintered SiC such as Carborundum's recently announced sintered  $\alpha$ -SiC.(E-1) The properties and advantages of these two materials will be discussed in later sections.

#### SiC GRAIN PRODUCTION

Practically all of the SiC grain produced in the world today is made by the Acheson process developed in 1891 by Edward G. Acheson, the founder of The Carborundum Company. Using a small iron plumbers bowl, a carbon electrode and a mixture of clay and powdered coke he found that by heating the mass electrically he could cause crystals of a hard black material to form on the electrode. The material was soon found to be silicon carbide, a previously unknown material which found a ready market as an abrasive. Scale-up to commercial practice has resulted in the currently used "Acheson" electric furnace (Figure E-1) which is over 40 feet long by 10 feet wide and 10 feet high.

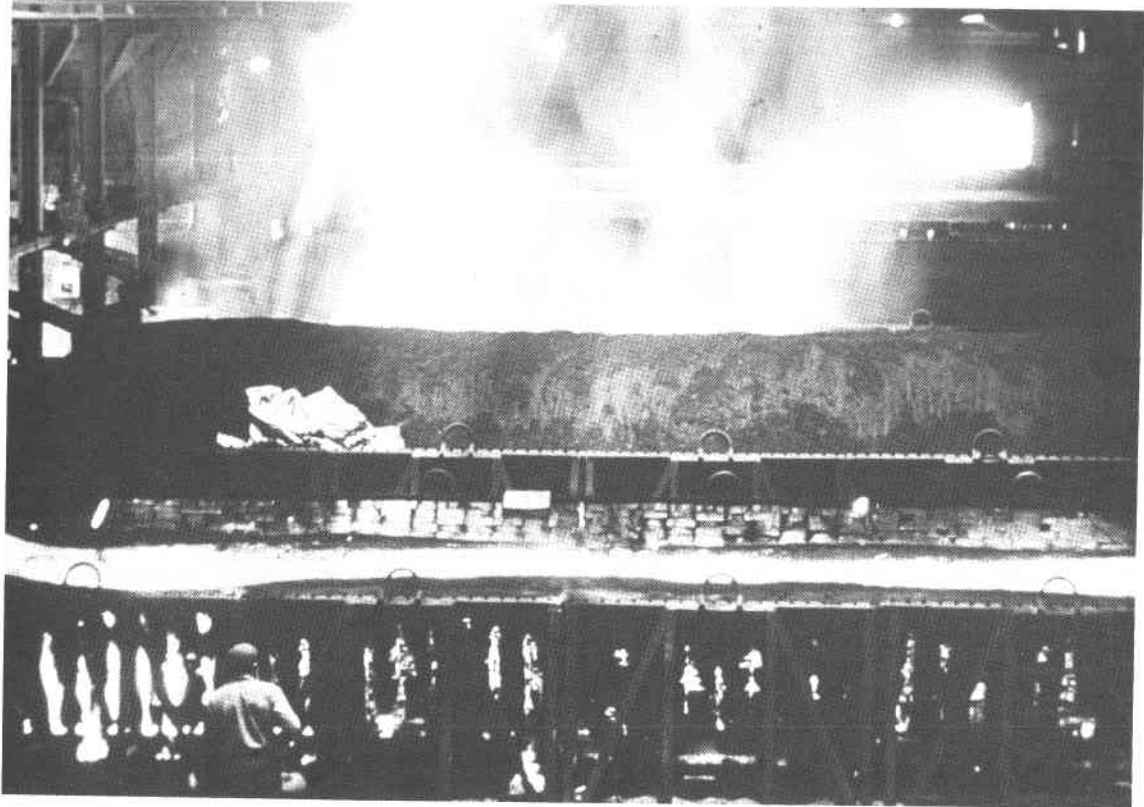


Figure E-1. The Acheson Furnace for SiC Grain Production

The major constituents of the charge are sand (60%) and coke (40%). Sawdust is added so that, on burning out, it will increase the porosity of the charge and thus promote circulation of the reacting vapors. Salt is also frequently added to react with iron and similar impurities of the raw materials to produce volatile chloride compounds and increase the purity of the product.

The raw materials are thoroughly mixed and deposited in the furnace trough to the level of the electrodes. At this point a core of granular carbon or graphite is tamped in place connecting the two electrode terminals and additional batch is piled over the core.

A voltage is applied to the electrodes and current passes through the core. At the beginning of the run this voltage may be as high as 300 volts. As the temperature rises the resistance gradually drops and the voltage requirement may decrease to about 200 volts.

The temperature of the central core will reach 1900°C at the end of the first five hours and thereafter rises more slowly to reach a maximum of over 2400°C after about 18 hours. From then until the end of the 36-hour run the core temperature falls off to become constant at about 2040°C.

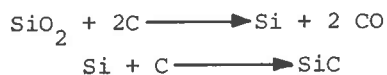
After the run, the current is turned off, the furnace is allowed to cool and the side walls are removed. The charge is now found to consist of an outer zone of unreacted or partially reacted mix which has served as heat insulation between the hotter zones of the furnace and the side walls. This material is separated out and may be refurnaced with another charge. The next zone begins where the temperature has reached the reaction range, and here is found the crystalline silicon carbide which is removed for processing into grain. The central zone where the coke or graphite core was placed is found to contain only graphite, the coke having been converted to graphite at the temperatures involved. There may also be voids at this point where the graphite has reacted with silica to form more silicon-carbide crystals, but the temperature at the core has been above the dissociation range of the reaction product so that the vapors have migrated to the cooler second zone and no silicon carbide is found at the core. The graphite from the core is separated from the crystals and may be used as core material for another furnace run.

Silicon carbide forms from the reaction of silicon and carbon at or above the melting point of the silicon, 1430°C.

The reaction of silica with carbon as usually written is:



Baumann (Ref. E-2, E-3) confirmed that this is a vapor phase reaction which proceeds in two steps, the second step being almost instantaneous, and the reaction beginning at about 1500°C.



It is this reaction on which the usual furnace procedure is based, but in order that the reaction may go on at a reasonable rate, the furnace temperatures are much higher.

The crude crystalline silicon carbide is found to be a mass of interlocking crystals which must be broken up into grains of various sizes, and impurities removed. Pan mills, jaw and roller crushers or other attrition schemes are used

to reduce the size of the grain. Vibrating screens are used to separate out coarse fractions. Fine particles are sized by wet grading or air separation. Caustic soda or acids are used for dissolving metallic and oxide impurities and the powders are washed to remove salts.

#### FORMATION OF DENSIFIED SiC

The techniques used to form dense, high strength SiC bodies fall into either the reaction-sintering or the solid-state-sintering categories. Both methods can utilize grain produced by an Acheson type process.

Reaction-sintering of SiC was developed in the 1950s in both the U.S. and England. In this country, researchers of the Carborundum Company pioneered this work by developing a process (Ref. E-4, E-5) in which SiC grain and carbon are mixed and formed into a body which is then infiltrated with silicon. The silicon which infiltrates the body reacts with the carbon present to form SiC thus bonding the existing SiC grains together. Excess free Si fills the voids with result when lower density C and Si react to form SiC. The result of this process is a matrix consisting of prexistent  $\alpha$ -SiC grain bonded together by reaction product  $\alpha$ -SiC, with isolated regions of free Si. The English process is similar except that a vacuum is used instead of an inert atmosphere (Ref. E-6).

The microstructure and properties of the KT-SiC which results from this process depends to a great extent on the materials which are used in the original mix. The high strength and reliability of Super KT-SiC are a result of the use of finer grain SiC, and more thorough control of proportions, mixing and subsequent processing. The microstructure and therefore properties of Super KT and "Refel," which resulted from the English Development, are similar.

To date, the fabrication of KT-SiC shapes has utilized only the processes of extrusion, cold pressing and machining in the "green" state. The applications of this material have not required more complex shapes. With the development of the higher reliability Super KT, however, applications are envisioned which require more advanced techniques. As a result, the methods of extrusion, transfer and injection molding, casting, isostatic and die pressing are being developed for complex shape fabrication. Some success with forming large radius curved tubes and joined tube sections has been achieved in the parallel program EPRI Project RP545-1, "Coal Fired Prototype High Temperature Continuous Flow Heat Exchanger". Some of the components fabricated for this program using Super KT SiC are shown in Figure E-2.

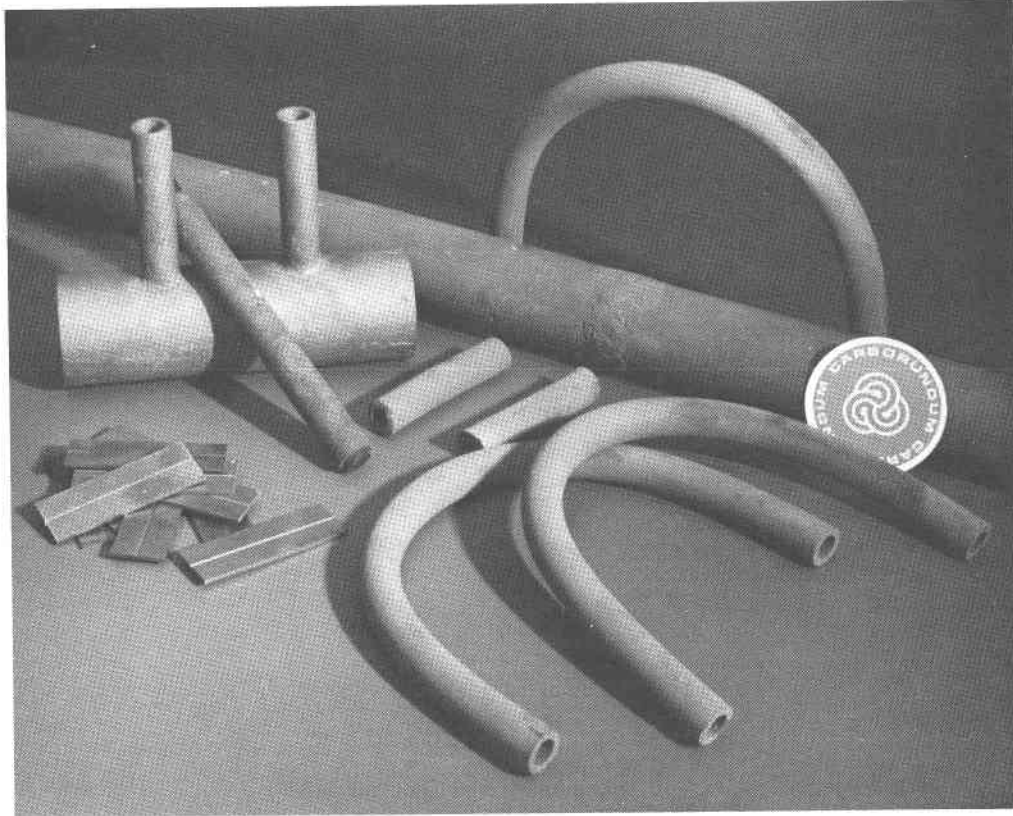


Figure E-2. Super KT-SiC Components Fabricated for EPRI Coal-Fired Heat Exchanger Program

Recently, researchers of General Electric Company announced the pressureless sintering (Ref. E-7) of  $\beta$ -SiC powder. This powder was made by a vapor phase reaction process. Development of sintering and shape-fabrication techniques (Ref. E-8) has proceeded since that time but has been hampered mainly by unavailability of powder, transformation of  $\beta$  to  $\alpha$  phase, and excess grain growth resulting in large tabular grains subject to low fracture stress. While significant improvements in properties have been made, control of microstructure and shrinkage remains a nontrivial problem. In addition, the unavailability of powder has restricted more rapid or wider development.

On June 7, 1976, the Carborundum Company announced (Ref. E-9) the development of processes for producing sinterable  $\alpha$ -SiC powder from the Acheson process, and the development of methods to sinter this material to high densities (> 98%). This set of processes removes the major obstacles to successful utilization of solid-

state sintering for fabrication of high-performance SiC shapes. The powder used is submicron, high surface area material to which proprietary activating agents are added to produce sintering at temperatures between 1900° and 2400°C. Being an  $\alpha$ -phase powder the transformation problem is eliminated and through proper control, grain growth is restricted to an innocuous level.

The same shape fabrication methods are being developed for sintered  $\alpha$ -SiC as listed for Super KT. While solid-state sintering does not require liquid infiltration as does reaction sintering, precise control of mixing, forming and furnacing is required to produce uniformity of the 18% linear shrinkage encountered and thus produce parts to close tolerance. Significant progress has been made to date as shown by the air-foil and nozzle shapes shown in Figure E-3.

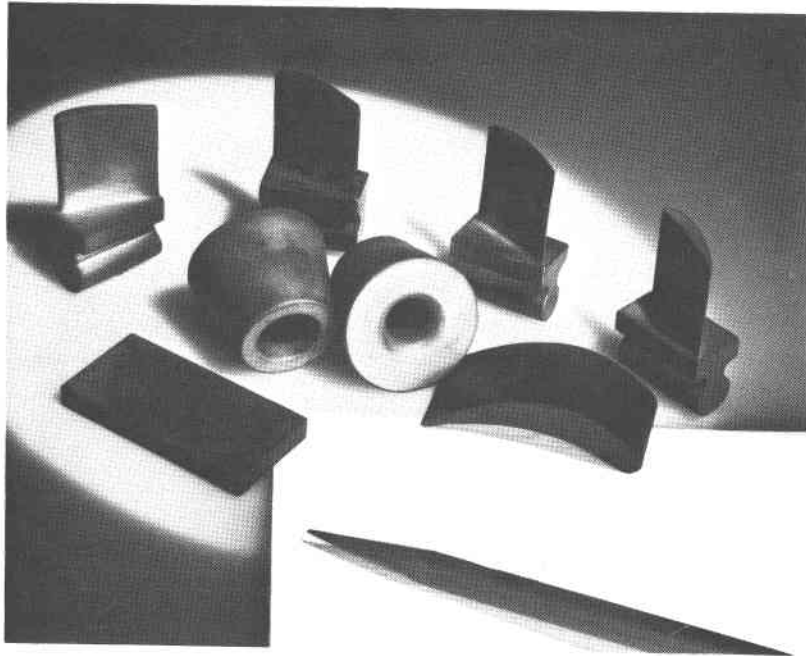


Figure E-3. Sintered  $\alpha$ -SiC Components

#### PROPERTIES OF SiC

Selection of materials for various components of high-temperature machines such as the solar collector/heat exchanger must be based to a large extent on reliable engineering data. While data on structure insensitive physical properties can be used with reasonable confidence, the structure sensitive mechanical properties require considerable caution for several reasons. First, many of the ceramic

materials considered for these applications remain in a developmental state and their mechanical properties are subject to improvement and/or refinement. Second, the development of data based on material fabricated by the same techniques used for prototype or production parts has in general not been obtained. Third, the properties of ceramic materials are subject to different laws than those governing the behavior of ductile metals, so that data acquisition and interpretation and component design require different procedures. Basically, while the failure of metal structures is governed by dislocation motion as well as void formation and grain boundary sliding, the failure of ceramic structures occurs overwhelmingly as a result of brittle crack propagation. Failure in ceramics is therefore of a statistical nature, involving the concepts and procedures of fracture mechanics as well as distributions of flaw sizes and strengths. Clearly much work needs to be done, and many gaps exist in tables of data. There is however a considerable body of literature which can be consulted on specific topics.

#### Strength

Figure E-4 shows a comparison of strength levels as indicated by the 3-point bend test. Features to be noted here are the general level of strength and the temperature at which rapid decline occurs. While many metal alloys have superior strength at low and intermediate temperatures, their properties decline rapidly above 900°C. The strength levels of reaction-bonded silicon nitride (RBSN) and the alumina-silicate materials are considerably below those of the silicon carbides. Most oxide ceramics lose strength rapidly above 1200°C as seen by the curve for alumina. The highest strengths available from ceramic materials at or above 1200°C are provided by the silicon carbides. Reaction-sintered silicon carbides such as Super-KT (SKT) exhibit high strength levels to temperatures approaching the melting point of the free silicon they contain. Recent process improvements have shown the possibility of even higher strength levels. Above 1400°C (2550°F) all of the before-mentioned ceramics retain only residual strength levels. Sintered  $\alpha$ -SiC however maintains its strength up to the highest temperatures used in testing (1650°C [3000°F]). Since material and process optimization is continuing, even higher strengths are anticipated and, as indicated in Figure E-4, encouraging results have been seen.

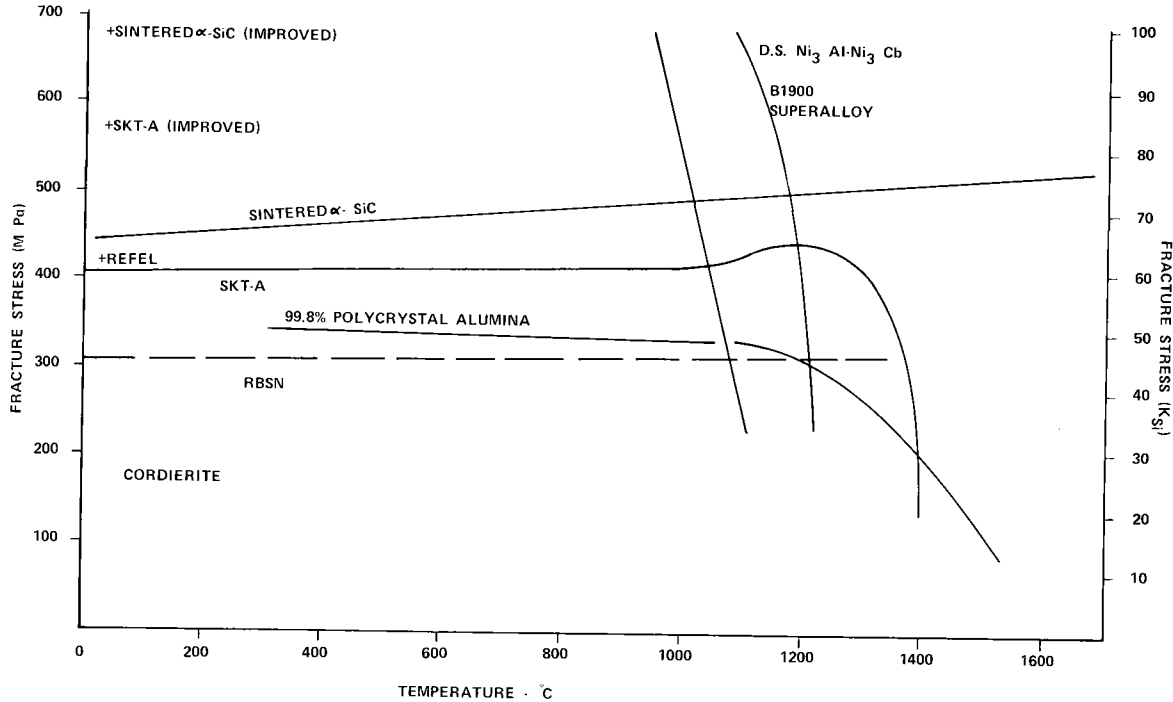


Figure E-4. Strength (3 pt Bend) of High-Performance Materials

#### Creep/Fatigue Resistance

The performance of metal alloys in high-temperature service is limited not by their ultimate strength, but by their creep and fatigue resistance. Similarly, while ceramic materials must be designed with this ultimate strength in mind, the practical design limitations may be established by phenomena such as slow crack growth and processes analogous to the creep and fatigue of metals.

Slow-crack-growth investigations have been performed for many glass and crystalline ceramic systems, but very little information is available for reaction-sintered or solid-state-sintered silicon carbide. The extent of slow crack growth in reaction-sintered silicon carbide is unknown, but it is expected to be measurable in the temperature range 1200-1400°C. Measurements on solid-state-sintered  $\beta$ -SiC have shown that slow crack growth is not observed below 1400°C (Ref. E-10) so that similar behavior is expected for sintered  $\alpha$ -SiC.

Viscous-grain boundary creep has been observed in many ceramics including hot-pressed silicon nitride, but has not been studied in reaction-sintered or solid-state-sintered silicon carbide. Again, because of the free silicon present in

the reaction-sintered material, a measurable rate is expected, whereas no creep is expected in sintered  $\alpha$ -SiC below 1400°C.

### Physical Properties

Table E-1 is a comparison of the physical properties of the silicon carbides and polycrystalline alumina. Since these properties are largely structure insensitive they can be taken as representative of these materials as they are optimized.

Table E-1  
PHYSICAL PROPERTIES OF CERAMIC MATERIALS

PROPERTY-MATERIAL	R.T.	TEMPERATURE °C		
		600	1000	1200
Elastic Modulus GPa ( $10^6$ psi)				
SKT-A	365 (53)	344 (50)	338 (49)	331 (48)
Sintered $\alpha$ -SiC	410 (59.5)			
RBSN	80-220 (11.6-32)			
99.8% $Al_2O_3$	406 (59)	393 (57)	379 (55)	365 (53)
Thermal Conductivity cal./cm.sec.°C				
SKT-A	0.197	0.060		
Sintered $\alpha$ -SiC	0.216	0.12		
99.8% $Al_2O_3$	0.080	0.040	0.028	
Thermal Expansion %				
SKT-A	-	0.3	0.45	0.55
Sintered $\alpha$ -SiC	-	0.28	0.44	0.54
99.8% $Al_2O_3$	-	0.25	0.41	0.63

### JOINING TECHNIQUES

#### Ceramic-Ceramic Joints

The problem of joining silicon-carbide components to form larger or more complex structures has received only moderate attention. Structurally sound joints have been made in prototype parts with a technique which forms a joint by the same

process by which KT-SiC is made—silicon infiltration and reaction of a porous carbon-rich zone. Considerable further work needs to be done on this problem. There are several approaches which should be examined and there are two aspects which need consideration. The two aspects of the problem are joint geometry and joint materials.

Joint geometry will be largely dictated by the materials used, their strength and use requirements. There are several possible geometries:

- Butt joint--tube ends flat and perpendicular to the axis
- Slanting joint--tube ends cut on a plane at an angle to the tube axis
- Tapered joint--tube ends beveled
- Step joint--either concentric steps or circumferential steps
- Sleeved joint

The justification for use of any except the butt joint is to increase the bonding area and therefore bond strength. Slant joints and step joints would be more difficult to prepare, fixture and fill with material than the tapered joint. The sleeved joint would provide the largest bonding area and be easily fixtured. Depending on joint material strength, either the tapered or sleeved joint would provide the greatest integrity.

There is a limited choice of joint materials due to the required operating environment. For KT or SKT-SiC, there is a choice between joint material which is similar to the base material, and that which is not. For structures which can be formed, joined in the green (unfired) state and then siliconsized (fired), this is the preferable method as it results in nearly undetectable joints with strength near that of the base material. For large structures this does not appear practical at the present time. Similar joint material can and has been used to join already fired components, but the problems of full infiltration and cracking on cooling have not been fully resolved. Alternative materials for these joints appear to be the alloys and intermetallic compounds between the IVB to VIB metals (Ti, V, Cr, Zr, Nb, Mo, Hf, Ta, W) or Fe group metals, and the elements B, C, Al and Si. Many compounds exist in this group which melt in the temperature range 1400-2500°C which is required for use in the anticipated maximum operating range of 1100-1400°C. Preformed foils of these materials could be applied to the joint which would then be heated to cause bonding. The wetting of SiC by these compounds is unknown however, as is the strength and oxidation resistance of the joints. The lower strength of the joint material may be compensated for by increased joint

area in design, and the ductility exhibited by many intermetallics at elevated temperatures could be beneficial. Obviously, considerable effort is required to determine which of these materials and designs provides the best solution to the joining problem. Some work in this area is currently being performed under sub-contract for EPRI Project RP545-1, "Coal Fired Prototype High Temperature Continuous Flow Heat Exchanger."

### Ceramic-Metal Joints

The surface environment of the ceramic-to-metal joint is different than the interceramic joint in that it is exposed to lower temperatures, but must allow for differential thermal expansion of the ceramic and metal components. Again one must consider both the design and materials aspects of the problem. The design problem is to:

- Allow for the difference in thermal expansion of  $13.5 \times 10^{-6} \text{ }^\circ\text{C}^{-1}$  for carbon steel and  $4.9 \times 10^{-6} \text{ }^\circ\text{C}^{-1}$  for silicon carbide
- Provide a gas tight seal
- Provide mechanical stability and support the weight of the SiC tubes

The seal can be made by metallizing the end of the SiC tubes, and brazing to the metal components, use of a graded seal approach, or a simple flanged joint can be made in which a SiC flange is allowed to slide relative to a metal flange during expansion or contraction. Ceramic metallization is a well-developed technology, which could be readily applied to SiC, allowing the brazing approach to be practiced. The severe thermal expansion mismatch at this joint however would lead to very large tensile hoop stresses in the SiC on heating and in the steel on cooling. A graded seal approach would reduce these stresses, but add other material uncertainties.

A design utilizing a silicon-carbide flange, joined to the SiC tube by the method of the preceding section, would allow for the differential thermal expansion, and if a superalloy "O" ring seal were used, would provide a gas tight joint.

### CERAMIC DESIGN METHODOLOGY

The strength of ceramic materials has been found to be controlled by the stress necessary to cause propagation of a suitably oriented flaw in the material. A modified Griffith criteria gives this stress as:

$$\sigma_f = \frac{1}{Y} \left( \frac{2 E \gamma}{C} \right)^{1/2} \quad (\text{E-1})$$

Where  $Y$  = a geometric constant

$E$  = Young's modulus

$\gamma$  = effective surface energy of the crack

$C$  = flaw (crack) size

Since all materials contain a distribution of internal and surface flaw sizes, there will be a distribution of strengths of test elements containing these flaws. The weakest link model of Weibull (Ref. E-11, E-12) has been used to describe this distribution:

$$P = \exp -D \left( \frac{\sigma_f - \sigma_u}{\sigma_o} \right)^m \quad (E-2)$$

Where  $P$  = survival probability

$D$  = the stressed volume

$\sigma_f$  = failure stress

$\sigma_u$  = zero probability stress

$\sigma_o$  = a "characteristic" stress

$m$  = Weibull modulus

Performing a series of tests and fitting the data to this equation or its logarithmic equivalent will yield the parameters of the strength distribution.

It has also been found that under some conditions of temperature, stress, and atmosphere, most ceramic materials are subject to slow growth of the preexistent flaws. The rate at which cracks grow is unique to a given stress state and environment, so that the time for any given flaw to grow to the size which is necessary for catastrophic propagation and fracture can be predicted. It is thus possible to construct stress-probability-time (SPT) diagrams for materials given sufficient experimental data (Ref. E-13).

Analytical procedures, such as the finite element method, have been developed to determine the stress levels experienced throughout a body subjected to external or internal thermomechanical influences. In this method, the body is broken down into a finite number of geometrical elements and the interaction of these elements is traced until equilibrium is achieved. Thus, any real machine or component may be analyzed and the levels of stress developed at all points can be determined. The probability of failure, or the time to failure of any such point can then be determined from the SPT diagram for that material.

As a result of the use of these tools, much of the uncertainty can be taken out of design of components using brittle materials. In addition, if it can be determined that there are no flaws larger than a certain size, either by proof testing or NDI, the life of such components can be assured.

#### FABRICATION OF LARGE SiC STRUCTURES

Straight tubing of the size required for both the bench-model and commercial-size units are standard items in extruded KT-SiC. Work is currently in progress to extend this technology to Super KT and sintered  $\alpha$ -SiC. Joining of tubes is practical in the manufacture of Globar heating elements and to a limited extent in heat exchanger and chemical process tubing as discussed in previous sections, however, further development of joining technology is advisable.

Because of the lack of ductility in ceramic materials it is not advisable to transport large fabricated assemblies over long distances. In addition, furnaces are not envisioned which will be capable of firing the entire 40-foot long U-tube proposed for the solar collector/heat exchanger. As a result, field assembly, joining and erection techniques need to be developed. Based on the discussion in previous sections, the problem of field fabrication breaks down to developing a firing method for the interceramic joints, and a question of whether this should be done in place or at ground level and the entire U-tube hoisted into place. Fixturing could certainly be developed to accomplish the latter, so that the problem to be addressed here is the method of joining.

The requirements for forming a structurally sound joint of any of the types discussed are an inert atmosphere and a source of heat capable of raising the tube temperature around the joint uniformly to 1500°-2000°C. The most effective way to accomplish this is with a suitably-designed, oxide ceramic-tube atmosphere container with adequate internal insulation and through which the field of an induction heating coil will pass, heating the SiC by self-resistance. Fixturing would be required to keep the tube ends aligned and pressed together.

#### SUMMARY

Use of large, high-temperature structures such as the solar energy collector/heat exchanger, require a choice of materials which considers material properties, reliability, forming and fabrication, cost and availability. For operation at temperatures above 900°C (1650°F), metallic materials are not available which can

provide the structural strength required at a reasonable cost so that use of ceramics is essential. The material property requirements are high strength, creep resistance, oxidation resistance, impermeability, good thermal conductivity and thermal shock resistance. A comparison of the properties of silicon carbide with those of other candidates shows its clear superiority in all areas. There are now two types of silicon carbide which are being optimized to provide the reliability required for this and other high-temperature applications. These materials are reaction-sintered Super KT and the new solid-state-sintered  $\alpha$ -SiC. Extrusion technology exists for forming the tube sections required, and is currently being adapted for these high-reliability forms of SiC. Other fabrication techniques are being developed which will provide the U-bend and flange components. Since the methods of forming Super KT are closer to existing technology for tube manufacture, it is recommended that the bench-model heat exchanger be fabricated using Super KT. While the cost of these materials in large quantities cannot be accurately predicted, the raw materials used are plentiful and of low cost. Process development is proceeding so that high yields will allow significant cost reductions. The cost of the bench-model heat exchanger shown in the attachment, therefore, reflects only a small cost premium for tubing over the current selling price of standard KT.

#### REFERENCES

- E-1 Coppola, J. A. and C. H. McMurty, "Substitution of Ceramics for Ductile Materials in Design," Presented at the National Symposium on Ceramics in the Service of Man, June 7, 1976, Carnegie Institution, Washington, D.C.
- E-2 Ruff, O., "Formation and Dissociation of Silicon Carbide," Trans. Electrochem Soc. 68, 87-109 (1935).
- E-3 Tone, F. J., "High Temperature Products of Silicon," Ind. Eng. Chem., 23, 1312-1316 (1931).
- E-4 U. S. Patent 2,938,807.
- E-5 Taylor, K. M., "Improved Silicon Carbide for High Temperature Parts," Materials and Methods, Oct. 1956.
- E-6 U. S. Patent 3,495,939.
- E-7 Prochazka, S., "Investigation of Ceramics for High-Temperature Turbine Vanes," Final Report NASC Contract Rept. No. SRD-72-035 (March 1972) (AD742857).
- E-8 Giddings, R. A., C. A. Johnson, S. Prochazka, R. J. Charles, "Fabrication and Properties of Sintered Silicon Carbide," General Electric Co. Rept. No. 75CRD060, April 1975.
- E-9 "High Performance Ceramic Developed," Chem. and Eng. News, June 14, 1976, p. 8.

- E-10 Evans, A. G., F. F. Lange, "Crack Propagation and Fracture in Silicon Carbide," J. Mat. Sci. 10, 1659-1664 (1975).
- E-11 Weibull, W., Ing. Vetenskaps Akad. Handl. 155, 5 (1939).
- E-12 Weibull, W., "A Statistical Distribution Function of Wide Applicability," J. Appl. Mech. 18, 292 (1951).
- E-13 Davidge, R. W., J. R. McLaren, G. Tappin, "Strength-Probability-Time (SPT) Relationships in Ceramics," J. Mat. Sci. 8, 1699-1705 (1973).

## Appendix F

### RECEIVER TOWER DESIGN

#### OBJECTIVE

The objective of this appendix is to provide a conceptual design for a support tower, turbine generator support structure, and a receiver support structure for a solar power generating station; also to provide preliminary cost estimates for these components.

#### DESIGN CRITERIA

##### Plant Site Criteria Affecting the Structural Design

The plant is to be located in California, Seismic Zone 3. The plant is to be operational when the wind at 30-ft elevation is 30 mph. (At greater velocities it is assumed that the heliostat field would be shut down.)

##### Tower-Height Considerations

Tower height-turbine size combinations considered are:

- 700 ft--60 MW (see Figure F-1)
- 1300 ft--60 MW
- 840 ft--25 MW
- 450 ft--25 MW

##### Geometry

Preliminary arrangements on the turbine room floor and on the cavity receiver support level were considered to be suitable for a conceptual design of the structural support system (see Figures 6-11 through 6-17).

##### Loads

The 60-MWe turbine generator weighs approximately 880 tons. The 25-MWe turbine-generator weighs approximately 500 tons. These weights include the startup motor and the regenerators.

Each of the four receiver cavities weighs approximately 350 kips, including the insulation and framing system. Detailed loads are given on the General Electric drawings for the turbine generator.

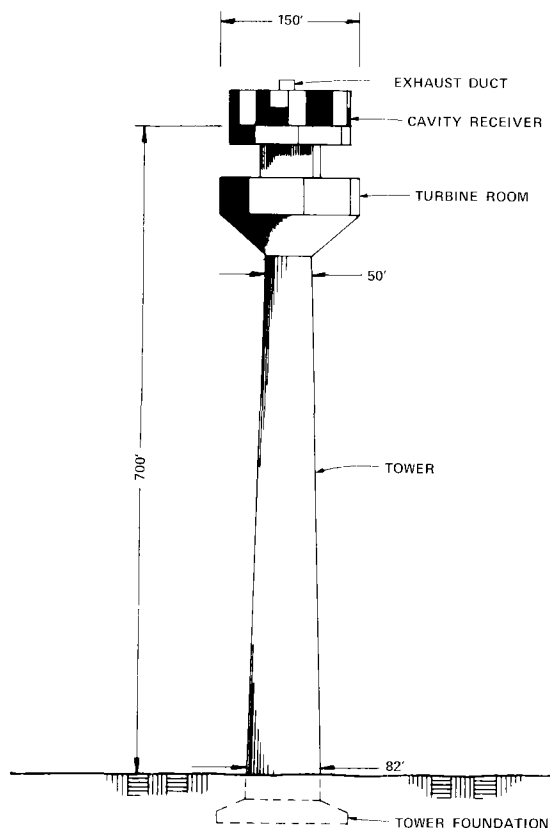


Figure F-1. EPRI Gas Turbine Support Tower

#### Structural Materials

Concrete	$f'_c = 4000$ psi (tower), 3000 psi (foundation mat) $f'_c =$ ultimate strength of concrete
Reinforcement	Grade 60
Steel	A36

#### Design Codes and References

Design codes and references are as follows.

- ACI 318-71 for reinforced concrete (excluding the chimney).
- ACI 307-69 for reinforced concrete chimney.
- AISC for structural steel.
- B&V Standard Practices Manual S-419.01 for wind pressures.

#### Construction and Erection Considerations

The construction of the support structure must utilize proven construction techniques. A means must be provided for transporting the components of the

turbine generator and the receivers to the top of the tower. Furthermore, provision must be made to lower to the ground and raise equipment components which cannot be serviced on the turbine room floor.

## STRUCTURAL DESIGN OF SUPPORT TOWER

### Design Criteria

The tower is designed as a conventional reinforced concrete chimney according to ACI 307-69. Therefore, the nominal thickness is assumed to be 1/24 of the outside diameter. At the top, where the steel frames into the chimney, the wall thickness should be increased to perhaps 5 feet. The outside diameter increases 5 ft in every 100 ft.

For the 60-MW plant the top outside diameter is assumed to be 50 ft; for the 25-MW plant, 45 ft. These diameters are considered appropriate for the plant arrangements. (The top of the chimney is approximately 100 ft. below the center of the receiver cavity.)

### Economic Criteria

Reinforced concrete is assumed to cost \$325/yd<sup>3</sup> in the chimney. The high cost is attributed to the complexity of the reinforcement and the slipforming process. Numerous embedments must be placed during the slipforming (e.g., for structural steel legs for the turbine support structure and for installation rails attached to the chimney). The cost per cubic yard is approximately supported by a study of recent fossil plant stack costs.

### Analysis and Design Procedure

The chimney is designed to resist gravity plus wind, and gravity plus seismic loads (see Figure F-2). The four power-height configurations were analyzed seismically according to the following steps. All computations were approximate.

- Compute the weight of all components atop the chimney.
- Convert this weight to an equivalent tower height.
- Compute the fundamental period of vibration of the "equivalent" chimney.
- For a Zone 3 earthquake, for a chimney with the above fundamental period of vibration, compute the total lateral seismic force, or base shear.

- From studies on the 10-MWe solar plant (B&V Project 7021), assume this seismic force acts as  $2/3$  the chimney height. (This assumption is in lieu of a lengthy analysis.) This gives the seismic overturning moment.
- At the base, for the geometry assumed in "Design Criteria" above, the normal and shear stresses are computed.
- If the normal stresses are reasonable, it is assumed that the chimney size is workable, although probably not the optimum size. It is assumed that the seismic shear stresses will be handled by special diagonal reinforcement if the capacity of the concrete itself is insufficient.

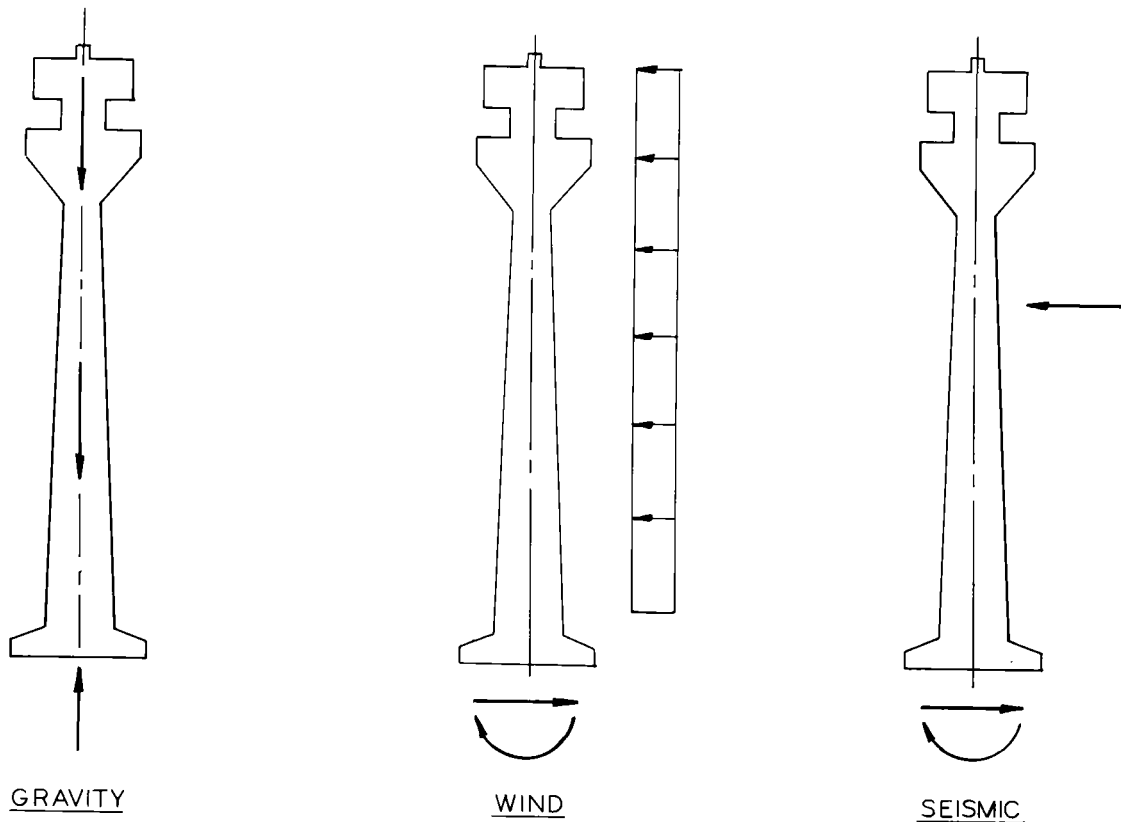


Figure F-2. Loads

Results of the Study of Four Possible Configurations

The results of the preliminary designs are presented in Table F-1. The normal stresses in the reinforced concrete chimney were acceptable, so the assumed chimney geometry was reasonable, if not optimal. All four designs require seismic reinforcement. That is, reinforcing bars placed on a 45-degree angle to

Table F-1  
COST COMPARISON

CONSTRUCTION CRITERIA	60-MW PLANT		25-MW PLANT	
	700' TOWER HEIGHT	1300' TOWER HEIGHT	450' TOWER HEIGHT	840' TOWER HEIGHT
Dimensions				
Top OSD	50'	50'	45'	45'
Base OSD	82'	112'	64.5'	84'
Top thickness	25"	25"	22.5"	22.5"
Base thickness	41"	56"	32.25"	42"
Tower, \$325/yd <sup>3</sup>				
Volume conc.	13,200 yd <sup>3</sup>	39,600 yd <sup>3</sup>	5,500 yd <sup>3</sup>	15,500 yd <sup>3</sup>
Weight	53,500 k	160,600 k	22,200 k	62,900 k
Cost	\$4,300,000	\$12,900,000	\$1,800,000	\$5,100,000
Top Structure, \$400/yd <sup>3*</sup>				
Volume conc.	5,200 yd <sup>3</sup>	5,200 yd <sup>3</sup>	3,500 yd <sup>3</sup>	3,500 yd <sup>3</sup>
Weight conc.	21,000 k	21,000 k	14,000 k	14,000 k
Cost	\$2,100,000	\$2,100,000	\$1,400,000	\$1,400,000
Foundation Mat, \$125/yd <sup>3</sup>				
Diameter	140'	190'/210'***	120'	150'
Thickness, max	22"	38"/40"	17"	24"
Volume conc.	12,500 yd <sup>3</sup>	39,900/51,300 yd <sup>3</sup>	7,100 yd <sup>3</sup>	15,700 yd <sup>3</sup>
Weight	50,600 k	161,600/207,800 k	28,800 k	63,600 k
Cost	\$1,600,000	\$5,000,000/\$6,400,000	\$900,000	\$2,000,000

Table F-1 (Cont.)

COST COMPARISON

CONSTRUCTION CRITERIA	60-MW PLANT		25-MW PLANT	
	700' TOWER HEIGHT	1300' TOWER HEIGHT	450' TOWER HEIGHT	840' TOWER HEIGHT
Totals**				
Weight	125,100 k	343,200 k*** 389,400 k	65,000 k	140,500 k
Estimated Cost	\$8,000,000	\$20,000,000 \$21,400,000	\$4,100,000	\$8,500,000

\* Assume, all structural components made of concrete.

\*\* Does not include equipment.

\*\*\* First value for 10 TSF bearing pressure, second value for 30 TSF bearing pressure, bearing does not control for lower towers.

the horizontal, placed in the center of the reinforced concrete wall, spiral up the chimney until the shear stress in the chimney is low enough that the concrete can carry the seismic shear without the aid of the seismic reinforcement.

### Conclusions

Any of the towers sized as recommended in the table could be constructed. However, there are intangible problems involved in constructing very tall towers. The only reinforced concrete tower yet built over 1000 ft tall, to our knowledge, is the Canadian National Railways tower in Toronto, the world's tallest free-standing structure at about 1500 ft. Obviously an extensive detailed design is warranted once a concept has been selected.

## STRUCTURAL DESIGN OF TOWER FOUNDATION

### Design Criteria

Under seismic loading there should be no uplift of the foundation. Also, the maximum foundation pressure must not exceed an allowable bearing pressure. The bearing capacity of the supporting material is a site-dependent parameter. For this study it is assumed that the site would be excavated to competent rock, presuming it is available at a reasonable depth. Two allowable bearing pressures are evaluated, 10 tons/ft<sup>2</sup> (very stiff soil or soft rock) and 30 tons/ft<sup>2</sup> (medium rock).

### Economic Criteria

Reinforced concrete in the foundation mat is assumed to cost \$125/yd<sup>3</sup>.

### Analysis and Design Procedure

For the vertical gravity loads and seismic moments, the combined stresses were computed for trial sizes of circular mats. The process is an iterative one. It is necessary that

$$\frac{P}{A} + \frac{Mc}{I} \leq 10 \text{ tsf or } 30 \text{ tsf} \quad (\text{bearing})$$

and

$$\frac{P}{A} - \frac{Mc}{I} \geq 0 \quad (\text{no uplift})$$

### Results of the Study of Four Possible Configurations

The results of the preliminary designs are given in Table F-1. For all but the 1300-ft tower the mat size is governed by the criterion for no uplift. Only for the 1300-ft tower on material with allowable 10 tsf bearing capacity did the bearing pressure actually govern.

### ECONOMIC COMPARISON OF THE FOUR POSSIBLE CONFIGURATIONS

#### Comparison Criteria

In order to develop total costs for the four possible configurations the chimney and foundation mat costs previously discussed were combined with an estimate for the cost of the top structures. The latter cost was estimated from an approximate quantity takeoff of the configuration proposed by Systems Engineering. The upper structure was assumed to be of reinforced concrete which had a unit cost of \$400/yd<sup>3</sup>. The 25-MW unit was assumed to have 2/3 the volume of the 60-MW unit (turbine floor diameter somewhat smaller, only 2 cavities).

#### Results of the Comparative Study

The results are given in Table F-1.

#### Conclusions

The results in Table F-1 were coupled with other costs developed by Systems Engineering in order to arrive at the optimal overall design. Systems Engineering concluded that all further studies should assume a 60-MW plant on a chimney with the receivers located 700 ft above the ground. In the remainder of this report no other configurations are presented.

#### WIND DEFLECTIONS OF TOWER

The wind drift of the 700-ft, 60-MW tower was computed by using the average wind load per foot of tower height and the moment of inertia of the tower at mid-height. Obviously this approximate analysis procedure is intended only to quickly compute the order of magnitude of the deflection. An analysis of the tower as a uniformly-loaded cantilever beam of uniform cross-section indicated that the total deflection at the turbine level under a 30 mph wind (specified at 30 ft above the ground) is of the order of 1.2 inches. Values for a range of wind velocities are given in Table F-2. It should be noted, however, that total deflection may not

be an important consideration in the design of the equipment because it is relative deformations between support points which cause stresses in equipment and shaft curvature. In order to compute these more important deflections the members must be sized and the entire upper structure modeled and analyzed as a space frame. The longest natural period of vibration of the tower is of the order of 2.5 seconds. The lowest natural frequency is therefore about 0.4 Hz, probably low enough to avoid significant inertial problems with turbine bearings due to wind gusts but a detailed study would be appropriate.

Table F-2  
DEFLECTIONS AT TURBINE FLOOR DUE TO WIND

BASIC WIND VELOCITY AT 30-FT ELEVATION (mph)	TOTAL DEFLECTION AT TURBINE FLOOR (inches)
30	1.2
40	2.0
50	3.2
60	4.6
70	6.3
80	8.2
90	10.3
100	12.8
110	15.5
120	18.4

#### STRUCTURAL DESIGN OF TURBINE GENERATOR SUPPORT STRUCTURE

##### Design Criteria

The support floor must be sufficiently rigid in all directions that relative displacements of the turbine generator support points are minimized. The floor system must be designed for all of the static and dynamic loads provided by the manufacturer, piping loads, and equipment laydown loads.

### Conceptual Design of the Support Structure

The finished floor should be of reinforced concrete to serve as a wearing surface and vibration damper. Furthermore, there is probably a psychological advantage for workers and visitors in that the concrete would provide a reassuring image of strength in such a tall tower. However, if the upper structure were to be constructed entirely of reinforced concrete then the weight would be significant and probably lead to serious design problems with the chimney, particularly for the seismic load. Certainly formwork for a concrete structure would be difficult to construct for such complex geometry. It is anticipated, but cannot yet be proven conclusively, that the structural steel framing will be more economical than reinforced concrete framing. Undoubtedly the steel erection would proceed more quickly than concrete work, thereby saving time on the schedule. Therefore, unless further design work is performed for both alternatives, including the design of the chimney for both cases, it seems wise to proceed with a structural steel frame with reinforced concrete floors.

The support floor in the region of the regenerators (GE design) must be depressed approximately 2'-0". This is an undesirable design constraint, the necessity for which should be pursued. The structure cost increase created by this constraint should be considered.

The floor framing scheme is shown on Figure F-3. Four main trusses in each direction, each about five feet deep, form a space grid to support the equipment and the adjacent floor load. These trusses bear on the top of the chimney and are supported also by diagonal struts that frame into two levels of the chimney. These struts are radial except for those under the two interior trusses supporting the turbine generator for which the struts are parallel to the trusses to permit the installation hoist to travel between the trusses. Four secondary trusses, perhaps also five feet deep, but of lighter construction than the main trusses, pass from the intersection of the main exterior trusses to the exterior wall. These trusses carry not only turbine room floor loads but also carry, through one vertical member, the column loads from the structure above. These four main columns probably are built up from plates. The remainder of the floor is framed with rolled W-section (wide-flange beams). Around the outside walls, at the ends of all radial beams and trusses, there are columns that support the walls and roof of the turbine room. Extensive bracing of these walls gives rigidity to the turbine room wall and roof system. The roof framing is shown on Figure F-4.

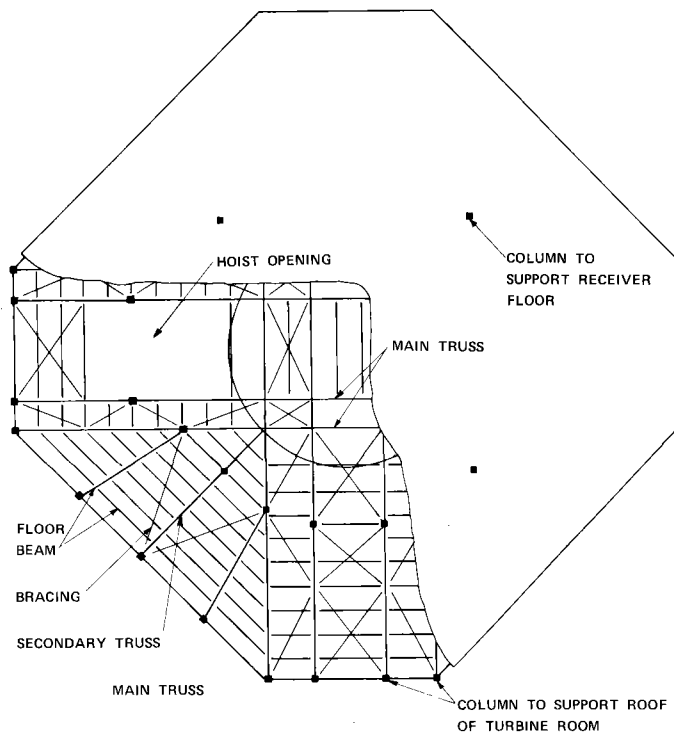


Figure F-3. Plan View of Framing for Floor of Turbine Room

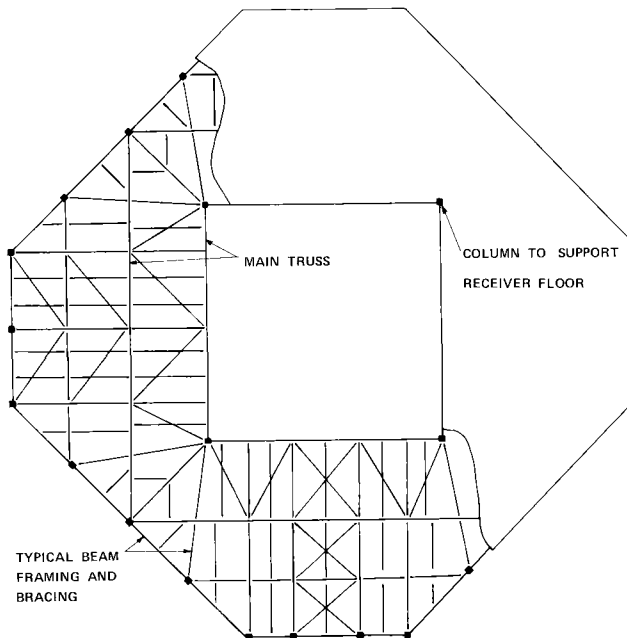


Figure F-4. Plan View of Framing for Roof of Turbine Room

## STRUCTURAL DESIGN OF CAVITY RECEIVERS AND SUPPORT STRUCTURE

### Design Criteria

The framing around the cavity must be rigid to prevent fracture of the brittle ceramic materials used within the cavity. The support structure for the cavity receivers must be sufficiently rigid in all directions that relative movements of the piping anchor points do not unduly stress the piping. All structural steel must be protected from the intense heat in the neighborhood of the cavities.

### Conceptual Design of the Receiver Support Structure

Figure F-5 indicates a framing concept for the structural steel for the cavity. A finished floor of reinforced concrete is to be provided for access to the cavities. As shown on Figure F-6, the support structure is assumed to be framed of eight structural steel trusses which form a space grid supported on the four columns. Rolled sections for floor beams and bracing complete the system.

## STRUCTURAL DESIGN OF BRACING SYSTEM

### Design Criteria

A horizontal plane and vertical plane structural steel bracing system is required throughout the structures in order to provide rigidity during wind and seismic activity, to prevent structural instability of the space truss (a problem because of the configuration), and to prevent lateral buckling of trusses and floor beams.

### Conceptual Design of the Bracing System

The diagonal braces which support the perimeter of the turbine room floor from the chimney are assumed to be box sections built up from plates, similar to columns frequently used in major bridges. All other bracing could probably be rolled W or WT sections.

## CONSTRUCTION AND INSTALLATION PROCEDURES

### Foundation Mat Construction

In order to provide an adequate supply of concrete for the construction of the mat and the chimney, a portable concrete batch plant may be required at the site. The foundation mat would be of conventional construction, using the supporting rock for bottom and side formwork. The mat concrete would probably be placed in about five pours.

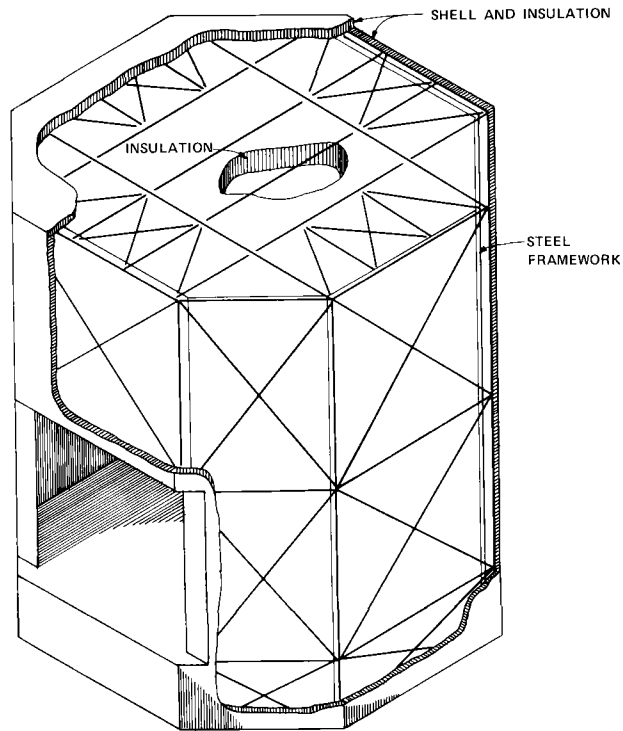


Figure F-5. Structural Framing for Cavity Receiver/Heat Exchanger

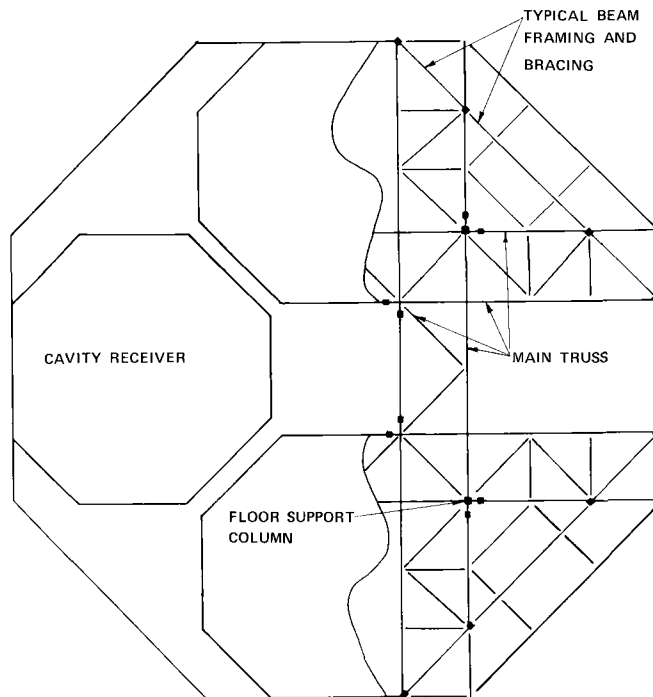


Figure F-6. Plan View of Framing for Cavity Support Floor

### Chimney Construction

It is anticipated that a specialty contractor such as M. W. Kellogg would be retained to slip-form the reinforced concrete chimney. The requirements for diagonal seismic reinforcement and placing of numerous embedments and some block-outs will cause the chimney to be more expensive than those for fossil fuel plants.

### Erection of Structural Steel for the Turbine Generator Support Structure

A small top-mounted crane could be used to raise the structural steel components to the turbine support floor level. The use of truss, rather than plate girder, construction will reduce the load-handling requirements. Once the main trusses have been erected and diagonally braced, then placement of the secondary trusses with their diagonal bracing and floor beams could proceed. Steel decking could immediately be placed on the floor beams to provide working surface. Unless the steel erector chose to do otherwise, the floor could be completed except for the equipment installation area between the main trusses under the air-intake ducts. (Normally, no concrete would be placed until the steel erection is completed.)

Installation of the rail-mounted hoist on the chimney (see "Installation of the Equipment" below) could be undertaken before or after the structural steel and concrete is completed but not concurrently with these activities because of the danger to workers below from falling objects. Clearly, the hoist could be used to advantage by the steel erector if it were installed as early as possible. For example, secondary truss components could be preassembled off the site rather than assembled from individual pieces atop the tower. Furthermore, many components could be raised in one lift with the hoist. The small crane would be used to position the members.

### Erection of Structural Steel for the Cavity Receiver Support Structure

The top-mounted crane would be used to position all remaining structural steel--cavity receiver support structure, bracing in the horizontal and vertical planes, miscellaneous steel (stairways, ladders, grating, etc.). The steel erector would undertake a study of the most efficient placement sequence.

### Installation of the Equipment

Major items of equipment are too heavy to be lifted by a conventional top-mounted crane with a long boom. One obvious solution is to install a rail-mounted hoist

which travels up the side of the chimney (see Figure F-7). Such a scheme is borrowed from bridge erection techniques where winch systems are frequently used. Two hoist lines would travel over sheaves mounted on a (probably temporary) frame atop the chimney, through a series of blocks to reduce the line load and then to a double-drum electric winch which would probably be mounted at and attached to the base of the chimney. An equalizer system would be required to split the load of the two lines and a safety braking system would have to be devised to prevent the hoist from falling should a line break.

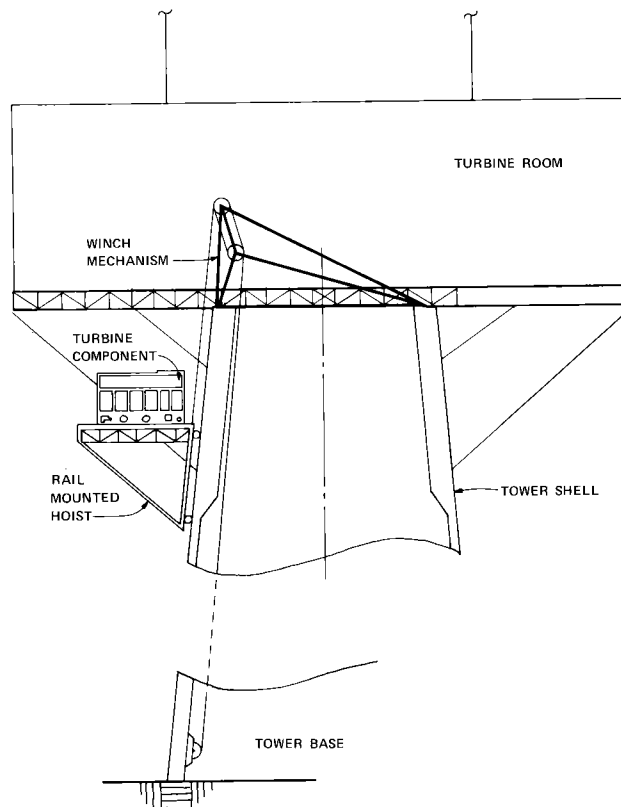


Figure F-7. Equipment Installation Hoist

The hoist would rise between the two main trusses which support the turbine generator, in the area under the air-intake ducts. Equipment would be placed on skid beams on the hoist platform as well as on the support floor in order to facilitate moving the equipment horizontally. "Come-alongs" could be used to pull the equipment over greased skid beams and sand jacks or hydraulic jacks

could be used to lower the equipment on the sole plates or anchor pads. The sequence of installation of the equipment would obviously be important. Certain items would have to be temporarily located until other items were installed. Probably the hoist would have to be dismantled prior to final placement of all equipment. Obviously the startup motor, parts of the intake duct, and some other components could not be positioned until the hoist opening had been closed off.

If a major item of equipment had to be replaced then the hoist would again have to be installed, the hoist opening made accessible, and the equipment skidded over to the hoist. Alternatively, the generator rotor or small components at that end of the turbine generator system could more easily be lowered by installing a portable hoist near the ends of and between the adjacent two main trusses which could lower the load vertically on two lines. A section of the floor could be removable to facilitate such hoisting work. This concept could be repeated near the ends of, and between, the two main trusses which run in the perpendicular direction. The main rail-mounted hoist would then be used only for installation of most equipment and removal of the heaviest components.

An alternative location for the hoist opening would be between the main trusses perpendicular to the axis of the turbine generator system. This location would not affect the major equipment items if the heavy regenerators could be relocated so that they are not located over the interior truss.

#### ELEVATORS, STAIRS, AND LADDERS

A personnel and small equipment elevator would be installed to rise vertically within the chimney to about 20 feet below the top of the chimney. (The hoisting mechanism would be located above the last elevator stop.) A caged ladder with rest platforms, or preferably a stairway, must parallel the route of the elevator. Until the final equipment arrangement has been determined, the location of an elevator and stairway for the top 20 feet cannot be specified. If there is not room for a hydraulic elevator or stairway to the turbine room floor from within the confines of the chimney then these systems would operate from a platform on the outside of the chimney. The stair and elevator would be sheltered by the enclosure around the diagonal struts and be accessed via a mandoor through the chimney.